A thesis presented for the degree of

Master of Science

on

Synthesis and Self-Assembly of Gold and Gold-Silver Nanorods

by

Maarten Bransen

under supervision of

Jessi E. S. van der Hoeven.
Prof. Dr. Alfons van Blaaderen
Prof. Dr. Petra E. de Jongh

for the course

Nanomaterials: Chemistry and Physics

May 21, 2017

Universiteit Utrecht

Soft Condensed Matter
Inorganic Chemistry and Catalysis
Debye Institute for Nanomaterials Science
Faculty of Science
Universiteit Utrecht

Abstract

Gold nanoparticles are widely studied because of their interesting optical properties and chemical stability, with applications such as (photo)catalysis, surface-enhanced Raman spectroscopy, data storage and photothermal (cancer) treatment. In particular, gold nanorods (AuNRs) have been extensively studied due to their excellent plasmonic properties. The anisotropic shape of the nanorods results in both a strong and highly tunable plasmon resonance from 500 to 1200 nm, depending on the aspect ratio of the rods. In addition to this, the plasmonic properties of the AuNRs can be tuned and enhanced by self-assembling the rods into larger structures, whereby plasmonic hot spots are created between the particles. Enhanced plasmonic properties in the visible spectrum can be achieved by introducing a second metal such as silver, which has superior plasmonic properties compared to gold. In this project, we first synthesized Au-Ag nanorods with either a core-shell or a homogeneously alloyed structure. The latter could be achieved by heating the Au-Ag core-shell NRs under an inert or reducing atmosphere, without losing the anisotropy of the NRs. We studied the influence of composition and metal distribution on the optical properties and gained insight into the influence of the gas atmosphere on the alloying. Secondly, the plasmonic properties of AuNRs could be enhanced by self-assembly into novel plasmonic structures. The phase behaviour of silica-coated AuNRs was studied in 2D and in spherical confinement via solvent evaporation. Using this method it was possible to form spherical supra-particles consisting of ordered AuNRs, which may be interesting for applications such as SERS and plasmon-enhanced fluorescence due to plasmonic hot-spots between the tips of aligned AuNRs.

Contents

Chapter 1

Introduction

All throughout history humans have been intrigued by the properties of gold. It is one of very few metals that can be widely found on earth in its metallic state, and it is likely to be the first metal we have ever found and worked with [1, 2]. Its apparent resistance against chemical reactions such as oxidation lies at the basis of its use in art and jewellery and earned gold the title of 'noble metal'. For most of human history, gold was assumed to react with nothing but a handful of materials. Since the advent of nanotechnology however, we know these bulk properties do not hold when the size of gold objects is reduced to the nanoscale range. Many of the bulk characteristics vanish and remarkable new properties appear. The increased surface to volume ratio leads to an increase in chemical reactivity and a lower melting point. When the particle size is reduced to the typical length scale of physical phenomena, confinement effects may appear that lead to drastically different behaviour. The size of (gold) nanoparticles is thus an important factor for the properties of the material [3–5]. One of these properties that is a direct result of confinement effects is the interaction of nanoparticles with light. For small (1–100 nm) gold particles the absorption of light is due to the localised surface plasmon resonance, which is the collective oscillation of the free electron gas in the metal. Since the frequency of this oscillation, and thus the frequency of light it interacts with, is directly related to the size of the particle, the absorption peak can be tuned by varying the particle size.

Unbeknownst to them, Roman artisans already used this over 1700 years ago in one of the first known examples of noble metal nanoparticles as a colourant: the Lycurgus cup (Fig. 1.1). Due to the effects of scattering and absorption of the nanoparticles embedded in the material, the reflected and transmitted light differ in colour, which makes the cup seemingly change colour depending on the direction it is illuminated and viewed from. The secret of this material was only unravelled when the material was examined with an electron microscope in the 1980's, revealing ~50–100 nm gold and silver nanoparticles [6]. It was in much the same way that the presence of gold in their materials allowed medieval artists to obtain the bright red and purple colours in stain-glass windows for churches. Unlike organic and inorganic dyes, these colours never degraded or bleached upon prolonged light exposure. It was properties like these, that inspired scientists to work on the development of nanostructured materials. Since the 1980's, the number of publications on nanotechnology and gold nanoparticles have grown exponentially [4].

Figure 1.1: The Lycurgus Cup, the first known example of dichroic glass where the colour changes depending on whether light is reflected (left) or transmitted (right). Reprinted from [6]

It is nowadays possible to synthesise nanoparticles with a high degree of control over the chemical composition, size, shape, monodispersity and surface properties. This enabled the development of synthesis methods for materials with (optical) properties that are unlike that of any known bulk material. In this work, we study the properties of *rod-like* gold nanopartiles, which do not only have a nanometer

scale size, but also an anisotropic shape. When particles have an anisotropic shape, confinement effects will be different in the different directions and for gold nanorods, this results in a splitting of the localised plasmon resonance modes into two: the transversal and the longitudinal directions. The absorption of light by gold nanorods (AuNRs) due to SPR therefore consists of two distinct peaks. While the transverse SPR is similar to that of spherical particles with an extinction maximum between 500 and 540 nm, the longitudinal surface plasmon resonance (LSPR) can be tuned over a wide range of wavelengths from the visible ($\sim$ 600 nm) to far into the near-IR ($\gg$ 1200 nm). This tuning is achieved purely by varying the aspect ratio, the ratio between the length and diameter L/D, of the nanorod [4, 7–9].

1.1 Applications

Because of their remarkable size and shape specific properties, gold nanoparticles are useful for a range of applications in industry, research and medicine. We discuss here some of the relevant applications of AuNRs in general and of the research in this thesis specifically. In industry, gold nanoparticles can be used for heterogeneous catalysis. Despite the unreactive nature of the bulk material, supported AuNPs show good activity and selectivity for many reactions such as CO oxidation and selective oxidation and hydrogenation. Moreover, gold catalysts are often active at much lower temperatures than other materials which makes safer and more environmentally friendly reaction conditions possible [10–13]. Unlike many other materials, it is even possible to use unsupported colloids as catalysts due to the excellent stability of gold [13]. While some work has been done on the properties of anisotropic particles in catalysis, much remains unclear and currently industrial applications are mainly limited to particles with an isotropic shape [3, 14, 15]. The well-defined tunable structure and electronic properties of gold nanorods in combination with our ability to characterise them very precisely make them ideal as a model system for fundamental studies of catalytic processes. Moreover, their tunable optical absorption may make them potential candidates for plasmon-enhanced (photo)catalysis where the absorption of a photon improves the reaction speed or selectivity [14, 16].

For biological application the AuNRs are of interest because their absorbance can be tuned to have a maximum between 600 and 1350 nm, where human tissue has the lowest absorption for electromagnetic radiation [17–19]. Unlike ionising radiation and x-rays, IR-radiation does not cause any damage to healthy tissue at the dose-rates needed for deep tissue penetration. Furthermore, gold nanoparticles of >5 nm are considered non-toxic and biocompatible, and can be functionalised with many ligands for selective targeting of tissues and tumours, for drug delivery applications and for enhanced cell-uptake [20, 21]. Due to the coupling of the plasmon resonance with phonons, they can be used for photothermal treatment where the AuNRs locally heat their environment. This IR-irradiated heating can be strong enough to destroy tissue with minimal damage to surrounding areas [7, 19, 20, 22]. In addition to treatment, the particles can be used at lower light intensity to act as contrast agent for in-vivo imaging [23]. Lastly, gold nanoparticles can be used as drug delivery agents by adsorption of biologically active molecules. Excitation of the LSPR may be used to selectively control uptake and release of medicines [20]. A third major application of AuNRs is in nanoscale sensing. This is generally achieved with surface-enhanced Raman scattering (SERS). There, the strong electric field of the resonating electron promotes the signal for Raman-spectroscopy, a commonly used complement to IR-spectroscopy for the identification or organic molecules [7, 24, 25]. Lastly, AuNRs may have applications in data storage [26], optoelectric devices and in enhancement of the properties of photonic crystals [27]. For different applications, the requirements on the properties of the particles vary greatly. For some applications such as SERS and catalysis rough morphologies may be preferable, while others rely on smooth defect-free nanocrystals. For bioimaging the near-IR wavelengths are useful while nanoplasmonic devices or photocatalysts could be more effective in the visible.

1.2 Aim and outline

The aim of this work is therefore to increase the tunability and improve upon the optical properties of gold nanorods for various applications. To achieve this, we use two main approaches: firstly, we use self-assembly methods to obtain novel plasmonic structures of AuNRs. Secondly, we add silver as second metal to combine the plasmonic properties of Ag and AuNRs.

Similarly to the influence of the change in shape on the plasmon resonance, the particles can show new behaviour as a result of *collective* properties when two or more particles are brought close to each other. Between the tips of (aligned) AuNRs, the electric fields from both particles combine which yields a much higher field enhancement than an individual particle. Furthermore, the plasmon resonances of both particles can couple, giving rise to collective oscillation modes which do not occur in individual Au nanoparticles [28–32]. We use self-assembly approaches to obtain ordered structures that may exhibit such collective properties [33]. From a fundamental point of view it is interesting to study the inter-particle interactions in high volume fractions, as shape anisotropy can lead to new phase behaviour and many self-assembled structures with new properties exist [29].

Furthermore, the electronic and thereby optical properties can be strongly influenced when a second metal is introduced. It was recently shown by our group that it is possible to replace part of the surface of silica-coated AuNRs with Ag, Pt or Pd by controlled etching and metal overgrowth [34]. With this method both rough and smooth metal surfaces can be created depending on the metal and the thickness of the layer and the LSPR can be tuned over a wider range. A major downside of AuAg core-shell particles is their poor chemical stability, and long term storage remains challenging. It has been shown that the stability of AuAg particles can be greatly increased by mixing the metals into a homogeneous alloy [35]. A very recent development in the SCM group is to explore the possibility of converting core-shell like nanorods (CSNRs) into homogeneous alloys *without* losing the shape anisotropy. By tuning both the composition and distribution the LSPR peak can be tuned precisely. It was discovered that this can be achieved for AuNRs overgrown with silver, platinum and palladium by heating the particles in an inert atmosphere [36]. One of the aims of this project is to gain insight into the processes that occur during the alloying, in particular under different atmospheric conditions.

In Chapter 2 we provide an overview of some of the general theory underlying this research, such as the plasmon resonance and phase behaviour of rod-like particles. In Chapter 3 we discuss the background, methods and results of the synthesis of the gold nanorods used throughout this work, based on theory and methods reported in the literature. In addition to this, we discuss experiments in which centrifugation techniques were used for purification of the gold nanorods. In Chapter 4 we describe methods and results of two types of silica coatings we used for the particles in preparation for further steps. Chapter 5 covers our experiments with silver overgrowth and alloying of AuNRs. Chapter 6 treats the synthesis and characterisation of self-assembled monolayers and spherical assemblies (supra-particles). Lastly, we draw and discuss some conclusions (Ch. 7), and we provide suggestions for further research (Ch. 8).

Chapter 2

Theory

In this chapter we provide a brief overview of some of the relevant theory to provide the reader with a theoretical basis for reading this work. The subjects discussed here were chosen by the author because of their relevance to the general concepts of this research and are all established in this field. Theory specific to only small parts of this research will be discussed in the appropriate sections throughout this work.

2.1 Electron microscopy

Electron microscopy is one of the most widely used methods for characterisation of nanomaterials, and the practical considerations of transmission electron microscopy (TEM) are well-known amongst most researchers in materials science. However, because a considerable part of the analysis in this work is based on electron micrographs, it is worthwhile to briefly discuss the theory behind electron microscopy and to reiterate some considerations and limitations of the various imaging methods used in this research.

2.1.1 The (transmission) electron microscope

An overview of the transmission electron microscope and the signals generated under illumination of the electron beam are given in Figure 2.1 (beam angles are exaggerated for clarity). The electrons are generated in the top of the device, either by thermionic emission (in a tungsten filament or LaB_6 crystals) or by tunnelling (in field emission guns, FEGs). The electrons are then accelerated in an electric field, the potential of which is an important characteristic of the imaging process. Acceleration voltages for TEM are typically between 100 and 300 kV. The beam is then focussed on the sample by the condensor system that generally consists of two lenses. The condenser lenses and aperture determine the size and intensity of the illuminated area on the sample. The objective lens creates the image which is then selected and magnified by the intermediate and projection lenses in the projector system. By insertion of the objective aperture it is possible to select only the direct beam in bright field TEM mode (BF-TEM) or scattered electrons in electron diffraction mode (ED), while blocking the other electrons.

Most of the signals generated during interaction of the electron beam with the sample can be used for detection, and they are each associated with their own imaging mode. The most common imaging mode is bright field TEM (BF-TEM, often simply called TEM), where the entire area of interest is illuminated and the image generated from the transmitted direct beam. When electrons are absorbed or scattered upon interaction with a particle, the intensity of the electron beam in that spot will be decreased and it will thus appear darker in the final image. The (empty) background scatters and absorbs the least amount of electrons, and will thus appear bright (hence: bright field). Instead of illuminating the entire image simultaneously, it is also possible to focus the beam into a small spot and scan over the sample in a line-by-line fashion, such that signals that do not form an image can be collected. This is the principle behind scanning transmission electron microscopy (STEM). By using an annular (ring shaped) detector

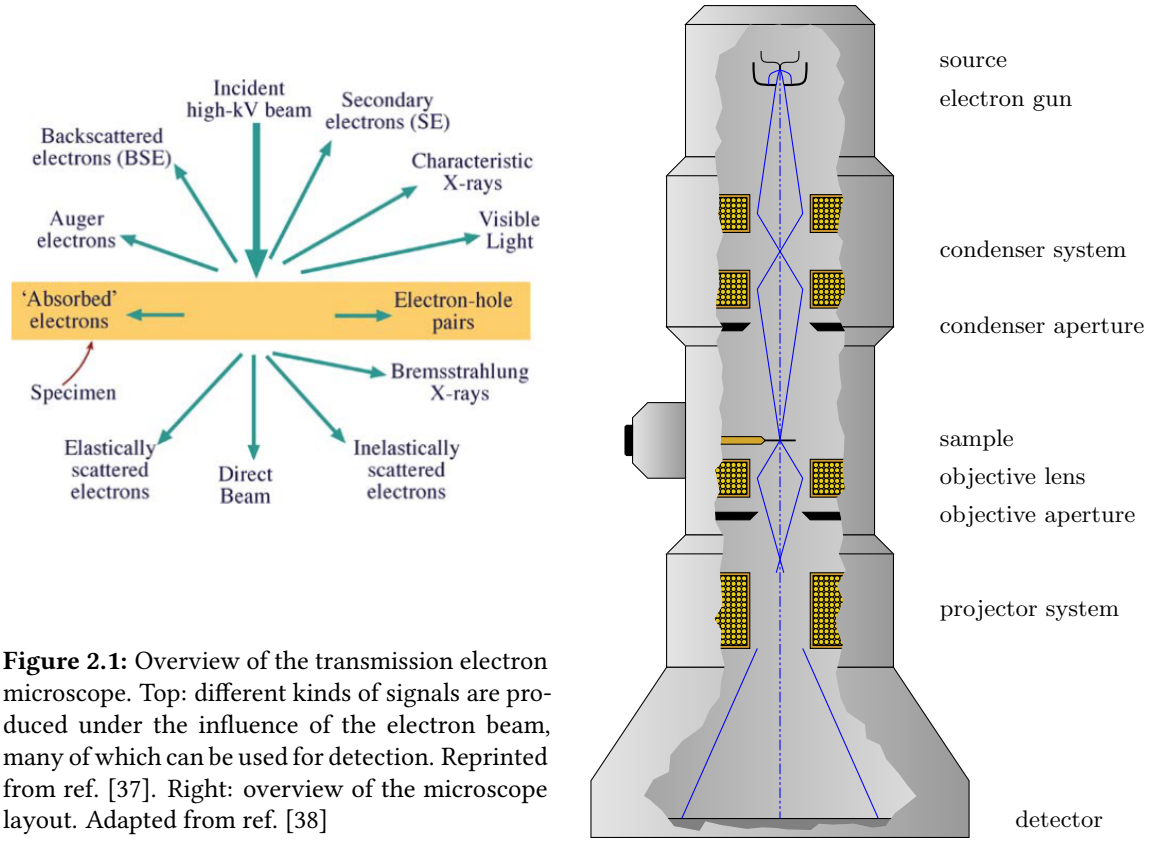

Figure 2.1: Overview of the transmission electron microscope. Top: different kinds of signals are produced under the influence of the electron beam, many of which can be used for detection. Reprinted from ref. [37]. Right: overview of the microscope layout. Adapted from ref. [38]

the scattered electrons can be detected while omitting the direct beam. If the height of the detector is chosen such that only electrons scattered at high angles are detected, the signal strength depends only on the transmitted thickness and the atomic number of the material ($I \propto Z^{\sim 1.7}$), as scattering close to the core is incoherent and diffraction effects do not occur. If a particle is present, electrons are more likely to be scattered in that spot and thus a higher signal intensity will be measured, while few scattered electrons are detected in the (empty) background. This method is therefore called high angle annular dark field scanning transmission microscopy (HAADF-STEM) [39–41].

Due to inelastic scattering events, electrons can be excited out of core levels of atoms in the sample. Characteristic x-rays are emitted when valence electrons subsequently relax to fill the core-hole. Spectroscopic (element specific) imaging can be achieved by energy dispersive x-ray spectroscopy (STEM-EDX) which works by analysing the spectrum of these x-rays emitted by the sample. It is also possible to measure the same energies by measuring the energy loss of the transmitted electrons in electron energy loss spectroscopy (STEM-EELS) but this is not used in this work [42]. Backscattered or secondary electrons (the electrons that are ejected from the atoms in the sample due to collision with the incoming electron beam) can be imaged to image specifically the surface of the material. While it is possible to combine STEM with a secondary electron detector, generally SEM is not performed in a TEM but rather in a dedicated scanning electron microscope (SEM). These are operated at much lower acceleration potential to maximise interaction and minimise the depth of the imaged surface [43].

2.1.2 Limitations of electron microscopy

While TEM is a very useful tool, there are several important limitations that should be considered. Firstly, there are some major contraints for the sample. Because the TEM operates in high vacuum, samples must be completely dried after deposition on a carbon-coated copper grid. This may not accurately represent the particles in dispersion, and capillary forces or other drying effects may distort the sample. An example of this effect is that it is very hard to judge based only on TEM images whether particles were aggregated or whether they grouped together during drying. Because a sufficient number

of electrons must be transmitted for detection, the sample should also be sufficiently thin. Especially for heavy elements such as gold, a sample of some hundreds of nanometres may already completely block the electron beam. Changes in the sample may also be induced during the imaging by interactions between the high-energy electrons and the sample: beam damage. The different ways in which beam damage can occur are the following:

- Heating. Energy transfer in inelastic scattering events can cause a local temperature change which quickly reaches a steady state due to thermal conduction in the sample. These elevated temperatures can melt particles and weaken materials. The heating is mainly governed by the electron current to the sample which can be reduced by the use of a smaller condenser aperture.
- Atomic displacement. If a high energy electron is scattered by a nucleus, this is associated with a transfer of momentum and energy from the electron to the nucleus, which may cause it to displace (for example creating defects in crystallographic lattices). Displacement effects are mainly dominant at high incident energy and can be prevented by lowering the acceleration voltage. A special case of atomic displacement is *sputtering*, where atoms are ejected from the surface. Sputtering occurs on the side where electrons exit the sample and occurs mostly for low-Z elements.
- Electrostatic charging. Charging of the sample, while predominantly a problem in SEM, can occur in the TEM due to the emission of secondary electrons away from the sample. The copper grid and carbon coating are conductive and normally ground the sample enough to prevent charge build-up, but in insulating samples Coulombic forces from excess charge can cause considerable sample damage.
- Radiolysis. Some materials, in particular organic molecules, can undergo chemical reactions induced by inelastic scattering effects. This can involve breaking bonds and creating free radicals that can undergo further reactions. Radiolysis is mainly a problem for environmental TEM but may cause structural changes in some samples.

For a more detailed discussion of beam damage effects and how to recognise and prevent them we refer the reader to the review by Egerton, Li and Malak [44]. In this work, we image almost exclusively gold, silver and silica, which are highly stable under the influence of the electron beam. Melting and heating effects can occur if there is a large density of particles, but this takes a much larger electron flux than that is necessary for recording images. The (porous) silica we used as protective shell is more sensitive than the gold and silver, and collapse of the porous structure of this material occurred at prolonged exposure to the electron beam. An example image of beam-damage from this research is given in the appendix (Fig. B.2). For the majority of this work, beam damage effects were not of importance.

Lastly, because TEM has the ability to look at very high magnifications, this also means the field of view is very small. The part of the sample that can be imaged is only a tiny fraction of the total sample and may not represent the rest of the sample accurately. As an example, it is possible that differently shaped particles separate upon drying (as is sometimes the case for rods and spheres, see for example Figure 6.1C), or that important features are missed if they are low in number. To prevent bias from the imaging process as much as possible, samples were always imaged at different magnification and in several different places on the TEM-grid. To assure that statistics such as particle size distributions were correct, a large number of particles (typically ~100) must be measured. Where possible, TEM results should be compared to other (ensemble) measurement techniques.

2.1.3 3D electron microscopy

BF-TEM and STEM are *transmission* techniques, and thus all 3-dimensional information is projected into the 2D imaging plane and any information expressed in the z axis (perpendicular to the imaging plane) is lost. It is however possible to obtain 3D information from the sample if it is imaged at multiple different angles, as each angle provides information about a different 2D projection in 3D space. The full 3D structure of a sample is thus somehow contained in a set of images with all rotations from -90°

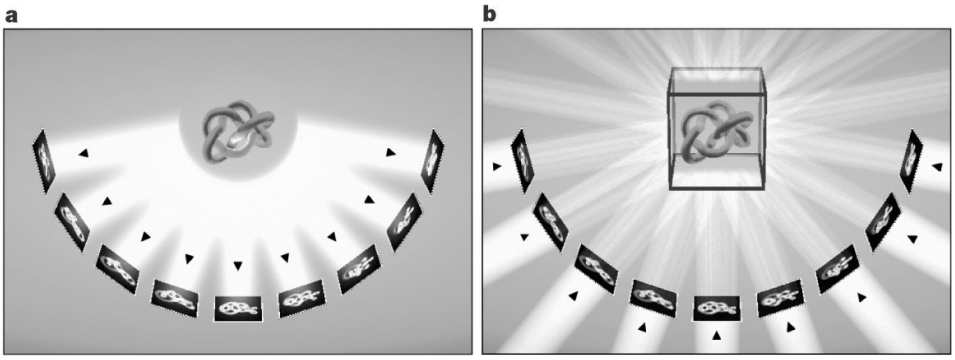

Figure 2.2: Schematic of a: the forward projection (the imaging process in the TEM) and b: the back-projection. Reprinted from ref. [45].

to 90°. This principle lies at the basis of electron tomography, a method for 3D-TEM. In reality however, the data is limited to a discrete and limited set of images. Because of this, a reconstruction algorithm that approximates the true structure from it's 2D projections must be used. In addition to this, due to practical limitations such as the microscope layout and shadowing effects of the holder, the tilt range of the sample is limited to typically ±70°. This means there is missing data in certain directions (the missing wedge) which introduces artefacts into the reconstructed volume.

The two most common reconstruction methods are weighted back projection (WBP) and simultaneous iterative reconstruction technique (SIRT). A back-projection (Fig. 2.2) is the opposite operation of the forward-projection, the image transformation that occurs in the microscope when the electron beam passes through the 3D volume and expresses this in intensity values on a 2D plane. In the back projection, each detector pixel is projected back into the reconstruction volume at an angle corresponding to the original tilt angle. Where many rays cross, the intensity is higher and the shape of the original (unknown) object appears. Naturally, this introduces a very large amount of lines or streaking artefacts running through the volume that partially obscure the true structure. The back-projection is thus an imperfect inverse of the forward projection that cannot be calculated exactly. In WBP, a weighing function or a Fourier-space filter is used to remove these low frequency artefacts introduced by the back-projection. SIRT on the other hand is an iterative method that improves the reconstruction by solving for the reconstruction that most accurately returns the measured dataset. It makes use of the fact that the forward projection *can* be calculated exactly and that the original dataset forms a perfect reference. In SIRT, an ordinary back-projection is preformed first to create a trial reconstruction. The trial reconstruction is then forward projected again, but the resulting projection data will differ from the original dataset due to the imperfections of the back-projection. The difference between the two is then back-projected and used to update the trial volume. This can be repeated until convergence is reached or for a predetermined number of iterations. Both methods have their advantages and disadvantages. WBP is computationally very fast, simple to understand and leads to reconstructions which appear sharp. At the same time, WBP deals poorly with artefacts from the missing wedge and strongly reconstructs noise. SIRT takes much longer to compute (since the back-projection has to be calculated every iteration step) but leads to much smoother noise-free reconstructions [46–49]. Many other reconstruction techniques exist, each with their own advantages and disadvantages. For a detailed discussion of the theory and practical aspects of electron tomography, we refer readers to our recent literature report [50].

It is also possible to obtain 3D reconstructions of a sample using SEM. By itself SEM does not give true 3D information although it does reveal surface topology and some surface reconstruction can be achieved based on shading. It is however possible to combine SEM with a focussed ion beam (FIB-SEM) so that a sample can be milled, revealing the internal structure. A complete volume can be analysed by serial block-face imaging: repeated imaging and removal of slices with the ion beam. While the resolution of SEM is considerably lower than that of (HR-)TEM, sub-nm resolution is nowadays

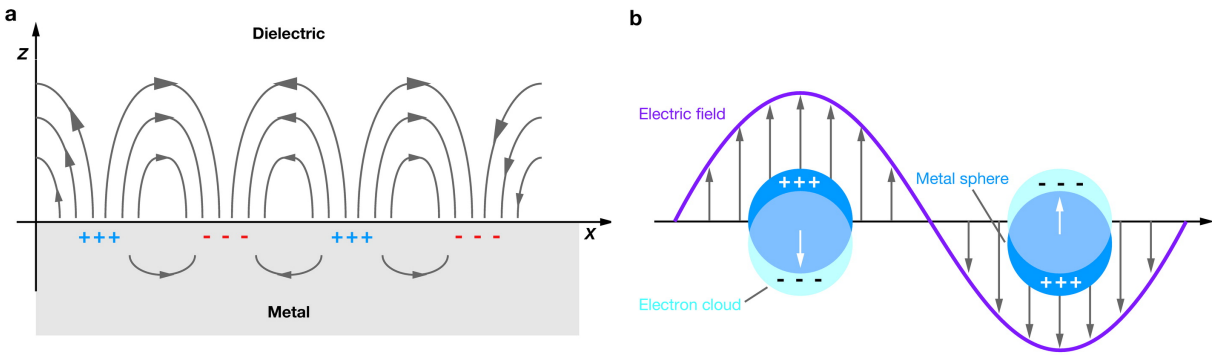

Figure 2.3: A: Surface plasmon polaritons at the metal-dielectric interface of a bulk metal. The arrows indicate the electric field, which is strongly enhanced near the interface and decays exponentially into the dielectric and the bulk. B: the localised surface plasmon resonance confined in a particle with $r \ll \lambda$. Reprinted from ref. [55].

possible in the xy plane. The z-resolution is limited by the thickness of the slices removed by the ion beam which can be as little as 3 nm [43]. FIB-SEM is a destructive technique and one section can only be imaged once. Because SEM is possible over many orders of magnitude, FIB-SEM is suitable for analysis of large volumes and samples that are much thicker than in TEM-tomography. Lastly, it is possible to use FIB-milling to prepare thin sections for tomography which combines advantages of both methods.

2.2 Plasmon resonance

The optical properties of metallic nanoparticles are dominated in the visible region by plasmon resonance. Because electrons in metals are effectively free, they can undergo collective motion when placed in an electric field such as that of electromagnetic radiation. This gives rise to surface plasmon polaritons: delocalised electromagnetic waves travelling over the metal-air interface. The electrons collectively move back and forth between the metal surface (the lattice of positive ions) and the dielectric (the non-conducting environment around the metal, for example air) which is depicted in Figure 2.3a. In the bulk these waves in the electron density are quickly lost due to absorption and scattering effects ($\ll$1 fs in bulk gold, but typically 15 fs for AuNRs [51]), which depends strongly on the properties of the metal and the roughness of the surface [52]. Differences between the plasmonic properties of different metals are expressed via the material and energy dependent dielectric function. Using Drude's theory of free electrons, the dielectric function is described by known constants and experimental parameters in equation 2.1:

$$\epsilon(\omega) = \epsilon_1 + i\epsilon_2 = \epsilon_m - \frac{\omega_P^2}{\omega^2 + \Gamma^2} + i\frac{\omega_P^2 \Gamma}{\omega(\omega^2 + \Gamma^2)} \tag{2.1}$$

where ω is the frequency, ϵ_m the dielectric constant of the medium, Γ is a damping constant (which is fitted from experimental data) and ω_P is the plasma frequency, which is given by:

$$\omega_P^2 = \frac{ne^2}{\epsilon_0 m_e} \tag{2.2}$$

with n the electron density, e the electron charge, ϵ_0 the permittivity of free space and m_e the relative electron mass. Γ encompasses all scattering and damping effects such as electron-electron, electron-phonon interaction, but also surface and defect effects [53, 54]. Plots of the dielectric functions for gold and silver can be found in the appendix in Figure B.1.

If the metal particle size is reduced to typically 10 - 100 nm, the surface plasmon waves become confined in the particles and ultimately form a standing wave over the whole particle whereby the entire electron cloud shifts with respect to the positive lattice of the nuclei (Fig. 2.3b). Because the plasmon is now confined in the particle, it is no longer delocalised and referred to as the localised surface plasmon resonance. Like the bulk surface plasmon polariton, this oscillation occurs at a certain

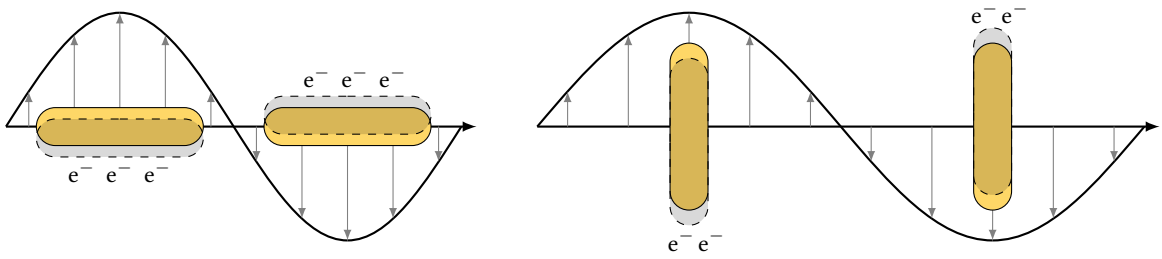

transverse surface plasmon resonance (TSPR) longitudinal surface plasmon resonance (LSPR)

Figure 2.4: The transverse and longitudinal surface plasmon resonance in nanorods under the influence of the electric field of light (not to scale). When the wavelength of the light matches the resonant frequency of the electron cloud, the extinction reaches a maximum.

resonance frequency and will most strongly interact with light of the correct energy, giving rise to a distinct peak in the absorption spectrum. Since this effect arises from confinement of the plasmon resonance in the particle, it depends on the size of the particle. The position of the optical absorption peak can therefore be tuned by changing the particle size [53, 55]. The dependency of the extinction of plasmonic nanoparticles on the particle size is theoretically described by Mie theory. The optical extinction cross-section for spherical particles is given by:

$$C_{ext} = \frac{24\pi^2 R^3 \epsilon_m^{2/3}}{\lambda} \frac{\epsilon_2}{(\epsilon_1 + 2\epsilon_m)^2 + \epsilon_2^2} \tag{2.3}$$

where R is the particle radius, λ the wavelength, ϵ_m the dielectric constant of the medium which is assumed to be constant, and ϵ_1 and ϵ_2 are the real and the imaginary part of the dielectic function of the metal respectively. We note that this is a dipole approximation that ignores multipolar resonances, which may be important in certain cases. It is also assumed that the entire electron cloud feels the same electric field at the same time, in other words the size of the particle must be much smaller than the wavelength of the incoming photons [53, 56].

When particles have an anisotropic (nonspherical) shape, the plasmon resonance gets a directional dependency as the resonance in one direction will occur over a different length than the resonance in the other directions. In the case of nanorods this results in two distinct plasmon modes, the longitudinal surface plasmon resonance (LSPR) in along the length of the particle, and the transversal surface plasmon resonance in the directions perpendicular to the long axis as can be seen in Figure 2.4. We note that the abbreviation LSPR is used frequently in the literature to denote the *localised* SPR of nanoparticles in general, but for clarity is used in this work only to denote the *longitudinal* SPR (which is strictly speaking also a localised SPR).

The optical extinction spectra of nanorods can be predicted using Mie-Gans theory, an extension of Mie theory for spheroids. The extinction cross-section C_{ext} of a plasmonic particle is then given by:

$$C_{ext} = \frac{2\pi V \epsilon_m^{3/2}}{3\lambda} \sum_j \frac{P_j^{-2} \epsilon_2}{\left(\epsilon_1 + \frac{1-P_j}{P_j}\epsilon_m\right)^2 + \epsilon_2^2} \tag{2.4}$$

where V is the volume of the particles, λ the wavelength of the light, ϵ_m the dielectric constant of the medium, and ϵ_1 and ϵ_2 are the real and the imaginary part of the dielectic function of the metal respectively. P_j gives the oscillation modes in the three directions due to the particle shape (determined by the radii A, B and C with $A > B = C$) and is given by the following equations for spheroids:

$$\begin{aligned} P_A &= \frac{1-e^2}{e^2}\left[\frac{1}{2e}\ln\left(\frac{1+e}{1-e}\right) - 1\right] \\ P_B &= P_C = \frac{1-P_A}{2} \end{aligned} \tag{2.5}$$

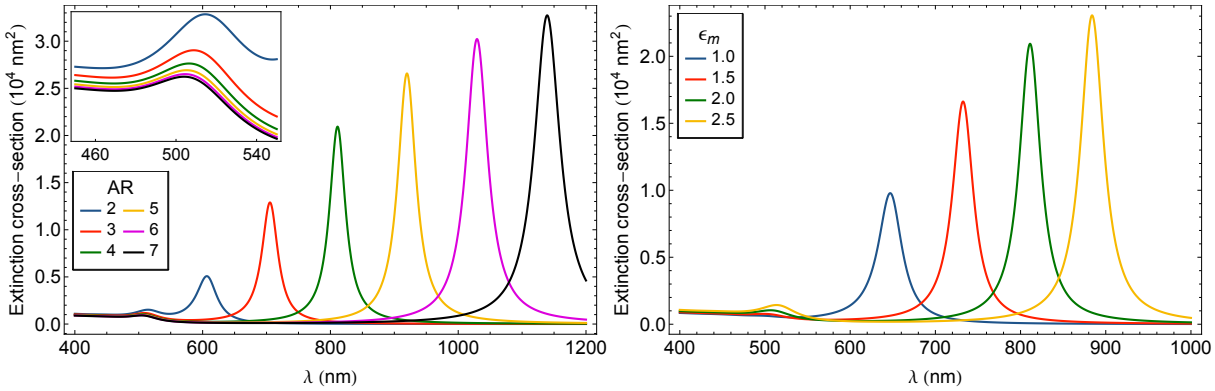

Figure 2.5: Optical extinction spectra of AuNRs calculated with Mie-Gans theory (using Eq. 2.4). Left: influence of the aspect ratio on the SPR of AuNRs while ϵ_m was kept constant at 2.0. The inset shows the TSPR in more detail. Right: influence of ϵ_m on the SPR while the AR was kept constant at 4. Data for the dielectric function for Au were obtained from ref. [61].

with the ellipticity e that depends only on the aspect ratio and is defined as

$$e = \sqrt{1 - \left(\frac{B}{A}\right)^2} \tag{2.6}$$

where A and $B = C$ are the radii of the spheroid analogous to the length and diameter of a rod. The volume V of a spheroid can be calculated using

$$V = \frac{4\pi}{3}\left(\frac{A}{2}\right)\left(\frac{B}{2}\right)\left(\frac{C}{2}\right) \tag{2.7}$$

but can also be determined from experimental data. Figure 2.5 gives the theoretical aborption spectra for AuNRs of various aspect ratios. With increasing aspect ratio, the longitudinal SPR of gold nanorods shifts more towards the infrared and the extinction cross-section increases. The transversal SPR undergoes little to no peak shift upon an increasing aspect ratio. A similar trend is observed if the dielectric constant of the medium is changed, so a peak shift is expected if the solvent is changed or for example if a silica shell is grown over the AuNRs [53, 57–59]. A limitation of these equations is that the analytical expression is available only for spheroids, while the AuNRs synthesised by most methods are more accurately described as spherocylinders. Using numerical methods however, expressions for spherocylinders have been obtained, and they give qualitatively similar results [59, 60].

Based on Eq. 2.4 an increase in the particle volume gives rise to a larger cross-section but does not affect the position of the LSPR peak, as the volume is only a wavelength-independent prefactor. In reality sufficiently small nanoparticles are necessary for the localised plasmon resonance as Mie-Gans theory relies on the assumption that the particle size is small with respect to the wavelength of the incoming light. When the particle size increases further, bulk damping effects start to dominate and the plasmon resonance peak diminishes [53,58]. On the other hand, if particles are small with respect to the mean free path of electrons in gold (~ 20 nm), surface scattering effects contribute considerably to the decay of the plasmon resonance. It was found that AuNRs with a diameter between 10 and 20 nm have the longest dephasing time, and consequently the narrowest linewidth. Lastly, a major contribution to the damping of the plasmon resonance is excitation of intraband transitions in the metal, which occurs predominantly when the resonant energy is larger than 1.8 eV (690 nm), so longer lifetimes are observed for AuNRs with a higher aspect ratio [20].

2.3 Phase behaviour of rod-like particles

Compared to isotropic particles, the anisotropy of rod-like particles gives rise to new phase-behaviour in the form of (liquid) crystals. Liquid crystals are phases that are somewhere between liquids, which

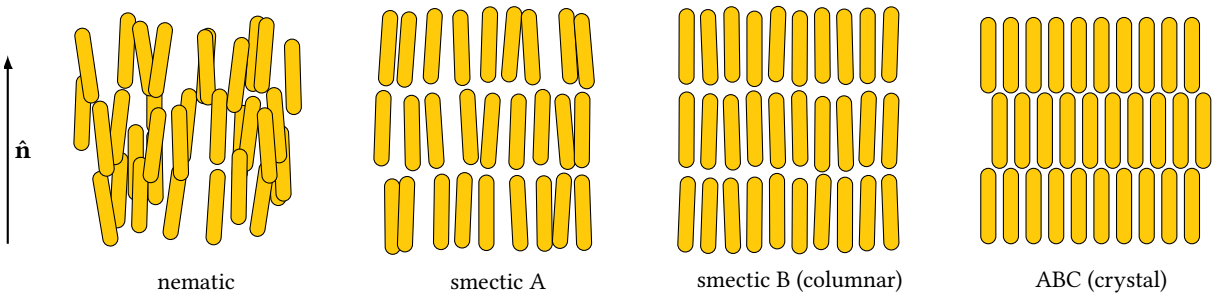

Figure 2.6: (Liquid) crystal phases of rod-like particle with only orientational ordering (nematic), with orientational and positional ordering in layers (smectic), or with long range orientational and positional ordering (crystals).

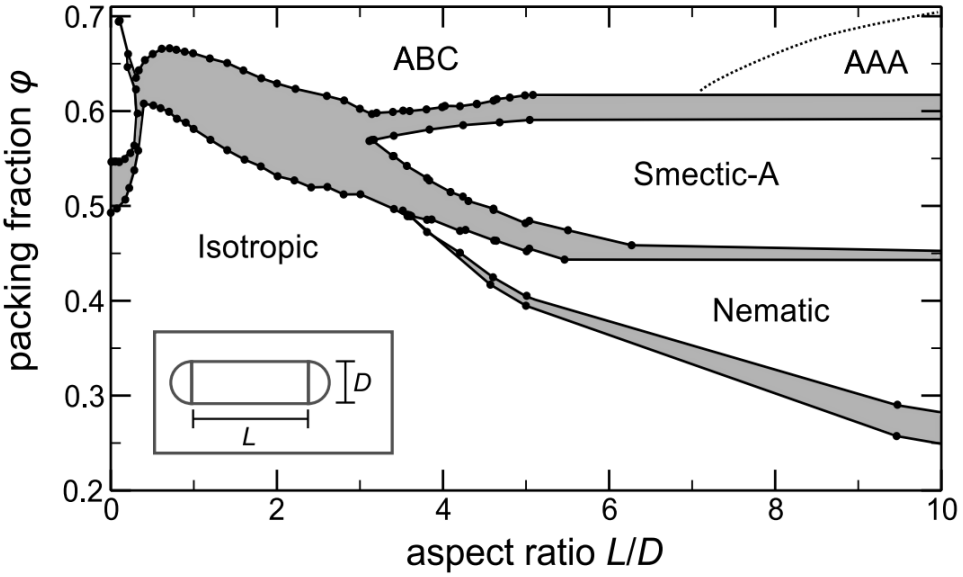

Figure 2.7: Phase diagram of hard-core spherocylinders from computer simulations, the grey areas indicate coexistence. Reprinted from ref. [63] based on data from [65]. Note that here the length L is the cylinder length, whereas we use L to refer to the end-to-end distance.

posses no orientational or positional ordering, and crystals, which are ordered in all directions. Some examples are shown schematically in Figure 2.6. In a nematic phase, the particles show orientational alignment with a net average director, but the centres of mass are isotropically positioned in space such as in a liquid. Smectic phases show orientational ordering as well as positional ordering in one dimension as they consist of regularly stacked layers with a characteristic layer spacing. These lamellar structures often have the main orientational axis perpendicular to the plane of the layers (such as in smectic A and B). In smectic A phases the rods are positions isotropically within the layer, while in smectic B there is semi-long range (hexagonal) ordering of the rods within one layer. Other variations include tilting of the rods with respect to the plane of the layers (smectic C, not shown), chiral structures (cholesteric) and many others (up to smectic L) have been reported. Lastly, there are fully crystalline systems such as AAA and ABC where there is long range positional ordering within the layers which is correlated to that of the next layer and thus extends in 3 dimensions [62–64].

A phase diagram for hard spherocylinders based on Monte Carlo simulations is shown in Figure 2.7. It is shown that for $AR \geq 4$ nematic and smectic phases can be expected, while for sufficiently high volume fraction crystals are most stable. It was found that for charged particles this behaviour changes as the effective length and diameter due to charge repulsion are now more important, and it was found that the charge destabilises the smectic A and more so the nematic phase, while stabilising columnar phases like smectic-B and crystals [66, 67]. In addition to charge, experimental systems such

as silica or gold rods are not perfectly monodisperse. It seems intuitive that polydispersity in the length will disturb the formation of smectic layers while polydispersity in the diameter may disturb ordering within layers. It was found in simulations that for a polydipersity of $\sigma > 8\%$ the smectic A phase is gradually destabilised while nematic and columnar phases become more favourable until a critical point at $\sigma \approx 18\%$ above which the smectic A disappears completely [68, 69].

The degree to which there is orientational ordering in a system can be expressed by the nematic order parameter, which compares the orientation of each rod with the *nematic director* $\hat{\mathbf{n}}$ which is the dominant or "average" orientation of the entire system. The 2D and 3D nematic order parameters S_{2D} and S_{3D} are given by

$$S_{2D} = 2\left\langle \cos^2 \psi \right\rangle - 1 \tag{2.8}$$

$$S_{3D} = \frac{2}{3}\left\langle \cos^2 \psi \right\rangle - \frac{1}{2} \tag{2.9}$$

where ψ is the angle between the main axis of the individual rods and the nematic director $\hat{\mathbf{n}}$. This is a convenient parameter because for a fully aligned system $S = 1$ while for a randomly oriented (isotropic) system $S = 0$. This order parameter thus only describes orientational order and does not distinguish between different liquid crystal structures such as nematic and smectic crystals.

Chapter 3

Synthesis of gold nanorods

A great number of articles has been devoted to the synthesis of AuNRs because of their potential for applications, but certainly also because of the long lasting challenges in their synthesis. Synthesising AuNRs with good monodispersity and particularly a large shape-yield, has been challenging [8, 70–73]. From early on during and shortly after nucleation until the end of the growth, the tendency of particles to grow into the thermodynamically stable (near) spherical shape has to be overcome. A major breakthrough in AuNR synthesis was the development of the seeded growth approach. This separates the two crucial events in the synthesis that require almost opposite reaction conditions: nucleation and growth. For nucleation, a very rapid reduction of the gold is needed to obtain many small particles. For the directed growth, a slow reduction of gold is desired to obtain monodisperse particles and to make optimal use of methods for kinetic shape control. The rodlike shape is out-of-equilibrium (inherently thermodynamically unstable), and thus thermodynamic control over the shape cannot be used. If the reaction conditions are too slow, any process is an equilibrium process following a thermodynamic path, but if the reaction proceeds too fast other reactions in addition to the facet-specific reaction that leads to rod-growth can occur.

3.1 AuNR synthesis: breaking shape anisotropy

Surfactants are commonly used in nanoparticle synthesis to stabilise the particles in a solvent. In the synthesis of AuNRs, cetyl trimethylammonium bromide (CTAB) is the most widely used surfactant. In the method we use most (see Sec. 3.1.1), CTAB is used in combination with NaOL to form a binary surfactant mixture [74]. Here the role of these molecules is not only to maintain a stable surface, but also to assist the formation of the anisotropic shape. Selective binding of the CTAB to certain gold facets can sterically block those sites for additional gold atoms, leading to a decreased rate of growth in these directions. When other crystal facets are still available for the gold they grow fast with respect to the CTAB-blocked facets, leading to the elongated rod-shape where the long sides are formed by the CTAB-stabilised facets. The anisotropic shape is thus the result of *kinetic* control, and not a result of any thermodynamically favoured structure. For AuNRs growth occurs mainly along the {111} facets (that end up exposed only on the tips of the rods) while the long sides of the rods are composed of the facets that grow slowly. For single crystalline AuNRs prepared with the CTAB method, the long (lateral) sides consist of alternating {100} and {110} facets [70, 73, 75, 76]. When different surfactants are used, AuNRs with a different exposed surface (such as the {520}) can be synthesised [77, 78]. Murphy *et al.* proposed that the specific binding of CTAB on some of the facets can be explained by the similar size of the CTA^+ cation and the distance between adsorption sites. For this mechanism the adsorption of the Br^- ion plays a crucial role [7, 71]. It has also been suggested that CTAB micelles can form a cylindrical soft template for the formation of the rods [79], although this theory has been subject of some debate in the literature [78].

It is important to note that a small amount of silver nitrate is added to assist the formation of the rods, which has a direct effect on the aspect ratio. This size control by varying silver concentration is

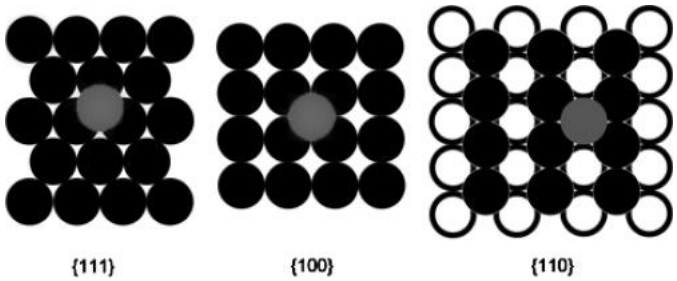

Figure 3.1: Adsorption sites for silver atoms at different gold facets. The highest coordination of silver occurs for the {110} plane which is expected to have the highest rate of UPD. The white circles represent atoms one layer deeper in the metal. Reprinted from ref. [80].

consistent with earlier synthesis protocols [81]. The exact role of the silver in the synthesis of AuNRs is still widely debated, but a number of mechanisms has been proposed [8, 82]. Firstly, the silver ions may form a facet-specific capping agent in combination with the bromide ions from CTAB. These Ag^+Br^- species hinder the addition of Au to the {100} and {110} facets leading to preferential deposition on the tips of the rods. NMR and mass spectra point towards the presence of AgBr or $Ag^+Br{-}CTA$ species present at washed AuNRs [71, 80, 81]. A second possibility is the adsorption of silver atoms onto specific surface sites of the particle due to underpotential deposition (UPD). This process relies on a decrease in reduction potential for Ag(I) due to the influence of highly unsaturated gold at the surface. Under experimental conditions the Ag(I) will not be reduced to form a bulk silver layer on the particles, however, the reduction potential can be lower for Ag(I) in a favourable surface site. This effect is expected to be stronger for the {110} facet than for the {100} and {111} facets based on the geometry of these facets (Figure 3.1). The formation of a partial silver layer can decrease the rate of gold-adsorption on those facets [80, 82].

A third possibility suggested is that the Ag(I) ions sufficiently alter the shape of the CTAB-micelles to form a cylindrical bilayer. The micelles can then act as soft template for the template-assisted formation of the rods while confining the gold particle to adapt its formation to the the rod-like shape of the micelle-cavity [79]. It is currently unclear whether such rod-like micelles are formed under the reaction conditions in the AuNR synthesis and the explanation of rod growth due to CTAB as soft template is generally considered obsolete after experiments with different surfactants [8, 29]. We therefore consider mainly the first two processes although it may well be a combination of various factors that leads to the rod-like shape. It has been reported very recently, that silver predominantly influences the symmetry breaking point where the spherical seed starts growing anisotropically, while having little influence on further growth of the rod [83]. Using energy dispersive X-ray spectroscopy (EDX), an element specific electron microscopy technique, it was demonstrated that the silver is mainly present at the surface of the AuNRs which is consistent with all mechanisms [84]. The presence of silver atoms on the surface should be kept in mind, as in many applications such as catalysis and optical effects these surface atoms may have a considerable influence on the properties.

3.1.1 Ye & Murray synthesis

The synthesis most commonly used in this work to make the AuNRs is a method reported by Ye & Murray *et al.* [74]. This method gives high control over the size and aspect ratio and yields highly monodisperse AuNRs for most sizes. The rods obtained are mono-crystalline with little to no defects. A schematic overview of the synthesis protocol is depicted in Figure 3.2. Exact experimental details of the synthesis are given in Section 3.2.1. A seed solution is prepared by reduction of Au^{3+} with $NaBH_4$ (a strong reducing agent) in the presence of CTAB. In addition to the seed mixture a growth mixture is prepared in which gold atoms can be deposited along certain facets of the seed crystals, but in which no new nuclei are formed. Sodium oleate (NaOL) is added to the growth mixture, which contains a double bond that can (partially) reduce the Au(III) ions present in the growth mixture to Au(I), which

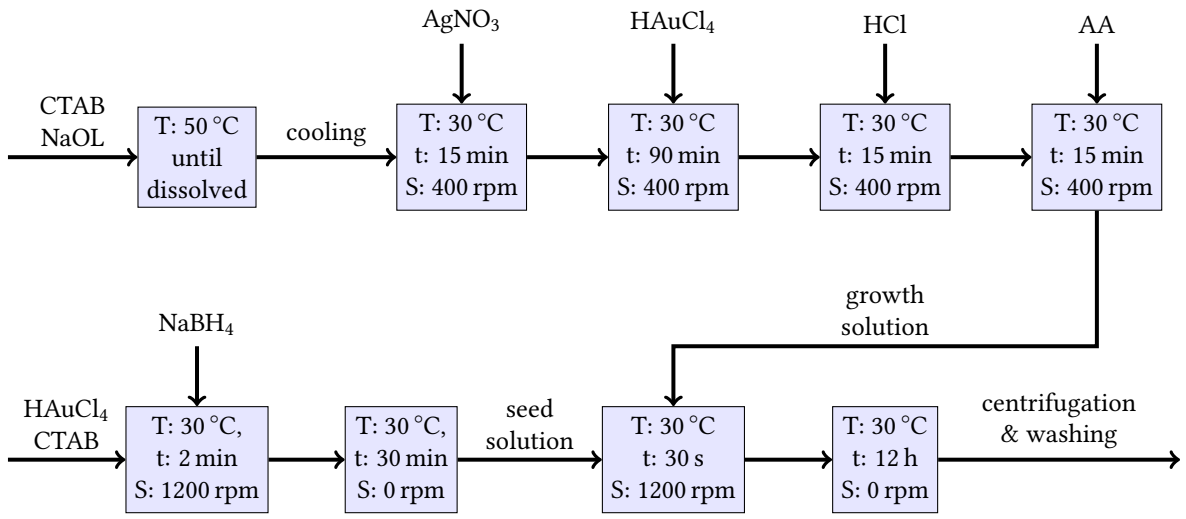

Figure 3.2: Schematic overview of the synthesis of AuNRs. A seed and growth solution are prepared separately, a small amount of seed solution is then added to the growth solution and NR-growth occurs. T: temperature, t: reaction time until the next step, S: stirring speed.

is evidenced by the disappearance of the yellow-orange colour. After 90 minutes, ascorbic acid (AA, vitamin C) is added which facilitates a slow further reduction of Au(I) to Au(0) catalysed by the seed particles. Due to the 2:3 molar ratio of AA to Au(I) the synthesis has a maximum yield of 67%. When the seed particles are added to the growth solution, gold is grown mainly along the {111} facets and rod-like particles will be formed [74]. Afterwards, the particles can be separated from the synthesis solution and washed with nanopure H_2O by means of centrifugation and redispersion. The particles can be redispersed in a 5 mM solution of CTAB and stored for long periods of time.

Ye & Murray *et al.* have reported an extensive investigation into the various parameters that can be used to control the size and aspect ratio of the gold particles. The general trends in synthesis parameters and particle shape they found can be summarised as follows:

1. a decreasing pH leads to an increase in length and decrease in thickness, giving precise control over the aspect ratio
2. decreasing the amount of seed solution leads to an increase in particle volume
3. increasing the CTAB concentration leads to a decrease in particle volume, mainly affecting the diameter
4. AR monodispersity increases with smaller aspect ratio

The influence of pH on the aspect ratio can be understood by realising that H^+ slows down the reduction of Au(I) by ascorbic acid. AA is known to have a reduction reactivity that depends on the pH [85], which we discuss in more detail in Section 5.3. The slow reaction rate results in a stronger influence of the facet-selective blocking by CTAB, and giving atoms more time to find the more accessible ends. The influence of the number of seeds added is straightforward as each seed grows out to a rod. The amount of gold precursor available in the growth solution runs out quicker when more seeds are present while for low seed concentration the amount of precursor per seed is large. A decrease in diameter at higher CTAB concentration can simply be explained by (and is evidence for) the selective blocking of the facets on the side of the rod.

3.1.2 Tips for successful AuNR synthesis

Due to the complicated nature of the synthesis protocol and the many parameters involved it can be difficult to improve if any problems with shape impurities and polydispersity arise. The method is

highly reproducible for those experienced with the procedure, but it may take synthesis of multiple batches to get good results when attempted in a new laboratory. We would therefore like to provide the reader with some notes and tips on aspects of the synthesis that are of importance but may be overlooked when trying to reproduce the synthesis, or that may be crucial to a successful synthesis but excluded from the experimental section of articles. A detailed discussion of some of these tips is also provided in the article of Scarabelli & Liz-Marzán *et al.* [78]. They included several highly detailed synthesis protocols.

Care should be taken when choosing which chemicals to be used, since different suppliers or different purities from the same supplier may contain small amounts of contaminants that may have a big effect. It was for example shown that AuNR synthesis can be successful or fail when nothing is changed but the CTAB supplier due to trace amounts of iodide present in some of the supplies [86, 87]. The success was even found to vary from lot to lot when the same supplier was used, and detailed information on the chemicals used should always be provided when reporting a AuNR synthesis [88, 89]. In addition to this, some of the chemicals used are to be stored in special ways: $NaBH_4$ should always be stored under vacuum of N_2 as it can react with atmospheric moisture. $AgNO_3$ should be kept in the dark to prevent photodegradation and contact with metal objects (such as a spatula) is to be avoided at all time. Sodium oleate should be kept in the fridge. The use of vials with a metal-coated cap should be avoided, in particular for solutions of $HAuCl_4$, HCl and $AgNO_3$ as metal may dissolve and contaminate the solution. The water used should be fresh ultra-pure (Milli-Q) quality and checked regularly as it is one of the major sources of irreproducibility of AuNR synthesis. Aside from excess ions, the pH may vary leading to varying results [78].

Glassware and stirring bars used in the synthesis (in particular the flask containing the growth solution) should always be cleaned with aqua regia, rinsed with plenty distilled water and dried in an oven. This is to prevent any gold particles from previous syntheses to act as seeds in the new growth solution. The total reaction volume, i.e. the scale of the reaction, can influence the results as diffusion of reactants and heat becomes relatively slow if the volume is larger. The temperature of the reaction is important during several steps, as the CTAB can crystallise when the temperature is too low while a temperature that is too high may induce secondary nucleation or decreased kinetic shape control. If solutions are heated to dissolve the surfactants, one must make sure they are cooled completely to the appropriate temperature before adding the seeds. Adequate stirring is necessary to prevent concentration gradients that lead to polydispersity. We found that in particular stirring after addition of HCl and AA are important. Because CTAB solutions have the tendency to foam, reactants should always be added below the foam to assure complete mixing. If there are problems during the synthesis, a small scale (10 mL) reaction can be used to limit these effects and narrow down the cause of any issues [78].

3.1.3 Alternative synthesis methods

Two alternative synthesis methods for obtaining high aspect-ratio rods were tested to expand the range of aspect ratios that could be synthesised. Wu & Huang *et al.* [90, 91] reported a multi-step seeded synthesis with nitric acid (HNO_3) to obtain large AuNRs with an aspect ratio of 19 and length of ~350 nm. Due to their large volume and aspect ratio these particles are not suited for most plasmonic applications, but their large size also means that they have a high aspect ratio even if a thick silica shell is grown. The method works by first synthesising CTAB-stabilised seeds and then adding them to a growth solution containing Au^{3+}, AA, CTAB. A small amount of the resulting solution is then immediately added to a second flask with growth solution, and again a small amount is taken immediately and added to a third flask with growth solution which was acidified with HNO_3. Nanorod growth then occurs over the course of 12 hours during which the rods sediment to the bottom while spherical particles remain in the top solution.

The second method we used was a seedless method reported by Xu & Liang *et al.* [92] to synthesise AuNRs with aspect ratios up to 20. The AuNRs reported for the Xu & Liang *et al.* synthesis are much smaller than those from the Wu & Huang *et al.* method. The high aspect ratio is achieved mostly

by strong suppression of gold deposition on the lateral facets, thus keeping the diameter very small (<10 nm). A growth solution is prepared with $HAuCl_4$, CTAB and hydroquinone as a soft reducing agent and addition of a small amount of $NaBH_4$ initiates nucleation followed by gradual growth. Similar to the Ye & Murray *et al.* method, $AgNO_3$ and HCl are added to the growth mixture to control the reaction kinetics and thus the resulting particles. Control over the aspect ratio is achieved mainly by changing the HCl concentration.

3.2 Experimental

3.2.1 Ye & Murray AuNR synthesis

Preparation of the seed solution: an aqueous 0.1 M CTAB solution was heated to ~ 50 °C and stirred to dissolve any crystals and cooled to 30 °C. Then, 10 mL of the CTAB solution was added to a 40 mL scintillation vial which was placed in a 30 °C water bath and a magnetic stirring bar was added. The temperature of the water bath was kept constant for the rest of the reaction. An aqueous solution of 50 mM $HAuCl_4$ was filtered using a syringe filter (0.45 µm cut-off), 51 µL of the filtered solution was added to the CTAB solution while stirring at 400 rpm during which a colour change to deep orange was observed. The solution was left to stir for several minutes. A 0.1 M $NaBH_4$ solution was prepared by quickly weighing $NaBH_4$ and immediately dissolving it in ice-cold H_2O. 120 µL of the solution was then immediately added to 1.88 mL ice-cold H_2O to obtain a concentration of 6 mM $NaBH_4$. The stirring speed of the CTAB/gold solution was turned up to the maximum speed (1200 rpm) and 1 mL of the $NaBH_4$ solution was rapidly added, after which the mixture quickly turned black and then gradually to a light brown. Stirring was turned off after 2 min and the seeds were left to age at 30 °C for at least 30 minutes up to a maximum of several hours.

Preparation of the growth solution: 7.00 g CTAB and 1.23 g NaOL and 250 mL H_2O (by weight) were added to a 500 mL Erlenmeyer flask, placed in a 50 °C water bath and a large stirring bar was added. A stopper was used to close the flask during all subsequent steps and only removed to add reactants. The mixture was stirred at 400 rpm until the CTAB and NaOL were fully dissolved, after which the water bath was cooled to 30 °C while stirring continued. When it the temperature had stabilised, x mL of a 10 mM $AgNO_3$ solution was added. 5 mL of the filtered 50 mM $HAuCl_4$ solution was diluted to 1 mM with 245 mL H_2O (by weight) and added to the growth mixture, which quickly turned to an orange colour and then slowly colourless and was left to stir at 400 rpm for 90 min until it was completely colourless. Then, y mL 37% HCl was slowly added and stirring was continued for 15 min. 1.25 mL of an aqueous 64 mM AA solution was added and stirring continued for 15 min. Then, z mL of the seed solution was added and after 15 stirring was turned off and the mixture was left to react overnight. A colour change from colourless to light pink, then a deep red to dark brown occurred over the course of several hours.

Table 3.1: Parameters used for the Ye & Murray synthesis of AuNRs, where x refers to the volume of 10 mM $AgNO_3$, y the volume of HCl 37% and z the volume of seed solution. # refers to the number of batches made with that particular method.

method ID	*AR*	x (mL)	y (mL)	z (mL)	#
YM1	~4.5	7.2	2.1	0.8	8
YM2	~7.0	9.6	4.8	0.4	2
YM3	~7.0	9.6	5.4	0.8	2[a]
YM4	~6.5	9.6	4.2	0.8	1
YM5	~1.5	4.8	1	0.2	1[a]
YM6	~5.0	4.8	4.2	0.05	1[a,b]

[a] these were made on a 25 mL scale with all volumes scaled accordingly
[b] this was made using 9 rather than 7 g CTAB

Here, different values of x ($AgNO_3$), y (HCl) and z (seeds) were taken to obtain rods with different aspect ratios, which is summarised for several methods we used in Table 5.3. YM1 was used to make the rods used for etching and silver deposition and generally resulted in AuNRs with an *AR* of ~4.5. In some cases the *AR* was lower when this method was used, which always coincided with the presence of cubic particles and was resolved when the growth solution was given more time to homogenize before and after addition of AA. The YM2 method was mostly used for preparing high-AR AuNRs for self-assembly.

3.2.2 Wu & Huang synthesis

1 mL 1 M aqueous CTAB, 250 µL 10 mM aqueous $HAuCl_4$ and 8.75 mL H_2O were added to an aqua regia cleaned 40 mL vial containing a magnetic stirring bar and placed in a 30 °C water bath. A 10 mM $NaBH_4$ solution was prepared freshly with ice cold H_2O and 350 µL was added while vigorously stirring (1200 rpm). A colour change to light brown indicated formation of small gold seeds. 100 mL of an aqueous growth solution was prepared containing 25 mM $HAuCl_4$ and 1 mM CTAB. Two 25 mL Erlenmeyer flasks were labelled A and B, 4.5 mL of growth solution and 25 µL 0.1 M aqueous AA solution were added to both flasks. A 100 mL Erlenmeyer flask was labeled C, 45 mL growth solution, 250 µL 0.1 M aqueous AA solution, and 300 µL 0.1 M aqueous HNO_3 solution were added. Stirring bars were added to A, B and C and stirring was turned up to 1200 rpm. 400 µL of the seed solution was added to A, then within several seconds 400 µL of flask A was transferred to flask B. After several seconds, 4 mL of flask B was transferred to flask C. After ~ 1 min, stirring in flask C was turned off and the mixture slowly turned purple and then brown. It was left to react overnight after which a black sediment was visible on the bottom of the flask. The supernatant was removed and the sediment was redispersed in 10 mL H_2O, centrifuged at 1500 g for 15 min and redispersed in 8 mL 5 mM aqueous CTAB solution.

3.2.3 Xu & Liang synthesis

9.65 mL of a 0.15 M aqueous CTAB solution was added to an aqua regia cleaned 40 mL vial containing a magnetic stirring bar and placed in a 25 °C water bath and stirred at 400 rpm. 196.8 µL of an aqueous 25.4 mM $HAuCl_4$ solution, 50 µL of an 100 mM aqueous $AgNO_3$ solution and 500 µL of a 50 mM aqueous hydroquinone solution were added to the vial. Then, a certain amount of 1.19 M aqueous HCl was added, we used 10, 15 or 20 µL which we denote as method XL1, XL2 and XL3 respectively. A 10 mM $NaBH_4$ solution was freshly prepared with ice-cold H_2O and 15 µL was quickly added to the vial while stirring vigorously (1200 rpm). After 30 seconds, stirring was turned off and the mixture was left to react overnight, during which the colour changed to dark brown. The particles were collected using centrifugation (8000 g for 15 min), redispersed in H_2O, centrifuged (8000 g for 15 min) and redispersed in 3 mL 5 mM CTAB. For the 100 mL scale synthesis (XL4) all volumetric quantities were increased by a factor 10 and a 300 mL erlenmeyer flask was used. Stirring after $NaBH_4$ addition was maintained for 2 minutes and centrifugation times were increased by a factor of 2.

3.3 Results

3.3.1 Ye & Murray method

TEM micrographs of several samples of AuNRs synthesised with the Ye & Murray method are given in Figure 3.3, TEM-images of more samples are shown in the appendix (Fig. B.3, B.4 and B.5). Statistics and size measurements from TEM imaging are summarised for part of the samples in Table 3.2. The AuNRs could be synthesised with many different aspect ratios which was confirmed with FTIR extinction spectroscopy and with size measurements from the TEM data. In good correspondence with the theory, the particles possess an increasing LSPR peak wavelength with increasing aspect ratio, regardless of the volume of the AuNRs. The width of the LSPR-peak is determined predominantly by the polydispersity of the samples, and is somewhat wider than the spectra reported by Ye & Murray *et al.* suggesting that

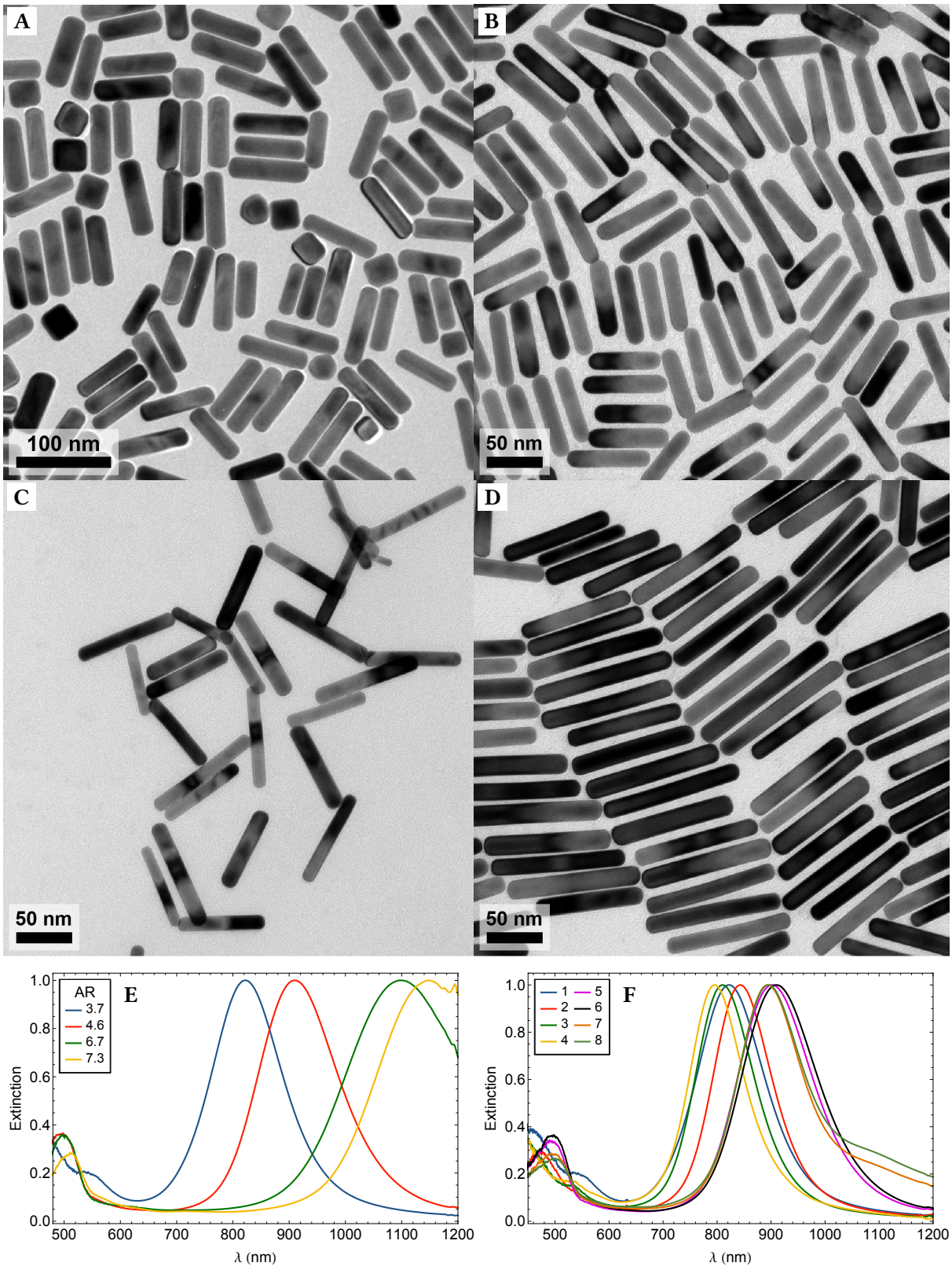

Figure 3.3: A–D: BF-TEM images of AuNRs synthesised using the Ye & Murray method with parameters specified in Table 3.1. A: YM1 method with a large number of shape contaminants, and an aspect ratio of 3.7±16%. B: YM1 method, *AR*=4.7±9.7%. C: YM4 method, *AR*=6.7±14%. D: YM2 method, 7.3±11%. E: normalised FTIR extinction spectra corresponding to the samples in A–D. F: normalised FTIR extinction spectra of 8 batches of AuNRs synthesised with the YM1 method, numbering is chronologically.

Table 3.2: Overview of the results of AuNRs synthesised with the Ye & Murray method

Method	Batch	L (nm)	D (nm)	AR	V (10^4 nm^3)	λ_{max} (nm)
YM1	1	89.9±12.7	24.8±3.7	3.67±16%	4.1±1.3	822
YM1	2	91.5±7.8	23.0±2.2	4.01±11%	3.5±0.8	843
YM1	3	88.2±7.4	24.4±2.3	3.65±12%	3.8±0.8	810
YM1	5	77.7±8.4	17.1±1.8	4.59±12%	1.6±0.4	902
YM1	6	75.3±8.6	16.5±2.0	4.60±13%	1.5±0.4	910
YM1	7	74.7±9.3	14.9±1.4	5.05±14%	1.2±0.3	894
YM1	8	72.5±7.4	15.5±1.3	4.90±9%	1.3±0.3	895
YM2	1	119.5±14.0	16.5±2.1	7.30±11%	2.5±0.7	1150
YM2	2	111.3±12.9	15.9±1.6	7.02±11%	2.2±0.6	1148
YM3	1	80.5±13.1	11.6±1.7	7.02±11%	0.8±0.3	1114
YM3	2	100.5±16.2	14.6±2.2	7.03±22%	1.6±0.6	1099
YM4	1	78.5±12.0	12.3±1.8	6.53±20%	0.9±0.3	1075

in our case, the polydispersity is larger. From size measurements on various samples we know that the polydispersity in the aspect ratio is typically between 10 and 14%. In all samples there were particles with other shapes but the relative amounts varied. In most instances the percentage of non-rodlike particles was < 5%, and these shape impurities consisted mainly of spherical particles with diameters similar to those of the rods. In two syntheses with the YM1 method (specifically: the first two) that were performed for this research there were slightly more shape contaminants including also some cubic particles (Fig. 3.3A) causing an increased extinction peak at 550 nm. These shape contaminants are most likely a result of concentration and temperature gradients during the synthesis as a result of insufficient stirring, as these issues were considerably reduced when longer stirring times were used and extra care was taken to avoid contaminations. AuNRs with a high aspect ratio (YM2 method) contained slightly more spherical particles in both cases.

In total, 8 batches of AuNRs were prepared using the YM1 method. FTIR extinction spectra of these batches (numbered in chronological order) are shown in Figure 3.3F. It can be seen that varying results were observed in different batches as there is a considerable spread in the peak positions, which corresponded well to the aspect ratio from TEM size measurements. When two batches of AuNRs were prepared side-by-side using the same solutions and seeds, the results were always well-reproducible (see for example batches 5&6 or 7&8). This indicates that the variation in the results is most likely due to small differences in precursor concentration or the seed solution. In one instance, two batches prepared side-by-side (7&8) had a tail in the LSPR spectrum due to the presence of higher AR AuNRs in both samples, it is unclear what the cause of this is. It is not possible to comment in detail on the reproducibility for the Ye & Murray *et al.* synthesis with other parameter sets as no other methods were used more than twice (YM2 and YM3). In the case of the YM2 method, two batches were synthesised independently using different stock solutions and seeds and the results in both cases were highly similar which suggest good reproducibility. In the case of the YM3 method the two batches differed strongly in volume and polydispersity. We suspect that this is related to the fact that the first batch was synthesised on a 25 mL scale and the second was synthesised on a 500 mL scale.

Based on the gold concentration and the amount of reducing agent (AA and NaOL), about 2/3 of the Au^{3+} is reduced to gold nanoparticles. This leads to a theoretical particle concentration of 65 mg L^{-1}, excluding any additional weight due to CTAB on the surface. For particles of 100×20 nm, this amounts to a particle concentration of $\sim 1.1 \cdot 10^{14}$ L^{-1}. These values can be used as reference, in combination with the intensity (maximum value) of the LSPR optical extinction peak to get an estimate of the particle concentration during the various reaction steps and experiments. To determine the gold concentration more precisely we attempted flame atomic absorption spectroscopy (F-AAS) and found that the gold signal could be measured only when the particles were collected with centrifugation, dissolved in pure *aqua regia* and subsequently diluted with water to 10 V% *aqua regia*. Due to some issues with the

stability and accuracy of the calibration series, no accurate concentration determination with AAS was done. Inductively coupled plasma atomic emission spectroscopy (ICP-AES) was found to be more precise under similar conditions due to the higher sensitivity and was used to determine the gold concentration of a sample of AuNRs (AR = 3.7). 200 µL of the sample with an optical extinction maximum of 2.25 was dissolved with 50 µL *aqua regia* and diluted with water to a total volume of 5.00 mL. The gold concentration of the diluted sample from ICP-AES analysis was found to be 244±3.4 µg L^{-1}, which corresponds to 2.71 mg L^{-1} for a sample with an extinction maximum of 1. The amount of silver in the sample of gold rods remaining from the synthesis was found to constitute a molar fraction of less than 0.05.

3.3.2 Wu & Huang method

The Wu & Huang *et al* synthesis was reproduced 2 times and in both cases the results were similar. A representative TEM image of the resulting particles in the sediment is shown in Figure 3.4A, optical extinction spectra of the particles and the supernatant are shown in Figure 3.4E. Rodlike particles were present with L=583 nm, D=37 nm and AR = 17.0 ± 36%. In addition to the rods, a large number of spherical particles and (triangular) platelets can be seen making the relative shape yield very low unlike the results reported by Wu & Huang *et al.* [91]. The extinction spectrum shows a broad line without any particular features which may be due to the combined contributions of many different shapes and sizes of particles. No LSPR peak is observed as it would be positioned much further into the IR than the measuring range of our device. The top solution of the synthesis contained mostly spherical particles resulting in the peak at 550 nm. The low shape yield when compared to the literature may be a result of the sensivity of the synthesis protocol to the timing of the seed addition steps. Colour change as a result of particle growth can be seen within seconds after seed addition and subsequent additions to the second and third vial which means that a difference in the time between subsequent pipetting steps of seconds can make a large difference in the final result. As a result, reproducing the results accurately is very challenging. Because of the poor shape yield we did not consider the Wu & Huang *et al.* synthesis for further steps.

3.3.3 Xu & Liang method

TEM images and optical extinction spectra of AuNRs synthesised with the Xu & Liang *et al.* method are shown in Figures 3.4 B–D & F. We used the seedless synthesis with parameters that are reported to yield AuNRs with AR = 15. We could not reproduce these results as we found rods with L=151 nm, D=29 nm and AR = 5.2 ± 16%, as well as a large number of spherical particles (Fig. 3.4B). We increased the amount of HCl solution we added from 10 µL (method XL1) to 15 µL (XL2) and 20 µL (XL3) to obtain a larger aspect ratio, the results are shown in Figure 3.4 C and D. The particles we obtained with method XL2 had the following dimensions: L=121 nm, D=15 nm and AR = 8.0 ± 36%. The particles we obtained with XL3 were very similar and had the following dimensions: L=118 nm, D=14 nm and AR = 8.3 ± 28%. The extinction spectra confirm that a large number of spherical particles are present in all three cases, but more so in XL1 than in the others. The width of the peaks indicates a large polydispersity in the aspect ratio. Based on the peak position, the aspect ratio of XL2 is slightly larger than that of XL3 which contradicts size measurements from TEM images, but this may be due to the majority of both peaks being outside of the measuring range of our device.

We scaled the synthesis of XL3 from 10 mL to a 100 mL scale and found particles with a lower aspect ratio and very similar to those in Figure 3.4B (results not shown), which were grown with only half the amount of HCl (XL1). This indicates that insufficient mixing may be the main cause for the differences between our results and the results reported by Xu & Liang *et al.*. At different stirring speeds during the $NaBH_4$ addition, the initial gold particles may be different in size and number which will drastically influence the resulting particles. This is a common problem with seedless methods and often the demands and ideal conditions for fast nucleation and gradual growth are very different. In seeded growth methods these issues are prevented because the separate small scale seed synthesis

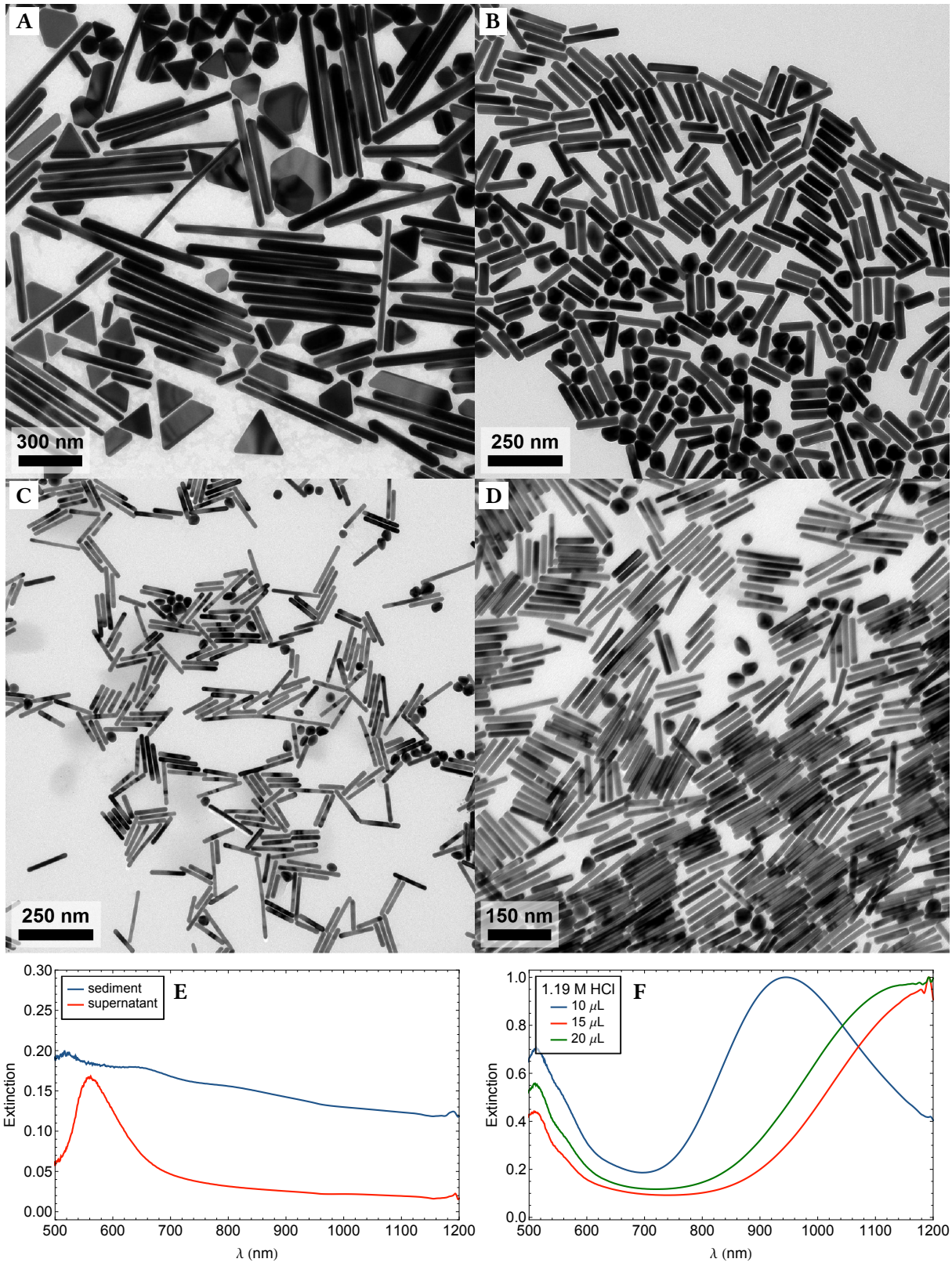

Figure 3.4: TEM images of AuNRs synthesised with A: the Wu & Huang *et al.* method [91] and $AR = 17$. B–D: the Xu & Liang *et al.* method [92] and varying amount of 1.19 M HCl. B: XL1 method (10 µL HCl, $AR = 5.2$). C: XL2 method (15 µL HCl, $AR = 8.0$). D: XL3 method (20 µL HCl, $AR = 8.3$). E: extinction spectra corresponding to the sediment (containing the rods) and the supernatant (mostly platelets) of the Wu & Huang *et al.* method. F: extinction spectra corresponding to samples shown in B–D.

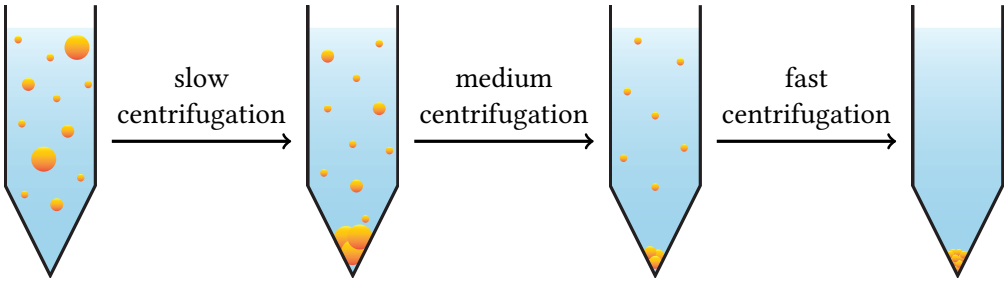

Figure 3.5: Schematic representation of repeated centrifugation. The supernatant is collected and centrifuged again. By tuning the speed and duration, different particle fractions can be obtained.

ensures consistency in the seeds while only during growth the parameters are changed [20,78]. Because we could not reproduce the synthesis of high-AR AuNRs on a larger scale, and because of the large polydispersity of the particles, this method was not used for the remainder of this work.

3.4 Purification by centrifugation

Although the AuNR synthesis generally has a high yield of rod-like particles, shape-impurities can be found which are comprised mainly of spherical and cube-like particles. In addition to these shape-impurities, there is a certain polydispersity in the dimensions of the AuNRs leading to a distribution of particle-volumes. Both the shape and size polydispersity are unfavourable for self assembly as they may prohibit the formation of ordered phases or lead to unwanted phase behaviour. In addition, the use of AuNRs as model system for catalysis is mainly proposed because of their well-defined structure, which relates directly to the purity and monodispersity. While in principle these properties can be achieved by careful and high quality synthesis, results varied from batch to batch. We investigated several methods based on sedimentation to fractionate and purify the nanorods and narrow the shape and/or size distribution of AuNR batches with increased amounts of shape impurities.

3.4.1 Repeated centrifugation

In the most simple case of centrifugation, one can rely on the different sedimentation velocities of particles of different size and/or shape. If slow centrifugation is employed, only the particles with the largest sedimentation coefficients will sediment. The sediment can then be removed and the supernatant, which still contains the smaller particles, can be centrifuged again to obtain another fraction. A typical use for this method would be to separate out the heaviest and lightest by-products by centrifuging the particle dispersion twice. A schematic overview of this is given in Figure 3.5. First, the speed is chosen such that aggregates and heavier impurities sediment while the good particles remain dispersed. The supernatant, containing the particles, is then centrifuged such that the particles only just sediment while lighter impurities remain in the supernatant. The sedimented particles can then be collected and redispersed for further use.

We investigated whether such a repeated process could be used to separate the AuNRs based on their volume and thus increase their monodispersity. We used relatively slow centrifugation as it was found that a large fraction of the particles already sediments in a short time at these low radial forces. In a typical experiment, 500 µL of concentrated rod solution and 3.5 mL H_2O were added to a 5 mL Eppendorf tube and centrifuged at 500 g for 5 min. Afterwards, the supernatant was carefully collected and transferred to a new Eppendorf tube. This tube was then centrifuged again and the centrifugation and transfer of the supernatant were repeated another 3 times. The last supernatant was centrifuged at 15 000 g to collect all remaining particles. The sedimented particles were dispersed in 1 mL nanopure water each time after the supernatant was removed. Using TEM imaging and FTIR extinction spectroscopy, we found little to no evidence of separation of AuNRs from Au spheres, and no

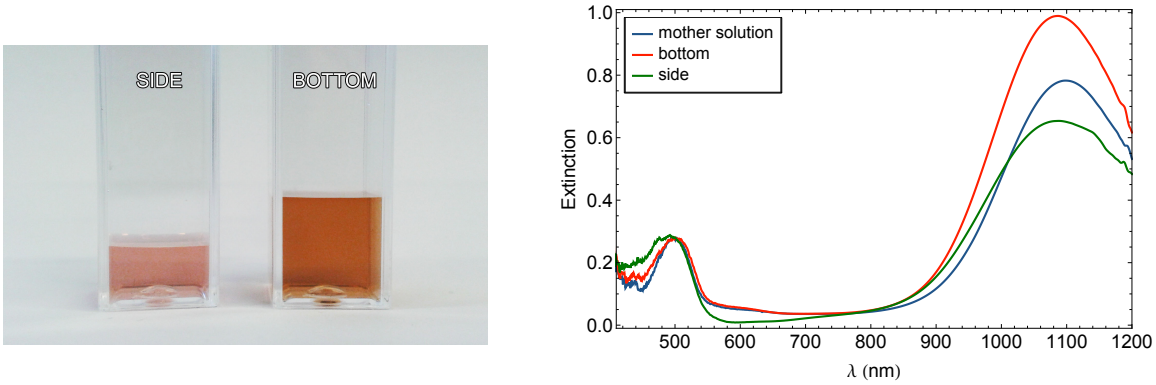

Figure 3.6: Photographs (left) and FT-IR extinction spectra (right) of fractions obtained from the bottom and the side of the tube. The extinction spectra were normalised to the peak at ~ 500 nm which arises mainly from the shape impurities. A higher ratio of the LSPR-peak to the peak at 500 nm indicates a higher purity of AuNRs.

evidence of separation based on NR aspect ratio. The IR-extinction spectra (not shown) of the different fractions show little to no differences indicating that the rods in each fraction are nearly identical. In some cases very small (10 nm) spherical particles had a slight preference to stay in the supernatant, but a considerable fraction was always present in the sediment once the majority of AuNRs had sedimented Repeated centrifugation was however effective in the separation of particles with large size differences, such as the removal of aggregates or seed particles remaining after the synthesis. Lastly, particles with sufficiently different densities such as small silica spheres could be washed away in such a manor.

3.4.2 Shape effects in sedimentation

Recently it was reported in the literature that due to their different sedimentation behaviour during centrifugation, rods and spheres can sediment preferentially on the side or the bottom of a centrifuge tube [93]. The exact mechanism of this process is unclear, but is generally considered to be an effect of the different sedimentation velocities of the particles. Sharma & Srinivasarao *et al.* [93] derived the following expression for the ratio between the equilibrium sedimentation velocities of rods (spherocylinders) and spheres:

$$\frac{v_{rod}}{v_{sphere}} = \frac{s_{rod}}{s_{sphere}} = 6\left(\frac{D}{R}\right)^2\left[2\ln\left(\frac{L}{D}\right) - (v_{\parallel} + v_{\perp})\right] \tag{3.1}$$

where v_{rod} and v_{sphere} are steady state sedimentation velocities, s_{rod} and s_{sphere} sedimentation coefficients, D and L the diameter and length of the rods, R the diameter of the spheres and $v_{\parallel}$ and $v_{\perp}$ unknown correction factors for the orientation dependency of the rods. It is clear from this formula that the separation efficiency of rods and spheres with centrifugation will be dominated by the ratio between their diameters because of the quadratic dependency. The aspect ratio L/D of the rods on the other hand, appears in a logarithmic term and will only have a significant influence if $D/R \approx 1$, but will lead to a small effect in all cases.

Using a procedure adapted from Sharma & Srinivasarao *et al.* [93] we investigated the sedimentation behaviour of a mixture of AuNRs and cubic and spherical by-products. 5 mL of the concentrated particle solution (AR 6.6) as obtained after the YM3 synthesis (Section 3.2.1) was diluted to 30 mL with H_2O in a 50 mL centrifuge tube and centrifuged for 15 min at a radial force of 12 000 g in a fixed angle rotor. ~ 25 mL of the supernatant was removed carefully without disturbing particles sedimented on the wall. Using a 100 µL pipette the particles on the bottom of the tube were carefully collected and dispersed in an aqueous solution containing 5 mM CTAB. The particles sedimented on the side of the tube were redispersed in the remaining supernatant. Photographs and FT-IR extinction spectra of the two fractions are depicted in Figure 3.6. A clear difference in the two fractions can be observed visually and in the ratio of the two peaks visible in the absorption spectra. The higher intensity of the LSPR peak (relative

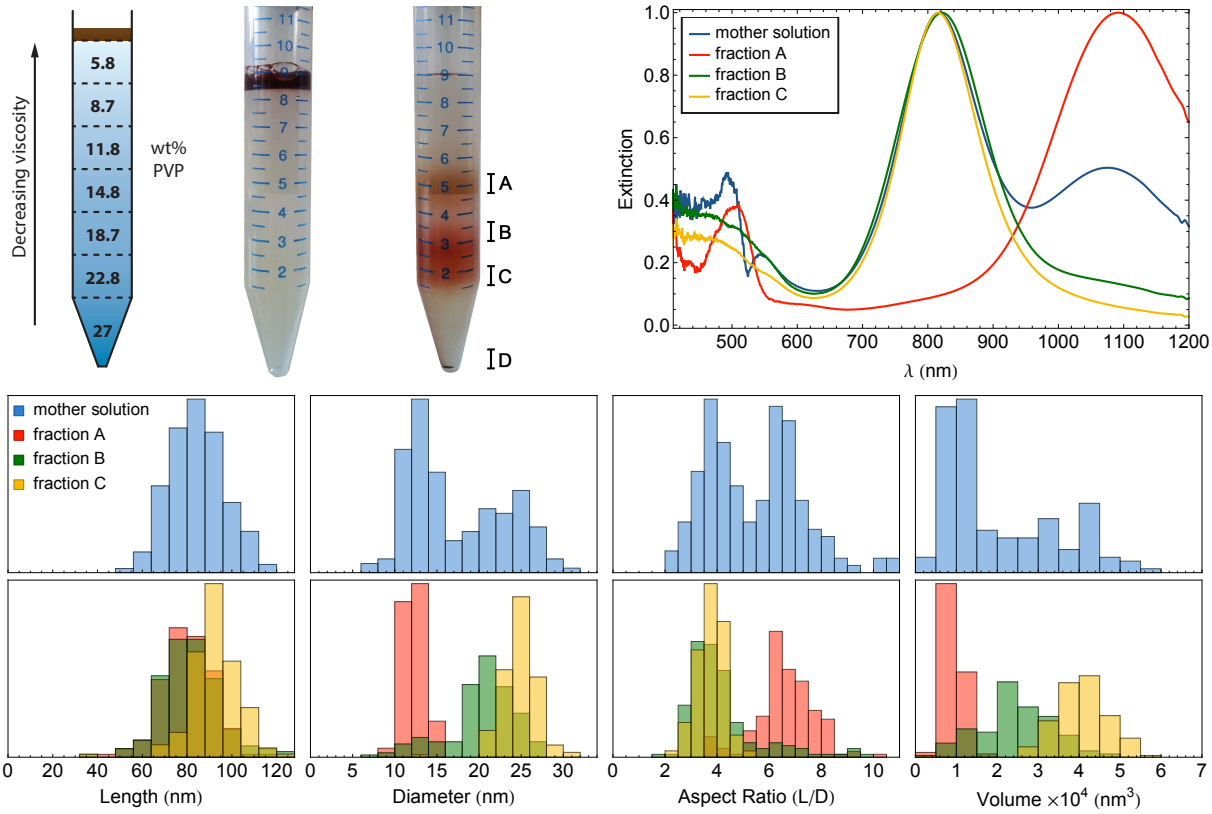

Figure 3.7: Photographs of centrifuge tubes before and after viscosity gradient centrifugation and normalised optical absorption spectra of different samples taken from the tube. A mixture of two distinct rod sizes was used.

to the peak at ~ 500 nm which originates mainly from the plasmon resonance of spherical and cubical particles) for the fraction on the bottom of the tube indicates a higher purity of the AuNRs. TEM was used to analyse the fractions; representative images can be found in the appendix (Fig. B.6). Depending on the exact diameters of samples, this method may be useful to remove a large part of the shape contaminants, but this comes at the cost of loss of a large part of the sample.

3.4.3 Viscosity-gradient centrifugation

It has been shown that polydisperse reaction mixtures can be fractionated based on size in a viscosity gradient [94]. Unlike density gradient centrifugation, where the final position of a particle is determined by the density of the particle and the density of the medium, the viscosity solely affects the sedimentation rate. In principle, after a long time all particles will reach their equilibrium position on or near the bottom of the tube. What is affected, however, is the sedimentation velocity of the particles. Since the hydrodynamic drag of a particle depends strongly on the shape, particles with a similar mass/volume but a different aspect ratio sediment at a different speed. By tuning the viscosity and the centrifugation speed and time, a good separation can be achieved. Because the forces of gravity/centrifugation scale with particle mass and hydrodynamic drag with the surface area, it is expected that particles with larger mass sediment at a higher velocity.

Solutions of different viscosities were prepared by diluting varying amounts of PVP (40 000 g mol^{-1}) in a solution containing 5 mM CTAB to keep the particles stable. A viscosity gradient was made by carefully stacking a certain amount, (in most cases 1.5 mL) of each solution on top of each other with a glass pipette, starting with the solution containing the highest weight percentage of PVP. A full overview of the concentrations of PVP (expressed in wt% w.r.t. H_2O) and their stacking order in the centrifuge tube can be seen in Figure 3.7. When added carefully, the layers do not mix due to their different PVP concentrations and slightly different densities. Lastly, 500 µL of a concentrated solution

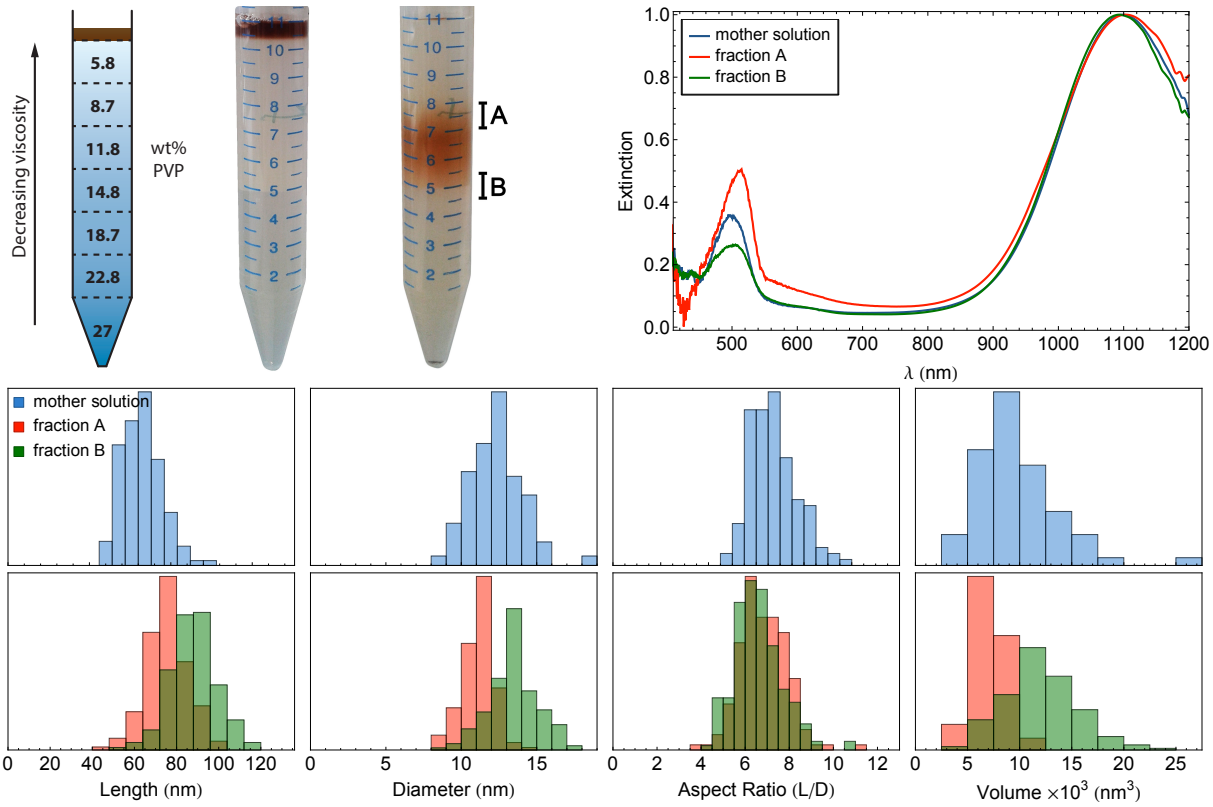

Figure 3.8: Schematic overview of the viscosity gradient stack and images of the tubes before and after centrifugation. The separation occurred based on particle volume but no effects of the aspect ratio are seen. The separation of spherical particles (as evidenced by the extinction at 500 nm is thus most likely a volume effect.

containing AuNRs was added on top. The tube was centrifuged at 4000 g for 3 hours using a swinging bucket rotor (SBR). We note that the use of a fixed angle rotor is not possible as the radial force must be applied exactly parallel to the gradient. Otherwise, particles quickly sediment on the side of the tube and slide downwards. This effect is already observed to a small extent when the tube is placed off-center in the bucket of the SBR. For successful separation, the tubes must therefore always be placed in the centre of the bucket.

To verify our hypothesis that separation occurs mainly if rods have a strongly different diameter, we tested the viscosity gradient method for a sample containing two clearly distinct samples of AuNRs. This sample was prepared by mixing 300 µL of a concentrated solution of particles synthesised using the YM1 synthesis (batch 1, see Tab. 3.2, Sec. 3.1.1) with 300 µL of a concentrated solution containing particles made with the YM4 method (batch 1). A viscosity gradient was prepared with 1.5 mL of a 27 wt% PVP solution, 1 mL of the 22.8, 18.7, 14.8, 11.8 and 8.7 wt% PVP solutions and 2 mL of a 5.8 wt% PVP solution. The (aqueous) solutions were carefully stacked on top of each other (in order of high to low concentration from bottom to top) in a 15 mL centrifuge tube. 500 µL of the rod-sample was added drop-wise on top. The tube was centrifuged at 4000 g for 2.5 hours in a centrifuge equipped with a SBR. Photographs taken before and after centrifugation are shown in Figure 3.7. Afterwards, samples of approximately 1 mL each were taken at different positions in the tube with a syringe and a needle with a tip that was bent 90° to prevent disturbance of the fractions due to a vertical fluid flow. The samples were diluted to ~ 4 mL with nanopure water and concentrated by means of centrifugation. The sediment was washed with 4 mL of an aqueous solution containing 5 mM CTAB, centrifuged and redispersed in 1 mL 5 mM CTAB. FT-IR extinction spectra were recorded and are depicted in Figure 3.7.

The optical extinction spectra shows two clear peaks from the LSPR of the two sets of particles. The top and bottom fraction of the AuNR band in the tube (A and B) both contain only one of these peaks, indicating that highly efficient separation has occurred. The width of the bands however, remains broad.

The sample in the middle of the AuNR band corresponds mostly to one of the two dominant peaks in the spectrum of the mother solution, rather than a peak lying halfway between the two. This indicates that the separation is not purely based on the AR, and that particles of similar aspect ratio may end up at different height. TEM imaging and corresponding size measurements confirm this and demonstrate that separation occurs predominantly based on volume. As the volume of the particles depends more strongly on the diameter than on the length of the particles, selection based on diameter is possible. A small part of the particles ended up on the bottom of the tube, this contained mostly extremely large particles and some small aggregates.

The viscosity gradient method was subsequently tested for a sample with a more realistic spread in the particle size distribution (YM4 method, batch 1, Tab. 3.2). Photographs, FTIR extinction spectra and particle size distributions from TEM are all shown in Figure 3.8. The FTIR extinction spectra of the mother solution and both fractions differ only in the peak at 500 nm, while the position and broadness of the LSPR peak is near identical in all cases. The absence of a change in LSPR peak position directly indicates that there is no separation based on the aspect ratio. The same conclusion can be drawn from the TEM size distributions: separation occurs purely based on volume and not based on shape. This does mean that separation of spherical particles can be efficiently achieved since their volume is typically much smaller, which corresponds to the height of the peak at 500 nm that was measured. The separation methods we investigated thus did not reliably separate polydisperse rod-like samples. Furthermore, the large number of washing steps involved combined with the inherent losses of selecting only a small fraction of particles, means that many AuNRs are lost in the process. Other methods for AuNR purification have been reported, relying for example on density gradient centrifugation [95], depletion [96] or partial etching [97]. Because it was found that higher monodispersity with fewer shape-impurities could be achieved using careful AuNR synthesis, we decided not to pursue these methods further.

Chapter 4

Silica coating of gold nanorods

The AuNRs are colloidally stabilised in polar solvents by a surfactant layer on the surface consisting of mainly CTAB, and as long as CTAB is present the particles are stable for long periods of time (>1 year). When the AuNRs are washed multiple times with H_2O or other solvents that do not contain surfactant, the double layer will be removed from the surface causing the AuNRs to aggregate. For many applications it is desirable to stabilise the particles in other solvents and to shield the strong Van der Waals attractions between the cores, which can be achieved by coating the AuNRs with a silica shell. Silica is a very widely used material for the stabilisation of nanoparticles and apart from preventing aggregation, there can be many more advantages of a gold-core silica-shell structure. Although gold is known to have a high chemical stability by itself, a silica shell may form a protection against oxidising environments or inversely protect the environment from reactions occurring on the gold surface. Due to the extensive knowledge on the chemistry of silica surfaces and the variety of silanol reagents, it enables easy modification of the surface with functional groups such as polymers [98], DNA [99] or hydrophobic groups [100]. We note that direct functionalisation of the Au surface has been reported with for many molecules, but these methods remain challenging due to the unstable nature of unprotected AuNRs [20, 29]. The thermal stability against deformation and loss of the anisotropic shape is known to be improved by the presence of a silica shell [101]. Lastly, (porous) shells can act as a template for synthesis of rods [102, 103], branched structures [34, 104] and chiral selectivity [105].

We synthesised AuNR@SiO_2 core-shell structures using two different methods that resulted in core-shell particles with either a relatively thick and highly mesoporous shell which we call AuNR@*meso*-SiO_2, or AuNRs with an ultra thin silica layer which we denote as AuNR@thin-SiO_2. The main motivation behind the porous silica shell was that it enabled us to synthesise the bimetallic particles in Chapter 5, since mass transport from and to the AuNRs is still possible through the mesopores. The main motivation for AuNR@thin-SiO_2 was to simultaneously maximise the aspect ratio of the total particle (including silica) for self-assembly (Chapter 6) and retain the electric field enhancement and coupling of the plasmon resonance which occurs only within very close distance from the surface. Lastly, the synthesis of a protective shell that still retains the electric field enhancement of the AuNRs is of interest for SERS.

4.1 Experimental

4.1.1 Adapted Gorelikov & Matsuura method for AuNR@*meso*-SiO_2

Using optical extinction spectroscopy, a dilution factor for AuNRs in 5 mM CTAB solution as obtained from the Ye & Murray synthesis was determined such that the LSPR extinction maximum was 1.0. The AuNR dispersion was then added to a 300 mL Erlenmeyer flask an diluted with H_2O and aqueous 5 mM CTAB solution to a concentration such that diluting another 10x gave $Abs_{max} = 1.0$ for $AR = 4$ and $Abs_{max} = 1.2$ for rods with $AR = 7$ (160 mg L^{-1} of Au, ~2.5x more concentrated than during the synthesis), *and* such that the final concentration of CTAB was 1.5 mM. The dispersion was stirred

with a magnetic stirring bar at 400 rpm and per 100 mL of the AuNR dispersion, 1 mL 0.1 M aqueous NaOH solution was added. 400 µL TEOS was diluted with 1.6 mL ethanol and 300 µL of the ethanolic TEOS solution (per 100 mL AuNR dispersion) was slowly added to the particles. After 45 minutes, again 300 µL of ethanolic TEOS was added, and after another 45 minutes this was repeated. If the total volume of the AuNR dispersion was not 100 mL, the volumes of NaOH and TEOS solution were scaled accordingly. The mixture was left to react for 2 days while stirring at 400 rpm after which the particles were collected using centrifugation (8000 g for 25 min), redispersed in water, centrifuged (8000 g for 25 min), redispersed in ethanol, centrifuged (8000 g for 25 min) and redispersed in ~20 mL ethanol for storage.

4.1.2 AuNR@thin-SiO_2 with APTES or MPTMS

An adapted version of a method reported by Wang & Tian *et al.* [106] was used to grow thin shells with an amino coupling agent ((3-aminopropyl)triethoxysilane, APTES). 667 µL AuNRs in 5 mM aqueous CTAB as obtained from the Ye & Murray synthesis was diluted with 667 µL H_2O, centrifuged (8000 g for 10 min) and redispersed in ~8 mL H_2O such that the concentration was equal to that of the AuNR synthesis (~60 mg L^{-1}, such that diluting 4x with H_2O gave $Abs_{max} = 1.0$ for $AR = 4$ and $Abs_{max} = 1.2$ for rods with $AR = 7$). A 1 mM aqueous APTES solution was prepared and left to hydrolise for 10 minutes after which 160 µL was added to the AuNR dispersion while stirring vigorously (1200 rpm). The mixture was subsequently left to react for 15 minutes. An acidified sodium silicate solution (0.54 wt% at pH=10.02) was prepared by adding 100 µL 27 wt% sodium silicate solution and 300 µL 0.1 M HCl to 4.6 mL H_2O. Then, 1.28 mL of the acidified sodium silicate solution was added to the rods after which they were left to react overnight. Large aggregates were visible which could not be redispersed using ultrasonication but could be removed by filtration through a syringe filter (1 µm cut-off radius). The particles were collected using centrifugation (7000 g for 10 min), redispersed in 8 mL H_2O, centrifuged, redispersed in 8 mL ethanol, centrifuged and finally redispersed in 2 mL ethanol.

As an alternative we used a method developed by Tiansong Deng [107] that utilises a thiol coupling agent ((3-mercaptopropyl)trimethoxysilane, MPTMS). Again, a 60 mg L^{-1} AuNR dispersion was prepared as described above. To 8 mL of the dispersion was added 80 µL of a 5 V% ethanolic solution of MPTMS while stirring vigorously (1200 rpm). A 0.54 wt% solution of sodium silicate was prepared by mixing 100 µL 27 wt% sodium silicate solution with 4.9 mL H_2O, 1.28 mL of this was added to the AuNRs followed immediately by 640 µL 0.1 M aqueous NaOH. The reaction was left to proceed overnight after which the particles were washed as described above for the Wang & Tian *et al.* method.

4.1.3 Coupling agent free method for AuNR@thin-SiO_2

AuNRs could be coated with an ultra-thin layer of silica using the method we developed with the following procedure: 667 µL concentrated AuNRs in 5 mM CTAB as obtained during the synthesis were diluted with 667 µL H_2O and collected using centrifugation for 10 min at 8000 g. The supernatant was discarded and the particles were redispersed in an amount of H_2O such that the concentration of AuNRs was the same as at the end of AuNR synthesis (~60 mg L^{-1}, such that diluting 4x with H_2O gave $Abs_{max} = 1.0$ for $AR = 4$ and $Abs_{max} = 1.2$ for rods with $AR = 7$). A 0.54 wt% sodium silicate solution was prepared by adding 100 µL sodium silicate solution (27 wt%) to 4.9 mL H_2O. Then, 640 µL of the 0.54 wt% sodium silicate solution was added to 8 mL of the AuNR dispersion under vigorous stirring (1200 rpm). The mixture was left to react for 45 minutes. The reaction was stopped by centrifugation (7000 g for 10 min) and redispersion in 4 mL H_2O. The particles were centrifuged again and redispersed in 4 mL ethanol, centrifuged and redispersed in 2 mL ethanol, centrifuged and finally stored in 1 mL ethanol. The reaction was performed at room temperature. The silica-coating could easily be scaled to larger quantities by scaling all volumes accordingly, a total reaction volume of ~70 mL was typically used for a large batch of AuNRs@SiO_2. Only the parameters for centrifugation during washing were adapted slightly because of the use of larger centrifuge tubes, to 6000 g for 30 min.

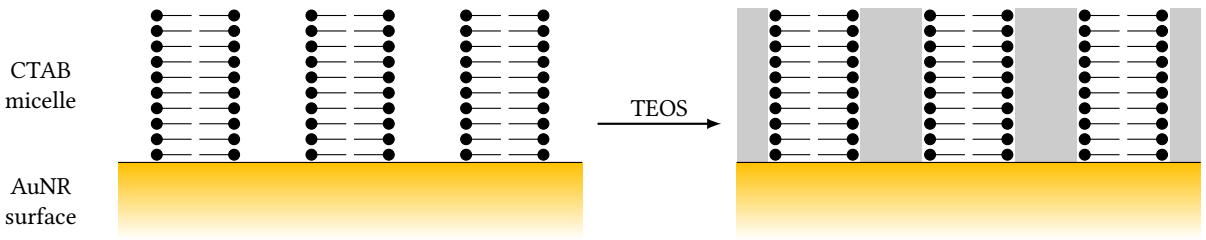

Figure 4.1: Schematic overview of the formation of mesoporous silica. The cylindrical CTAB micelles on the surface form a soft template for the ordered porous structure and can be washed away after the silica-coating is completed. We note that the way the micelles are attached to the surface may not be represented accurately as it is likely that a CTAB double layer covers the surface.

4.2 Coating of AuNRs with a thick mesoporous silica-shell

We synthesised AuNR@*meso*-SiO_2 with a method based on the protocol by Gorelikov & Matsuura [108] and very similar to that of Wu & Tracy [98] which was reported before in ref. [34]. It is a relatively simple single-step method for CTAB stabilised AuNRs. Full experimental details are given in Sec 4.1.1. In this method the silica is added in the form of the common silica precursor tetraethyl orthosilicate (TEOS) which condenses into silica and ethanol in the presence of H_2O. The pH of the solution is increased by the addition of NaOH as the hydrolysis of TEOS occurs much faster when it is base-catalysed, while at the same time it increases the solubility of the silica which brings the growth closer to an equilibrium. The TEOS is added in 3 seperate steps with 45 minute intervals to keep the concentration below the critical concentration for silica nucleation at any point in time. The reaction is performed in the presence of CTAB which serves three purposes. Firstly, it ensures colloidal stability of the AuNRs by the formation of a double layer on the surface that gives the particles a positive charge. Secondly, the gold surface itself does not act as nucleation site for silica condensation and often special organic coupling agents are needed to prime the surface for binding to the silica. In this synthesis, CTAB serves such a purpose due to electrostatic attraction (the CTAB bears a positive charge while silica is negatively charged under reaction conditions) and it has been reported that the CTAB acts as a nucleation site for silica. Initially silica oligomers are created which form SiO_2–CTAB primary particles that subsequently aggregate on the surface of the gold and grow further by monomer addition [109, 110].

Lastly, the CTAB is needed to obtain the porous structure of the silica which is depicted schematically in Figure 4.1. Since the CTAB concentration is above the critical micelle concentration (0.9 mM [111]), micelles are present which adsorb on the gold surface. These micelles form a template for the pores in the silica as the silica shell can only grow around the CTAB micelles but not replace them. Interestingly, CTAB is known to posses micelles of many structures depending on the concentration, solvent and other reactants present, and it is the self-organisation of these micelles that determines the shape and structure of the resulting pores [112]. This is employed in the synthesis of many highly porous silica structures such as the MCM materials: MCM-41 (long cylindrical pores with hexagonal ordering), MCM-48 (3D cubic pores) and MCM-50 (lamellar structure). These structures are made by growing silica around micelles with these specific geometries and subsequent removal of the surfactant. A similar control over the pore geometry is likely possible here, as both radial [98,108] and parallel [104] pore structures have been reported, but this is not investigated in this work.

EM images of the silica-coated AuNRs are shown in Figure 4.2. The resulting silica shell has a thickness of around 20 nm that can be increased by increasing the number of TEOS additions. The pores have an average diameter of 2–3 nm separated by walls of 2 nm although these measurements may be inaccurate due to the low resolution of the SE-SEM images. Additionally, it is possible to measure the pore size from gold branches grown into the pores (see Sec. 5.5) which gave a pore size of 4.5 nm under the assumption that the gold branches accurately represent the shape of the pores. The silica-coated particles are colloidally stable in H_2O, methanol and ethanol but slight dissolution and degradation of the silica shell occurred if the particles were stored in H_2O for more than several

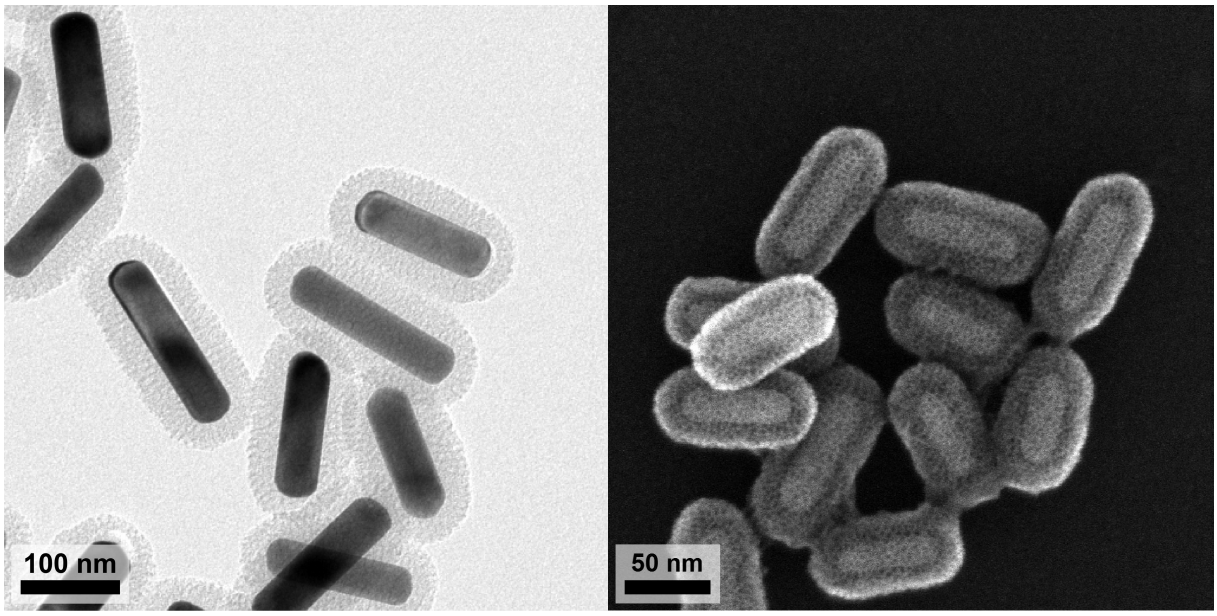

Figure 4.2: BF-TEM (left) and SE-SEM (right) images of AuNR@*meso*-SiO_2. A sponge-like porous structure can be seen.

days. The degradation could also be reduced by storing the particles at 4 °C. After shell growth is completed, the CTAB can be washed out with H_2O or ethanol to open up the pores although complete removal remains challenging with this method. Alternatively, thermal treatment in an oxygen-rich environment can be used to decompose the remaining CTAB entirely, but subsequent redispersion of the treated AuNRs@SiO_2 is limited. In addition to this, considerable thermal reshaping of the AuNRs can take place at 500 °C depending on the volume and aspect ratio of the AuNRs. A thermal treatment can strengthen the silica shell by assuring that the silanol groups condense completely, which does not happen in the low temperature synthesis (30 °C). As a result the shell is more flexible and more soluble than conventional (fully condensed) silica nanomaterials. We did some preliminary experiments in an attempt to increase the strength of the silica shell where the particles in ethanol were heated to 100 °C under high pressure in an autoclave, but this lead to irreversible aggregation of the AuNRs.

The evolution of the silica growth was studied over time by taking samples as the reaction progressed (as described in Sec. 4.1.1). TEM images of the first two samples are shown in the appendix (Fig. B.7). It was found that 45 minutes after the first TEOS addition very thin (>4 nm) inhomogeneous patches of silica can be seen on the surface but large parts of the surface remain bare. This corresponds well to the a formation mechanism where CTAB nucleates small silica particles than aggregate on the surface [109]. Directly after the sample was taken, a second TEOS addition was performed. A sample was taken 45 minutes later and revealed particles coated with a rough silica layer with an average thickness of 13 nm. After another 45 minutes (without a third TEOS injection) we found that the shell thickness had not considerably increased (14 nm) but was much more smooth and similar in appearance to the resulting particles after the normal two day synthesis method. From this experiment we can conclude that the shell growth occurs relatively fast after a sufficient TEOS concentration is reached after which the initially rough structure smooths out, which can be attributed to the dissolution equilibrium in the alkaline aqueous reaction mixture. We expect that the particles do not significantly change after the initial 2–3 hours.

Other methods have been reported to control the thickness of the silica shell. The concentration of CTAB (around the critical micelle concentration, CMC) can be used to tune the thickness between ~10 and ~30 nm since free micelles lead to secondary nucleation of silica which reduces the available precursor for the shell and thus leads to a thinner shell [110]. Silica-shells with a thickness between 2 and 17 nm have been synthesised by terminating the shell growth with poly(ethylene glycol) silane (PEG-silane) before a thick shell has formed. The time at which PEG-silane is added then determines

the thickness of the shell. A similar approach could be used with other silanes, which has the advantage of direct functionalisation of the surface. If the porosity of the shell is undesirable, a closed Stöber silica shell can be grown around the particles in a second step [108].

4.3 Coating of AuNRs with an ultra-thin silica-shell

To study self-assembly of high aspect-ratio rods, it was necessary to use an ultra-thin silica coating (2-4 nm) as the thickness of the mesoporous shell previously described decreases the aspect ratio considerably, and growing high-aspect ratio rods ($AR \geq 8$) without the presence of shape impurities remains challenging. Several methods are reported in the literature to coat gold nanoparticles with a thin silica layer, but they all rely on the same concepts [99, 106, 113–115]. Gold nanoparticles in aqueous dispersion reacted with a coupling agent that contains a functional group which can bind to the gold surface (typically amino or thiol groups) and a silanol (typically a trimethoxy- or triethoxysilane) group that can react with a silica precursor to form a shell. A diluted sodium silicate solution (water glass) is used as precursor for silica. The growth speed can be controlled by adjusting the pH, because the rate of condensation of sodium silicate increases as pH decreases [116]. Alternatively, shortening the reaction time results in thinner silica shells whilst increasing temperature increases the shell growth speed. It is generally considered important to tune the amount of coupling agent added. When too much is added it can lead to crosslinking and aggregation of particles, but when too little is added the gold is only partially covered with silica or not at all. Ideally the concentration of AuNRs and crosslinker is chosen such that it is slightly below that for a complete monolayer coverage of all particles [113].

4.3.1 Influence of the coupling agents

Experiment for silica-coating with sodium silicate were performed via several different methods using (3-mercapto-propyl)trimethoxysilane (MPTMS), (3-aminopropyl)triethoxysilane (APTES) or no coupling agent. Full experimental details are given in Section 4.1.3. We found that, unlike reported in the literature, adding a silane coupling agent is not necessary to obtain an ultra-thin homogeneous silica layer. In fact, addition of a coupling agent such as MPTMS or APTES prior to addition of the silica precursor did not give good results in any of our experiments. Minor clustering (2 to 3 particles per cluster) was observed which occurred prior to growth of the silica-shell (Fig. 4.3A), causing multiple particles to become enclosed in a single shell. This could be easily distinguished from clustering after shell growth due to the smaller inter-particle spacing, the cold welding that occurs when the bare gold surfaces come into contact or the deformation behaviour under the influence of the electron beam. The clustering was also visible during the reaction as a colour change occurred due to the plasmon-coupling of rods that come into close contact. When no coupling agent is used these issues did not occur and complete coverage of the gold surface with a thin silica layer (typically between 2 and 3 nm) was still observed.

Curiously, the presence of the coupling agent in the silica shell also demonstrated a 'self-etching' process inside of the silica shell. Using BF-TEM imaging, many AuNRs could be seen that had a smaller size than the silica shell grown around them, some examples are shown in the appendix (Fig. B.8). The volume of the deformed nanorods was unchanged from the initial AuNRs used in the silica-coating, which indicates that rather than etching of the tips, a reshaping to lower aspect ratio occurs. This deformation was observed for at least half of samples prepared with a coupling agent, but always only occurred locally in one place on a TEM-grid where *all* particles were deformed, while the vast majority of the TEM-grid contained particles that were *all* unaffected. The frequency with which and degree to which these effects were observed scaled roughly with the concentration of coupling agent used, but this is difficult to quantify due to the relatively low frequency of occurrence and the small field-of-view of the TEM. The fact that these effects were observed with such a dependency on location on the TEM grid means either that there is a very selective and strong effect for the particles to collect together when drying, or the effects we observed are related to the effects of the TEM grid or the electron beam. Since

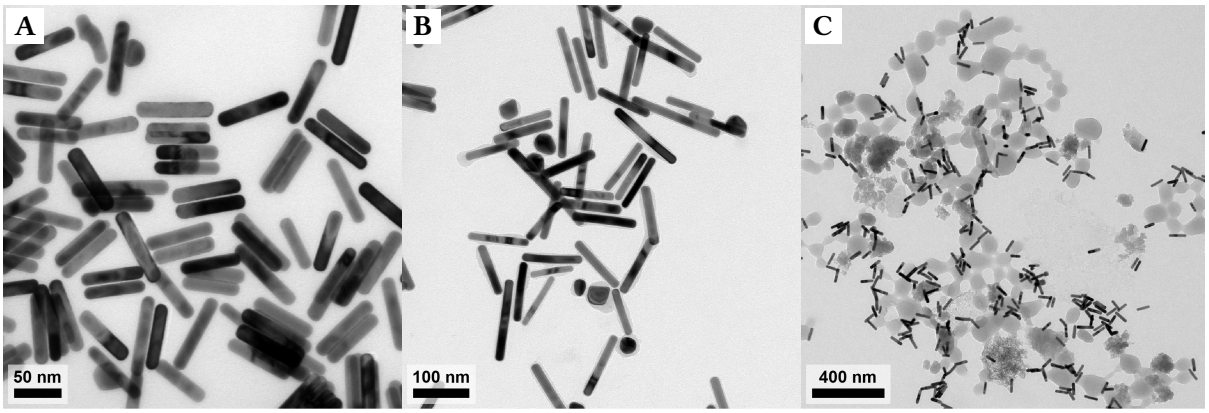

Figure 4.3: silica shells grown with various parameters. A: a high concentration of MPTMS leads to side-by-side clustering of the AuNRs during silica shell growth. B: AuNRs with a rough inhomogeneous silica shell. C: 'secondary nucleation' or contamination of silica species when the sodium silicate concentration is high.

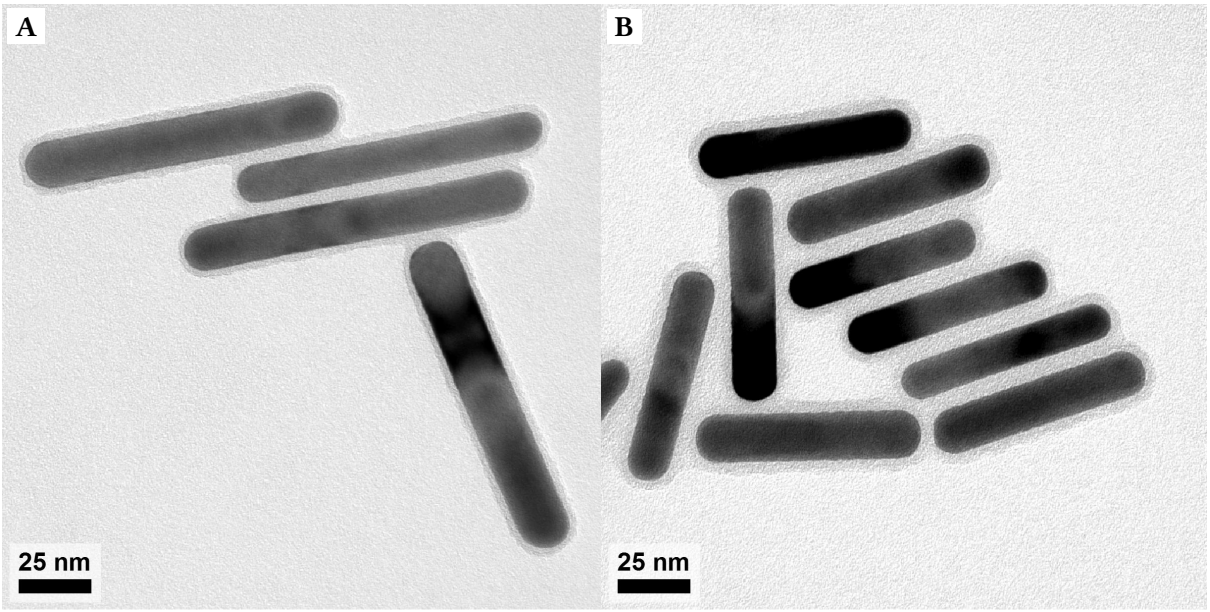

Figure 4.4: AuNR@thin-SiO_2 with the coupling-agent free method. A: standard method with a single addition of 80 µL 0.54 wt% sodium silicate solution per 1 mL of AuNR dispersion and a reaction time of 45 minutes. B: increased shell thickness after a second shell growth step.

drying forces are huge and drying was fast, it is extremely unlikely that separation of the deformed and undeformed particles occurs with such selectivity and precision for particles with nearly identical hydrodynamic shape. Furthermore, no spectral evidence was seen for the reduced aspect ratio. We therefore conclude that these effects are a result of effects of the electron beam combined with the presence of species that strongly bind gold inside of the silica shell. It is possible that local heating of contaminations or excitation of the plasmon resonance by the electron beam accelerate this process. Lastly, it could be that silica with a high percentage of silane coupling agent is softer and thus deforms more easily.

The formation of a thin silica shell was observed in all experiments we performed, which indicates the strong preference of silica for the Au surface, contrary to what is reported in the literature. This is most likely related to the presence of a substantial amount of CTAB on the gold surface to maintain their stability in the sample. For one AuNR sample we tested the concentration of sodium silicate had to be adjusted (40 µL of 0.54 wt% sodium silicate solution per 1 mL of AuNR dispersion) to obtain thin monodisperse silica shells. If 40 µL sodium silicate solution per 1 mL of AuNR dispersion was used,

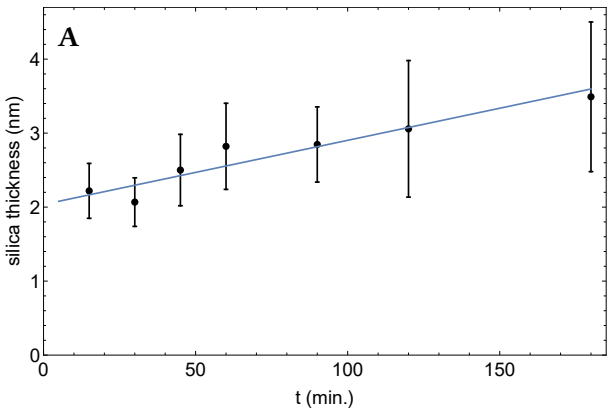

Figure 4.5: Evolution of the silica shell thickness over time. Samples were taken at regular time intervals after the sodium silicate was added. The samples were immediately centrifuged and washed to stop the reaction. At least 70 size measurements were used for each sample. We note that the polydispersity may be larger than in reality due to the resolution of the images and size measurements in relation to the shell thickness.

rough shells were obtained that varied widely in thickness. The exact reason for this is not investigated further in this work, but we suspect it may be related to the presence of HCl from the synthesis that is not washed away sufficiently, as the pH strongly influences the reaction speed. An alternative explanation is that the CTAB concentration is different, but the issues were not resolved by an extra washing step with 5 mM CTAB solution. The silica coating protocol is not highly sensitive to the concentration of AuNRs and it is therefore not necessary to determine the particle concentration exactly each time once the dilution factor for a sample has been checked by absorption at least once. The concentration of CTAB on the other hand seems rather important for the stability of the AuNRs during the reaction and is currently mainly determined by washing parameters used before the silica-coating. If the AuNRs stored in 5 mM CTAB are diluted with H_2O prior to the reaction, the concentration of CTAB is still high and this may induce secondary nucleation of silica. If the particles are diluted with a large volume of H_2O before centrifugation, or centrifuged and redispersed in H_2O two or more times, the concentration of CTAB is too low to sustain a coverage of the particles which causes them to aggregate before a protective silica layer can be formed. We found that good results for the particle stability were obtained when the particles in 5 mM CTAB were diluted 50/50 with H_2O followed by centrifugation and redispersion. This maintained stability of the AuNRs long enough for a silica layer to form, although we note that the particles cannot be stored in this way for longer than several hours. It is generally best to prepare the dispersion from a stock solution with 5 mM CTAB directly prior to the reaction.

A BF-TEM image of the particles grown in such a manner without coupling agent is shown in Figure 4.4A. Additional images of other samples prepared using the same method are shown in the appendix (Fig. B.9). The particles were covered with a thin silica shell that was smooth and had a consistent thickness for all particles in the sample regardless of their size or shape. There was however quite a large variety in thickness between different samples, even when prepared using the same particles, reactant concentrations, reaction time and washing parameters. We suspect that these differences may be related to small changes in silica concentration and pH, as these mostly depend on the volume of liquid remaining after centrifugation and removal of the supernatant. The temperature was not controlled during the reaction and may be of influence as well. In some cases, in particular those prepared from one specific batch of AuNRs, the shells we obtained were rough and inhomogeneous within the sample (Fig. 4.3B). This roughness could be reduced, but not completely omitted, by using a 50% lower sodium silicate concentration. In all cases the resulting particles were stable in H_2O and ethanol, indicating complete coverage of the surface with silica.

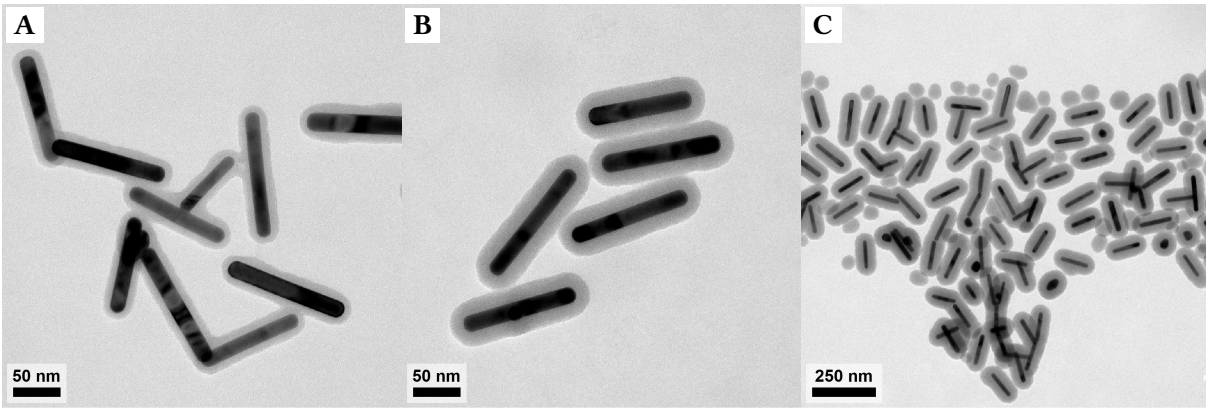

Figure 4.6: Growth of a Stöber-like silica shell with controlled thickness. A: Particles after 30 min. of reaction with 100 µL of a 1 V% ethanolic TEOS solution. The roughness in the silica was already present in the initial thin silica shell and not a result of the secondary layer. B: Particles after reaction overnight with 100 µL of a 1 V% ethanolic TEOS solution. C: Particles after reaction overnight with 200 µL of a 20 V% ethanolic TEOS solution.

4.3.2 Reaction speed and shell thickness

The growth of the silica layer happens relatively quickly after the addition of the silica precursor and complete coverage of the gold was already observed after 15 min. The thickness of the silica shell as function of time is given in Figure 4.5. This is in direct contradiction to the literature where reaction times of typically 1 to 2 days are reported for a reaction at room temperature, although it is not reported what happens within minutes after the addition of silica precursor. This is remarkable given that we do not acidify the sodium silicate solution such as in the work by Liz-Marzán *et al.* [113] and Li *et al.* [106], which is typically done to increase the reaction speed. When using an acidified sodium silicate solution as precursor, silica contaminations and secondary nucleation were observed as a result of the fast reaction (Fig 4.3C). Similar problems occurred when the volume of sodium silicate that was added was doubled in an attempt to further increase the shell-thickness, despite the increase in pH of the final solution this was accompanied with. It was possible to obtain thicker shells without a considerable increase in secondary nucleation if additional sodium silicate was added in a seperate step. For this method, 8 mL particle dispersion was first prepared and reacted with sodium silicate for 45 minutes in the same way as before, after which the particles were collected with centrifugation and subsequently redispersed in 8 mL H_2O. Then, 320 µL 0.54 wt% sodium silicate solution was added and the mixture was stirred for another 45 minutes after which the particles were washed as before.

An alternative method to increase the shell thickness is to use the initial thin layer for further growth with established methods for silica coating, such as a Stöber-silica like growth [100, 113, 117]. This enables for more facile control of the thickness as it depends directly on the amount of precursor added. Furthermore, the properties of the resulting silica are well-understood, contrary to the water-glass shell that results from the sodium silicate method. AuNR@thin-SiO_2 was dispersed in 10 mL of a 4:1 V:V ethanol:H_2O at a concentration such that 4x dilution with ethanol gave a LSPR maximum extinction of 4.0. Per 10 mL of dispersion, 200 µL of a 0.1 M NaOH solution was added, followed immediately by 100 µL of an ethanolic TEOS solution while stirring rapidly. The concentration was tuned for different shell thickness between 1 and 20 V%. The reaction was stopped either after 30 minutes or the left overnight, and the rods were washed in the same way as described in Sec. 4.1.3. BF-TEM images of particles with different shell thickness are shown in Figure 4.6. The slow monomer addition of silica from the controlled TEOS condensation preserves the shape of the original particle very well and the rods have a smooth spherocylindrical shape. If particles with a rough initial silica layer were used the resulting Stöber shell retained this rough shape. If the concentration of TEOS was too high, secondary nucleation occurred (Fig. 4.6C). Due to the thick shell, the particles had excellent colloidal stability. Due to time constraints no attempts were made to grow even thinner secondary shells or to use these particles for self-assembly.

Chapter 5

Synthesis and Properties of Bimetallic Nanorods

The plasmonic properties of nanoparticles do not depend only on their shape and size, but also on their composition as we have discussed in section 2.2. The plasmonic properties of the AuNRs are widely tunable, but they are ultimately limited to a certain spectral range and extinction cross-section, in particular in the visible range of the spectrum. It is however possible to utilise the plasmonic properties of other materials by combining them with the gold. Silver nanoparticles are known for their good plasmonic properties in the visible region as there is less damping and the intraband transitions are located at higher energy than gold. A combination of silver and gold can lead to properties not present in particles consisting of only one of the two metals, particularly tunability in the visible range with high extinction cross-section. The ratio between the two metals and their respective morphologies provide additional parameters to tune the optical properties [53, 54, 118, 119]. Furthermore, bimetallic particles are of great interest because of their catalytic properties. Both gold and silver show unique catalytic activity for a variety of reactions, but bimetallic particles can offer more than simply the sum of the two individual components (so called 'synergistic effects') [80, 120, 121]

We use the AuNRs as a basis for gold-silver bimetallic nanorods that possess properties of both Au and Ag, as well as the unique properties of the rod-like shape. Because we start with only the AuNRs, the large degree of control of the shape and size is mostly maintained. The growth of a silver shell of controlled thickness around these particles assures that the shape is largely preserved while the gold-silver ratio can be maintained. A silver overgrowth on directly on AuNRs has been reported before with resulting particles having a brick-like shape and gold-silver ratios (V:V) between 7 and 57 [122] The synthesis of bimetallic core-shell particles that we use is based on the method developed in our group by Deng *et al.* [34], a schematic overview of the different steps is given in Figure 5.1. The particles are first coated with a silica layer (AuNR@*meso*-SiO_2) and then partially etched to obtain a cavity in the silica shell with the shape of the original AuNR. The shell then acts as a template during the epitaxial growth

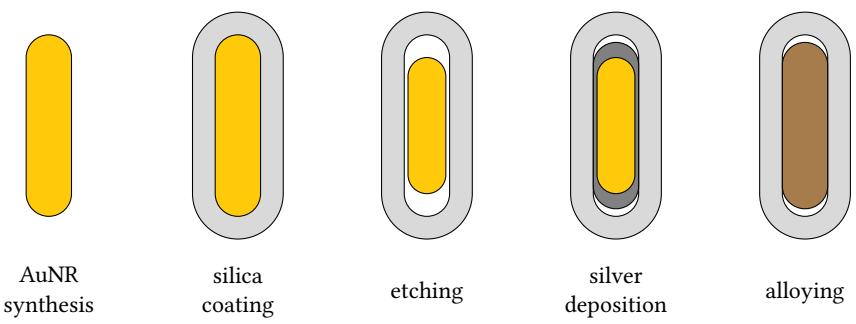

Figure 5.1: Outline of the different steps in the synthesis of bimetallic particles. In this chapter, we discuss etching with H_2O_2/HCl, deposition of a silver shell and alloying.

of a silver shell by reduction of silver nitrate on the surface of the AuNRs. Such a template effect in the synthesis of anisotropic metal nanoparticles has already been demonstrated before [102, 123]. The epitaxial growth is a result of the very small lattice mismatch of gold and silver. In a last step, we alloy the particles by heating to 500 °C [36].

5.1 Experimental

5.1.1 Etching

In a typical etching experiment, 5 mL of a concentrated dispersion of silica coated AuNRs in ethanol was diluted with 3 mL methanol. The particles were collected using centrifugation (9000 g for 10 min). The supernatant was removed and the particles were washed with 8 mL methanol, centrifuged (9000 g for 10 min) and redispersed in a volume of methanol (typically ~ 50 mL) such that the maximum extinction of the LSPR peak was 3.0 (for particles with AR 4) and transferred to a 100 mL round bottom flask with stirring bean. Per 50 mL particle dispersion, 1 mL of a concentrated HCl solution (37 wt% in H_2O) was added while stirring at 400 rpm. A 0.06 wt% H_2O_2 solution was prepared by diluting 20 µL of a 30 wt% aqueous H_2O_2 solution with 9.98 mL of methanol. Per 50 mL particle dispersion, 1 mL of the diluted H_2O_2 was added to the AuNRs while stirring at 400 rpm. The flask was placed in an oil bath at 60 °C and stirring was continued for a certain time (generally around 15 min) during which a colour change could be observed due to the changing size and aspect ratio of the AuNRs. The flask was then removed from the oil bath and a large volume of ice-cold ethanol (~ 50 mL) was added to quench the reaction. The particles were collected with centrifugation (8000 g for 20 min), washed with ethanol (50 mL), centrifuged, washed with ethanol (50 mL) and centrifuged again. The sediment was redispersed in 10 mL of ethanol and stored for further use.

Etching in ethanol was achieved in a qualitatively similar way with the exception of methanol being replaced by ethanol and an increased etching time. The silica coated AuNRs were directly diluted with ethanol (without aid of centrifugation) to obtain a dispersion with an extinction maximum of 3.0. The 0.06 wt% H_2O_2 solution was prepared by diluting 20 µL of a 30 wt% aqueous H_2O_2 solution with 9.98 mL of ethanol. The etching time was increased slightly to ~ 20 min. The particles were washed twice with ethanol and stored in ethanol. This could not be reproduced on a large scale (50 mL) as etching occurred very slowly.

5.1.2 Silver overgrowth: Deng *et al.*

For the silver overgrowth the protocol by Deng *et al.* [34] was slightly modified, that is, pure water was used instead of a PVP-solution to reduce secondary nucleation. In a typical experiment, 2 mL of the etched particles as described in Section 5.1.1 were diluted with 2 mL H_2O and collected using centrifugation (9000 g for 10 min). The sediment was redispersed in 4 mL of H_2O, centrifuged, and redispersed in a volume of H_2O (typically 9 mL) such that the extinction maximum of the LSPR peak was equal to 2.1. This dispersion was stored for a maximum of 2 days at 4 °C prior to use to prevent degradation of the silica shell in an aqueous environment.

Core-shell particles were prepared as follows: 300 µL of the aqueous Au-core dispersion was transferred to a 4 mL glass vial, and 30 µL of a x mM aqueous $AgNO_3$ solution was added. Here, x refers to the concentration of silver, that could be varied from 0 to ~5 mM (depending on the degree of etching) to obtain a different shell thickness. The vial was placed in a shaker for several minutes to ensure homogeneous mixing. 30 µL of a $4 \cdot x$ mM solution of ascorbic acid (AA) was then rapidly added and the vial was quickly placed in the shaker. The concentration of AA was chosen such that it was always 4x higher than the concentration of the $AgNO_3$ solution used. Upon addition of AA a rapid colour change to green was observed, indicating the shift of the LSPR due to the formation of the silver shell. The dispersion was left to mix for 30 minutes to ensure a complete reduction. The shaker was stopped and 3.64 mL H_2O was added. The particles were collected with centrifugation (8000 g for 10 min), redispersed in 4 mL H_2O, centrifuged, and redispersed in 1 mL H_2O.

For a larger scale version of this synthesis the method was slightly altered: 2.5 mL of the aqueous Au-core dispersion was transferred to a 20 mL glass vial containing a large stirring bean, and 250 µL of a 0.5 mM aqueous $AgNO_3$ solution was added while stirring at 400 rpm. After several minutes, the stirring speed was increased to ~ 1000 rpm and 250 µL of a 2 mM AA solution was rapidly added. Stirring was continued for 30 minutes after which the particles were washed as previously described except with volumetric quantities scaled accordingly.

5.1.3 Silver overgrowth at reduced temperature

An aqueous solution of the etched Au-cores was prepared as described in Section 5.1.2. 10 mL of this solution was added to an aqua regia clean 40 mL vial with a stirring bean. The vial was placed in an ice bath and slowly stirred for 10 min to reach a stable temperature. 1 mL of an aqueous 1 mM $AgNO_3$ solution was added while stirring. Then, the stirring speed was turned up to 1200 rpm and 1 mL of an aqueous 1 mM AA solution was rapidly added. Stirring was continued for several minutes after which the reaction mixture was aged for 10 minutes in the ice bath to ensure a complete reduction of the silver. The vial was taken out and left for 10 minutes to warm up to room temperature and complete the reaction. The particles were collected with centrifugation (8000 g for 10 min), redispersed in 4 mL H_2O, centrifuged, redispersed in 4 mL ethanol, centrifuged and redispersed in 4 mL ethanol.

5.1.4 Silver overgrowth at reduced pH

In all cases an aqueous solution of the etched Au-cores was prepared as described in Section 5.1.2. For small scale silver deposition at different acid concentrations, 5 2 mL Eppendorf tubes were labelled A to D and to each tube the following solutions were added: 1 mL of the Au-cores, 100 µL of a freshly prepared 1 mM $AgNO_3$ solution and x µL of a 0.1 M HCl solution where x was varied for the different samples and can be found in Table 5.3. The mixture was homogenised with a vortex mixer. Then, 100 µL of a 4 mM AA solution was rapidly added and the tube was immediately closed and mixed with a vortex-mixer for 20 s, and placed in an ultrasonic bath and left to react for 2 h. 1 mL of H_2O was added and FT-IR extinction spectra were recorded which can be found in Figure 5.8D. 2 mL of H_2O was added and the particles were collected with centrifugation (8000 g for 10 min), redispersed in 4 mL ethanol, centrifuged and redispersed in 1 mL ethanol. Large scale synthesis of core-shell nanorods (CSNRs) using HCl was typically done on a 50 mL scale: 50 mL of aqueous cores (at a concentration such that the LSPR extinction maximum equals 2.2) was added to a 100 mL round bottom flask and 5 mL of a 2 mM $AgNO_3$ solution was added while stirring at 400 rpm. 300 µL 0.1 M HCl was slowly added and a slight colour change could be observed. Then, stirring was increased to 1200 rpm and 5 mL 8 mM AA was rapidly added after which the mixture gradually turned green/brown over the course of ~1 min. Stirring was continued for at least 30 min to allow the reaction to complete, after which the particles could be collected with centrifugation (8000 g for 20 min), redispersed in 40 mL H_2O, centrifuged, redispersed in 40 mL ethanol, centrifuged and redispersed in 5 mL ethanol.

5.1.5 Alloying

To alloy the particles, AuAgNRs dispersed in ethanol were dried in a 4 mL glass vial at 30 °C under a light nitrogen stream. The glass vial (without cap) was then placed in its entirety in a glass gas-flow reactor tube that was closed with an air-tight cap. A nitrogen flow of 200 mL min^{-1} was used for > 5 min to flush all residual air out of tube and to test if the setup was completely leak proof. The tube was then placed in a computer controlled oven set to 30 °C while the gas mixture and flow were regulated automatically with mass-flow controllers. The tube was flushed for 30 min with 30 mL min^{-1} of the desired gas mixture (pure N_2, 20/80 O_2/N_2, 20/80 H_2/N_2, 20/80 CO/N_2, all ratios by volume) at 30 °C. The gas flow was then reduced to 10 mL min^{-1} and the oven was slowly heated to 500 °C with a heating ramp of 5 °C min^{-1} after which it was left to cool, which took ~6 h. The particles were then redispersed in ethanol using ultrasonication and stored at 4 °C.

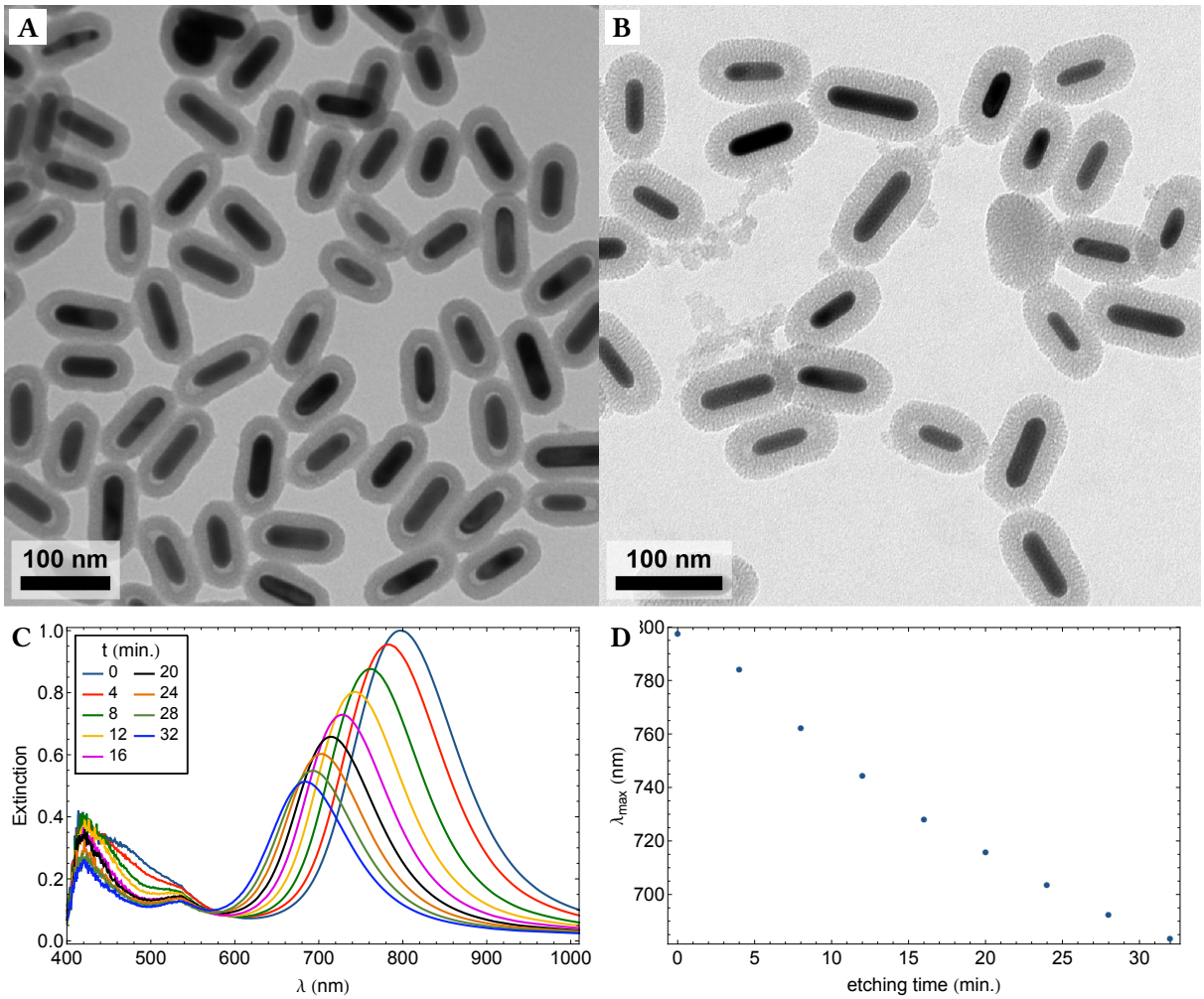

Figure 5.2: Etching of AuNR@*meso*-SiO_2. A&B: BF-TEM images of etched AuNRs. C: FT-IR extinction spectra taken during the etching show an approximately linear trend in both peak position and intensity in the measured regime. D: LSPR peak-position as a function of etching time.

5.2 Etching of SiO_2-coated AuNRs

In order to facilitate the growth of a silver shell, sterical hindrance by the silica-shell should be minimised. Deng *et al.* used an oxidative etching procedure where the outer layer of gold was dissolved through the pores of the silica shell and washed away, leaving a spacing between the AuNR and the silica shell. The size of this spacing could be conveniently tuned using the reaction time and/or temperature. The reproducibility of this protocol however is not ideal as only freshly prepared AuNRs@silica could be etched and equal reaction time does not always lead to an equal degree of etching. It was suspected these issues arose from the use of dissolved atmospheric oxygen as oxidant, as the oxygen content of methanol depends on many parameters. To circumvent this an adapted protocol developed by J.E.S van der Hoeven was used, that utilises diluted H_2O_2 as oxidant. Typically, the addition of 2 V% concentrated hydrochloric acid (37% HCl) followed by the addition 2 V% of a solution of 0.06 wt% H_2O_2 in methanol was sufficient. Etching was triggered by quickly heating to 60 °C and could be quenched by adding cold methanol or ethanol.

Because the use of large volumes of methanol is undesirable from a health and safety point of view, especially when open containers have to be used (for example when removing the supernatant after centrifugation) we studied whether the etching procedure could be done in ethanol. While in principle the etching occurred in a similar fashion, it was found that the protocol was poorly reproducible and did not work very well for volumes exceeding ~10 mL. While etching did occur in ethanol, the time it

Table 5.1: Overview of the results of some of the etching experiments in methanol. Subscripts i and f stand for 'initial' and 'final', referring to the sizes before and after the etching. t refers to the etching time.

t (min.)	H_2O_2 dil. (V%)	L_i (nm)	D_i (nm)	AR_i	L_f (nm)	D_f (nm)	AR_f	Vol. loss (%)
13	0.17	92±8	23±2	4.0±0.46	65±9	22±2	3.0±0.51	38
15	0.06	92±8	23±2	4.0±0.46	69±11	22±2	3.1±0.49	30
15	0.06	92±8	23±2	4.0±0.46	72±11	22±2	3.2±0.49	27
15	0.06	92±8	23±2	4.0±0.46	72±10	22±2	3.3±0.50	27
18	0.06	92±8	23±2	4.0±0.46	65±9	22±2	2.9±0.45	36
10	0.17	72±11	19±2	3.8±0.60	57±9	18±2	3.2±0.51	25
10	0.17	72±11	19±2	3.8±0.60	66±10	19±2	3.6±0.47	10

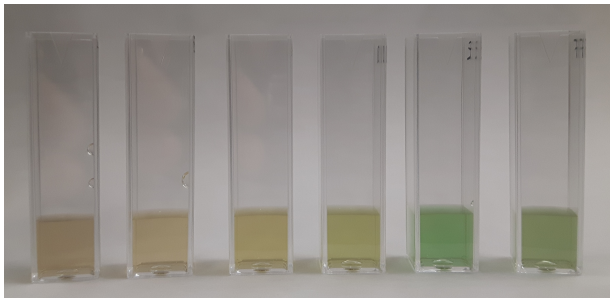

Figure 5.3: Photograph of AuAg CSNRs made with (from left to right) 0.5, 1.0, 1.5, 2, 3 and 4 mM $AgNO_3$ and cores that were etched for 10$. The samples were diluted 2x with H_2O.

took varied for two different batches of the same sample at the same concentration. The exact reason for this is unknown and was not studied further, but may be related to effects of the temperature. As a compromise it was found that only the etching itself has to be done in methanol, while quenching the reaction and washing the particles can be done with ethanol, thereby limiting the amount of methanol and risk of exposure.

TEM images of samples etched for different times under similar conditions are shown in Figure 5.2 and show empty space in the silica shell and a decreased length while the diameter only decreased slightly. FTIR-extinction spectra of the AuNRs during the etching procedure are shown in Figure 5.2 and show a blue-shift of the peak position as a result of the decreasing aspect ratio of the nanorods. The peak shift follows a roughly linear trend in time which allows for easy control over the degree of etching by quenching the reaction after a certain time. The decrease in the peak intensity is a result of both the decreasing aspect ratio and the decreasing volume. Some of the results from size measurements of AuNRs before and after etching are given in Table 5.1. The etching speed fluctuated somewhat between samples, but generally a small scale test gave a good indication of the parameters needed. In some cases, such as the two samples etched for 10 minutes, there were large differences in the degree of etching (the percentage of gold that is etched), but these can be explained by the scale of the reaction. When a small sample was tested (4 mL methanol) etching started immediately upon placement of the flask in the oil bath and 25% of the gold was etched after 10 minutes. When this was repeated using the same parameters but on a larger scale (32 mL methanol), it took longer for the volume to fully heat up in the oil bath, causing the etching to start later. As a result, only 10% of the gold was etched after 10 minutes. These issues can be circumvented by first heating the mixture and then adding the HCl and H_2O_2. The fluctuations between different batches were not a major issue as the progress of reaction could easily be followed with FTIR-spectroscopy by taking and measuring small samples.

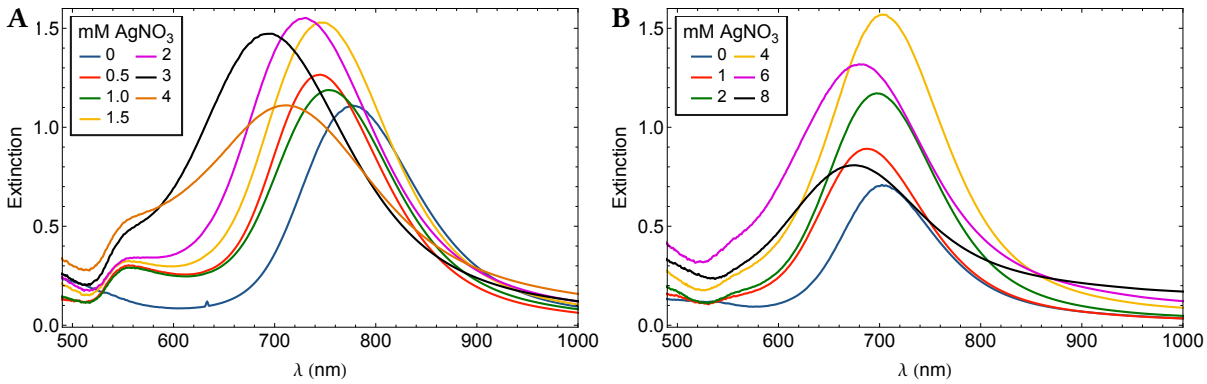

Figure 5.4: Silver deposition with an increasing $AgNO_3$ concentration. A: FTIR extinction spectra of the AuAg CSNRs made with Au cores that were 10% etched, The samples were diluted 2x with H_2O before measuring the spectrum. B: FTIR extinction spectra of the AuAg CSNRs made with Au cores that were etched 38%, The samples were diluted 3x with H_2O before measuring the spectrum.

Table 5.2: Overview of results of AuAg CSNRs synthesised from two batches of etched AuNRs. The first batch ($V_{Au} = 1.67 \cdot 10^4$ nm) was 10% etched and had little space. The second batch ($V_{Au} = 2.17 \cdot 10^4$ nm) had 38% of the Au etched away resulting in a larger void. V_{Ag} was calculated by subtracting the core volume from the total volume.

$AgNO_3$ (mM)	V_{Au} (10^4 nm^3)	V_{Ag} (10^4 nm^3)	X_{Au}	AR (L/D)	λ_{max} (nm)
0	1.67	0	1.00	3.6±13%	776
0.5	1.67	0.29	0.85	3.6±15%	745
1.0	1.67	0.75	0.69	3.3±15%	753
1.5	1.67	1.40	0.55	3.3±15%	749
2.0*	1.67	1.37	0.55	3.2±16%	730
3.0*	1.67	3.43	0.33	2.7±20%	695
0	2.17	0	1.00	3.0±17%	702
1.0	2.17	0.75	0.75	2.8±12%	688
2.0	2.17	1.73	0.56	2.9±14%	697
4.0	2.17	3.38	0.39	2.8±16%	703
6.0*	2.17	6.08	0.26	2.4±15%	678

*these samples contained secondary nucleation

5.3 Synthesis of AuAg core-shell nanorods

Experimental details of the silver deposition, which were slightly different than reported in the literature, can be found in Section 5.1.2. The thickness of the resulting silver layer, and thus the gold/silver ratio could be controlled in several ways, such as a change in the etched AuNR concentration, a change in etching time, the amount of $AgNO_3$ solution added or the concentration of the $AgNO_3$ solution. We used the $AgNO_3$ concentration as the main method of controlling silver shell thickness, and the etching time to assure that sufficient space is present in the silica shell. When a short etching time / concentration is used, the maximum concentration of $AgNO_3$ that can be used is low. Figure 5.4A shows extinction spectra of samples prepared with varying silver concentration and Au cores that were etched to a limited degree (10 minutes with 0.066 V%H_2O_2, 10% of the gold was etched away) thus keeping the size of the core large and creating space for a Ag shell of limited thickness. With increasing silver concentration, the intensity of the peak increases and the position undergoes a blue-shift. It should be noted that the peak shift is not always a blue shift, and depends on many factors such as the molar fractions of gold and silver, the shape and morphology of the surface, the volume and aspect ratio of the total particle and the dielectric constant of the medium. All of these may change from sample to sample and during the reaction itself.

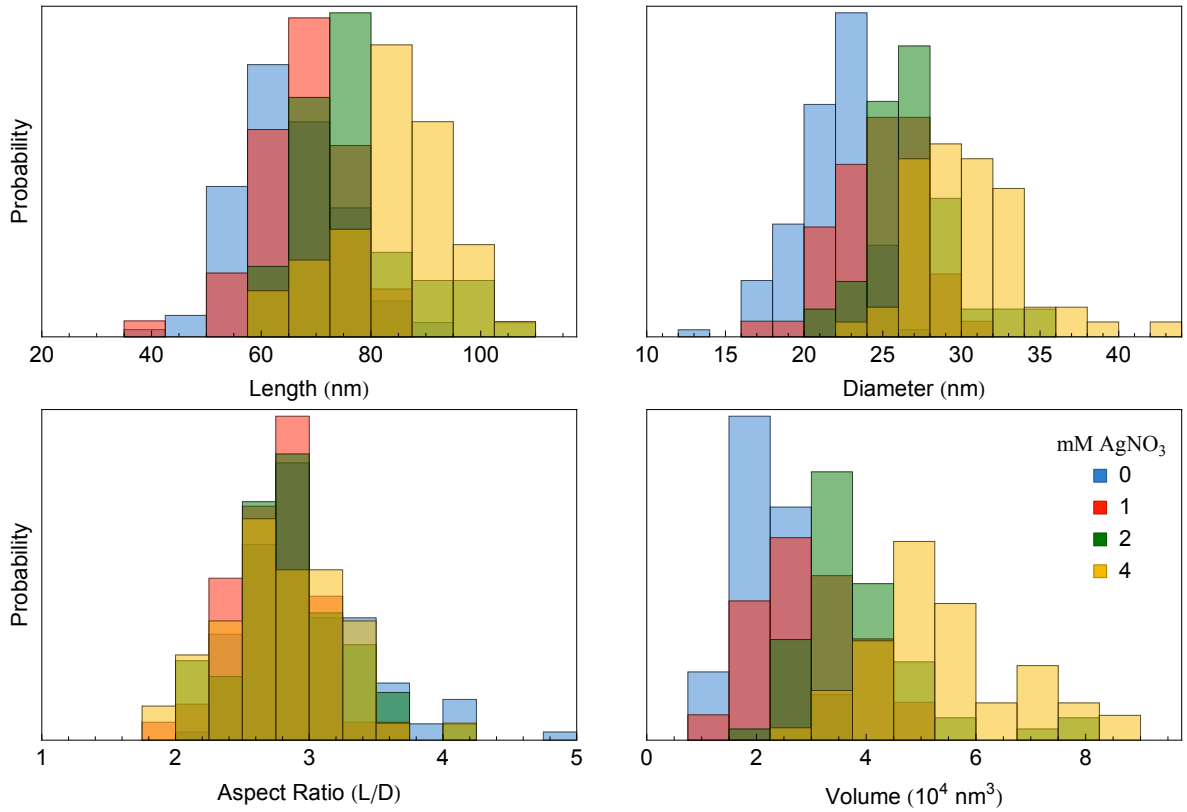

Figure 5.5: Size distributions of AuAg CSNRs synthesised with cores etched to a 38% volume decrease and different $AgNO_3$ concentration.

When an $AgNO_3$ concentration of 2 mM or more is used, peak broadening occurred and extinction at ~550 nm increased. Using TEM, these effects were confirmed to be a result of both secondary nucleation and increased inhomogeneity due to bursting silica shells. When particles were used that were etched to a larger degree (38%), a considerably higher silver concentration up to 4 mM could be used to obtain a thicker silver shell without problems (Fig. 5.4B). In this case broadening of the extinction peak and the formation of silver particles were not observed until the $AgNO_3$ concentration was 6 mM. The molar fraction of both metals can be estimated based on the volume of gold and silver in the particles, which can be determined by measuring the volume of the cores and the core-shell particles. The molar fractions are then calculated using the following equation:

$$X_{Au} = 1 - X_{Ag} = \frac{x_{Au}}{x_{Au} + x_{Ag}} \tag{5.1}$$

Where subscripts denote the metal, X is the molar fraction and x the average number of moles per particle, given by $x = V/\bar{V}$ with V the measured volume and $\bar{V}$ the molar volume (10.21 and 10.28 $cm^3\ mol^{-1}$ for Au and Ag respectively).

Results of gold-silver core-shell nanorods (AuAg CSNRs) synthesised based on the two batches of etched AuNRs are summarised in Table 5.2. We note that even though the second batch was etched to a larger degree, the volume of the gold core is larger. This is a result of the larger starting volume of the AuNRs@*meso*-SiO_2 used, and not of insufficient etching. Size distributions of the second batch and some of the resulting AuAg CSNRs are also given in Figure 5.5. In both cases, the results from TEM measurements confirm the findings based on the FTIR extinction spectra. A silver shell grows preferably onto the gold surface with an increasing thickness for increasing silver concentration, until a threshold is reached. Up to that point, the aspect ratio decreases slightly in some cases. At silver concentrations above this threshold, secondary nucleation starts to dominate, the AR decreases rapidly and many of the silica shells crack due to the pressure of the increased silver volume. Since this threshold depends on the empty space within the silica shell and since it corresponds with the concentration at which

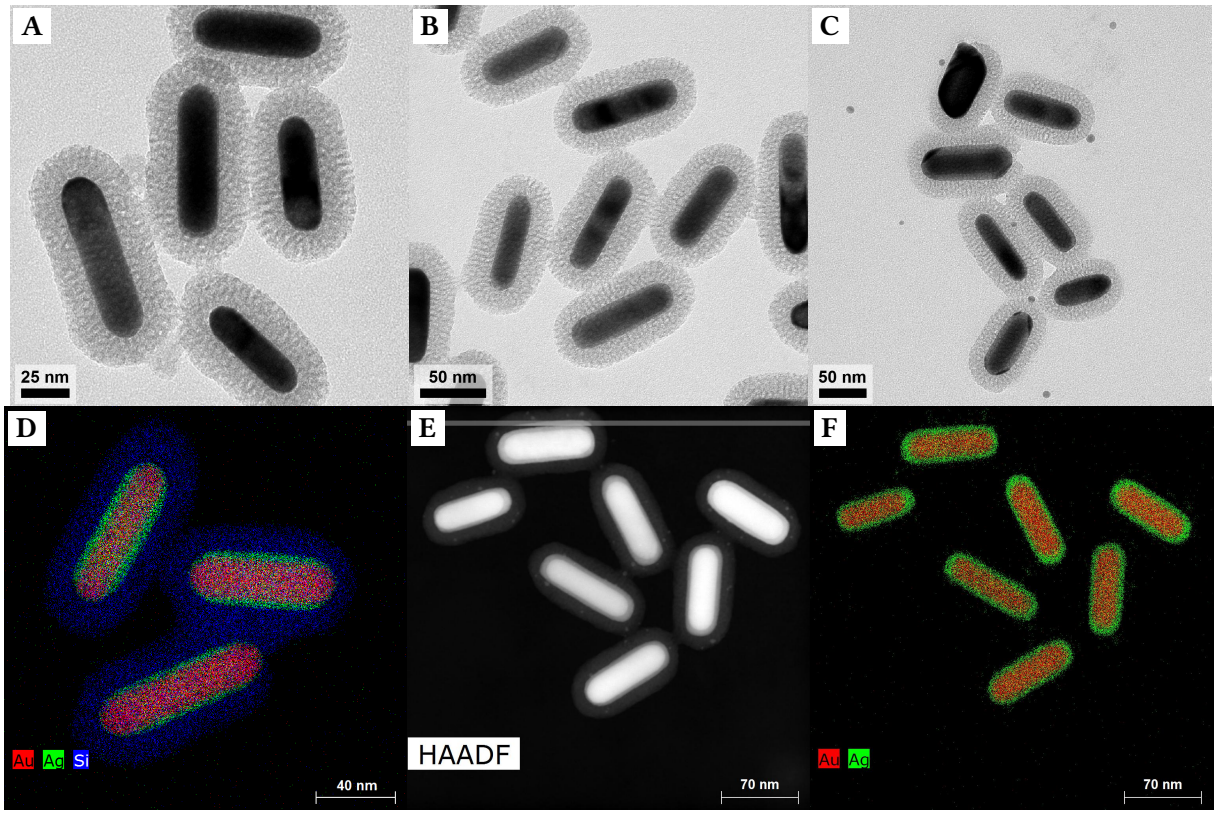

Figure 5.6: A–C: BF-TEM images of AuAg CSNRs synthesised with cores etched for 10 min. and different $AgNO_3$ concentrations. A: 0.5 mM $AgNO_3$, the Ag shell is too thin to observe in BF-TEM for individual particles. B: 1.5 mM $AgNO_3$, a core-shell structure is clearly visible for most particles. C: 2.0 mM $AgNO_3$, small Ag particles are observed and some silica shells are broken. D: STEM-EDX map showing the core-shell-shell structure of Au, Ag and Si for AuAg CSNRs grown with 1 mM $AgNO_3$. D&E: HAADF-STEM and STEM-EDX images of AuAg CSNRs grown with 2 mM $AgNO_3$.

shells start to crack, we conclude that this is the maximum amount of silver that can be deposited within the shell. When the amount of silver is increased further, only two possibilities remain: silver growth outside the shell or destruction of the silica. The change in the position of the LSPR can be explained predominantly by the change in AR, although effects of the different dielectric functions of gold and silver are of course expected. The increase in the peak intensity is largely an effect of the increasing particle volume.

5.3.1 Scaling up CSNR synthesis

One of the major difficulties in the synthesis of Ag@Au CSNRs with the method by Deng *et al.* is the small scale and therefore small number of particles obtained. When this method is scaled up, large inhomogeneities are found in the shell thickness throughout the sample, and the experiments are more prone to the formation of silver particles due to secondary nucleation. These problems can also occur on the small scale if the samples are not rapidly mixed directly after addition of ascorbic acid. Based on these observations we suspected mixing of the ascorbic acid and silver ions to be the limiting factor in the success of the metal overgrowth. This is likely the result of the extremely rapid reduction of Ag^+ by AA as a colour change is observed directly after addition of the reductant. If the local concentration of Ag^+ and AA exceed the critical nucleation concentration, silver nanoparticles can be nucleated. We therefore propose that for a successful metal overgrowth, mixing and full homogenisation of the reactants should occur on a shorter time scale than the reaction itself. This can be achieved in two ways, one can 1) increase the mixing speed and 2) slow down the reaction rate. A third option is to perform the synthesis in many small batches, but this is time consuming and only possible if the method is

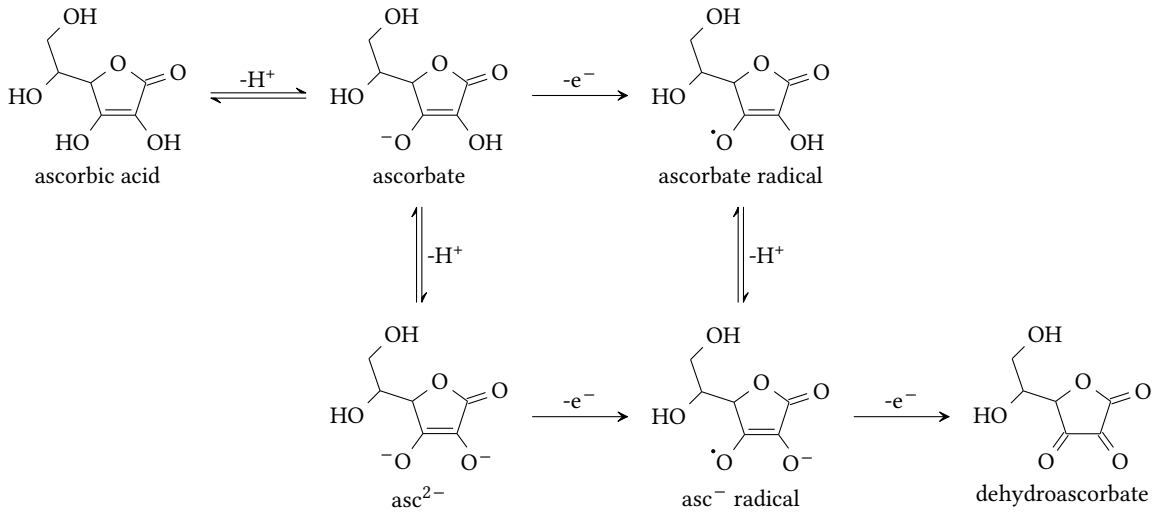

Figure 5.7: reaction mechanism for the oxidation of ascorbate to dehydroascorbate. Adapted from [125]. pK_a values for the first and second deprotonation are 4.17 and 11.57 respectively [126, 127].

highly reproducible. Our experiments show that for the small scale method this is not the case. While mixing speed is initially easy to increase experimentally (for example by using a bigger stirring bean or by stirring at a higher radial speed) it quickly reaches a practical maximum with the standardised magnetic setup. Sub-second homogenisation of volumes much larger than several mL is not possible with conventional lab techniques. Furthermore, it is difficult to standardise and depends heavily on many parameters such as volume, vessel shape and size and stirring method.

Reducing the reaction rate on the other hand, can be achieved in several ways. It is important to realise that the particle formation can depend strongly on kinetic effects, and that changing the reaction rate can lead to a difference in the particles obtained. Ideally this could be used as a method to control the morphology of the bimetallic particles. One of the most commonly used methods to control the reaction rate is by controlling the temperature. The relationship between reaction kinetics and temperature is expressed in the Arrhenius equation [124]:

$$k = Ae^{-\frac{E_a}{k_B T}} \tag{5.2}$$

where k is the reaction rate, E_a the activation energy of the reaction, T the absolute temperature, k_B the Boltzmann constant and A a pre-exponential factor. This is essentially a Boltzmann-exponent for the probability of particles to have sufficient energy to cross the energy barrier, and it is clear that an increased temperature leads to an increase in the reaction rate and visa versa. To test whether a reduced temperature and thus reaction rate leads to increased monodispersity and decreased secondary nucleation we performed the silver overgrowth at reduced temperature by suspending the reaction vial in an ice-bath. Experimental details can be found in Section 5.1.3. The colour change to green upon addition of silver was spread out over at least several seconds indicating a lower rate of silver deposition than in the experiments at room temperature. The procedure was repeated 4 times to obtain a larger quantity of AuAg CSNRs and to evaluate reproducibility of the protocol, FT-IR extinction spectra of the different batches (named A to D) are given in Figure 5.8. It is clear that only minimal differences between the batches exist as the peak position and height depend strongly on the thickness of the silver layer. The batches were mixed to yield a total volume of 12 mL after washing. Representative TEM images are given in the appendix (Fig. B.10). The AuAg CSNRs had an average length of 77±8 nm, an average diameter of 28±2 nm and an aspect ratio of 2.7±0.28. The molar fraction gold was 0.59.

Another more chemical method to reduce the reaction rate is to decrease the reduction strength or available amount of reductor (AA) at any given time. In the case of ascorbic acid this can be achieved by lowering the pH which can be understood based on the reaction mechanism of the oxidation of AA (Figure 5.7). In order to donate two electrons to the silver, two H^+ must be removed from the ascorbic

Table 5.3: acidity molar ratio HCl:AA and reaction times for the silver deposition at low pH. x is the volume of 0.1 M HCl added per 1 mL of Au-core dispersion. The reaction time was estimated based on the time it took until no more colour change could be observed by eye. The Au cores used were etched for 15 minutes and had AR=3.3±15%, V_{Au}=2.57 · 10^4 nm^3 and λ_{max}=736 nm. 1 mM $AgNO_3$ and 4 mM AA were used.

x (µL)	pH	[HCl]/[AA]	reaction time	V_{Au+Ag} (10^4 nm^3)	X_{Au}	$AR(L/D)$	λ_{max} (nm)
0	3.91	0.0	< 1 s	3.97±29%	0.65	2.7±12%	688
1	3.74	0.2	~10 s	3.89±22%	0.66	2.7±11%	707
4	3.39	1.0	~1 min	3.90±23%	0.66	2.8±11%	705
8	3.12	2.0	> 10 min	3.94±27%	0.66	2.6±12%	715
20	2.75	4.9	> 30 min	3.92±27%	0.66	2.7±13%	725

acid. The presence of a higher concentration of H^+ will drive these equilibria to the protonated (and inactive) species. The pK_a for loss of the first proton is 4.17 [126], which means that under neutral conditions almost all AA will be present in the form of ascorbate, the active species. When the pH is lowered to 3 on the other hand, less than 10% of the AA is present as ascorbate. This limits the speed of the reaction to the speed at which AA converts to ascorbate, thus slowing the reaction down. Ruiz *et al.* proposed that under acidic conditions loss of the second electron is the rate limiting step [128]. It is however important to realise that we use a 4 times excess of AA w.r.t. Ag(I) (or 8 times if you account for two electrons e.g. two reduced silver atoms per AA molecule) and full oxidation of AA is not needed for full reduction of the silver. We therefore assume that only the reaction rate of the first electron is relevant and that further oxidation of AA occurs via a different pathway, for example recombination of two ascorbate radicals to form ascorbate and dehydroascorbate. If this is the case, the equilibrium conditions of the dissociation of the first proton will have the strongest influence on the reaction rate.

We studied the silver deposition at low pH via the addition of HCl prior to the reduction on a small scale. Experimental details of the procedure can be found in Section 5.1.4. As initial test, the influence of pH on the reaction rate could be estimated based on the time it took for the sample to fully turn green due to the shift of the LSPR. The acidity had a strong effect on the reaction rate and shows promising results for use as means of kinetic reaction control. TEM analysis revealed that in all cases the particles obtained were homogeneous CS-particles with a smooth Ag layer and no secondary nucleation, aggregation or broken shells (Figure 5.9). Although no degradation of the silica shells could be seen, the TEM grids of samples with higher acid concentration contained slightly more silica contaminations, which indicates the possible dissolution of the silica shell at lower pH. While there is a minimum in solubility for amorphous silica at pH 7, and the addition of acid increases the solubility slightly to a maximum around pH 3, this increase in solubility is very small and the effect is much stronger when increasing rather than decreasing the pH [129]. It was found that a decrease in pH did not measurably degrade the silica shell on a time-scale of the reaction. Storage over a longer time than ~1 day was done in ethanol to prevent such issues.

The reaction could be followed in-situ by performing the silver deposition reaction in a cuvette while measuring the FTIR extinction spectrum at regular time intervals. The evolution of the extinction spectrum was measured for etched AuNRs using 1 mM $AgNO_3$ and 4 mM AA. Prior to the addition of AA, a certain volume of 0.1 M HCl was added to the cuvette, we used volumes of 0.25%, 0.50%, 0.75% and 1.00% of the volume of the core dispersion. For each sample, the AA solution was rapidly added and the cuvette was swirled for 2 seconds to mix the sample, and then immediately placed in the FTIR spectrometer. Time between addition of the AA and the start of the first measurement was roughly 10 seconds. The spectra were automatically recorded at regular time intervals depending on the speed of the reaction. The dataset with 0.75 V% 0.1 M HCl is shown in Figure 5.8B, the other samples can be found in the appendix (Fig. B.11). The maximum extinction is plotted versus the reaction time for the different samples (Fig. 5.8C) and clearly shows a decrease in reaction rate with increasing acid concentration (decreasing pH). It should be noted that the detection limit of our device (Abs = 2.5) was reached quickly for two samples and that the constant value they reach is higher in reality than could

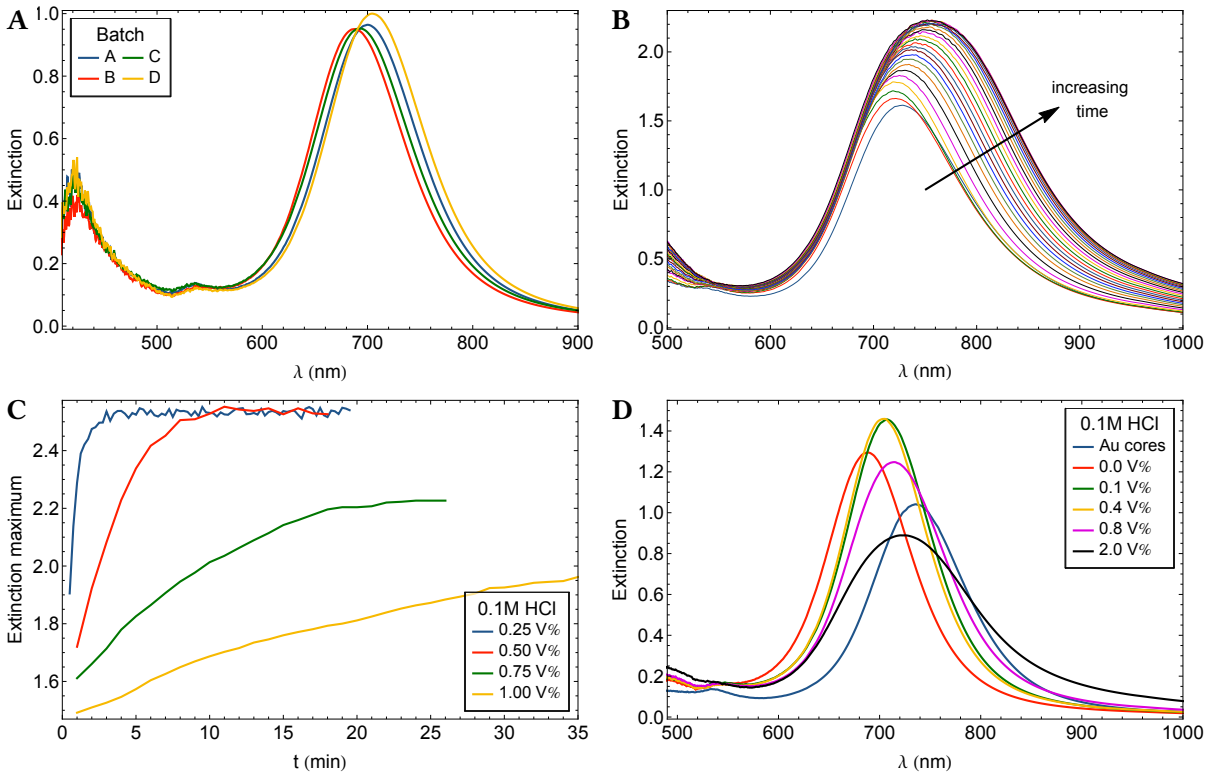

Figure 5.8: FT-IR extinction spectra of CS-NRs. A: comparison of different batches synthesised at low temperature. B: evolution of the spectrum over time during the silver deposition at pH 3.15 (0.75 V% 0.1 M HCl) with a time interval of 1 minute between the start of the measurements. C: the LSPR maximum extinction as a function of the reaction time. D: ex-situ measurements of AuAg CSNRs synthesised at varying pH. B–D were al on a 1 mL scale.

be measured. This problem would be prevented by performing the reaction in a more dilute system, but a change in these parameters will change the course of the reaction and make the results harder to compare with our other experiments. It can be deduced however that at high acid concentration, the maximum intensity reached after the reaction is completed (no more change in the spectrum) is lower than for the samples with less acid. This trend corresponded with ex-situ FTIR extinction spectra of diluted samples after the silver deposition (Fig. 5.8D). A red shift was observed with increasing acid concentration while the extinction has a maximum intensity at around 0.1–0.4 V%. When the acid concentration is increased further, the peak starts to broaden. During the in-situ measurements we observed that at the highest acid concentration (1.00 V%, pH 3.03) the particles started to aggregate and sediment slowly, causing the intensity to drop after 40 minutes (appendix Fig. B.11C).

Based on the small scale experiments, the ideal amount of added acid is 4 µL 0.1 M HCl per 1 mL of AuNR-core dispersion to slow the reaction down enough for effective mixing without strong dissolution of the silica shell. When higher silver concentrations were used to grow thicker shells, the amount of acid was increased slightly to 6 µL 0.1 M HCl per 1 mL of AuNR-core dispersion to compensate for the higher AA concentration. To demonstrate the effectiveness of the reduced growing speed for up-scaling, a large batch of 55 mL was made using 2 mM $AgNO_3$ and 0.6 V% 0.1 M HCl. The particles were comparable to those obtained from small scale silver deposition with good coverage of all AuNRs, homogeneous silver layer thickness and no nucleation of new silver particles.

5.4 Alloying of bimetallic nanorods

We studied the formation of alloyed Au_XAg_{1-X}NRs from the AuAg CSNRs by means of heating, where X is the molar fraction of gold. In the bulk phase, gold and silver have a negative mixing enthalpy for

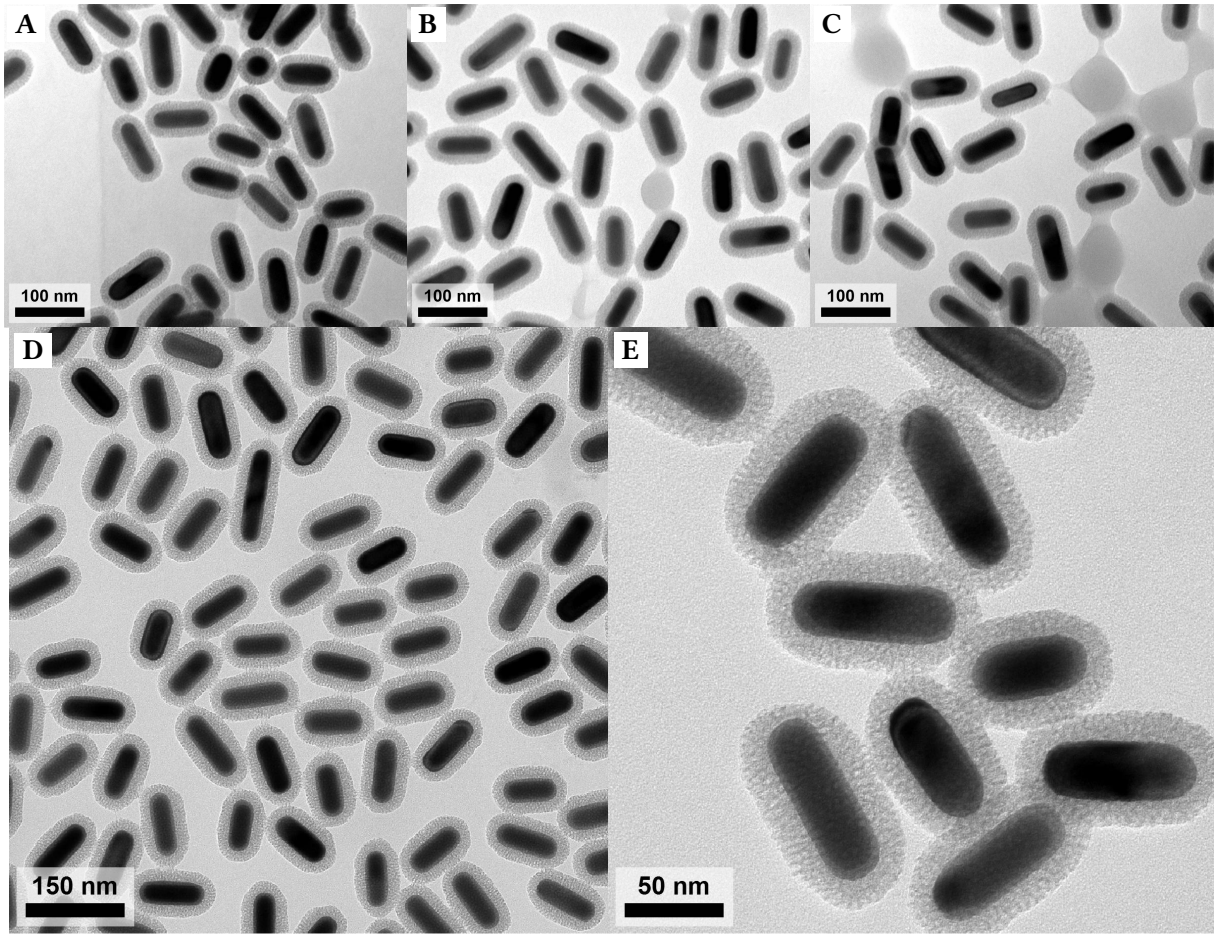

Figure 5.9: TEM images of AuAg CSNRs grown at different acidities. A: without HCl (pH 3.91), B: 0.4 V% 0.1 M HCl (pH 3.39) and C: 2.00 V% 0.1 M HCl (pH 2.75). D&E: large scale (55 mL) batch

all gold silver ratios, and thus mixing is always energetically favourable [130, 131]. The structure of the gold-silver alloy is a solid solution with random placement of the Au and Ag atoms on the face-centered cubic (fcc) lattice [130]. The ΔH_{mix} for bulk Au and Ag in the liquid phase depends on the mole fractions of gold (X_{Au}) and silver (X_{Ag}) via Eq. 5.3 [131]:

$$\Delta H_{mix} = X_{Au}X_{Ag}(-16.803 - 3.233X_{Au} + 4.525X_{Au}^2)\text{kJ mol}^{-1}. \tag{5.3}$$

It is unlikely that these values will be accurate for the case of our particles as the nano-scale size strongly influences the energetics and mixing most likely does not take place in a fully liquid phase due to the low alloying temperature. Many studies on thermodynamic properties and stability of AuAg nanoalloys have been reported with varying conclusions [132]. Molecular dynamics simulations of small (<1000 atoms) spherical Au-Ag alloy particles demonstrated favourable mixing similar to the bulk phase but with slightly lower energy gain [133, 134]. For very small nanoclusters and nanocrystals it has been reported that the lower surface energy of Ag combined with the small enthalpy of mixing leads to surface segregation whereby the silver concentration on the surface of the particles is higher than in the centre. Such an effect influences the surface properties and the plasmon resonance [118, 132]. In experimental studies on larger particles such an effect was not found [35, 119, 135] and surface seggregation of silver after the alloying was also reported previously for our system [36]. The melting points of small particles in simulations was between 600 and ~720 °C for both core-shell spheres and alloys, while a silver shell generally melts at slightly lower temperature than the gold core [133, 134]. In any case, these melting temperatures are far higher than those used in our alloying, which explains in part how the out-of-equilibrium shape can be preserved.

Results of the alloying of AuAg CSNRs under different gas atmospheres are shown in Figure 5.10.

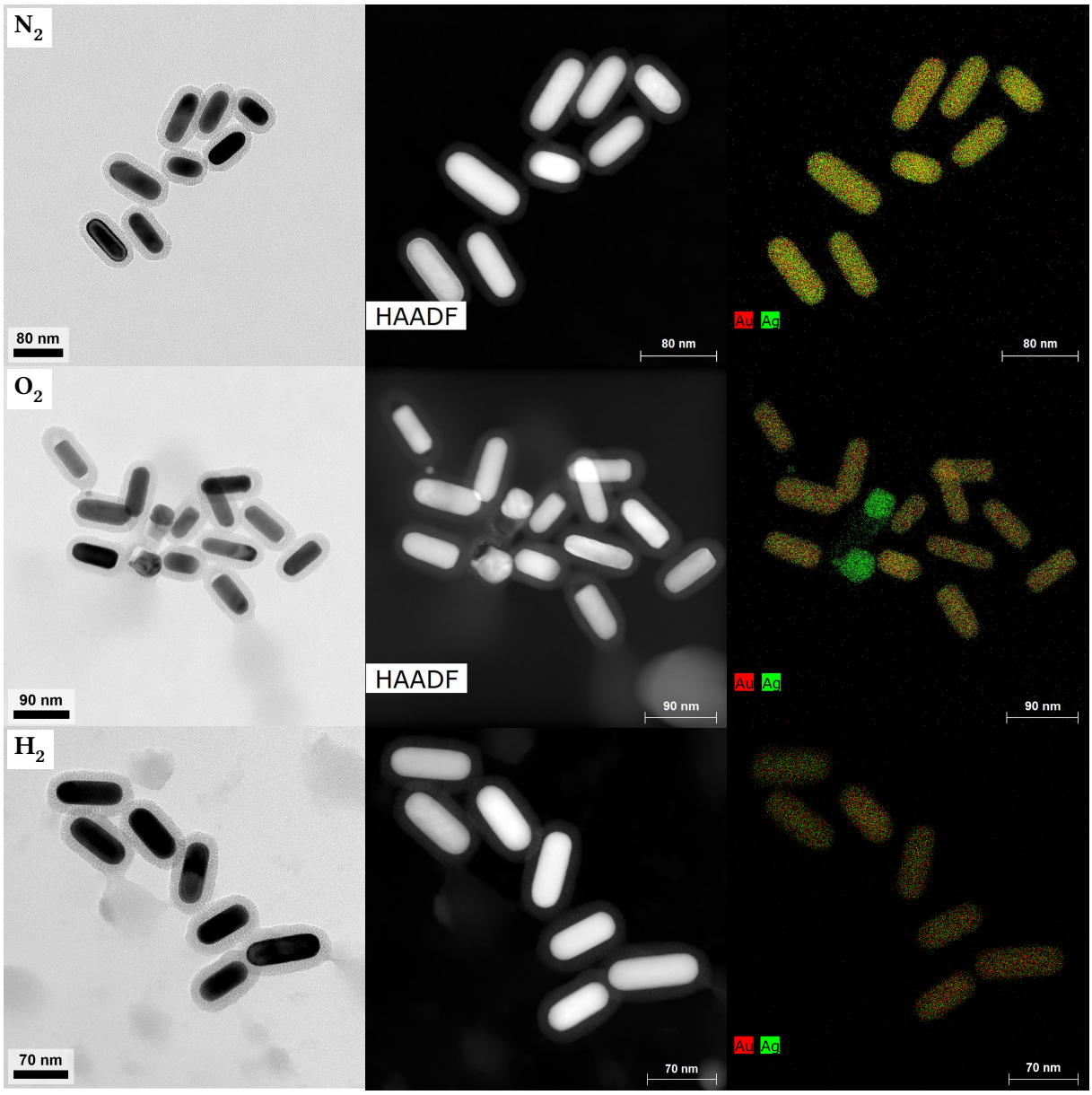

Figure 5.10: BF-TEM images (left), HAADF-STEM images (middle) and EDX-maps (right) of AuAgNRs alloyed under different atmospheres.Top: particles alloyed under N_2 atmosphere. Middle: particles alloyed under synthetic air (20 V% O_2 in N_2). Bottom: particles alloyed under 20 V% H_2 in N_2.

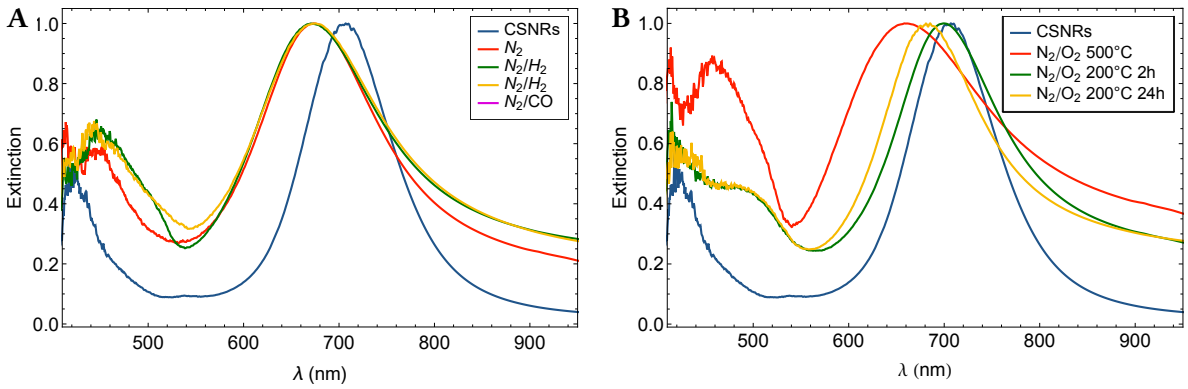

Figure 5.11: A: normalised FTIR extinction spectra of particles alloyed in inert or reducing atmosphere. B: normalised FTIR extinction spectra of particles alloyed in synthetic air.

When the AuNRs are alloyed with a low heating ramp (5 °C min^{-1}) to a maximum temperature of 500 °C in a nitrogen environment (10 mL min^{-1} N_2), which is considered inert to the particles, we see that the core-shell structure has made place for a mixed phase. EDX-STEM mapping was used to image cold and silver separately, and confirmed that homogeneous alloys were obtained. Size measurements of the particles before and after alloying confirmed that no deformation occurred as the AR remained constant at 2.7. When the same procedure was used but under a synthetic air atmosphere (20% O_2 and 80% N_2, V:V) however, results were quite different. In most particles, deformation occurred which was visible due to the empty space in the silica shells near the tips. Size measurements confirmed this finding and the aspect ratio of the rods went from 2.7 to 2.4. Furthermore, large metallic particles were observed on the TEM grid, outside of the silica shells of the NRs. EDX-STEM revealed that these particles consisted solely of silver, while the NRs consisted mostly of gold with some silver. Because the presence of an oxidising environment had such a strong influence on the results of the alloying, it was interesting to see what the effect of a reducing environment would be. For this purpose, two batches of the same particles were alloyed under 20% H_2 in N_2 and 20% CO in N_2 atmospheres (by volume) respectively. Images are shown in Figure 5.10 for H_2 and in the appendix in Figure B.12A&B for CO. For both particles alloyed under H_2 atmosphere and the particles alloyed under CO atmosphere, the results were highly similar to the particles alloyed under N_2 (appendix Fig. B.12A&B). In both cases the aspect ratio remained at 2.7 and no silver or other particles were observed outside of the silica shell. EDX-STEM showed homogeneous alloys in the case of particles alloyed in H_2. No EDX-STEM mapping was done for the particles alloyed in CO, but no particles with a core-shell structure were observed in BF-TEM and the optical extinction spectrum was consistent with an alloy. The particles alloyed in H_2 could be redispersed more easy than samples alloyed in other atmospheres. This may be related to reduced condensation of -OH groups on the surface of the silica, but may very well be a coincidental observation.

The extinction spectra of the alloyed AuAgNRs show a similar pattern. The spectra of the samples alloyed in 100% N_2, 80/20 N_2/H_2 and 80/20 N_2/CO have nearly identical spectra (Fig. 5.11A) with a LSPR maximum at ~675 nm (~20 nm lower than the AuAg CSNRs) confirming that the presence of a reducing atmosphere does not influence the alloying or deformation of the AuAg CSNRs in any other way than an inert atmosphere. A larger background extinction is seen over most of the wavelength range, which we attribute to increased scattering of (small) aggregates because full redispersion of the particles after heating was challenging. Extinction spectra for samples alloyed in synthetic air were all distictly different (Fig. 5.11B). When the standard heating programme (5 °C min^{-1} up to 500 °C followed by ~6 h of cooling) was used in combination with a synthetic air atmosphere, a much stronger peak broadening occurred and the LSPR extinction maximum shifted further to the visible (661 nm). The large peak shift is a result of the lower aspect ratio due to deformation, the broadness of the peak is a result of both scattering of aggregates and the varying degree of deformation. To obtain more information about the alloying in (synthetic) air, we heated the particles to 200 °C where alloying is not expected. The AuAg CSNRs were heated to 200 °C (5 °C min^{-1}) and kept at this temperature for 4 h, which roughly corresponds to the time particles are at a temperature higher than 200 °C during the standard 500 °C heating programme. The spectrum shows almost no shift of the LSPR indicating little to no alloying or deformation, which was confirmed with BF-TEM imaging (appendix Fig. B.12C). When 24 h of heating at 200 °C was used, a slightly larger shift of the LSPR to 681 nm was measured, but a core shell structure was still observed in TEM imaging indicating no considerable mixing of Au and Ag had occurred. There were some signs of minor deformation such as small silver particles and flattened tips of the AuAgNRs, but nothing near the scale for the particles alloyed in air at 500 °C.

The deformation that was observed in air is a peculiar observation that is consistent with previous findings in our group [36], although it should be noted that these effects are far less severe in our experiments than in the experiments reported there. In those experiments, the aspect ratio decreased from 2.7 to only 1.7 while almost 50% of the metal volume was lost due to silver migration. An important difference between these experiments is that we use a slow heating ramp while previously the particles were heated quickly to 400 °C which was maintained for 30 min. Other experiments on the same system

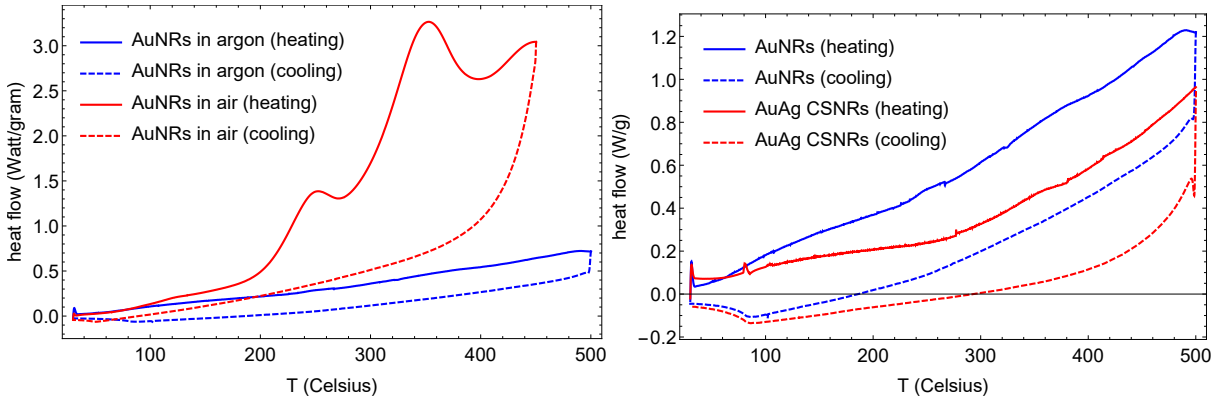

Figure 5.12: DSC curves of AuNRs@*meso*-SiO_2 in different gas atmospheres (left) and a comparison between AuNRs@*meso*-SiO_2 and AuAg CSNRs in argon atmosphere (right). The heating speed was 5 °C min^{-1} and the cooling speed was 10 °C min^{-1} for all measurements. The y-axis is exothermic.

with a lower heating ramp (such as in-situ synchrotron measurements by J.E.S. van der Hoeven) showed a similar decrease in the deformation and the silver migration. An experiment to confirm this would be to heat two batches of particles at a low and high heating rate respectively. While initially it seems intuitive that this effect is a result of some silver oxide species, this is unlikely to be a full explanation as Ag_2O is thermodynamically unstable at temperatures above 200 °C, and up to this temperature no real deformation was observed [136]. It has been suggested that despite this, the surface of Ag nanoparticles may be oxidised even at higher temperature, which could affect the mobility of silver species through silica materials [137, 138].

A wide range of processes could occur in the complicated environment of the interface between the metal, silica and air. To study processes that occur during the alloying we turned to differential scanning calorimetry (DSC), the results are shown in Figure 5.12. First, we compared the heat curves of AuNR@*meso*-SiO_2 in inert (argon) atmosphere and in air. The choice for AuNR@*meso*-SiO_2 rather than actual bimetallic particles was made because they are easier to synthesise and a relatively large amount of sample is needed per measurement (>2 mg). It should be noted that these results were part of preliminary tests and that the two measurements were not on particles from the same batch, so differences observed could in principle stem from that. The spectra show striking differences for inert and oxidising atmosphere as the latter is dominated by (at least) three large exothermic peaks. This pattern corresponds well to the decomposition (burning) of CTAB and in agreement with TGA measurements on similar samples, that showed weight loss associated with a.o. CO_2 and H_2O. When the particles are heated under argon atmosphere, the CTAB cannot burn and thus these peaks are not observed. No other significant peaks could be detected for AuNR@*meso*-SiO_2 under argon atmosphere. While the concentration of CTAB is most likely lower in the AuAg CSNRs than in AuNR@*meso*-SiO_2 because of the etching and the repeated washing steps, it is likely that some CTAB remains in the pores and that its decomposition may play a role during the alloying. From TGA measurements, we know that the CTAB comprises 11 wt% of the particles after the silica coating so heating effects can be substantial.

Although enhanced mobility of silver oxide species may play a role in the deformation and especially migration of the silver atoms through the shell, we propose that the deformation is mainly an effect of local heating. When oxygen is present and CTAB decomposes, this strongly exothermic reaction may increase the heat very locally in the silica shell. This can increase the local temperature beyond the intended temperature of the system which in turn leads to loss of the aspect ratio. The higher temperature also brings the metals closer to their melting point and increases mobility. Lastly, it is possible that the decomposition gasses with possibly water condensing from the silica lead to an overpressure inside of the silica shell, driving particles and molecules residing in the pores out of the shell. For all these effects, the heating ramp will influence the results. When the heating is rapid, a large amount of the CTAB decomposes at once leading to a sharp increase in temperature. In addition, mixing of Au and Ag has not occurred at all and the more unstable silver shell is most exposed. Recent

experiments by J.E.S. van der Hoeven also provided a method to completely remove CTAB, and those particles did not deform more when heating under air than they did when heated in N_2, unlike AuNRs with CTAB still present.

When comparing the DSC curves for AuNR@*meso*-SiO_2 and AuAg CSNRs under inert environment, few differences between the two are observed. The absolute magnitude of the heat flow per mass differs, but these differences fall within the error in the measurement of the sample mass because of the very small amount of sample available (~2 mg). While some minor fluctuations can be observed, there are no major peaks identifiable related to the mixing enthalpy or melting. Other processes that occur and may appear in the DSC curves are: further condensation of the silica shell, evaporation of water and ethanol from the pores, desorption of CTAB and (surface) melting of the silver. These effects could not be unambiguously distinguished, but are in all cases far weaker than the heat flow due to CTAB decomposition and would most likely be masked completely in a measurement of AuAG CSNRs in air. For this reason and because of the labour intensive synthesis of large quantities of particles, we decided not to perform further DSC measurements on AuAg CSNRs in different environments.

5.5 Other morphologies and metals

Branched particles

The metal overgrowth procedure is versatile and overgrowth of several different metals has been shown simply by changing the metal precursor and slight adaptations of the concentrations of metal precursor and ascorbic acid. In addition to silver, core-shell particles with both Pt and Pd as a shell were reported. Interestingly, for these two metals both smooth and rough morphologies could be obtained depending on the reaction speed [34]. In this work, some preliminary experiments were done to increase the number of possible compositions and morphologies. Using the protocol for the silver overgrowth, but with a 1 mM $HAuCl_4$ solution instead of $AgNO_3$, we were able to grow an extra gold layer around the etched AuNRs (Fig. 5.13A). The resulting particles no longer had smooth sides like AuNRs produced with the Ye&Murray synthesis. The surface consisted of rough round features and small protrusions, without the sharp spikes that extend a considerable distance into the pores of the silica shell. Due to the irregular shape of the particles, a peak broadening with respect to the etched cores is observed. These particles may have enhanced properties for SERS due to the presence of corners and edges at which the electric field is amplified. For catalysis these particles may also be of increased interest, as their high surface curvature contains more reactive facets and dangling bonds.

Secondly, a galvanic replacement method was used to grow an additional gold layer around AuNRs. In this experiment, AuAg CSNRs were prepared as described previously. These bimetallic particles were then washed once and redispersed in an equal amount of water as during the silver deposition. A 1 mM $HAuCl_4$ solution was then added to the particles. Due to the higher reduction potential of Au^{3+} than of Ag^+, the silver shell can act as reducing agent for the gold. As a result, a colour change is observed immediately upon addition of the gold as the gold replaces the silver. We used a subsequent AA addition to assure completion of the reaction, but as a result of this it is expected that the silver is again reduced and deposited on the particles. The structure of the AuAgAu NRs (Fig. 5.13B) shows highly branched particles with spikes and small particles grown into the mesopores of the silica shell. In some cases, these spikes grew long enough to reach the outside of the shell where then a small metal particle could grow. It is expected that the spikes consist predominantly of gold and are formed during the galvanic replacement step, but this was not confirmed with EDX. The extinction spectrum (Fig. 5.13D) shows a larger broadening than the rough AuNRs due to the increased degree of branching. Furthermore, the extinction continues more into the infrared with increased extinction in the visible due to the presence of small particles in the shell. Aside for their possibly enhanced properties for SERS and catalysis, these branches can be used to probe the pore structure of the silica shell. We note that this can also be achieved by growing Pt or Pd spikes into the pores directly as is investigated in our group by J.E.S. van der Hoeven. Spiky branched AuNRs (without silver) have been reported elsewhere, and were indeed found to have increased SERS activity [104].

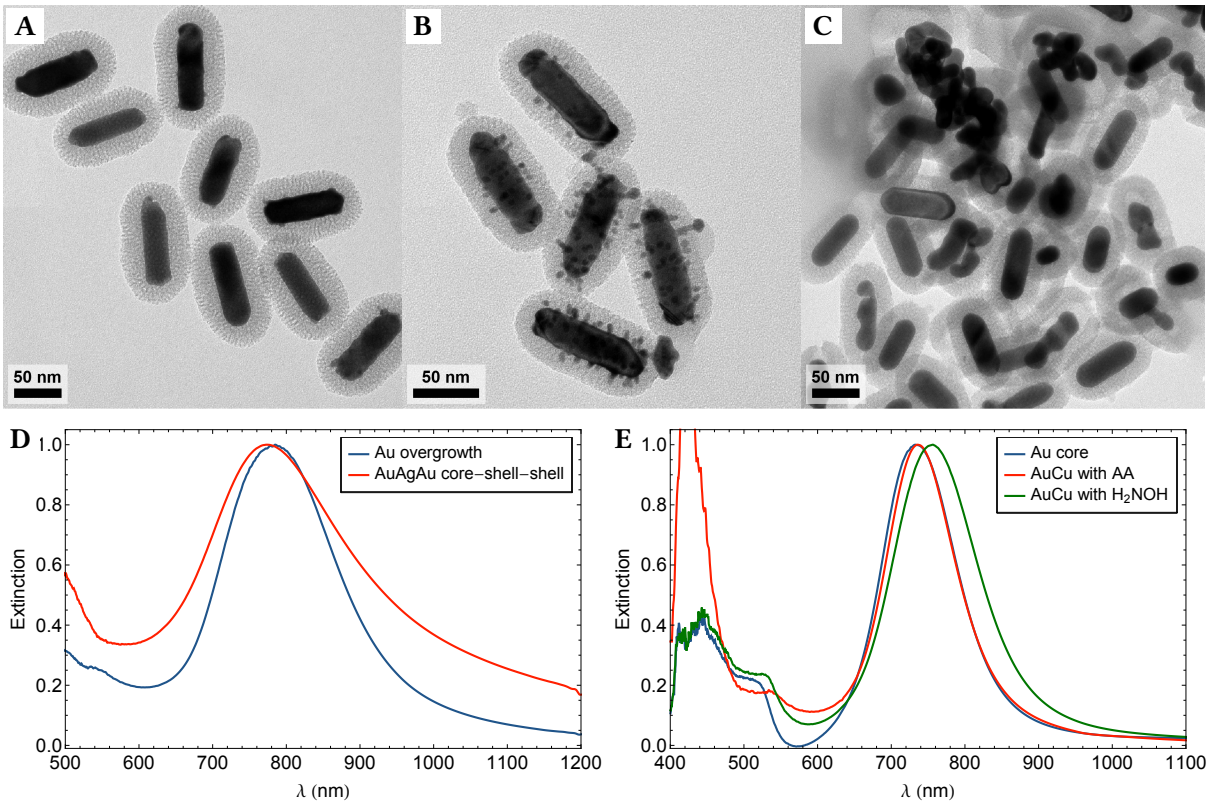

Figure 5.13: Alternative compositions and morphologies using the metal overgrowth method. A: AuNRs after an extra Au deposition. B: Au spikes by galvanic replacement of an Ag shell. C: nanoporous structures after dealloying of alloyed AuAg CSNRs. D: normalised FTIR extinction spectra of samples A&B. E: normalised FTIR extinction spectra of attempted Cu deposition.

Dealloying

The possibility of using the alloyed gold silver particles as a starting point for the formation of nanoporous gold was explored. Nanoporous gold has received considerable attention because of the high surface area, catalytic activity and plasmonic hotspots. These structures are usually synthesised by using a dealloying process: a gold-silver alloy is etched with concentrated nitric acid which dissolves the silver but leaves the gold. The resulting structure consists of a monocrystalline structure of ligaments and pores [139, 140]. Recently, a synthesis was reported for colloidal nanoporous gold spheres which used a similar process for fabricating alloyed AuAgNPs@SiO_2, but needed an extra etching step of the silica to make it sufficiently thin for diffusion of ions through it [135]. Our alloyed particles can be used for such a method directly due to the porosity of the shell. Furthermore, the anisotropy may increase the optical extinction and thus the enhancement of the plasmonic hot spots. When we used AuAg alloyed nanorods (ALNRs) with a $X_{Au} = 0.58$, no structural change of the AuAg ALNRs was observed. The low amount of silver is in this case insufficient to allow for etching into the alloy, and only silver at the surface is etched. We synthesised a batch of CSNRs with a very large amount of silver (two subsequent overgrowth steps with 3 mM $AgNO_3$ each). The resulting particles were extremely polydisperse (Fig. B.13) with the gold fraction X_{Au} as low as 0.09 for some particles, while others contained barely any Ag. The particles were then alloyed at 500 °C 20% H_2 in N_2 (by volume) as described previously.

Dealloying was achieved by first redispersing the particles in 250 µL H_2O followed by drop-wise addition of 250 µL concentrated nitric acid. After three hours of reacting at room temperature, the particles were washed with H_2O twice and in ethanol. Due to the small scale of this test it was not possible to measure an FTIR extinction spectrum. TEM images are shown in Figure 5.13C and in the appendix (Fig. B.13). Many deformed NRs are now seen, with varying structures. The larger structures all have a true porous structure similar to the literature, indicating that the dealloying was successful. A

large number of the smaller particles has some form of a hole or 'pore' running through it. The absence of a truly porous structure can be explained by the length scales involved. The width of the ligaments of nanoporous gold varies depending on the protocol, but is typically at least around 5–10 nm, which is only marginally smaller than the diameter of the AuNRs themselves. Lastly, a considerable number of the NRs seems unaffected but this can be explained by the presence of a large number of rods with a much higher Au:Ag ratio before dealloying. The large amount of broken and/or empty silica shells is a result of the strain introduced in the silver overgrowth, and not related to the dealloying itself.

Copper deposition

Finally, we attempted to expand the number of metals that can be used in the metal overgrowth protocol by exploring the synthesis of AuCu CSNRs. The presence of Cu has several advantages for catalysis due to the high reactivity of copper and copper oxides, while a combination with gold is expected to considerably improve the stability [141]. We note that direct synthesis of AuCuNRs has also been reported [142, 143]. In aqueous conditions, Cu(0) is not stable and will quickly oxidise to form Cu_2O. Epitaxial growth of Cu_2O on gold nanoparticles of various shapes has been reported and yielded interesting structures and morphology [9, 144]. Alloying of such anisotropic AuCu structures has not been reported yet to the best of our knowledge. When a protocol such as described for Ag was used with 2 mM $CuCl_2$, no evidence was found of a reaction occurring within 12 hours, even if the pH was increased to 10.9 with NaOH after addition of AA. When the concentrations of $CuCl_2$ and AA were increased ten-fold (to 20 mM and 80 mM respectively) and the pH was adjusted to 11.9, a rapid colour change to yellow occurred upon addition of NaOH. This colour change was found to be a result of the formation of small copper or copper oxide particles (appendix Fig. B.14) with a strong extinction between 400 and 500 nm. We found no evidence for the presence of copper on the surface of the gold nanorods. When 2 mM $CuCl_2$ and 6 mM $H_2NOH.HCl$ were used and ajusted to pH 11.7, a slight redshift of the LSPR occurred (~30 nm), however no core-shell structure was seen in TEM or HAADF-STEM.

Chapter 6

Self-Assembly of Nanorods

In this chapter, we study the spontaneous organisation of the rod-like particles into ordered (or disordered/isotropic) systems in 2D, confined to the liquid-air interface, and in 3D, in spherical assemblies. The main motivation for these studies is that collective plasmonic effects can occur in ordered samples, that lead to new plasmonic properties and 'hot-spots' where the electric fields of multiple AuNRs combine into a much stronger local field [30, 31, 145, 146]. In many studies on alignment of AuNRs, the surface is functionalised to promote certain structures [20, 33, 147], but we choose to use a silica coating to reduce (specific) attraction between the particles and study effects of predominantly the particle shape, as systems of (nearly) hard rods have been extensively studied using colloidal model systems and computer simulations.

6.1 Pattern formation of AuNRs on TEM-grids

2D self assembly of CTAB stabilized nanoparticles and AuNRs in particular has been explored theoretically and to some extent using electron microscopy. Bates & Frenkel [148] did a simulation study on 2D self assembly of hard rods and found that hard spherocylinders do not exhibit a nematic phase for $AR < 7$, and that rods of lower aspect ratio form crystals at high volume fraction but generally assume a globally isotropic phase with local smectic ordering at lower volume fraction. Before moving on to theoretically understandable but experimentally challenging systems of equilibrium 2D self-assembly, we can look at the behaviour of particles dried on a TEM grid and compare these to the literature. Patterns formed upon evaporation of a solvent containing CTAB-stabilised gold particles on a TEM grid were described by Sau & Murphy for drop casting the particles in dispersion on a TEM grid followed by evaporation of the solvent [149]. Many of these patterns could be recognised, but due to the complicated hydrodynamic effects and strong capillary forces during drying these methods are not suitable for reliable SA. Pattern formation after solvent evaporation on a TEM grid is often hard to reproduce and many different patterns can be observed on a single grid. Nikoobakht & El-Sayed *et al.* demonstrated the formation of ordered smectic-like structures on TEM-grids partially submersed vertically in an evaporating AuNR dispersion [75]. Several examples of structures we often observed in the TEM are shown in Figure 6.1. These grids were all prepared with particles in aqueous dispersion under ambient conditions. To highlight the influence of the drying speed on the pattern formation, we prepared a TEM grid by extra slow droplet evaporation in a closed H_2O-saturated environment without air currents over the course of 2 days. On this TEM-grid (Fig. 6.1D&E), much more ordered structures of AuNRs were observed than on grids of the same sample dried under ambient conditions. Despite the relatively low amount of particles, the AuNRs collected at high concentration in small regions and multilayer smectic stacks were found in places. Extremely fast evaporation of a dispersion in cyclohexane reproducibly resulted in networked ring-like features (Fig. 6.1D).

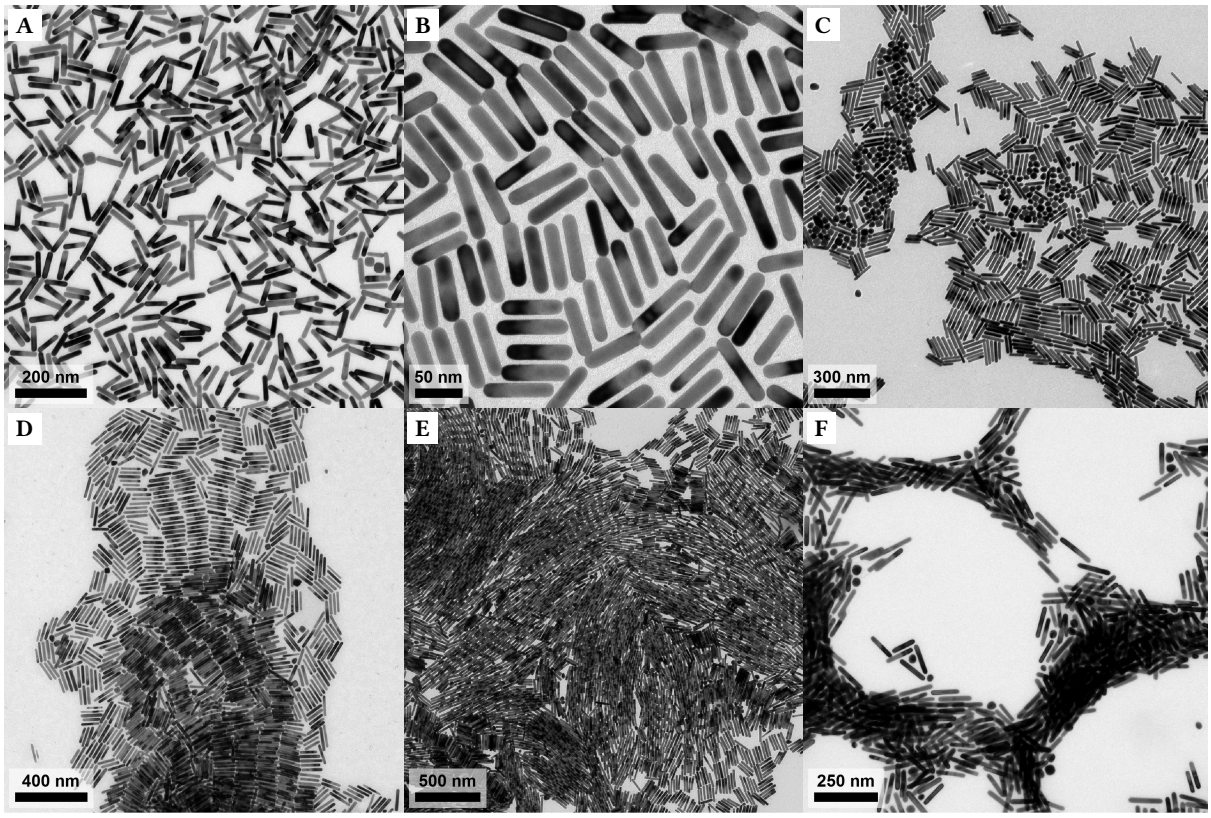

Figure 6.1: Ordering observed when a concentrated AuNR dispersion is dried on a TEM grid. A: isotropic "ordering" of AuNRs. B: overall isotropic phase with local smectic ordering. C: Separation of rod-sphere mixtures into regions rich in rods and regions rich in spheres. A–C were found on TEM-grids prepared by dropping 5 µL of a concentrated AuNR-dispersion in H_2O on the grid and allowing the water to evaporate under ambient conditions. D&E: ordered structures found on a TEM grid prepared by H_2O evaporation under a H_2O-saturated closed environment. F: ring-like structures due to extremely fast evaporation of cyclohexane under ambient conditions. The particles in F were functionalised as described in Sec. 6.3.

6.2 Experimental

6.2.1 SiO_2 surface modification with OTMS

Hydrophobic functionalisation of AuNR@*meso*-SiO_2 in toluene was achieved as follows: 3 mL of a dispersion of silica-coated AuNRs (0.8 g L^{-1}) was centrifuged (8000 g for 10 min) and the supernatant was removed as much as possible. By repeated addition of toluene, sonication and rapid pipetting the rods were transferred to a glass vial with the final amount of toluene totalling to 10 mL[1]. Then 1 mL OTMS and 1 mL butylamine were added and the vial was quickly placed in a sonication bath that was pre-heated to 50 °C, and sonication at 50 °C was maintained for 4 h. The vial was removed from the bath and left on a roller-mixer overnight to ensure completion of the reaction. The particles were collected with centrifugation (8000 g for 10 min) and washed once with toluene and once with cyclohexane. The particles were dispersed in 1.2 mL cyclohexane (equalling ~ 2 g L^{-1}) and stored for a maximum of several weeks at 4 °C to prevent evaporation of the solvent.

AuNRs with an ultra-thin silica shell could be functionalised with OTMS in ethanol as follows: 750 µL of the silica-coated AuNR dispersion was diluted with 1.75 mL ethanol. 250 µL OTMS and 125 µL butylamine were added sequentially and the vial was placed in a sonication bath at room temperature. The mixture was sonicated for 2 h during which it went cloudy as the particles precipitated together with a large volume of a plastic-like substance. Due to the ultrasonic waves the vial heated up to ~30 °C.

[1] repeatedly washing the eppendorf tube with toluene while sonicating is necessary as toluene acts as anti-solvent to the AuNRs and rapid aggregation and deposition on the walls tube occurs when sonication is stopped.

After two hours, the solid components of the mixture were collected using centrifugation (100 g for 30 s to sediment the precipitate and 5000 g for 30 s to compress it). The supernatant was removed and 4 mL of toluene was added which dissolved the sediment and dispersed the AuNRs. The NRs were collected with centrifugation (7000 g for 10 min), redispersed in 2 mL cyclohexane, centrifuged, redispersed in 2 mL cyclohexane, centrifuged, redispersed in 250 µL cyclohexane and stored at 4 °C to prevent evaporation of the solvent.

6.2.2 2D monolayer formation

OTMS-functionalised AuNRs (20 µL) were diluted with 500 µL cyclohexane. A 20 mL vial was filled for about three quarters with H_2O (MQ) and the particle dispersion was carefully dropped on the water surface forming a single droplet in the middle of the vial. A piece of parafilm was placed over the opening and penetrated approximately 10 times with a needle to allow the cyclohexane to slowly evaporate. After evaporation of the medium, a thin film of AuNRs could be seen floating on top. The area covered by the NR-film was typically several mm^2 and visible to the naked eye because of the strong optical extinction of the rods. The film was carefully scooped out of the water with a TEM grid which was subsequently dried in air. When ethylene glycol (EG) was used as substrate, 10 mL of EG was deposited in a 50 mL crystallising dish. 100 µL particle dispersion was carefully put on top and the dish was covered with a watch glass and a second crystallisation dish was placed upside down over the dish containing the liquid, and wetted with a small amount of additional cyclohexane to saturate the atmosphere. The setup was left undisturbed for at least an hour to allow for complete evaporation after which a sample could be scooped out with a TEM-grid and dried under vacuum.

6.2.3 Supraparticle synthesis

To form AuNR-supraparticles, 400 mg dextran and 50 mg SDS were dissolved in 10 mL H_2O. Then, 200 µL of the OTMS-functionalised silica-coated AuNRs (~2 mg L^{-1}) was added, and the mixture was emulsified. Emulsification was achieved either by using a Taylor-Couette type shear cell with a rotor spacing of 0.1 mm and a rotor speed of 7500 rpm, or by swirling a vial in a sonication bath for 1 minute. For both methods, the mixture was pre-emulsified by manual shaking and vortex mixing. The emulsion in a 4 mL vial was covered with parafilm which was penetrated several times with a needle to allow cyclohexane vapour to slowly escape, put in an orbital shaker and left swirling overnight to allow for full evaporation of the cyclohexane. Alternatively, a stirring bar at 400 rpm was used to prevent creaming of the oil droplets. The particles were collected with centrifugation (500 g for 30 min), redispersed in 4 mL H_2O, centrifuged, redispersed in 4 mL H_2O, centrifuged and redispersed in 500 µL H_2O. For the particles with thin silica, several samples were made using 200 mg dextran instead of 400 mg which seemed to increase ordering.

6.2.4 Tomographic reconstruction

5 µL of an aqueous dispersion of AuNR supra-particles was deposited on a quantifoil TEM-grid. HAADF-STEM tilt series were recorded for two supra-particles with tilt angles from −70° to 68° with tilt increments of 2°. The optimal focus was determined automatically at every tilt angle and manually adjusted when necessary. The datasets were adjusted for extreme values (for example because of x-rays hitting the detector) and aligned automatically using a cumulative cross-correlation method using ETomo, a program for tomographic reconstruction in the IMOD software package (version 4.9 on Windows) [150–152]. The data were binned 4 × 4 pixels and cropped to contain only the particle prior to the reconstruction to reduce noise and computation time. WBP reconstructions were performed as implemented in ETomo. SIRT reconstructions were performed using an algorithm in the ASTRA Toolbox for Matlab [153–155] and incorporated a positivity constraint (all negative values are set to 0). The full code is given in the appendix. Typically, 30 SIRT iterations provided a reasonable tradeoff between quality, noise and computation time. After the SIRT iteration, a cutoff value was determined

from the histogram of the reconstruction and used to truncate all excessively high intensity voxels. The grey-values were then normalised and the reconstruction was analysed in 3dmod, which is part of IMOD.

6.3 OTMOS functionalisation

To enable the use of reported methods for solvent-evaporation induced self-assembly, the particles needed to be stable in hydrophobic solvents such as toluene and cyclohexane. It is possible to directly phase-transfer AuNRs to hydrophobic solvents using a ligand exchange with thioalkanes [156–158] but the approach taken in this work is to utilise a silica-coating and then functionalise the silica surface, as this has several advantages with respect to stability and imaging. Silica surfaces grown by traditional methods such as aqueous or ethanolic TEOS condensation or using sodium silicate precursor are terminated by Si−OH groups and highly polar. A surface modification of the silica was necessary to stabilise the AuNRs in apolar solvents and to prevent phase transfer from the apolar to a polar phase. Octadecyltrimethoxysilane (OTMS) contains a silane-group that can bind to the silica surface and a long hydrophobic (C_{18}) tail, and is frequently used for the hydrophobic functionalisation of silica surfaces. It forms a densely packed alkane layer of 2 nm thickness on the surface which provides good stability in a wide range of hydrophobic solvents, and has a H_2O contact angle of $> 100°$ [159, 160].

For OTMS functionalisation of AuNR@*meso*-SiO_2 we used a protocol based on a method previously reported by our group (SCM) for (large) silica colloids [161, 162]. In this method, the silica-coated particles are first transferred to toluene which acts as an anti-solvent. The reaction of the silica-surface with the OTMS molecules is done in an ultrasonication bath to continuously disperse the particles as much as possible and thereby prevent crosslinking and keep the surface accessible. We use a very large (orders of magnitude) excess of OTMS as no reaction is expected to occur with the particles once the reaction is completed, and an accurate estimation of the total surface of the particles and the glass vial is impractical. While the reaction proceeds, the stability of the particles increases until they are fully dispersed. The excess reactants can then be washed away by centrifugation and redispersion. While this method works well for AuNR@*meso*-SiO_2, it cannot be used for AuNR@thin-SiO_2 due to the irreversible aggregation that occurs when transferring the particles to toluene. As a result of the thin silica shell and the large contact area, Van der Waals attractions between the gold cores are too strong for ultrasonication to overcome.

To omit the transfer to an antisolvent of the bare silica surface, a new protocol was developed for OTMS-grafting in ethanol (although similar approaches in polar solvents are known [163]). We used a similar OTMS concentration (10 V%) and a 2x lower concentration of butylamine (5 V%), lower temperature (30 °C) and shorter reaction time (2 h) to reduce the chance of degradation of the silica and aggregation of the particles. OTMS, butylamine and toluene are all fully miscible with ethanol at 30 °C, although interestingly this is only the case for fresh unreacted OTMS. Once hydrolised, the OTMS slowly precipitates/separates out of the solution. During the reaction in ethanol this could be observed as a large volume of solid-like components emerged and sedimented together with the particles. The substance, which we assumed to be an excess of hydrolised OTMS, appeared to be more soluble at elevated temperature ($\sim$ 50 °C). The (mostly solid) precipitate of the reaction could be separated from the ethanol by very slow and short centrifugation (100 g for 30 seconds) and was dark brown, while the ethanol supernatant was completely clear. This indicated that the AuNRs had precipitated together with the excess OTMS. The sediment could easily be redispersed in toluene by brief shaking or vortex-mixing which demonstrated the excellent stability of the functionalised particles in hydrophobic solvents. The nanoparticles can be seen in a toluene-water two-phase system before and after OTMS-functionalisation in Figure 6.2, showing the strong affinity of the particles for the respective polar and apolar phase before and after functionalisation.

Even with the altered protocol in ethanol, there were issues with the stability of AuNR@thin-SiO_2 in roughly half of the cases. In those batches, the particles aggregated sometimes during the reaction, but more often during subsequent washing steps with toluene and cyclohexane. In most cases the particles

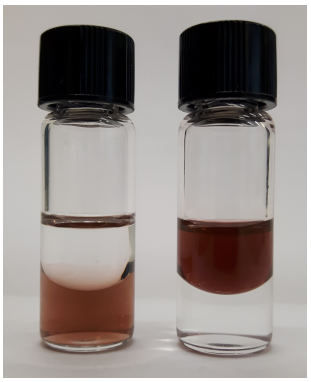

Figure 6.2: Photograph of the particles before (left) and after (right) OTMS-functionalisation. The top and bottom phase are toluene and H_2O respectively. The vials were vortex-mixed and left to phase separate before taking the image. The darker colour after functionalisation is due to a higher particle concentration.

could be redispersed succesfully in toluene (indicating successful surface modification) but subsequent washing steps caused aggregation. It is currently unclear what causes the instability, but we found that the aggregation depends strongly on the thickness of the silica-shell. When the shell was at least 4 nm thick the particles remained stable, while shells of 2–3 nm aggregated in most cases. When the silica shell was rough and inhomogeneous no aggregation was observed. When aggregation occurred, it was irreversible (in toluene, cyclohexane, ethanol and H_2O) and prevented the successful formation of supra-particles or 2D monolayers. The severity of the aggregation varied between many small clusters to a single large chunks visible to the naked eye. Many different washing methods were used, including slower centrifugation, longer sonication, washing with solvents containing 5 V% butylamine and fewer washing steps. While some samples exhibited better stability than others, no washing parameters were found that prevented aggregation for all samples. Work on preventing these issues is ongoing and expected to lead to better results in later steps.

6.4 Self-assembled monolayers

We used a 2-phase solvent evaporation approach to allow for slow formation of a monolayer on a substrate (water or ethylene glycol surface) under 2D confinement similar to those used for example in the formation of quantum-dot super-lattices [164, 165]. OTMS functionalised AuNRs were dispersed in cyclohexane and placed on top of a water surface. By controlling the particle concentration and evaporation-time, densely packed monolayers could be obtained over large areas (in the order of mm^2 up to more than 1 cm^2). Details of the method can be found in Section 6.2.2. Slow evaporation is crucial as it allows for the AuNRs to settle on the water-cyclohexane interface before the shrinking droplet forces them into a small volume. If the concentration is high or the evaporation is fast, multiple layers of particles are formed on top of each other. The monolayers could be transferred to a TEM-grid simply by scooping it from the water surface. Alternatively, ethylene glycol (EG) could be used as the substrate which had several advantages. Firstly, the higher viscosity of EG with respect to water makes the surface more stable and less prone to waves and vibrations that may disturb the self-assembly. and while scooping with the TEM grid. Secondly, the wetting properties of cyclohexane on EG are more favourable than on water as the droplet is more flat and spreads out over the surface, which reduces the chance of forming multiple layers on top of each other. Lastly, cyclohexane is mildly soluble in EG which allowed us to slow down the reaction more easily by saturating the EG and atmosphere with cyclohexane prior to addition of the particles. A downside of using EG is that it does not wet glass well enough to form a considerable meniscus, which would help to keep the cyclohexane droplet centred in the vial. Secondly, it is harder to scoop the layer without destroying it when EG is used and often droplets remain between the grid and the particle-layer.

Images of some the self-assembled monolayers (SAMs) are shown in Figure 6.3. When particles with

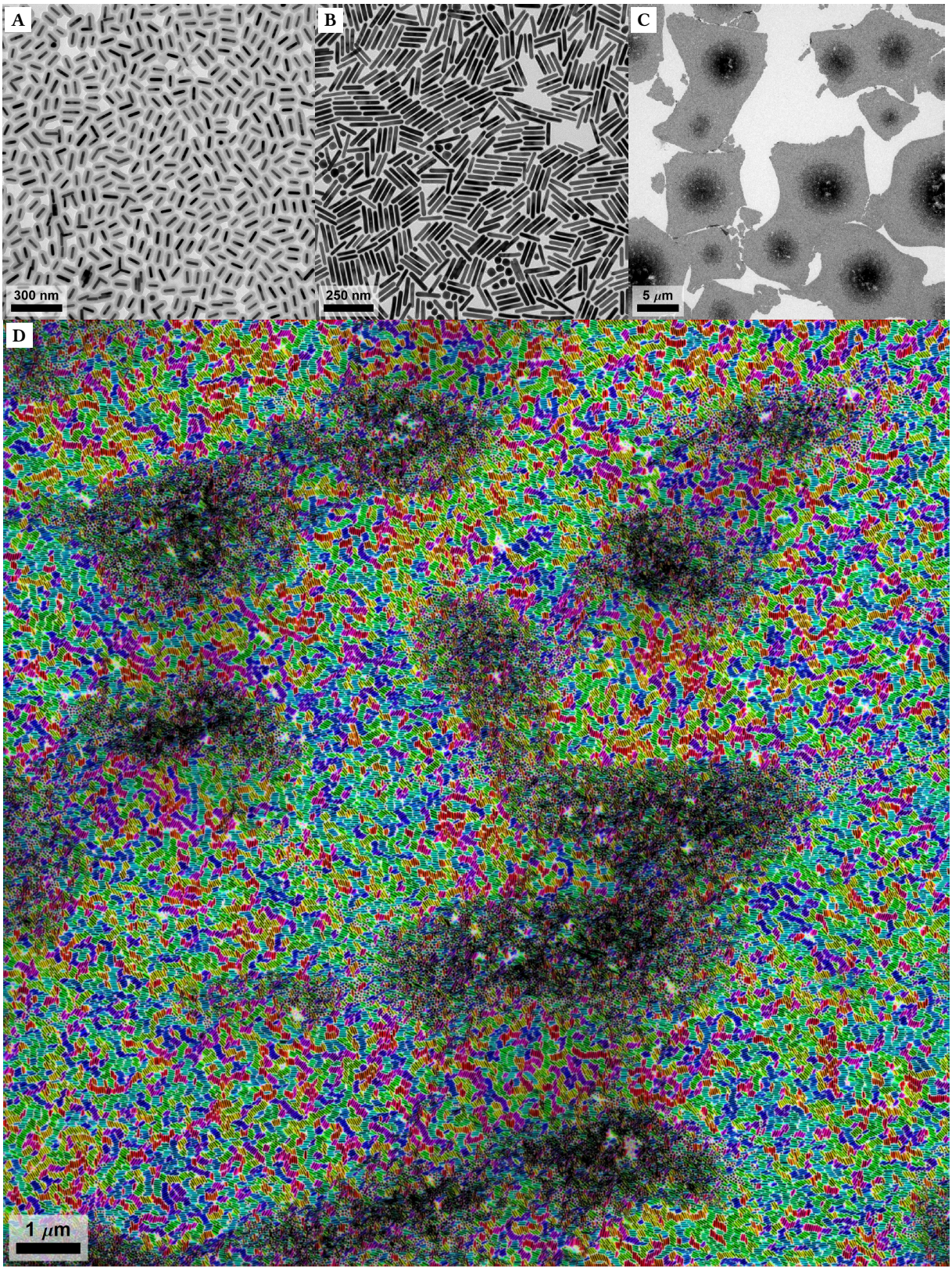

Figure 6.3: Self-assembled 2D monolayers of AuNRs. A: AuNRs with a thick silica shell ($AR = 1.8$) self-assembled on H_2O. B-D: AuNRs with a thin silica shell ($AR = 7$) self-assembled on ethylene glycol. B: detail of a monolayer shows the local smectic ordering. C: partial coverage of the interface when a lower particle concentration is used. D: low magnification overview with the rods coloured according to their orientation with OrientationJ. The NRs used in D has a rough silica shell.

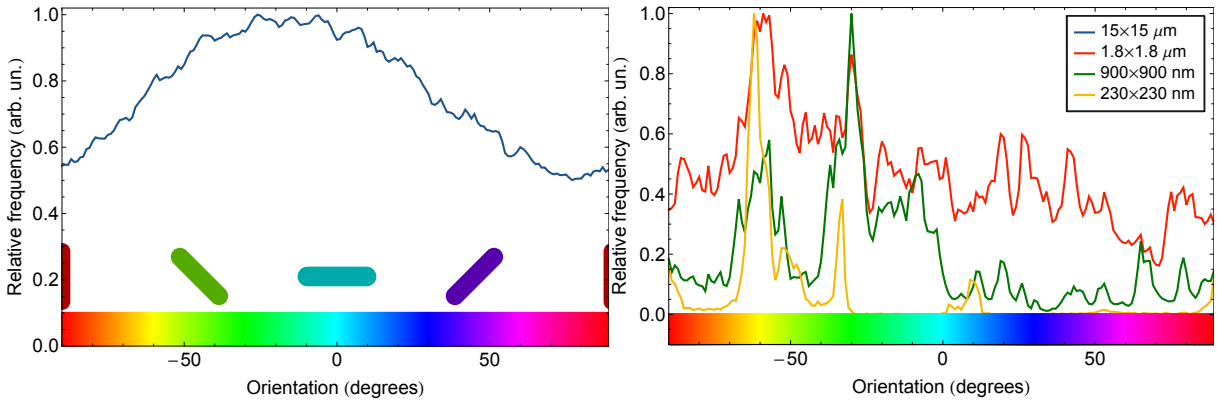

Figure 6.4: Left: distribution of the orientations of all pixels in Fig. 6.3D found with OrientationJ. Right: pixel orientation distributions of smaller sections of Fig. 6.3D. When the image size is on or below the order of the size of ordered domains, most pixels collapse into a single peak.

a thick silica shell are used, no long range ordering in the system is observed. This can be attributed to fact that the effective aspect ratio (that of the silica shell, ca. 1.9) is much smaller than for rods with a thin shell, as increasing the shell thickness leads to increasingly spherical particles. The particle shape is therefore not sufficiently rod-like to induce nematic or smectic ordering based purely on maximising the packing fraction under confinement. In addition to this, the thick shell largely shields the strong Van der Waals attractions between the gold cores that favours the maximum interface between the long sides of two AuNRs. Lastly, the shape of the silica shell is not always a nice spherocylinder. If many particles have more rounded sides, like in the case of prolate spheroids, this may decrease the chances of side-by-side ordering. There does appear to be some degree of very local ordering but this rarely persists over more than several particles. It is also possible that the disorder is related to the sensitivity of the H_2O–cyclohexane system to vibrations and air currents that keep it out of equilibrium.

The SAMs with AuNR@thin-SiO_2 are quite different in appearance and several properties can be noted straight away. Firstly, large aggregates were present in almost all of the systems we imaged. These aggregates are characterised by a more random open structure that extents in 3D (which was verified by tilting the sample in the TEM). We know that this is not a result of a excessively high AuNR concentration that leads to multiple layers on top of each other because they could be seen even when the concentration was too low to completely cover the surface (Fig. 6.3C). We suspect that the aggregates are created during the silica-coating and more so during OTMS-functionalisation. Secondly, the spherical impurities present from the AuNR-synthesis are predominantly located in or directly around the aggregates. Between the aggregates we see large "valleys" of mostly AuNRs that are locally ordered in rows of up to ~30 NRs wide. This ordering sometimes extends over multiple rows but this rarely exceeds a distance of $3L$. We note that some images we show (Fig. 6.3D, B.15 right) are of a SAM made with a rod-sample where the silica-shell possessed some form of roughness and inhomogeneity which may affect the ordering. In our analysis we did not see any major differences between these and other images where smooth AuNR@thin-SiO_2 particles were used.

To easily visualise and (to some extent) analyse the degree of ordering in the 2D system of AuNR@thin-SiO_2 we used OrientationJ [166], a plugin for the widely used open source image analysis program ImageJ [167,168]. OrientationJ determines a structure tensor for each pixel by calculating the local spacial derivative using a cubic B-spline interpolation over a Gaussian area around the pixel. The eigenvector with the largest eigenvalue then gives the local predominant orientation. From this a distribution of the orientations of all pixels can be plotted, and the local orientation can be visualised by assigning colour to the pixels depending on the orientation, a legend for the colour can be seen in Figure 6.4. OrientationJ can also calculate the dominant eigenvector for the entire image, which we used as the nematic director. Due to the high contrast of the TEM images and the corresponding sharp gradients, OrientationJ worked with single-particle precision even at very low magnifications. We found that the orientations are very slightly anisotropic ($S_{2D} = 0.15$) over large distance (Fig. 6.4) which we attribute

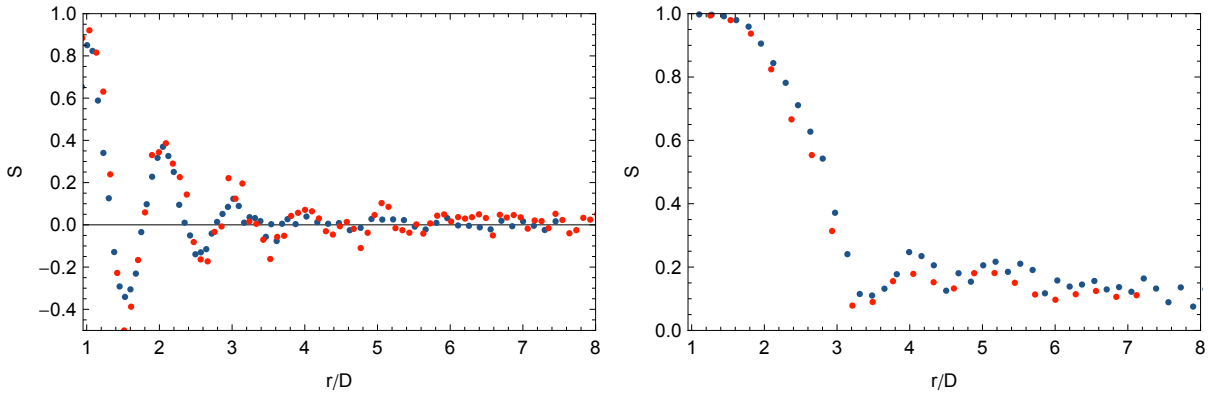

Figure 6.5: Orientational correlation functions for 2D monolayers of AuNR@meso-SiO_2 (left) and AuNR@thin-SiO_2 (right) with the distance r is normalised to the total particle diameter D. For each sample, two images were analysed and plotted in different colours.

to drying effects and potentially shear forces from scooping the sample on the TEM grid. At higher magnification these effects become obscured by the peaks of individual domains. When the analysed area is of the same order as the domain size, the distribution becomes a single sharp peak again.

While OrientationJ is convenient to visualise orientation and to determine the global order parameter (for whole images) it cannot easily be used to determine the length scale of local ordering. For this reason, a custom script for Wolfram Mathematica [169] was written to determine the particle positions and orientations. The full code is given in the appendix. Briefly: a thresholded edge detection was used to filter out only the edges of the high-contrast gold. The morphological components were automatically detected and selected based on predefined selection criteria (minimum and maximum width and minimum aspect ratio of the smallest bounding box of the shape). This removed spherical particles and overlapping particles that could not be detected individually. A list of the centre-of-mass coördinates and the bounding box orientations could then be extracted for analysis. Two images with the tracked rods are given as example in Fig. B.15 in the appendix.

We calculated the orientational correlation function which we defined in a similar fashion as the standard 2D nematic order parameter (Eq. 2.8). However, instead of determining ψ's for each particle with respect to the average of the whole image (expressed in $\hat{\mathbf{n}}$), we calculate individual ψ's for all particle pairs at a distance between r and $r + \Delta r$. These ψ's are plugged into Equation 2.8 and averaged over all ψ's in a distance bin with width Δr. This calculation is implemented computationally from a list of coordinates and orientations as following:

```
for r = r_min to r = r_max do
  for i = 1 to i = N do
    find all particles j between distance r and r + Δr from particle i;
    ψ_ij = |(θ_i − θ_j) mod π|;
  end i;
  S(r_ij) = 2⟨cos(ψ_ij)^2⟩ − 1;
  r = r + Δr;
end r;
```

where N is the total number of particles, $0 \leq \theta \leq \pi$ the angle with respect to the (arbitrary) orientation of the image and $\langle \ldots \rangle$ indicates an average over all particle pairs ij. We note that in this way all pairs are counted double, but due to the averaging this does not influence the results. This can be prevented with a possible gain in computation speed by removing each particle i from the list after it is evaluated.

The orientational correlation functions for 2D monolayers of AuNR@*meso*-SiO_2 and AuNR@thin-SiO_2 are given in Figure 6.5. We see that at a distance equal to the diameter of the particles (including silica) the particles are always fully aligned ($S = 1$), which is expected for any rodlike particle since the distance between the centres-of-mass of two particles can only come at such a close distance when the particles are perfectly adjacent. If a misalignment is present and overlap cannot occur, any possible

Figure 6.6: Schematic overview of the emulsion-droplet supraparticle synthesis from de Nijs and van Blaaderen *et al.* [170] for AuNR@SiO_2. Particles are dispersed in the droplet phase of an emulsion and compressed as the droplets slowly evaporate.

geometry with $S_{ij} < 1$ will result in a greater distance than $r = D$. In the same way, a complete misalignment ($\psi_{ij} = 90°$) cannot occur at a distance smaller than $r = (D+L)/2$. If no long-range order is present, we expect to find isotropic ordering in the limit of large r and thus $S(r_{max}) = 0$. By evaluating the inter-particle distance r for which S goes to 0 we get a measure for the length scale of preferential orientation.

For AuNR@*meso*-SiO_2 we see that $S(r)$ rapidly declines after $r = 1$ and then oscillates around 0, with maxima where r is a multiple of D. Because the system is relatively closely packed and most particles are in contact with others, aligned particles will mostly be found at multitudes of D while either an empty space or a misaligned particle between two particles is needed to find a ψ =0° at other inter-particle distances. For a conventional nematic order parameter negative values cannot occur because that would imply that the majority of particles is oriented away from the dominant direction of the particles, which is impossible. With our definition however negative values can be found when particle pairs at a certain distance are on average misaligned more than in an isotropic system. The oscillations quickly dampen out due to effects such as particle polydispersity, non-closed packing and randomness in the orientation, and we see that already at a distance of ~4–5 particle diameters the orientation is virtually uncorrelated. At longer distance the system behaves isotropic ($S = 0$) as expected. In the case of AuNR@thin-SiO_2 the behaviour is quite different. The initial decline of the correlation function is much more long ranged, but this can be mostly explained by geometric arguments as a 45° misalignment ($S_{ij} = 0$) cannot occur at $r/D < 2.5$ and a 90° misalignment ($S_{ij} = -1/2$) cannot occur for $r/D < 4$. Aside from this, there is a longer ranged correlation although this is not a very strong effect ($S = 0.1$–0.2). It does persist up to $\sim R/D = 15$ and $S \neq 0$ until $\sim r/D = 30$ (not shown here) which is much more long-ranged than the lower *AR* particles.

6.5 AuNR supra-particles

The supra-particles consisting of AuNRs were made via an emulsion droplet solvent evaporation method by de Nijs & van Blaaderen *et al.* [170, 171]. The method is similar to other reports [172], although different approaches can also be used to obtain such structures [173]. The droplet evaporation-method is depicted schematically in Figure 6.6. This method is similar to the 2D case, however now the mixture is emulsified to obtain finely dispersed droplets containing the particles. When these droplets shrink due to evaporation, the volume fraction of the AuNRs increases gradually as they are spherically confined. When the droplet has fully evaporated, a spherical assembly of the AuNRs remains which is held together due to the effect of continuous phase acting as an anti-solvent to the individual NRs. We used an cyclohexane in water emulsion with dextran and sodium dodecyl sulfate (SDS) as additives. The purpose of dextrane is predominantly to increase the viscosity of the continuous phase which improves emulsification with a shear-cell, but this also slows down phase separation and creaming due to the different densities of cyclohexane and water. SDS is a negatively charged surfactant that serves two

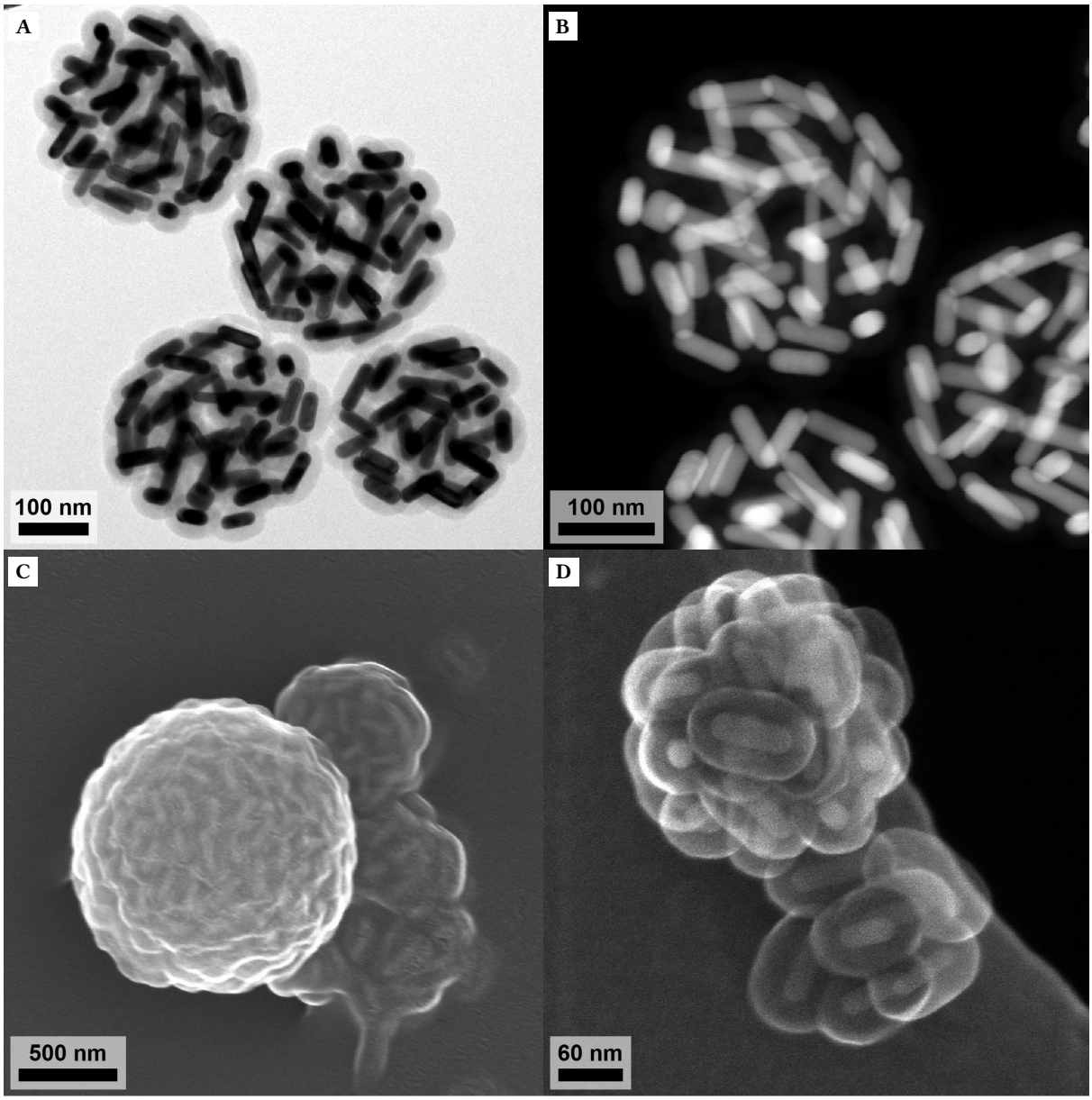

Figure 6.7: Spherical supra-particles of AuNR@*meso*-SiO_2 made with emulsion droplet self-assembly and shear-cell emulsification. A: BF-TEM. B: HAADF-STEM. C: BSE-SEM. D: SE-SEM

purposes. Firstly it stabilises the emulsion droplets and prevents coalescence during the drying phase so that evaporation can be completed before the phases start to separate. Secondly, as the SDS is on the cyclohexane-water interface it forms a layer around the particles once the droplet has evaporated, thereby stabilising the supra-particles in aqueous dispersion despite the hydrophobic nature of the individual AuNRs.

6.5.1 Supraparticles of low AR AuNR@*meso*-SiO_2

We synthesised the supra-particles with the two types of silica shell: AuNR@meso-SiO_2, Au AR = 4.0, total AR = 1.9, and the high aspect-ratio AuNR@thin-SiO_2, Au AR = 7.3, total AR = 7.0. EM images of the supra-particles made from AuNR@meso-SiO_2 are shown in Figure 6.7 and 6.8. The supra-particles have an average diameter of 325 nm ± 30% (N = 188) when made using a shear-cell and no individual AuNRs were observed outside of the SPs. When the emulsification was done by means of sonication, the average size and polydispersity are larger: 564 nm ± 48% (N = 170). Lastly, if the emulsion was mixed

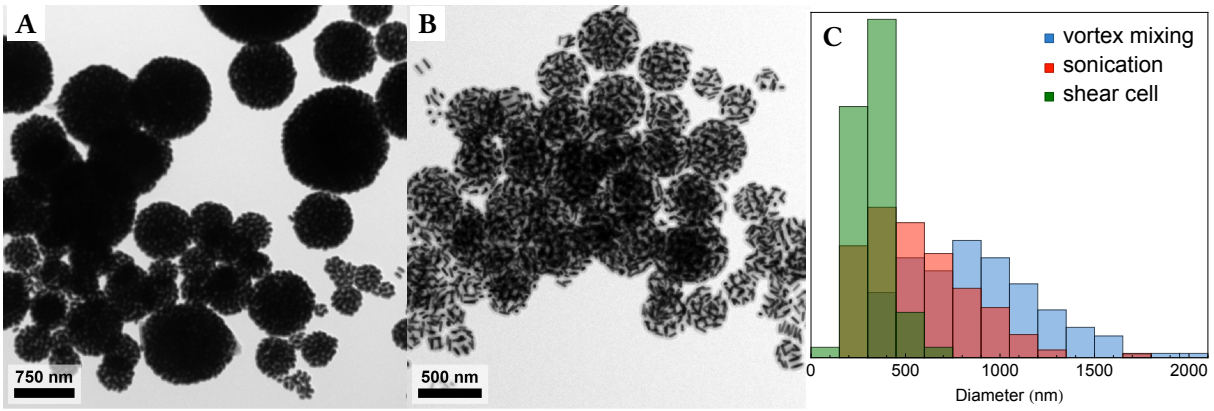

Figure 6.8: A: TEM image of supra-particles made with sonication-emulsification. B: TEM image of supra-particles made with CTAB. C: size-distributions for supra-particles made with different emulsification methods.

using a vortex mixer only, the diameter of the supra-particles was 910 nm ± 46% ($N = 155$). Histograms with the size distributions of the three emulsification methods are given in Figure 6.8C. Low resolution SEM images of these three samples can be found in the appendix (Fig. B.16) and clearly show the difference is size. These differences can be attributed to a difference in the size and polydispersity of the emulsion droplets as the particle concentration in cyclohexane was kept constant. While the shear cell provided the highest monodispersity and gives most control over the droplet size, sonication was used in most experiments in this thesis due to technical issues with the shear cell. An advantage of the polydispersity is that using one sample, the ordering in supra-particles of many different sizes can be analysed.

Irrespective of their size, the supraparticles are stable and do not aggregate although in all cases the particles sediment within an hour. The particles can be redispered by shaking or vortex mixing. This indicates good stability of the particles, which can be attributed to charge stabilisation. It is unlikely that the silica-shell possesses a significant surface charge after the functionalisation with OTMS, since the –OH groups that normally give rise to the silica surface charge are now replaced with the OTMS molecules. We therefore expect that the charge of the supra-particles is predominantly determined by the surfactant used in the emulsion. Using SDS, this will result in negatively charged supra-particles. To obtain sulphur-free supra-particles we replaced SDS in the synthesis with an equal molar concentration of CTAB. The resulting particles are expected to be positively charged. The supraparticle surface charge and particle size can be experimentally determined using electrophoresis, but this was not done in this work. The emulsion was dried at 30 °C in a water bath to prevent precipitation of the CTAB. Although supra-particles were formed, some individual AuNRs were also seen (Fig. 6.8B). This may be a result of the properties of CTAB such as the positive charge or different surface coverage, but may also result from the different drying method. Because of the water bath, an orbital shaker could not be used and a magnetic stirring bar was necessary to prevent creaming of the emulsion. When the CTAB concentration was increased slightly (20%), the ratio between the supra-particles and individual particles decreased.

To study the internal structure of the SPs we performed electron tomography experiments on SPs with AuNR@meso-SiO_2 and recorded two HAADF-STEM tilt series, one of a small particle (200 nm) and one of a large particle (500 nm). Details of the data acquisition and the reconstruction are described in Section 6.2.4 and some of the results are shown in Figure 6.9. We used both weighted back projection (WBP) and the simultaneous iterative reconstruction technique (SIRT) to reconstruct the datasets. The WBP reconstructions show sharp boundaries which makes them appear sharper to the eye. Artefacts due to misalignments and the missing wedge are strong and the background is large which reduces the contrast. While the reduced contrast was no issue for the smaller particle, it obscured all particles in the centre of the larger supraparticle. A reconstruction using 30 SIRT iterations was found to more accurately reconstruct the interior of the large supraparticle due to the higher contrast and reduced

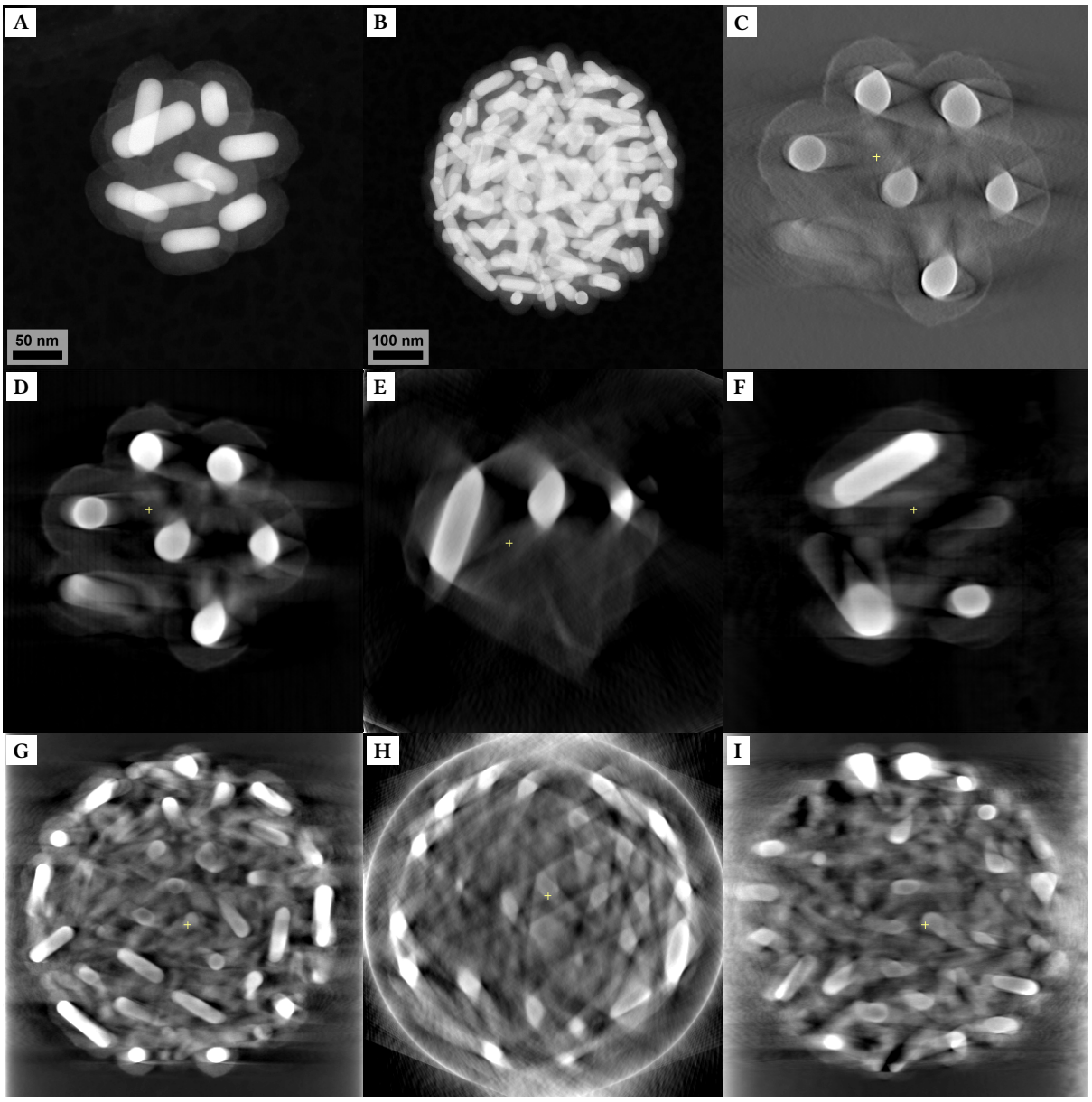

Figure 6.9: Tomographic reconstruction of AuNR supra-particles. A&B: projection image at 0° from the HAADF-STEM tilt series for a small and a large supraparticle. C: XY orthoslice of a WBP reconstruction of the small particle. D–F: XY, XZ and YZ crossections of a SIRT reconstruction of the small supraparticle, 40 iterations were used. G–I: XY, XZ and YZ orthoslices of a SIRT reconstruction of the large supraparticle, 30 iterations were used. The yellow cross in the orthoslices indicates the positions of the other two perpendicular planes that are depicted.

artefacts. Nonetheless, the reconstruction quality of the larger particle was considerably poorer than the smaller particle due to the cupping artefact, which makes large strongly scattering objects appear hollowed out. This is a result of the thickness and strong contrast of the gold: atoms on the inside of a particle receive a lower beam dose due to the scattering and absorption of the beam higher up in the sample. Once the electrons are scattered on the inside they have to penetrate a larger amount of material to get to the detector, which further reduces the signal strength [174–176]. In our case this effect occurs both within single AuNRs in the sample and in the particle as a whole. As a result the intensities of particles in the centre of the sphere have a lower absolute intensity than those on the outside, which makes reconstruction and analysis challenging. It is possible to correct for non-linear thickness effects but this requires knowledge on the absolute intensity of the incoming beam and measured signal as well as calibration of the detector [174]. An alternative is to use a higher acceleration potential to give

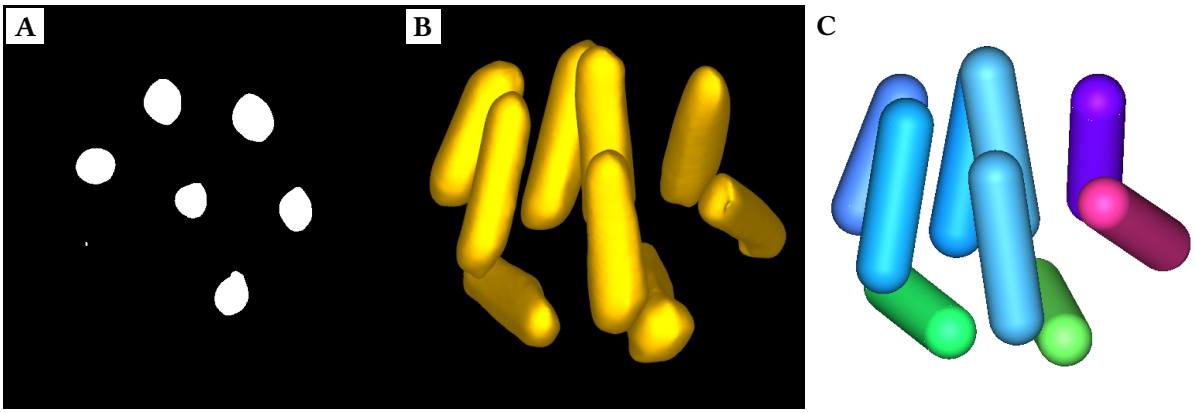

Figure 6.10: 3D particle visualisation of the tomographic reconstruction. A: thresholded xy orthoslice from the SIRT reconstruction. B: isosurface rendering of the thresholded model shown in A. C: visualisation of the 3D particle tracking where the colour indicates the orientation of the rod.

the electrons a bigger penetration depth, or to measure in incoherent bright field STEM, which suffers less from these effects.

Aside from artefacts from the missing wedge and non-linear thickness effects, there were considerable artefacts visible in the reconstructions due to tilt-axis misalignments. These artefacts can be seen for example in Figure 6.9C and are recognisable by their characteristic asymmetric crescent shape. Missing wedge artefacts on the other hand, are generally symmetric. The images were aligned prior to the reconstruction using a cross-correlation approach which is very efficient at removing the 'jitter' between subsequent images, but less so for removing a systematic drift of the sample over the entire tilt series. By using cumulative correlation (where each image is compared to the sum of the previous images as opposed to only comparing subsequent pairs) and limiting the correlation to only the particle and the least amount of background we tried to minimise the misalignment. Nonetheless, the rotation was not around a single consistent axis for the entire tilt series. Cross-correlation is more effective for more planar samples than for a spherical volume, and better methods have been proposed for nanomaterials such as the centre-of-mass alignment [177, 178]. As this method is not currently implemented in the most common software packages for tomographic reconstruction, they were not used in this work.

Another method to improve the quality of the reconstruction is to use a reconstruction method that incorporates more prior knowledge of the sample, such as the knowledge that the sample consists of a small number of different materials or that boundaries between materials are sharp. The discrete algebraic reconstruction technique (DART) is based on prior knowledge of the number and intensity of grey values in the sample. By limiting the allowed grey values in the reconstruction, artefacts are strongly supressed and the shape of particles is reconstructed much more accurately even the the quality of the dataset is limiting. While the intensities are generally not know *a priori* they can be estimated from algebraic reconstructions and by trial-and-error optimalisation of the reconstruction [179–181]. Using DART, we could successfully reconstruct the AuNRs in the small particle using only 15 DART iterations and 2 grey values (appendix Fig. B.17), although improvement is still possible. Unfortunately, it was not possible to remove the noise with further iterations due to limitations of GPU-memory. With further tuning we suspect it would be possible to also reconstruct the silica shells. The DART method could not be used for the large particle due to the large variance in grey values in the dataset. As an alternative the total variation minimization technique (TVM) can be used. TVM works in a similar way to SIRT, but in addition to minimizing the difference between the data and the reconstruction, it assures that the gradient of the image is sparse (mostly empty) which leads to sharp edges between materials. This strongly reduces artefacts and limits the number of grey values found in the reconstruction [182, 183]. Because this assumption is accurate for our sample we expect that a TVM reconstruction would be more appropriate and would facilitate considerably easier analysis due to the clean-up of the background. Due to time constraints and lack of a openly available code for TVM, it was not used in this work. Lastly,

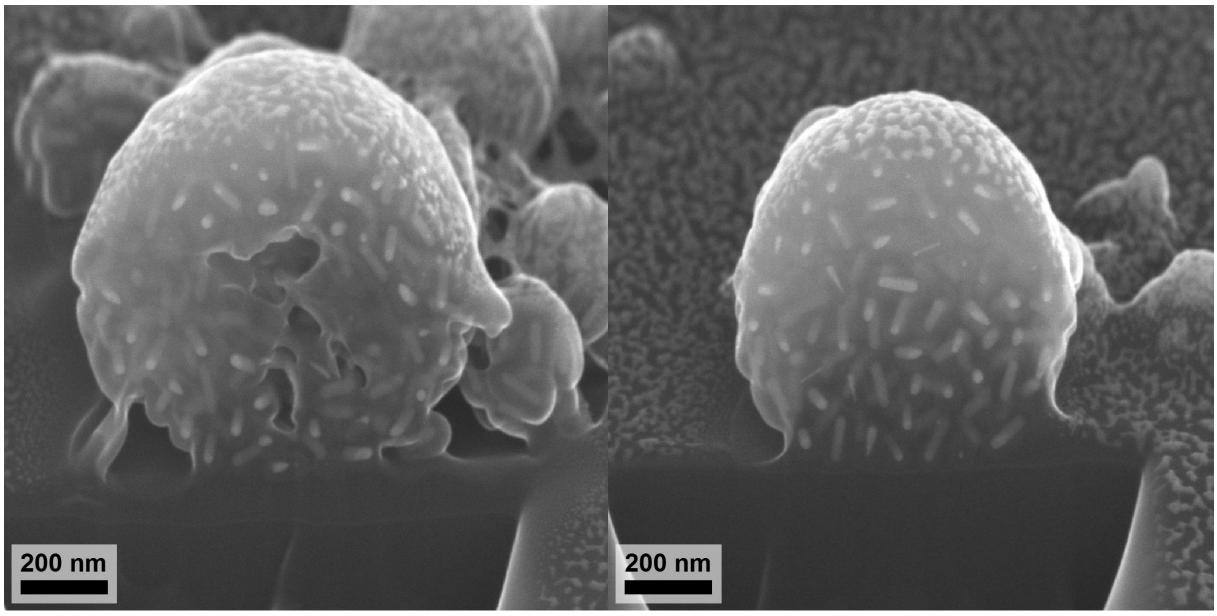

Figure 6.11: FIB-SEM cross-sections of supra-particles made from AuNR@*meso*-SiO_2. The particles were deposited on a silicon wafer and coated with 3 nm of Pt before the imaging. An acceleration voltage of 22.5 keV and a 'through-the-lens' detector for back-scattered electrons (TLD-BSE) were used.

it may be an interesting idea to use the very specific prior knowledge available on the particle shape and reconstruct the supraparticle under the constraints that it consists of discrete spherocylinders. While such a reconstruction has been used for large assemblies of spherical particles [176], it has not been reported for any anisotropic shapes.

For the small supra-particle it was possible to use a threshold in the SIRT reconstruction to generate a 3D isosurface rendering (Fig 6.10), or to use a real-space tracking algorithm to determine the positions and orientations of rod-like particles, which was developed in our group [63, 184]. Because this method relies on a smoothing step and a backbone search, where the centre of the particle is assumed to be bright, we used a SIRT reconstruction with a smaller number of iterations (20) as this leads to smoother reconstructions with less noise, and sharper boundaries are not important. The results of the rod tracking code are shown in Figure 6.10C and coloured according to the orientation in a similar fashion as OrientationJ, except in 3D. Because the particle is so small, the structure is determined mostly by the surface and does not provide much information about whether these particles can form ordered structures. In the larger particle, the intensity differences between the edge and the centre of the supraparticle were too large to allow for automated tracking of the rods. The rod-tracking algorithm either overfitted artefacts near the outside or missed out on rods in the centre, so no successful track could be obtained. By manually inspecting the reconstructed stack we determined that there was no evidence of preferential orientation of the AuNRs in the particle as even nearest neighbours were often found at completely different orientations.

In addition to tomography, We imaged the internal structure of the densely packed SPs by means of field ion beam SEM (FIB-SEM), where a focussed beam of gallium ions can be used to selectively remove part of the sample. The then exposed surface can be imaged with SEM. By repeatedly milling small slices and imaging of the milled surface a volume can be reconstructed. A major advantage of FIB-SEM with respect to ET is that much larger samples can be analysed and that it is a real space technique that does not require computationally challenging reconstruction. Downsides are that is has a lower resolution, it is a destructive method and that deformations from the milling can occur. Some results of FIB-SEM measurements on a supra-particles made from AuNR@meso-SiO_2 are shown in Figure 6.11. The measurements confirm the results from the tomographic experiments and show isotropic ordering of the AuNRs in the supraparticle. We note that this is a visual observation and this was not analysed statistically. In one of the particles we milled and imaged, empty regions can be seen near the centre of

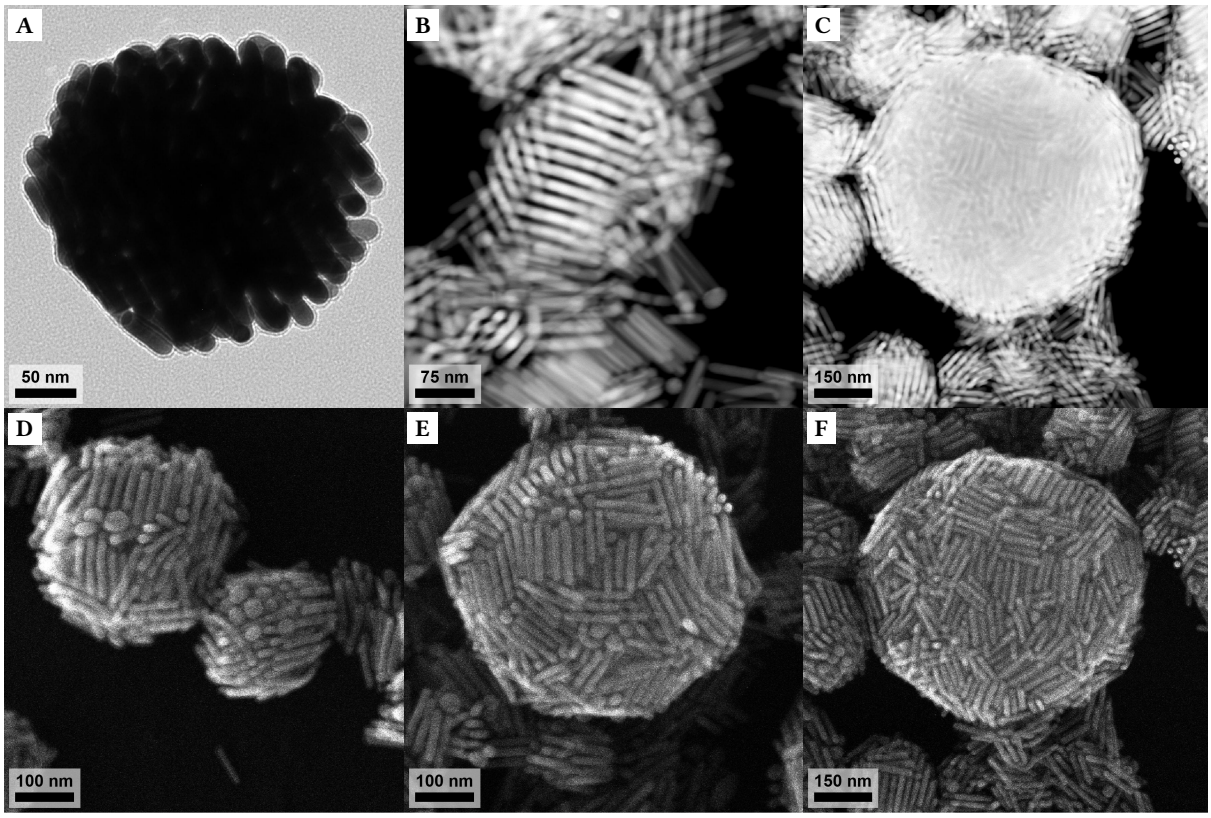

Figure 6.12: An ordered batch of spherical supra-particles AuNR@thin-SiO_2 made with emulsion droplet self-assembly. A: BF-TEM. B&C: HAADF-STEM. D–E: SE-SEM. C and E were recorded simultaneously.

the particle (Fig 6.11 left). This may be an effect of fast drying where particles near the interface form a shell and get jammed in this state before the droplet has fully evaporated. Previous experiments in our group by F. Montanarella have demonstrated a similar effect for supra-particles of quantum dots.

6.5.2 Supraparticles of high AR AuNR@thin-SiO_2

For the supraparticles composed of AuNR@*meso*-SiO_2, the silica shell successfully functioned as a spacer between the high-contrast gold particles in the TEM. This enables BF-TEM imaging up to reasonably large particle thickness as discussed in the previous section. In HAADF-STEM mode diffraction contrast effects are eliminated and larger particles can be imaged while still distinguishing the individual AuNRs. When analysing supra-particles made with AuNR@thin-SiO_2, imaging was more challenging. Due to the more densely packed AuNRs in the samples with the thin silica, it is considerably harder to image the inside of the supra-particles with AuNR@thin-SiO_2. EM images of the supra-particles are shown in Figure 6.12. In bright-field TEM the beam could not penetrate even the smaller particles, mainly due to diffraction contrast. The number of particles was enough to always have some AuNRs with their crystallographic lattice aligned to the electron beam. HAADF-STEM formed a major improvement as the internal structure of small SPs could be imaged which revealed a high degree of ordering in a large fraction of the supra-particles. The larger assemblies however were still too dense to reveal any structure in STEM imaging. By using a secondary electron detector in combination with STEM we could visualise the surface of the SPs, but this does not reveal the internal structure of the particles.

We imaged the internal structure of the densely packed supra-particles using FIB milling and SEM imaging of the exposed surface to analyse the structure and ordering inside of the particles. The results of FIB-SEM measurements on a SP are shown in Figure 6.13. While the exterior of the particles reveals no alignment over more than several particles, the majority of the inside consists of domains of ordered AuNRs. These domains however are randomly oriented with respect to each other, and no true smectic

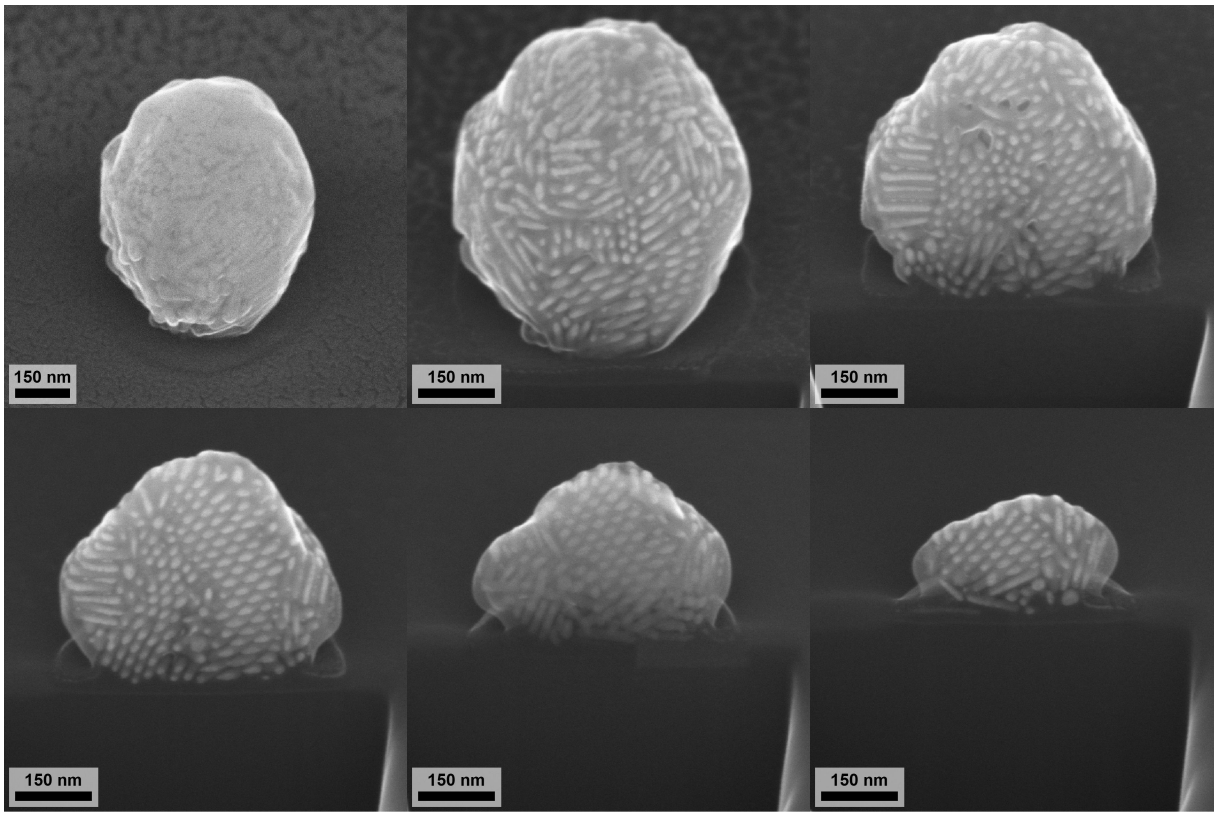

Figure 6.13: FIB-SEM slice-and-view of supra-particles with long aspect-ratio nanorods. From left to right and top to bottom a layer was milled away each time. Ordered domains that extend throughout a considerable portion of the particle can be seen on the inside without being visible on the surface. An acceleration voltage of 22.5 keV and a TLD-BSE detector were used.

or columnar order was observed. This is consistent with the results from the 2D SAMs although in 3D the number of particles per domain is much larger. Several particles were analysed as well as one of the larger structures of AuNRs that did not have a spherical shape (Fig. B.20). At the time of writing no full slice-and-view reconstruction of a particle has been measured. Remarkably, very little deformation of the individual AuNRs from the FIB milling is observed for both AuNR@*meso*-SiO_2 and AuNR@thin-SiO_2. The individual rods do not deform at the cutting plane and the resolution of both milling and imaging are easily good enough to reveal even small fragments of AuNRs. This may be related to the stabilising effects of the silica, although a recent FIB-SEM study on a similar structure reported stronger deformation after silica coating [185]. We did observe slight flattening of the smaller supra-particles during the milling, causing the spherical shape to become somewhat oblate. In future measurements we suspect this can be limited by performing the milling and imaging at cryo-temperatures.

6.5.3 Reproducibility

The experiments described here are a selection of a much larger number of tests and protocols, which had varying results. For that reason we would think it is worthwhile to discuss reproducibility and related findings in the synthesis of the AuNR SPs. OTMS-functionalisation and self-assembly of AuNR@meso-SiO_2 were highly reproducible under varying conditions. The thick silica shell sufficiently stabilises the particles to prevent unwanted aggregation under a wide range of conditions during the OTMS-functionalisation and subsequent washing. A shear cell, sonication and vortex mixing with manual shaking could be used to obtain finely dispersed emulsions with similar results. Drying in an orbital shaker or by stirring with a stirring bar yielded good results although in the latter case some larger aggregates formed.

Unfortunately this was not the case for the ordered particles. While the results shown here could

be reproduced eventually, it is worthwhile to point out that this had a success rate of approximately 1 in 4 in our experiments due to issues with stability of the AuNRs@thin-SiO_2. We suspect that this is related to the thickness of the silica shell as a difference in thickness of only one or two nm can have a considerable influence on the screening of the van der Waals forces and on charge stabilisation. We found that control over the precise thickness was poor with our protocol, but in cases where the silica shell was somewhat thicker ($\sim$ 4 nm) the aggregation did not occur. In the cases where the silica shell was thick and rough, no aggregation occurred but the roughness prevented ordering. For these samples supra-particles could be synthesised but they consist of isotropically oriented NRs (Fig. B.20). Lastly, in some cases even when the particles were seemingly stable we observed little to no ordering in the supra-particles.

Chapter 7

Conclusions

Gold nanorods are an exciting material with many unique and highly tunable properties. Their optical characteristics, in particular the longitudinal surface plasmon resonance, have received wide interest because of the strong optical extinction in the visible and near infrared, which makes them candidate for many applications. Using the binary surfactant synthesis by Ye & Murray *et al.* [74], we successfully synthesised gold nanorods with different sizes and aspect ratios. In some cases the particles contained spherical and cubic gold particles in addition to the rod-like particles, but these shape impurities could mostly be prevented by sufficient mixing and careful experimentation. When done under optimal conditions, the synthesis was highly reproducible and the large parameter space that can be used to tune the reaction makes it very flexible. The size, shape and optical properties of the AuNRs corresponded well with typical results in the literature. To explore the possibility of synthesising AuNRs with even longer aspect ratio, we used two other synthesis methods. With the synthesis by Wu & Huang *et al.* [90, 91] we could synthesise extremely elongated AuNRs, but the shape yield with this method was extremely low (<50%) as many nano-triangles and platelets were present. Additionally, the large size results in poor optical properties which makes these AuNRs less desirable for applications. We suspect the poor reproducibility is related to the seed addition steps where a change in timing of seconds can have drastically different results. Using the seedless synthesis methods of Xu & Liang *et al.* [92] it was possible to synthesise AuNRs with favourable size and aspect ratio, but the particles were very polydisperse. The method was poorly reproducible and our results differed considerable from the literature. Lastly, seedless methods are poorly scalable in general because the result depends strongly on mixing conditions during the nucleation of the gold particles.

We explored possibilities for removing shape contaminants by means of centrifugation for some of our samples that contained spherical and cubic gold nanoparticles. In addition, we studied if it was possible to separate gold nanorods based on their aspect ratio or size. We concluded that the separation achieved by (repeatedly) tuning the centrifugation speed and time under normal conditions does not have the separation efficiency to separate rods and other particles with similar volume. Such a method was only successful to remove large aggregates or very small particles (<10 nm in diameter) such as seeds remaining after the synthesis. By using a reported method for high speed centrifugation it was possible to achieve partial separation of rod-like and spherical particles based on the their preference to sediment either on the side or in the bottom of a centrifuge tube. The spherical particles sedimented preferentially on the side of the centrifuge tube while most of the rod-like particles sedimented on the bottom. The efficiency of the separation was reported to depend mostly on the ratio between the radii of the rods and the spheres and not the aspect ratio of the rods. What mechanism exactly determines the position in the centrifuge tube remains unclear. Lastly we used a method for viscosity gradient centrifugation where the viscosity of the solvent increases as particles go lower in the centrifuge tube. Using this method we demonstrated very efficient separation of a mixture of two samples of AuNRs with distinctly different AR and volume. The separation was however not efficient enough to considerably decrease the polydispersity of a sample of AuNRs from a single synthesis. It was found that the separation occurred based on the volume (and thus the mass) of the particles, and shape effects played no role.

After the synthesis, the AuNRs could be coated with a protective silica layer using two methods resulting either in a thick mesoporous shell (AuNR@*meso*-SiO_2) or a thin (presumably nonporous) waterglass silica shell (AuNR@thin-SiO_2). The mesoporous silica shells could be grown using literature methods [34,108] with CTAB as soft template for the formation of pores, which resulted in a sponge-like structure as observed with SE-SEM. The resulting particles were stable in water, methanol and ethanol. We reported, for the fist time, a method for the condensation of a very thin (as little as 2 nm) silica shell on gold nanorods that does not rely on silanol coupling agents to prime the gold surface. Our method is a very simple single step addition of sodium silicate solution to aqueous AuNRs without the need for precise control over the particle and precursor concentration, pH, reaction time and particle shape. The reaction time (typically 45 min.) is also much shorter than those reported in the literature (1–2 days). While the formation of a silica layer was highly reproducible under a wide range of conditions, control over the exact shell-thickness was poor and results varied between ca. 2 and 5 nm. Due to the large Van der Waals attraction between the AuNRs and the small shell, this can lead to large differences in particle stability. We suspect that these differences are related to the CTAB concentration during the coating, which is currently poorly controlled and largely unknown.

Using a literature method [34, 36] we could selectively etch part of the gold of AuNR@*meso*-SiO_2 through the silica shell using diluted H_2O_2 and HCl in methanol at elevated temperature. By controlling the reaction time, the degree to which the particles were etched could be controlled. These etched AuNRs were then overgrown with a silver shell as reported before [34, 36] to obtain AuAg CSNRs. By tuning the etching time and/or the silver precursor concentration the thickness of the silver shell, and thus the gold-silver ratio could be controlled. We synthesised particles with molar fractions of gold ranging from 1 to 0.26, but it is most likely possible to go even lower using longer etching times and higher silver concentrations. When the thickness of the silver shell significantly exceeded the available space due to etching, secondary silver particles were nucleated and some of the silica shells were cracked open, which led to strong broadening of the ensemble LSPR peak. The formation of a silver shell caused the optical extinction of the particles to increase and undergo a peak shift, although the magnitude and direction of this shift depends on many factors (change in AR, dielectric function of the particle, dielectric constant of the medium, morphology, etc.). The silver deposition method as reported (on a 300 µL scale, ~40 mg L^{-1}) is poorly scalable due to the rapid reaction and limitations on mixing speed. To synthesise bimetallic particles on a larger scale, we studied the influence of temperature and pH on the reaction rate. By performing the silver deposition in an ice-bath, the reaction proceeded visibly slower and could reproducibly be scaled at least 10-fold to 3 mL. Addition of a small amount of HCl to lower the pH was found to decrease the reaction speed as it influences the oxidation mechanism of ascorbic acid. We demonstrated good control over the reaction speed with in-situ FTIR extinction spectroscopy by changing the HCl concentration, and found that 0.4 mM HCl gives a good balance between a reduced reaction speed and stability of the particles. Using this method, the metal overgrowth could be scaled to >100 mL (~5 mg particles).

The bimetallic core-shell particles could be alloyed without loss of the anisotropic shape in a similar manner as recently reported [36]. A slow temperature increase (5 °C min^{-1}) up to a maximum temperature of 500 °C in a gas-flow reactor with mass-flow controllers was used to study the influence of the gas atmosphere on the alloying protocol. We found, in correspondence to the literature, that the presence of oxygen lead to deformation of the AuNRs and to migration of silver from the rods out of the silica shell. When inert (N_2) or reducing atmosphere (H_2 or CO) were used, no such effects were observed. The deformation could be attributed to local heating of the particles due to exothermic decomposition of CTAB surfactant present in the silica shell. How this leads to the migration of silver species remains unclear, but most likely relates to the fact that this process occurs before the alloying starts.

In addition to the formation of a silver shell, we demonstrated control over the morphology of the nanorods by using alternative overgrowth protocols. By deposition of a gold layer on etched AuNR@*meso*-SiO_2 particles were obtained with a rough surface with rounded features and some small spikes. When a gold solution was added to AuAg CSNRs, the galvanic replacement of the silver shell by the gold resulted in the formation of spikes in the pores of the silica shell. These particles had a very

broad extinction peak and it is expected that the electric field is enhanced strongly at the tips of the spikes. After synthesising and alloying gold-silver bimetallic nanorods with a very high silver content is was possible to use a 'dealloying' method with nitric acid, to obtain a nanoporous gold structure. We observed nanoporous gold, but truly porous structures were only possible for larger chunks of metal than the nanorods, as the width of the ligaments and pores in the porous gold were of the same size scale as the diameter of the nanorods. As a result, many particles appeared curvy and irregular, or contained one or multiple holes running through. We propose that synthesis of nanoporous gold nanorods is possible if AuNRs are used with a much larger volume, and a large silver shell is grown. It is currently unclear how the (optical) properties of an overall rod-like porous particle would compare to those of approximately spherical nanoporous gold particles. In addition to gold and silver, we did several preliminary tests to synthesis AuCu CSNRs. In our experiments, either Cu (or more likely Cu_2O) particles nucleated, or no metallic Cu or Cu_2O was observed at all. Apart from a peak shift in one experiment, no evidence for the formation of a copper shell was observed.

Since ordered structures of AuNRs can lead to enhanced collective properties we studied the self-organisation of silica-coated gold nanorods using solvent evaporation methods. To enable this we first functionalised the silica shell (AuNR@*meso*-SiO_2 or AuNR@thin-SiO_2) using OTMS. For the thick AuNR@*meso*-SiO_2 particles we could use a literature method that reacts OTMS with the silica surface in toluene, an antisolvent for the silica prior to functionalisation. In the case of AuNR@thin-SiO_2, the aggregation this induced was irreversible, and a new method was developed to functionalise the silica in ethanol. Using this new method, AuNRs with a sufficiently thick and stable silica shell (>~4 nm) could be reacted with OTMS in ethanol, after which the particles were stable in toluene and cyclohexane. In many cases (usually when the silica shell was >4 nm) aggregation of the particles occurred during transfer to cyclohexane, the cause for this is unknown. The ordering in self-assembled monolayers was studied by drying cyclohexane containing particles on the water-air or ethylene glycol-air interface. When AuNR@*meso*-SiO_2 was used (with an average AR of 1.9) no preferential orientation or ordering was observed visually or by computational analysis, other than very local geometric effects due to constraints preventing overlap. For AuNR@thin-SiO_2 we observed locally ordered domains with a high degree of short-ranged orientational correlation, but no true long range ordering.

Using an emulsion droplet evaporation method we prepared spherical supraparticles from the silica coated AuNRs. Using different emulsification methods it was possible to obtain different supraparticle sizes containing between only 2 or 3 up to thousands of AuNRs. Supraparticles made from AuNR@*meso*-SiO_2 were studied in 3D using HAADF-STEM tomography and FIB-SEM cross-sectioning, and exhibited isotropic orientation of the AuNRs inside, which we attribute to the low aspect ratio. Additionally, we prepared supraparticles from the high aspect-ratio AuNR@thin-SiO_2 and found that in some cases strong ordering was observed. For those samples, ordered domains of AuNRs were present in the particles which, to the best of our knowledge, has never before been reported in the literature for supraparticles of AuNRs. Orientational ordering that extended over the entire supraparticle was only observed for supraparticles <300 nm. Why ordering only occurred in some samples remained unclear, but it is expected that this is related to the nanorod stability as well as the drying conditions.

Chapter 8

Outlook

Since this study covered a broad range of subjects in a limited time-frame, it is far from complete and much work remains to be done. In this chapter we discuss some of the experiments needed to confirm or reject predictions made in this report as well as suggest some ideas for further research and related topics. It may for example be interesting to consider other synthesis methods for the AuNRs used for various experiments. A huge amount of attention has been devoted to the synthesis of AuNRs with an ever increasing domain of synthesis parameters, sizes and aspect ratios. This research is based heavily on one such synthesis method, while for different projects different properties are of interest and new possibilities are still being explored, such as CTAB-free and silver-free synthesis, or methods to achieve much higher monodispersity. In our experiments, it may very well be that lower polydispersity and the absence of spherical particles would have lead to a higher degree of ordering. Preliminary experiments with more monodisperse AuNRs with $AR = 5$ demonstrated ordered supraparticles similar to the results shown in this work, but with little to no spherical particles. Using citrate-stabilised seed particles it is possible to synthesise pentatwinned AuNRs, which have a very different crystallographic structure that may behave differently during alloying and catalysis.

In this work, no experiments on the catalysis of the gold or bimetallic nanorods were done. For any suitable model reaction, many different parameters could be varied to study their influence on the catalysis. Possibilities would be to vary particle size (surface to volume ratio), aspect ratio (ratio of different exposed facets), composition (gold/silver ratio), surface morphology (smooth/rough, gold/silver/alloy/nanoporous/other metals), influence of the plasmon resonance (excitation at varying light intensity), organisation (separate particles or ordered structures) or comparisons with other types of (gold) catalyst. The precise control over many of these properties, combined with the ability to precisely characterize them means that systematic investigation of many different parameters becomes available. The choice of model-reaction is non-trivial as gold is generally only very active at very small particle size. Another problem is that the amount of particles in a synthesis is typically very small for catalytic experiments, on the order of 1–10 mg.

Using electron energy loss spectroscopy (EELS) it is possible to directly map the intensity of the plasmon resonance [186]. It would be interesting to perform such measurements at a high resolution for the bimetallic nanorods and gain more fundamental insight into the influence of both chemical composition and morphology on the properties of the plasmon resonance. Because such experiments are performed in a high-resolution electron microscope with EELS capabilities, detailed structural and chemical information of the particle is present alongside of the intensity of the plasmon resonance at different energies. This enables for highly detailed correlation of the optical properties with the particle structure on a single particle level. While such measurements have been done for spherical gold-silver alloys [187], the optically more interesting alloy nanorods have not been studied with such single-particle methods. Additionally, the interaction between multiple particles at close distance can be mapped to understand the coupling of the plasmon and the presence of 'hot spots' in certain places.

To continue the self-assembly part of this research more experiments are needed to elucidate the influence of small quantities of CTAB on the formation of a thin silica shell using the water glass method.

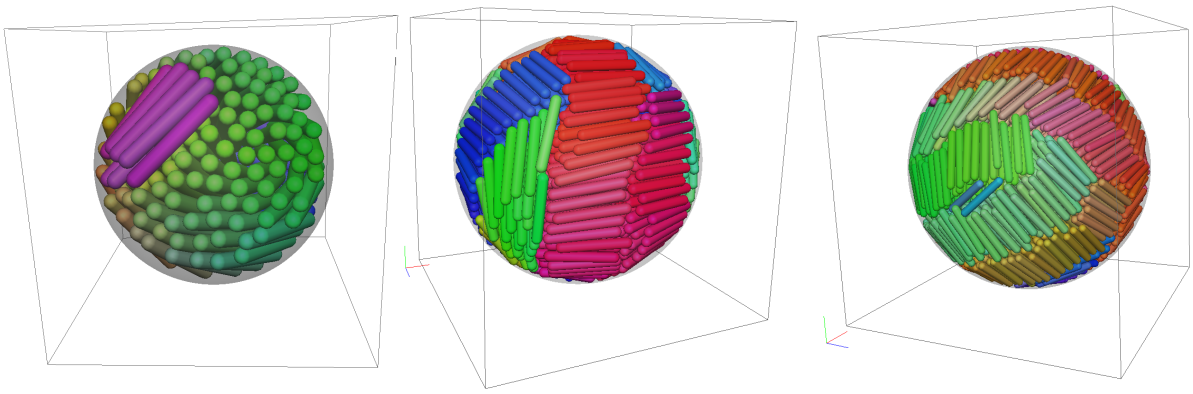

Figure 8.1: Preliminary results of simulations by Robin van Damme of the supraparticle synthesis for rods with $AR = 7$. At high volume fraction (>0.5) strong smectic ordering of the system is observed for most particle sizes. Curiously, small particles all exhibit chiral twisting.

We have limited evidence that the presence of a larger concentration of CTAB leads to increased shell-thickness but no systematic testing of this hypothesis was done. One method would be to repeatedly wash the particles with water containing known quantities of CTAB until the additional CTAB introduced by the particle surface can be assumed to be negligible, followed by growth of the silica shell. Repeating this for different CTAB concentrations, the influence of CTAB on the silica shell formation can be studied. While our method has major advantages over other literature methods, the poor control over the shell thickness is an issue that needs to be worked on. Further systematic investigation of the concentrations of AuNRs and sodium silicate as well as the pH, reaction time and reaction temperature can provide a more detailed insight into the shell growth. For SERS applications it would be of interest to see if the thin shell is indeed completely non-porous, which could be checked for example by adding an etching agent for the gold or by measuring SERS signals for molecules that strongly adsorb on the gold surface (like pyridine). The SERS signals of AuNR@thin-SiO_2 may be interesting by themselves as the shell is thin enough to allow for considerable electric field enhancement while simultaneously shielding the gold from contamination and degradation, in correspondence with recent reports on similar particles for shell-isolated nanoparticle-enhanced Raman spectroscopy (SHINERS) [106, 115].

The difficulties with alignment of the rods over a long range purely based on the particle shape would be hard to overcome, because the nature of these effects is inherently short-ranged. Even when local effects that lead to tip-to-tip alignment are strong, the smallest degree of flexibility may ultimately result in twisting and curves that may, depending on the application, be undesirable. One method to induce true long-range ordering in systems is to use external triggers with a directional component such as magnetic, gravitational, or electric fields. AuNRs have been shown to have a much higher diamagnetic response to magnetic fields than bulk gold. Furthermore, this response is anisotropic which induces a net torque on the AuNRs, causing them to align their long axis along the magnetic field. Unfortunately the diamagnetic effects are still small with respect to the thermal energy and considerable alignment is only found at extremely high magnetic fields (35 T) [188, 189]. A better approach may be to use an external alternating current (AC) electric field that can interact with the resonating electron cloud of the AuNRs. It has been shown in our group (SCM) that orientational alignment in liquid crystals of micron sized silica rods could be turned on and off by applying an external electric field, thereby controlling the optical response in the system [162]. Using such a method for gold nanorods would be interesting as it could demonstrate similar effects for particles with a completely different length scale and composition. To highlight the size differences between the silica and gold rods, a TEM image containing both a large silica rod and AuNRs is given in the appendix (Fig. B.21). Due to their strongly directionally anisotropic polarisability and the induced dipole moment they exhibit, AuNRs can be expected to show a similar alignment in an (AC) electric field. Several groups have indeed reported such an effect [190–194]. An interesting method could be to use the electric field component

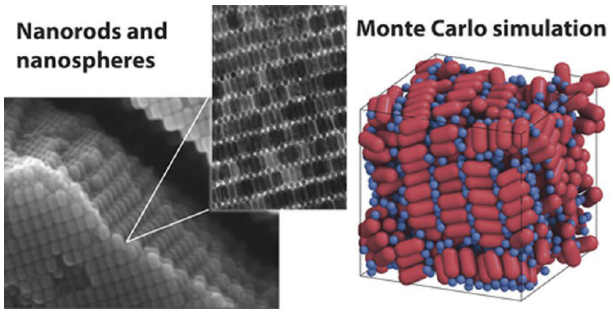

Figure 8.2: TEM images and Monte-Carlo simulations of binary smectic phases with long range ordering in systems of $NaYF_4$ rods and Fe_3O_4 spheres. Reprinted from ref. [200].

of electromagnetic radiation for this purpose. Since the excitation of the LSPR depends strongly on the polarisation of the light and the orientation of the particle, laser light will excite only particles parallel to the field. Because laser light is coherent, all particles see the same field and thus the electron clouds resonate in such a way the net electric fields at the tips would favour tip-to-tip alignment of the excited rods in one direction. Self-assembly under IR-laser excitation may thus induce alignment in the rods at high volume fractions. Lastly, alternative possibilities have been reported that induce alignment via additional materials such as micelles that align spontaneously or in external fields [195], patterned substrates [29, 196, 197], polymers [25, 29, 198] or anisotropic density in a gravitational field [146].

A more accurate analysis method for the ordering of the supraparticles would be to use serial block-face imaging (FIB-SEM slice-and-view) for a full real-space 3D reconstruction. This allows for particle tracking and statistical analysis of the structure, as well as theoretical calculations on the optical properties, based on coordinates and orientations extracted from the real structure. A full reconstruction of a large templated array of ordered silica-enclosed AuNRs was already reconstructed and analysed in such a way by Hamon & Liz-Marzàn *et al.* [33, 185]. To decrease the deformation due to the milling we aim to do these experiments at cryo-temperatures. For supraparticles of sufficient size (>2 µm) there is the possibility that so-called 'whispering-gallery' modes are observed, that lead to enhanced absorption due to internal resonance of waves inside of the particle [199]. To our knowledge these whispering gallery modes have never been observed in spherical superstructures of gold nanoparticles. The whispering gallery modes may increase the signal in SERS or other applications that rely on the local electric field enhancement. In this work no SERS measurements were performed, but the ordered supraparticles are expected to show strong enhancement of the Raman signal of organic molecules that can diffuse into the supraparticles due to the presence of plasmonic hot-spots. Comparisons between the SERS signals of individual silica-coated AuNRs and supraparticles can potentially demonstrate such an effect.

In our work we use oil-in-water emulsions for the supraparticle synthesis, but in principle there is nothing that prohibits the use of a water-in-oil emulsion. The major advantage of such a method is that no functionalisation of the silica shell is needed. As an alternative to the OTMS-functionalisation of AuNR@thin-SiO_2, we did some preliminary experiments with methanol-in-dodecane emulsions using SPAN80 and SDS as surfactants, which required some tuning to obtain stable emulsions. Because there is more experience in our group with the cyclohexane-in-water system and because water-soluble supraparticles are preferred, we decided not to pursue this method any further, but it may yield interesting results due to the higher particle stability of particles with a very thin (2–3 nm) silica shell before the OTMS functionalisation. Using a water-in-dodecane emulsion, the drying speed is expected to be slower than for cyclohexane and the larger silica charge may be advantageous to the ordering. Lastly this allows for facile incorporation of other water-soluble molecules or particles into the structure. By using methanol or ethanol in dodecane emulsion a water free supraparticle synthesis can be achieved. Another possibility is not to grow a silica shell but rather to directly functionalise the gold surface with apolar molecules. Several methods for thiol-functionalisation for hydrophobic AuNRs have been reported [156–158]. A protective silica shell may then be grown around the supraparticles after the

emulsion self-assembly.

Recent reports have demonstrated very interesting phase behaviour from systems of both rod-like and spherical colloids, where various binary smectic phases (Fig. 8.2) were observed depending on the size ratios of the rods and spheres [200–202]. In many cases rods and spheres are known to phase separate [203], but under the spherical confinement of the droplet self assembly this may be very different as all particles in the initial droplet ultimately will end up in the supraparticle. While this provides valuable fundamental insights into the phase behaviour of complex mixtures, it is also interesting for various applications as the spheres could be interchanged for different materials. When quantum dots are used, this method may place them in an ideal position for plasmon-enhanced fluorescence where the plasmon resonance enhances the excitation and/or emission of fluorescent particles or molecules, which can occur for instance due to selective enhancement of radiative relaxation while not affecting the non-radiative relaxation [110, 204, 205]. Other potentially interesting systems would be to form binary smectic supraparticles with porous (silica) spheres that allow for good diffusion of reactants or analytes into the plasmonic hotspots or to position catalytically active particles between the AuNRs. It may be useful to perform computer simulations to analyse under which circumstances such phases are expected in spherical confinement. Some results from preliminary simulations by Robin van Damme showed that for soft repulsive rods of $AR = 7$ ordered domains were present, in good agreement with our experimental results, while a further increase in the volume fraction caused alignment over multiple layers. Simulations of binary systems in such a way would be useful.

Acknowledgements

There are many people that contributed to this work in one way or another, and this thesis would be incomplete without thanking those involved. First of all I wish to thank my supervisors Alfons and Petra, that gave me the possibility to do this research in a very diverse multidisciplinary environment with more facilities and possibilities than a master student can wish for. You have both encouraged me to think and incorporate my own ideas, and given me all the space to pursue my personal interests. Your suggestions and comments during meetings and presentations have become vital elements of this work and gave ideas to expand upon when I needed them. But perhaps more important than that, I learned to always critically think not just about *what* to investigate, but also about *why* I was doing that. You both have your own interests, ideas and methods in research, and this taught me to always view problems and ideas from different perspectives. In the same way that bimetallic particles are more than just the sum of gold and silver, one can say that working on the interface between ICC and SCM has the "synergistic effect" of learning to combine fundamental interests in plasmonics and self-assembly with practical aspects such as synthesis and applications in catalysis. While it wasn't always easy, this is a very valuable skill to have learned. To no one do I owe my gratitude as much as to Jessi, my daily supervisor. I have greatly enjoyed this project for the entire duration, and that is for a large part because of the way we worked together. I immensely respect your ability to teach and explain things in a way that shows that you view me as a fellow scientist and not just as a student. You gave me the freedom to pursue my (sometimes wild) ideas and interests while always being closely involved and keeping me on the right track. You shared my excitement over good results but also helped me get going and stay motivated when experiments weren't working out. Your critical remarks and eye for detail helped to turn my presentations and this thesis from something decent into something *good*. But more than that, I thank you for being such a nice and fun person to be around!

Then there are many people that helped me with equipment, experiments and analysis. I wish to thank Hans Meeldijk and Chris Schneijdenberg for their help, trust and patience with electron microscopy. TEM has become by far the most important analysis technique upon which this research is based, which would have been impossible without being given the trust and help to operate these beautiful but complicated machines. I also thank Yang Liu for helping with the FIB-SEM measurements, Da Wang and Federico Montanarella for their help with the shear cell and suggestions on supra-particle synthesis, Rolf Beerthuis for his help with the calcination/reduction setup and letting me borrow his reactor when I broke my own, Stephan Jonker for helping with the AAS measurements, Relinde van Dijk - Moes for the ICP measurements and Jan-Willem de Rijk for the DSC measurements. I wish to thank Fabian Hagemans, Judith Wijnhoven and Relinde van Dijk - Moes for their technical support in the lab, and for the non-trivial task of keeping a lab full of chemists and physicists in a very neat and safe condition. Furthermore, I thank Wiebke Albrecht and Tom Welling for all their input and work for the alloying experiments, Robin van Damme for the preliminary simulations on the supra-particle self-assembly, Michiel Hermes, Thijs Besseling and Chris Kennedy for their help with the 3D rod-tracking code, Tiansong Deng for sharing his unpublished results and thoughts on silica-coating, OTMS functionalisation and supra-particle synthesis, and Marijn van Huis and Jovana Zečević for their supervision of my literature review on electron tomography, that was of great use for this thesis.

Finally, there were many people that contributed to the wonderful atmosphere and the great interdisciplinary working environment, which is arguably as important as the research itself. I want to thank all staff and PhD students of the SCM and ICC groups for making me feel welcome, for all the

nice talks we had and of course all the cookies and cake. To all the students and ex-students of the old and new student room: thank you so much! Marjolein, Barbera, Albert, thanks for keeping me company and all the fun we had during the first half of my thesis! Mayke, Rutger, Dido, Bertjan, Robin, Steyn, for conversations, table football, nice lunches and occasionally putting up with my rambling about research. Michel, for the banana desktop and other computer related help (and of course all of the above). Gideon, my former desk buddy, for all the nice talks and deep conversations on image analysis, order parameters and deadlines. Special thanks of course to Tom, for not just being a great guy but also working closely together (literally and thematically) throughout the project and all the discussions on nanorods, alloying, TEM and other things over the past 17 months. And *extra* special thanks to Heleen, for all of your *extra* nice comments. And thank you caffeine, because without you this thesis could not have existed.

Bibliography

[1] A. Johnson and B. Francis, *Durability of metals from archaeological objects, metal meteorites, and native metals*. Pacific Northwest Laboratory, 1980.

[2] A. Laguna, *Modern supramolecular gold chemistry: gold-metal interactions and applications*. John Wiley & Sons, 2008.

[3] E. Roduner, "Size matters: why nanomaterials are different.," *Chemical Society reviews*, vol. 35, no. 7, pp. 583–592, 2006.

[4] S. Eustis and M. a. El-Sayed, "Why gold nanoparticles are more precious than pretty gold: noble metal surface plasmon resonance and its enhancement of the radiative and nonradiative properties of nanocrystals of different shapes.," *Chemical Society reviews*, vol. 35, no. 3, pp. 209–217, 2006.

[5] C. Burda, X. Chen, R. Narayanan, and M. A. El-Sayed, "Chemistry and properties of nanocrystals of different shapes," *Chemical Reviews*, vol. 105, no. 4, pp. 1025–1102, 2005.

[6] I. Freestone, N. Meeks, M. Sax, and C. Higgit, "The Lycurgus Cup - A Roman Nanotechnology," *Gold Bulletin*, vol. 40, no. 4, pp. 270–277, 2007.

[7] C. J. Murphy, T. K. Sau, A. M. Gole, C. J. Orendorff, J. Gao, L. Gou, S. E. Hunyadi, and T. Li, "Anisotropic metal nanoparticles: Synthesis, assembly, and optical applications," *Journal of Physical Chemistry B*, vol. 109, no. 29, pp. 13857–13870, 2005.

[8] S. E. Lohse and C. J. Murphy, "The quest for shape control: A history of gold nanorod synthesis," *Chemistry of Materials*, vol. 25, no. 8, pp. 1250–1261, 2013.

[9] H. Chen, L. Shao, Q. Li, and J. Wang, "Gold nanorods and their plasmonic properties," *Chemical Society reviews*, vol. 42, no. 7, pp. 2679–2724, 2013.

[10] J.-H. Liu Wang, A.-Q., Chin, Y.-S., Lin, H.-P. and Mou, C.-Y., J. H. Liu, A. Q. Wang, Y. S. Chi, H. P. Lin, and C. Y. Mou, "Synergistic effect in an Au-Ag alloy nanocatalyst: CO oxidation," *Journal of Physical Chemistry B*, vol. 109, no. 1, pp. 40–43, 2005.

[11] A. S. K. Hashmi and G. J. Hutchings, "Gold Catalysis," *Angewandte Chemie - International Edition*, vol. 45, no. 47, pp. 7896–7936, 2006.

[12] B. K. Min and C. M. Friend, "Heterogeneous gold-based catalysis for green chemistry: Low-temperature CO oxidation and propene oxidation," *Chemical Reviews*, vol. 107, no. 6, pp. 2709–2724, 2007.

[13] Y. Mikami, A. Dhakshinamoorthy, M. Alvaro, and H. García, "Catalytic activity of unsupported gold nanoparticles," *Catal. Sci. Technol.*, vol. 3, no. 1, pp. 58–69, 2013.

[14] P. Priecel, H. Adekunle Salami, R. H. Padilla, Z. Zhong, and J. A. Lopez-Sanchez, "Anisotropic gold nanoparticles: Preparation and applications in catalysis," *Chinese Journal of Catalysis*, vol. 37, no. 10, pp. 1619–1650, 2016.

[15] X. Guo, Q. Zhang, Y. Sun, Q. Zhao, and J. Yang, "Lateral Etching of Core-Shell Au@Metal Nanorods to Metal-Tipped Au Nanorods with Improved Catalytic Activity," *American Chemical Society*, no. 2, pp. 1165–1175, 2012.

[16] S. Linic, U. Aslam, C. Boerigter, and M. Morabito, "Photochemical transformations on plasmonic metal nanoparticles," *Nature Materials*, vol. 14, no. 6, pp. 567–576, 2015.

[17] A. N. Bashkatov, E. A. Genina, V. I. Kochubey, and V. V. Tuchin, "Optical properties of human skin, subcutaneous and mucous tissues in the wavelength range from 400 to 2000 nm," *J. Phys. D: Appl. Phys*, vol. 38, pp. 2543–2555, 2005.

[18] A. M. Smith, M. C. Mancini, and S. Nie, "Bioimaging: second window for in vivo imaging," *Nature Nanotechnology*, vol. 4, no. 11, pp. 710–711, 2009.

[19] X. Huang, I. H. El-Sayed, W. Qian, and M. A. El-Sayed, "Cancer cell imaging and photothermal therapy in the near-infrared region by using gold nanorods," *J. Am. Chem. Soc.*, vol. 128, no. 6, pp. 2115–2120, 2006.

[20] X. Huang, S. Neretina, and M. A. El-Sayed, "Gold nanorods: From synthesis and properties to biological and biomedical applications," *Advanced Materials*, vol. 21, no. 48, pp. 4880–4910, 2009.

[21] K. Haume, S. Rosa, S. Grellet, M. Smialek, K. Butterworth, A. Solov'yov, K. Prise, J. Golding, and N. Mason, "Gold nanoparticles for cancer radiotherapy: a review," *Cancer Nano*, vol. 7, no. 8, 2016.

[22] X. Wu, J. Y. Chen, A. Brech, C. Fang, J. Wang, P. J. Helm, and Q. Peng, "The use of femtosecond lasers to trigger powerful explosions of gold nanorods to destroy cancer cells," *Biomaterials*, vol. 34, no. 26, pp. 6157–6162, 2013.

[23] W. I. Choi, A. Sahu, Y. H. Kim, and G. Tae, "Photothermal cancer therapy and imaging based on gold nanorods," *Annals of biomedical engineering*, vol. 40, no. 2, pp. 534–546, 2012.

[24] S. T. Sivapalan, B. M. Devetter, T. K. Yang, T. Van Dijk, M. V. Schulmerich, P. S. Carney, R. Bhargava, and C. J. Murphy, "Off-resonance surface-enhanced raman spectroscopy from gold nanorod suspensions as a function of aspect ratio: Not what we thought," *ACS Nano*, vol. 7, no. 3, pp. 2099–2105, 2013.

[25] P. Wang, L. Zhang, Y. Xia, L. Tong, X. Xu, and Y. Ying, "Polymer nanofibers embedded with aligned gold nanorods: A new platform for plasmonic studies and optical sensing," *Nano Letters*, vol. 12, no. 6, pp. 3145–3150, 2012.

[26] P. Zijlstra, J. W. M. Chon, and M. Gu, "Five-dimensional optical recording mediated by surface plasmons in gold nanorods," *Nature*, vol. 459, pp. 410–413, 2009.

[27] I. Venditti, "Gold Nanoparticles in Photonic Crystals Applications: A Review," *Materials*, vol. 10, no. 2, p. 97, 2017.

[28] D. Fava, Z. Nie, M. A. Winnik, and E. Kumacheva, "Evolution of Self-Assembled Structures of Polymer-Terminated Gold Nanorods in Selective Solvents," *Advanced Materials*, vol. 20, no. 22, pp. 4318–4322, 2008.

[29] L. Vigderman, B. P. Khanal, and E. R. Zubarev, "Functional Gold Nanorods: Synthesis, Self-Assembly, and Sensing Applications," *Advanced Materials*, vol. 24, no. 36, pp. 4811–4841, 2012.

[30] C. Hamon, S. M. Novikov, L. Scarabelli, D. M. Solís, T. Altantzis, S. Bals, J. M. Taboada, F. Obelleiro, and L. M. Liz-Marzán, "Collective Plasmonic Properties in Few-Layer Gold Nanorod Supercrystals," *ACS Photonics*, vol. 2, no. 10, pp. 1482–1488, 2015.

[31] L. S. Slaughter, Y. Wu, B. A. Willingham, P. Nordlander, and S. Link, "Effects of symmetry breaking and conductive contact on the plasmon coupling in gold nanorod dimers," *ACS Nano*, vol. 4, no. 8, pp. 4657–4666, 2010.

[32] A. M. Funston, C. Novo, T. J. Davis, and P. Mulvaney, "Plasmon coupling of gold nanorods at short distances and in different geometries," *Nano Letters*, vol. 9, no. 4, pp. 1651–1658, 2009.

[33] L. Scarabelli, C. Hamon, and L. M. Liz-Marzán, "Design and Fabrication of Plasmonic Nanomaterials Based on Gold Nanorod Supercrystals," *Chemistry of Materials*, p. acs.chemmater.6b02439, 2016.

[34] T.-S. Deng, J. E. S. van der Hoeven, A. O. Yalcin, H. W. Zandbergen, M. A. van Huis, and A. van Blaaderen, "Oxidative Etching and Metal Overgrowth of Gold Nanorods within Mesoporous Silica Shells," *Chemistry of Materials*, no. 27, pp. 7196–7203, 2015.

[35] C. Gao, Y. Hu, M. Wang, M. Chi, and Y. Yin, "Fully alloyed Ag/Au nanospheres: Combining the plasmonic property of Ag with the stability of Au," *Journal of the American Chemical Society*, vol. 136, no. 20, pp. 7474–7479, 2014.

[36] W. Albrecht, J. E. van der Hoeven, T.-S. Deng, P. E. de Jongh, and A. van Blaaderen, "Fully alloyed metal nanorods with highly tunable properties," *Nanoscale*, vol. 9, no. 8, pp. 2845–2851, 2017.

[37] D. B. Williams and C. B. Carter, *The Transmission Electron Microscope*. New York: Springer Science+Business Media, 2 ed., 2009.

[38] E. Jensen, "Example: Transmission Electron Microscope System," 2012. Retrieved from: http://texsample.net (02-11-2016). Licensed under Creative Commons BY 2.5.

[39] F. L. Deepak, A. Mayoral, and R. Arenal, *Advanced Transmission Electron Microscopy: Applications to Nanomaterials*. Springer International Publishing, 2015.

[40] M. A. van Huis and H. Friedrich, "Electron microscopy techniques," in *Nanoparticles: workhorses of nanoscience* (C. de Mello Donega, ed.), ch. 7, pp. 191–221, Berlin Heidelberg: Springer-Verlag, 2014.

[41] C. S. Kumar, *Transmission Electron Microscopy Characterization of Nanomaterials*. Springer, 2014.

[42] G. Möbus, R. C. Doole, and B. J. Inkson, "Spectroscopic electron tomography," *Ultramicroscopy*, vol. 96, no. 3-4, pp. 433–451, 2003.

[43] C. J. Peddie and L. M. Collinson, "Exploring the third dimension: Volume electron microscopy comes of age," *Micron*, vol. 61, pp. 9–19, 2014.

[44] R. F. Egerton, P. Li, and M. Malac, "Radiation damage in the TEM and SEM," *Micron*, vol. 35, no. 6, pp. 399–409, 2004.

[45] A. Sali, R. Glaeser, T. Earnest, and W. Baumeister, "From words to literature in structural proteomics," *Nature*, vol. 422, no. 6928, pp. 216–225, 2003.

[46] J. Frank, *Electron tomography: Methods for three-dimensional visualization of structures in the cell.* Springer New York, 2 ed., 2006.

[47] M. Weyland, "Electron Tomography of Catalysts," *Topics in Catalysis*, vol. 21, no. 4, pp. 175–183, 2002.

[48] J. Zečević, K. P. de Jong, and P. E. de Jongh, "Progress in electron tomography to assess the 3D nanostructure of catalysts," *Current Opinion in Solid State and Materials Science*, vol. 17, no. 3, pp. 115–125, 2013.

[49] M. Hayashida and M. Malac, "Practical electron tomography guide: Recent progress and future opportunities," *Micron*, vol. 91, pp. 49–74, 2016.

[50] M. Bransen, M. A. van Huis, and J. Zečević, "3D characterisation of nanomaterials by electron tomography," 2016. Literature study. Available on request.

[51] C. Sönnichsen, T. Franzl, T. Wilk, G. von Plessen, J. Feldmann, O. Wilson, and P. Mulvaney, "Drastic reduction of plasmon damping in gold nanorods," *Physical review letters*, vol. 88, no. 7, p. 077402, 2002.

[52] O. Benson, "Assembly of hybrid photonic architectures from nanophotonic constituents," *Nature*, vol. 480, no. 7376, pp. 193–199, 2011.

[53] A. Moores and F. Goettmann, "The plasmon band in noble metal nanoparticles: an introduction to theory and applications," *New Journal of Chemistry*, vol. 30, no. 8, pp. 1121–1132, 2006.

[54] M. G. Blaber, M. D. Arnold, and M. J. Ford, "A review of the optical properties of alloys and intermetallics for plasmonics," *Journal of Physics: Condensed ...*, vol. 22, no. 14, p. 143201, 2010.

[55] K. A. Willets and R. P. V. Duyne, "Localized Surface Plasmon Resonance Spectroscopy and Sensing," *The annual review of physical chemistry*, vol. 58, pp. 267–297, 2007.

[56] M. Hu, J. Chen, Z.-Y. Li, L. Au, G. V. Hartland, X. Li, M. Marquez, Y. Xia, and M. Hu, "Gold nanostructures: engineering their plasmonic properties for biomedical applications.," *Chemical Society reviews*, vol. 35, no. 11, pp. 1084–1094, 2006.

[57] W. Ni, X. Kou, Z. Yang, and J. Wang, "Tailoring longitudinal surface plasmon wavelengths, scattering and absorption cross sections of gold nanorods," *ACS Nano*, vol. 2, no. 4, pp. 677–686, 2008.

[58] S. Link, M. B. Mohamed, and M. A. El-Sayed, "Simulation of the Optical Absorption Spectra of Gold Nanorods as a Function of Their Aspect Ratio and the Effect of the Medium Dielectric Constant," *The Journal of Physical Chemistry B*, vol. 103, no. 16, pp. 3073–3077, 1999.

[59] S. W. Prescott and P. Mulvaney, "Gold nanorod extinction spectra," *Journal of Applied Physics*, vol. 99, no. 12, 2006.

[60] A. Brioude, X. C. Jiang, and M. P. Pileni, "Optical properties of gold nanorods: DDA simulations supported by experiments," *Journal of Physical Chemistry B*, vol. 109, no. 27, pp. 13138–13142, 2005.

[61] R. L. Olmon, B. Slovick, T. W. Johnson, D. Shelton, S.-H. Oh, G. D. Boreman, and M. B. Raschke, "Optical dielectric function of gold," *Physical Review B*, vol. 86, no. 23, p. 235147, 2012.

[62] P.-G. De Gennes and J. Prost, *The physics of liquid crystals.* Oxford University press, 1995.

[63] T. H. Besseling, M. Hermes, A. Kuijk, B. de Nijs, T. S. Deng, M. Dijkstra, A. Imhof, and A. van Blaaderen, "Determination of the positions and orientations of concentrated rod-like colloids from 3D microscopy data," *Journal of Physics: Condensed Matter*, vol. 194109, pp. 1–12, 2014.

[64] P. Oswald and P. Pieranski, *Smectic and columnar liquid crystals: concepts and physical properties illustrated by experiments.* CRC Press, 2005.

[65] P. Bolhuis and D. Frenkel, "Tracing the phase boundaries of hard spherocylinders," *The Journal of chemical physics*, vol. 106, no. 2, pp. 666–687, 1997.

[66] A. Kuijk, D. V. Byelov, A. V. Petukhov, A. van Blaaderen, and A. Imhof, "Phase behavior of colloidal silica rods," *Faraday discussions*, vol. 159, no. 1, pp. 181–199, 2012.

[67] E. M. Kramer and J. Herzfeld, "Avoidance model for soft particles. ii. positional ordering of charged rods," *Physical Review E*, vol. 61, no. 6, p. 6872, 2000.

[68] M. A. Bates and D. Frenkel, "Influence of polydispersity on the phase behavior of colloidal liquid crystals: A monte carlo simulation study," *The Journal of chemical physics*, vol. 109, no. 14, pp. 6193–6199, 1998.

[69] A. M. Bohle, R. Hołyst, and T. Vilgis, "Polydispersity and ordered phases in solutions of rodlike macromolecules," *Physical review letters*, vol. 76, no. 8, p. 1396, 1996.

[70] M. Grzelczak, J. Pérez-Juste, P. Mulvaney, and L. M. Liz-Marzán, "Shape Control in Gold Nanoparticle Synthesis," *Chemical Society Review*, vol. 37, no. 9, pp. 1783–1791, 2008.

[71] C. J. Murphy, L. B. Thompson, D. J. Chernak, J. A. Yang, S. T. Sivapalan, S. P. Boulos, J. Huang, A. M. Alkilany, and P. N. Sisco, "Gold nanorod crystal growth: From seed-mediated synthesis to nanoscale sculpting," *Current Opinion in Colloid and Interface Science*, vol. 16, no. 2, pp. 128–134, 2011.

[72] L. Vigderman and E. R. Zubarev, "High-yield synthesis of gold nanorods with longitudinal SPR peak greater than 1200 nm using hydroquinone as a reducing agent," *Chemistry of Materials*, vol. 25, no. 8, pp. 1450–1457, 2013.

[73] Q. Zhang, L. Han, H. Jing, D. A. Blom, Y. Lin, H. L. Xin, and H. Wang, "Facet Control of Gold Nanorods," *ACS Nano*, vol. 10, no. 2, pp. 2960–2974, 2016.

[74] X. Ye, C. Zheng, J. Chen, Y. Gao, and C. B. Murray, "Using binary surfactant mixtures to simultaneously improve the dimensional tunability and monodispersity in the seeded growth of gold nanorods," *Nano Letters*, vol. 13, no. 2, pp. 765–771, 2013.

[75] B. Nikoobakht, Z. L. Wang, and M. A. El-Sayed, "Self-Assembly of Gold Nanorods," *J. Phys. Chem. B*, vol. 104, no. 36, pp. 8635–8640, 2000.

[76] B. Goris, S. Bals, W. Van den Broek, E. Carbó-Argibay, S. Gómez-Graña, L. M. Liz-Marzán, and G. Van Tendeloo, "Atomic-scale determination of surface facets in gold nanorods," *Nature Materials*, vol. 11, pp. 930–935, 2012.

[77] E. Carbó-Argibay, B. Rodríguez-González, S. Gómez-Graña, A. Guerrero-Martínez, I. Pastoriza-Santos, J. Pérez-Juste, and L. M. Liz-Marzán, "The crystalline structure of gold nanorods revisited: Evidence for higher-index lateral facets," *Angewandte Chemie - International Edition*, vol. 49, no. 49, pp. 9397–9400, 2010.

[78] L. S, A. Sánchez-Iglesias, J. Pérez-Juste, and L. M. Liz-Marzán, "A "Tips and Tricks" Practical Guide to the Synthesis of Gold Nanorods," *Journal of Physical Chemistry Letters*, vol. 6, no. 21, pp. 4270–4279, 2015.

[79] N. R. Jana, "Gram-Scale Synthesis of Soluble, Near-Monodisperse Gold Nanorods and Other Anisotropic Nanoparticles," *Small*, vol. 1, no. 8-9, pp. 875–882, 2005.

[80] M. Liu and P. Guyot-Sionnest, "Mechanism of silver(I)-assisted growth of gold nanorods and bipyramids," *Journal of Physical Chemistry B*, vol. 109, no. 47, pp. 22192–22200, 2005.

[81] B. Nikoobakht and M. A. El-Sayed, "Preparation and growth mechanism of gold nanorods (NRs) using seed-mediated growth method," *Chemistry of Materials*, vol. 15, no. 10, pp. 1957–1962, 2003.

[82] C. J. Murphy, L. B. Thompson, A. M. Alkilany, P. N. Sisco, S. P. Boulos, S. T. Sivapalan, J. A. Yang, D. J. Chernak, and J. Huang, "The many faces of gold nanorods," *Journal of Physical Chemistry Letters*, vol. 1, no. 19, pp. 2867–2875, 2010.

[83] W. Tong, M. J. Walsh, P. Mulvaney, J. Etheridge, and A. M. Funston, "Control of symmetry breaking size and aspect ratio in gold nanorods: Underlying role of silver nitrate," *The Journal of Physical Chemistry C*, 2017.

[84] S. R. Jackson, J. R. McBride, S. J. Rosenthal, and D. W. Wright, "Where's the Silver? Imaging Trace Silver Coverage on the Surface of Gold Nanorods.," *Journal of the American Chemical Society*, vol. 136, no. 14, pp. 5261–3, 2014.

[85] G. Gramlich, J. Zhang, and W. M. Nau, "Increased antioxidant reactivity of vitamin C at low pH in model membranes," *Journal of the American Chemical Society*, vol. 124, no. 38, pp. 11252–11253, 2002.

[86] D. K. Smith and B. A. Korgel, "The importance of the CTAB surfactant on the colloidal seed-mediated synthesis of gold nanorods," *Langmuir*, vol. 24, no. 3, pp. 644–649, 2008.

[87] D. K. Smith, N. R. Miller, and B. A. Korgel, "Iodide in ctab prevents gold nanorod formation," *Langmuir*, vol. 25, no. 16, pp. 9518–9524, 2009.

[88] R. G. Rayavarapu, C. Ungureanu, P. Krystek, T. G. Van Leeuwen, and S. Manohar, "Iodide impurities in hexadecyltrimethylammonium bromide (CTAB) products: Lot-lot variations and influence on gold nanorod synthesis," *Langmuir*, vol. 26, no. 7, pp. 5050–5055, 2010.

[89] D. Shajari, A. Bahari, P. Gill, and M. Mohseni, "Synthesis and tuning of gold nanorods with surface plasmon resonance," *Optical Materials*, vol. 64, pp. 376–383, 2017.

[90] H.-y. Wu, H.-c. Chu, T.-J. Kuo, C.-l. Kuo, and M. H. Huang, "Seed-Mediated Synthesis of High Aspect Ratio Gold Nanorods with Nitric Acid," *Chemistry of Materials*, vol. 17, no. 25, pp. 6447–6451, 2005.

[91] H. Y. Wu, W. L. Huang, and M. H. Huang, "Direct high-yield synthesis of high aspect ratio gold nanorods," *Crystal Growth & Design*, vol. 7, no. 4, pp. 831–835, 2007.

[92] X. Xu, Y. Zhao, X. Xue, S. Huo, F. Chen, G. Zou, and X.-J. Liang, "Seedless synthesis of high aspect ratio gold nanorods with high yield," *Journal of Materials Chemistry A*, vol. 2, no. 10, p. 3528, 2014.

[93] V. Sharma, K. Park, and M. Srinivasarao, "Shape separation of gold nanorods using centrifugation.," *Proceedings of the National Academy of Sciences of the United States of America*, vol. 106, no. 13, pp. 4981–5, 2009.

[94] P. Qiu and C. Mao, "Viscosity Gradient as a Novel Mechanism for the Centrifugation-Based Separation of Nanoparticles," *Advanced Materials*, no. 23, pp. 4880–4885, 2011.

[95] B. Xiong, J. Cheng, Y. Qiao, R. Zhou, Y. He, and E. S. Yeung, "Separation of nanorods by density gradient centrifugation.," *Journal of chromatography. A*, vol. 1218, no. 25, pp. 3823–9, 2011.

[96] K. Park, H. Koerner, and R. A. Vaia, "Depletion-induced shape and size selection of gold nanoparticles," *Nano Letters*, vol. 10, no. 4, pp. 1433–1439, 2010.

[97] B. P. Khanal and E. R. Zubarev, "Purification of High Aspect Ratio Gold Nanorods: Complete Removal of Platelets Bishnu P. Khanal and Eugene R. Zubarev*," *Journal of the American Chemical Society*, vol. 130, no. 38, pp. 1–7, 2010.

[98] W. C. Wu and J. B. Tracy, "Large-scale silica overcoating of gold nanorods with tunable shell thicknesses," *Chemistry of Materials*, vol. 27, no. 8, pp. 2888–2894, 2015.

[99] I. E. Sendroiu, M. E. Warner, and R. M. Corn, "Fabrication of silica-coated gold nanorods functionalized with DNA for enhanced surface plasmon resonance imaging biosensing applications," *Langmuir*, vol. 25, no. 19, pp. 11282–11284, 2009.

[100] I. Pastoriza-Santos, J. Pérez-Juste, and L. M. Liz-Marzán, "Silica-coating and hydrophobation of CTAB-stabilized gold nanorods," *Chemistry of Materials*, vol. 18, no. 10, pp. 2465–2467, 2006.

[101] E. Gergely-Fülöp, D. Zámbó, and A. Deák, "Thermal stability of mesoporous silica-coated gold nanorods with different aspect ratios," *Materials Chemistry and Physics*, vol. 148, pp. 909–913, 2014.

[102] C. Gao, Q. Zhang, Z. Lu, and Y. Yin, "Templated synthesis of metal nanorods in silica nanotubes," *Journal of the American Chemical Society*, vol. 133, pp. 19706–19709, 2011.

[103] E. Gergely-Fülöp, N. Nagy, and A. Deák, "Reversible shape transition: Plasmonic nanorods in elastic nanocontainers," *Materials Chemistry and Physics*, vol. 141, no. 1, pp. 343–347, 2013.

[104] M. N. Sanz-Ortiz, K. Sentosun, S. Bals, and L. M. Liz-Marzán, "Templated Growth of Surface Enhanced Raman Scattering-Active Branched Gold Nanoparticles within Radial Mesoporous Silica Shells," *ACS Nano*, vol. 9, no. 10, pp. 10489–10497, 2015.

[105] W. Liu, Z. Zhu, K. Deng, Z. Li, Y. Zhou, H. Qiu, Y. Gao, S. Che, and Z. Tang, "Gold nanorod@Chiral mesoporous silica core-shell nanoparticles with unique optical properties," *Journal of the American Chemical Society*, vol. 135, no. 26, pp. 9659–9664, 2013.

[106] J. F. Li, X. D. Tian, S. B. Li, J. R. Anema, Z. L. Yang, Y. Ding, Y. F. Wu, Y. M. Zeng, Q. Z. Chen, B. Ren, Z. L. Wang, and Z. Q. Tian, "Surface analysis using shell-isolated nanoparticle-enhanced Raman spectroscopy.," *Nature protocols*, vol. 8, no. 1, pp. 52–65, 2013.

[107] T.-S. Deng, "Supraparticles of AuNRs." Manuscript in preparation.

[108] I. Gorelikov and N. Matsuura, "Single-Step Coating of Mesoporous Silica on CTAB- Capped Nanoparticles," *Nano letters*, vol. 8, pp. 369–373, 2008.

[109] R. I. Nooney, D. Thirunavukkarasu, Y. Chen, R. Josephs, and A. E. Ostafin, "Self-assembly of mesoporous nanoscale silica/gold composites," *Langmuir*, vol. 19, no. 18, pp. 7628–7637, 2003.

[110] N. S. Abadeer, M. R. Brennan, W. L. Wilson, and C. J. Murphy, "Distance and plasmon wavelength dependent fluorescence of molecules bound to silica-coated gold nanorods," *ACS Nano*, vol. 8, no. 8, pp. 8392–8406, 2014.

[111] A. Cifuentes, J. L. Bernal, and J. C. Diez-Masa, "Determination of critical micelle concentration values using capillary electrophoresis instrumentation," *Analytical Chemistry*, vol. 69, no. 20, pp. 4271–4274, 1997.

[112] S. Besson, T. Gacoin, C. Ricolleau, C. Jacquiod, and J.-P. Boilot, "Phase diagram for mesoporous CTAB-silica films prepared under dynamic conditions," *Journal of Materials Chemistry*, vol. 13, no. 2, pp. 404–409, 2002.

[113] L. Liz-Marzán, M. Giersig, and P. Mulvaney, "Synthesis of Nanosized Gold - Silica Core - Shell Particles," *Langmuir*, vol. 7463, no. 5, pp. 4329–4335, 1996.

[114] W. E. Doering and S. Nie, "Spectroscopic Tags Using Dye-Embedded Nanoparticles and Surface-Enhanced Raman Scattering," *Analytical Chemistry*, vol. 75, no. 22, pp. 6171–6176, 2003.

[115] J. F. Li, Y. F. Huang, Y. Ding, Z. L. Yang, S. B. Li, X. S. Zhou, F. R. Fan, W. Zhang, Z. Y. Zhou, D. Y. Wu, B. Ren, Z. L. Wang, and Z. Q. Tian, "Shell-isolated nanoparticle-enhanced Raman spectroscopy," *Nature*, vol. 464, no. 7287, pp. 392–395, 2010.

[116] J. Nordström, E. Nilsson, P. Jarvol, M. Nayeri, A. Palmqvist, J. Bergenholtz, A. Matic, and A. Tic, "Concentration- and pH-dependence of highly alkaline sodium silicate solutions," *Journal of Colloid and Interface Science*, vol. 356, no. 1, pp. 37–45, 2011.

[117] W. Stöber, A. Fink, and E. Bohn, "Controlled growth of monodisperse silica spheres in the micron size range," *Journal of colloid and interface science*, vol. 26, no. 1, pp. 62–69, 1968.

[118] G. Guisbiers, R. Mendoza-Cruz, L. Bazán-Díaz, J. J. Velázquez-Salazar, R. Mendoza-Perez, J. A. Robledo-Torres, J.-L. Rodriguez-Lopez, J. M. Montejano-Carrizales, R. L. Whetten, and M. José-Yacamán, "Electrum, the GoldâĂŞSilver Alloy, from the Bulk Scale to the Nanoscale: Synthesis, Properties, and Segregation Rules," *ACS Nano*, p. acsnano.5b05755, 2015.

[119] C. Wang, S. Peng, R. Chan, and S. Sun, "Synthesis of AuAg alloy nanoparticles from core/shell-structured Ag/Au," *Small*, vol. 5, no. 5, pp. 567–570, 2009.

[120] X. Li, Y. Yang, G. Zhou, S. Han, W. Wang, L. Zhang, W. Chen, C. Zou, and S. Huang, "The unusual effect of AgNO3 on the growth of Au nanostructures and their catalytic performance.," *Nanoscale*, vol. 5, no. 11, pp. 4976–85, 2013.

[121] H. Jiang, T. Akita, and T. Ishida, "Synergistic catalysis of Au@Ag core-shell nanoparticles stabilized on metal-organic framework," *Journal of the American Chemical Society*, vol. 133, pp. 1304–1306, 2011.

[122] Y. Okuno, K. Nishioka, A. Kiya, N. Nakashima, A. Ishibashi, and Y. Niidome, "Uniform and controllable preparation of Au-Ag core-shell nanorods using anisotropic silver shell formation on gold nanorods.," *Nanoscale*, vol. 2, no. 8, pp. 1489–1493, 2010.

[123] F. Wang, S. Cheng, Z. Bao, and J. Wang, "Anisotropic overgrowth of metal heterostructures induced by a site-selective silica coating," *Angewandte Chemie - International Edition*, vol. 52, no. 39, pp. 10344–10348, 2013.

[124] G. Rothenberg, *Catalysis: concepts and green applications*. John Wiley & Sons, 2015.

[125] S. B. Nimse and D. Pal, "Free radicals, natural antioxidants, and their reaction mechanisms," *Royal Society of Chemistry*, vol. 5, no. 35, pp. 27986–28006, 2015.

[126] H. Borsook and G. Keighley, "Oxidation-reduction potential of ascorbic acid (Vitamin C)," *Proc. Natl. Acad. Sci. U. S. A.*, vol. 19, no. Vitamin C, pp. 875–878, 1933.

[127] M. J. O'Neil, *The Merck index: an encyclopedia of chemicals, drugs, and biologicals*. RSC Publishing, 2013.

[128] J. J. Ruiz, A. Aldaz, and M. Dominguez, "Mechanism of L-ascorbic acid oxidation and dehydro-L-ascorbic acid reduction on a mercury electrode. I. Acid medium," *Canadian Journal of Chemistry*, vol. 55, pp. 2799–2806, 1977.

[129] G. Alexander, W. Heston, and R. Iler, "The solubility of amorphous silica in water," *J. Phys. Chem.*, vol. 58, no. 6, pp. 453–455, 1954.

[130] V. Ozolins, C. Wolverton, and A. Zunger, "Cu-Au, Ag-Au, Cu-Ag, and Ni-Au intermetallics: First-principles study of temperature-composition phase diagrams and structures," *Physical Review B*, vol. 57, no. 11, pp. 6427–6443, 1998.

[131] K. Fitzner, Q. Guo, J. Wang, and O. J. Kleppa, "Enthalpies of liquid-liquid mixing in the systems Cu-Ag, Cu-Au and Ag-Au by using an in-situ mixing device in a high temperature single-unit differential calorimeter," *Journal of Alloys and Compounds*, vol. 291, no. 1-2, pp. 190–200, 1999.

[132] R. Ferrando, J. Jellinek, and R. L. Johnston, "Nanoalloys: From theory to applications of alloy clusters and nanoparticles," *Chemical Reviews*, vol. 108, no. 3, pp. 845–910, 2008.

[133] W. Qi and S. Lee, "Phase stability, melting, and alloy formation of Au-Ag bimetallic nanoparticles," *The Journal of Physical Chemistry C*, vol. 114, pp. 9580–9587, 2010.

[134] S. C. Yeo, D. H. Kim, K. Shin, and H. M. Lee, "Phase diagram and structural evolution of Ag-Au bimetallic nanoparticles: molecular dynamics simulations.," *Physical chemistry chemical physics : PCCP*, vol. 14, no. 8, pp. 2791–6, 2012.

[135] K. Liu, Y. Bai, L. Zhang, Z. Yang, Q. Fan, H. Zheng, Y. Yin, and C. Gao, "Porous Au-Ag Nanospheres with High-Density and Highly Accessible Hotspots for SERS Analysis," *Nano Letters*, vol. 4, p. acs.nanolett.6b00868, 2016.

[136] D. R. Lide, *CRC Handbook of Chemistry and Physics, Internet Version*. Boca Raton, Florida: CRC Press, 2005.

[137] H. J. Bi, W. P. Cai, C. X. Kan, L. D. Zhang, D. Martin, and F. Trager, "Optical study of redox process of Ag nanoparticles at high temperature," *Journal of applied physics*, vol. 92, no. 12, pp. 7491–7497, 2002.

[138] J. Hu, W. Cai, H. Zeng, C. Li, and F. Sun, "Substrate dependent surface plasmon resonance evolution of ag nanoparticles treated in atmospheres," *Journal of Physics: Condensed Matter*, vol. 18, no. 23, p. 5415, 2006.

[139] D. Wang and P. Schaaf, "Nanoporous gold nanoparticles," *Journal of Materials Chemistry*, vol. 22, no. 12, pp. 5344–5348, 2012.

[140] T. Fujita, P. Guan, K. McKenna, X. Lang, A. Hirata, L. Zhang, T. Tokunaga, S. Arai, Y. Yamamoto, N. Tanaka, Y. Ishikawa, N. Asao, Y. Yamamoto, J. Erlebacher, and M. Chen, "Atomic origins of the high catalytic activity of nanoporous gold," *Nature Materials*, vol. 11, no. 9, pp. 775–780, 2012.

[141] C. L. Bracey, P. R. Ellis, and G. J. Hutchings, "Application of copper-gold alloys in catalysis: current status and future perspectives," *Chemical Society reviews*, vol. 38, no. 8, pp. 2231–2243, 2009.

[142] A. Henkel, A. Jakab, G. Brunklaus, and C. Sönnichsen, "Tuning plasmonic properties by alloying copper into gold nanorods," *Journal of Physical Chemistry C*, vol. 113, no. 6, pp. 2200–2204, 2009.

[143] S. Chen, S. V. Jenkins, J. Tao, Y. Zhu, and J. Chen, "Anisotropic seeded growth of Cu-M (M = Au, Pt, or Pd) bimetallic nanorods with tunable optical and catalytic properties," *Journal of Physical Chemistry C*, vol. 117, no. 17, pp. 8924–8932, 2013.

[144] C. H. Kuo, T. E. Hua, and M. H. Huang, "Au nanocrystal-directed growth of Au - Cu2O core - shell heterostructures with precise morphological control," *Journal of the American Chemical Society*, vol. 131, no. 49, pp. 17871–17878, 2009.

[145] B. Auguié and W. L. Barnes, "Collective resonances in gold nanoparticle arrays," *Physical review letters*, vol. 101, no. 14, p. 143902, 2008.

[146] B. D. Smith, D. J. Kirby, S. J. Boehm, and C. D. Keating, "Self-assembled binary mixtures of partially etched nanowires," *Particle and Particle Systems Characterization*, vol. 32, no. 3, pp. 347–354, 2015.

[147] M. a. Mahmoud, "Controlling the orientations of gold nanorods inside highly packed 2D arrays.," *Physical chemistry chemical physics : PCCP*, vol. 16, no. 47, pp. 26153–62, 2014.

[148] M. A. Bates and D. Frenkel, "Phase behavior of two-dimensional hard rod fluids," *Journal of Chemical Physics*, vol. 112, no. 22, pp. 10034–10041, 2000.

[149] T. K. Sau and C. J. Murphy, "Self-assembly patterns formed upon solvent evaporation of aqueous cetyltrimethylammonium bromide-coated gold nanoparticles of various shapes," *Langmuir*, vol. 21, no. 7, pp. 2923–2929, 2005.

[150] J. R. Kremer, D. N. Mastronarde, and J. R. McIntosh, "Computer visualization of three-dimensional image data using IMOD.," *Journal of structural biology*, vol. 116, no. 1, pp. 71–76, 1996.

[151] D. N. Mastronarde, "Dual-axis tomography: an approach with alignment methods that preserve resolution," *Journal of structural biology*, vol. 120, no. 3, pp. 343–352, 1997.

[152] D. N. Mastronarde and S. R. Held, "Automated tilt series alignment and tomographic reconstruction in imod," *Journal of Structural Biology*, 2016.

[153] W. van Aarle, W. J. Palenstijn, J. De Beenhouwer, T. Altantzis, S. Bals, K. J. Batenburg, and J. Sijbers, "The ASTRA Toolbox: A platform for advanced algorithm development in electron tomography.," *Ultramicroscopy*, vol. 157, pp. 35–47, 2015.

[154] W. V. Aarle, W. J. Palenstijn, J. Cant, E. Janssens, F. Bleichrodt, A. Dabravolski, J. D. Beenhouwer, K. J. Batenburg, and J. Sijbers, "Fast and Flexible X-ray Tomography Using the ASTRA Toolbox," *Optics Express*, vol. 24, no. 22, pp. 25129–25147, 2016.

[155] The MathWorks Inc., "MATLAB." Version 9.0.0 (R2016a), Natick, Massachusetts. 2016.

[156] D. Gentili, G. Ori, and M. Comes Franchini, "Double phase transfer of gold nanorods for surface functionalization and entrapment into PEG-based nanocarriers.," *Chemical communications (Cambridge, England)*, no. 39, pp. 5874–6, 2009.

[157] A. Wijaya and K. Hamad-Schifferli, "Ligand customization and DNA functionalization of gold nanorods via round-trip phase transfer ligand exchange," *Langmuir*, vol. 24, no. 18, pp. 9966–9969, 2008.

[158] B. Thierry, J. Ng, T. Krieg, and H. J. Griesser, "A robust procedure for the functionalization of gold nanorods and noble metal nanoparticles.," *Chemical communications (Cambridge, England)*, vol. 1, no. 13, pp. 1724–6, 2009.

[159] S. Suzuki, A. Nakajima, M. Sakai, J. H. Song, N. Yoshida, Y. Kameshima, and K. Okada, "Sliding acceleration of water droplets on a surface coated with fluoroalkylsilane and octadecyltrimethoxysilane," *Surface Science*, vol. 600, no. 10, pp. 2214–2219, 2006.

[160] H. Sugimura, A. Hozumi, T. Kameyama, and O. Takai, "Organosilane self-assembled monolayers formed at the vapour/solid interface," *Surface and Interface Analysis*, vol. 34, no. 1, pp. 550–554, 2002.

[161] M. Kamp, "Towards directional colloidal interactions," 2015. PhD thesis. Universiteit Utrecht.

[162] B. Liu, T. H. Besseling, M. Hermes, A. F. Demirörs, A. Imhof, and A. van Blaaderen, "Switching plastic crystals of colloidal rods with electric fields.," *Nature communications*, vol. 5, p. 3092, 2014.

[163] W. Wang, B. Gu, L. Liang, and W. Hamilton, "Fabrication of two-and three-dimensional silica nanocolloidal particle arrays," *The Journal of Physical Chemistry B*, vol. 107, no. 15, pp. 3400–3404, 2003.

[164] C. Schliehe, B. H. Juarez, M. Pelletier, S. Jander, D. Greshnykh, M. Nagel, A. Meyer, S. Foerster, A. Kornowski, C. Klinke, *et al.*, "Ultrathin pbs sheets by two-dimensional oriented attachment," *Science*, vol. 329, no. 5991, pp. 550–553, 2010.

[165] M. P. Boneschanscher, W. H. Evers, J. J. Geuchies, T. Altantzis, B. Goris, F. T. Rabouw, S. Van Rossum, H. S. van der Zant, L. D. Siebbeles, G. Van Tendeloo, *et al.*, "Long-range orientation and atomic attachment of nanocrystals in 2d honeycomb superlattices," *Science*, vol. 344, no. 6190, pp. 1377–1380, 2014.

[166] Z. Püspöki, M. Storath, D. Sage, and M. Unser, "Transforms and operators for directional bioimage analysis: A survey," in *Focus on Bio-Image Informatics*, pp. 69–93, Springer, 2016.

[167] C. A. Schneider, W. S. Rasband, and K. W. Eliceiri, "NIH Image to ImageJ: 25 years of image analysis," *Nature methods*, vol. 9, no. 7, pp. 671–675, 2012.

[168] J. Schindelin, C. T. Rueden, M. C. Hiner, and K. W. Eliceiri, "The ImageJ ecosystem: An open platform for biomedical image analysis," *Molecular reproduction and development*, vol. 82, no. 7-8, pp. 518–529, 2015.

[169] Wolfram Research Inc., "Mathematica." Version 10.1, Champaign, Illinois. 2015.

[170] B. de Nijs, S. Dussi, F. Smallenburg, J. D. Meeldijk, D. J. Groenendijk, L. Filion, A. Imhof, A. van Blaaderen, and M. Dijkstra, "Entropy-driven formation of large icosahedral colloidal clusters by spherical confinement.," *Nature materials*, vol. 14, pp. 56–60, 2015.

[171] B. de Nijs, "Towards crystals of crystals of nanocrystals: a self-assembly study," 2014. PhD thesis. Universiteit Utrecht.

[172] F. Bai, D. Wang, Z. Huo, W. Chen, L. Liu, X. Liang, C. Chen, X. Wang, Q. Peng, and Y. Li, "A versatile bottom-up assembly approach to colloidal spheres from nanocrystals," *Angewandte Chemie - International Edition*, vol. 46, no. 35, pp. 6650–6653, 2007.

[173] T. Wang, J. Zhuang, J. Lynch, O. Chen, Z. Z. Wang, X. Wang, D. LaMontagne, H. Wu, Z. Z. Wang, and Y. C. Cao, "Self-assembled colloidal superparticles from nanorods.," *Science (New York, N.Y.)*, vol. 338, no. 6105, pp. 358–63, 2012.

[174] W. Van den Broek, A. Rosenauer, B. Goris, G. T. Martinez, S. Bals, S. Van Aert, and D. Van Dyck, "Correction of non-linear thickness effects in HAADF STEM electron tomography," *Ultramicroscopy*, vol. 116, pp. 8–12, 2012.

[175] S. Bals, B. Goris, L. M. Liz-Marzán, and G. Van Tendeloo, "Three-dimensional characterization of noble-metal nanoparticles and their assemblies by electron tomography," *Angewandte Chemie - International Edition*, vol. 53, no. 40, pp. 10600–10610, 2014.

[176] D. Zanaga, F. Bleichrodt, T. Altantzis, N. Naomi Winckelmans, W. J. Palenstijn, J. Sijbers, B. van Nijs, M. van Huis, A. van Blaaderen, A. Sánchez-Iglesias, L. M. Liz-Marzan, J. Batenburg, S. Bals, and G. van Tendeloo, "Quantitative 3D analysis of huge nanoparticle assemblies," *Nanoscale*, no. 8, pp. 292–299, 2016.

[177] T. Sanders, M. Prange, C. Akatay, and P. Binev, "Physically motivated global alignment method for electron tomography," *Advanced Structural and Chemical Imaging*, vol. 1, no. 1, p. 4, 2015.

[178] M. C. Scott, C.-C. Chen, M. Mecklenburg, C. Zhu, R. Xu, P. Ercius, U. Dahmen, B. C. Regan, and J. Miao, "Electron tomography at 2.4-ångström resolution," *Nature*, vol. 483, no. 7390, pp. 444–447, 2012.

[179] K. J. Batenburg, S. Bals, J. Sijbers, C. Kübel, P. A. Midgley, J. C. Hernandez, U. Kaiser, E. R. Encina, E. A. Coronado, and G. Van Tendeloo, "3D imaging of nanomaterials by discrete tomography," *Ultramicroscopy*, vol. 109, no. 6, pp. 730–740, 2009.

[180] K. J. Batenburg and J. Sijbers, "DART: a practical reconstruction algorithm for discrete tomography.," *IEEE transactions on image processing : a publication of the IEEE Signal Processing Society*, vol. 20, no. 9, pp. 2542–2553, 2011.

[181] G. Van Tendeloo, S. Bals, S. Van Aert, J. Verbeeck, and D. Van Dyck, "Advanced electron microscopy for advanced materials," *Advanced Materials*, vol. 24, no. 42, pp. 5655–5675, 2012.

[182] B. Goris, W. Van den Broek, K. J. Batenburg, H. Heidari Mezerji, and S. Bals, "Electron tomography based on a total variation minimization reconstruction technique," *Ultramicroscopy*, vol. 113, pp. 120–130, 2012.

[183] B. Goris, T. Roelandts, K. J. Batenburg, H. Heidari Mezerji, and S. Bals, "Advanced reconstruction algorithms for electron tomography: From comparison to combination," *Ultramicroscopy*, vol. 127, pp. 40–47, 2013.

[184] T. Besseling, "Self-assembly of colloidal spheres and rods in external fields," 2014. PhD thesis. Universiteit Utrecht.

[185] C. Hamon, M. N. Sanz-Ortiz, E. Modin, E. Hill, L. Scarabelli, A. Chuvilin, and L. M. Liz-Marzan, "Hierarchical Organization and Molecular Diffusion in Gold Nanorod/Silica Supercrystal Nanocomposites," *Nanoscale*, pp. 7914–7922, 2016.

[186] M. N'Gom, S. Li, G. Schatz, R. Erni, A. Agarwal, N. Kotov, and T. B. Norris, "Electron-beam mapping of plasmon resonances in electromagnetically interacting gold nanorods," *Physical Review B*, vol. 80, no. 11, p. 113411, 2009.

[187] Y. Wu, G. Li, C. Cherqui, N. W. Bigelow, N. Thakkar, D. J. Masiello, J. P. Camden, and P. D. Rack, "Electron Energy Loss Spectroscopy Study of the Full Plasmonic Spectrum of Self-Assembled AuâĂŞAg Alloy Nanoparticles: Unraveling Size, Composition, and Substrate Effects," *ACS Photonics*, p. acsphotonics.5b00548, 2016.

[188] P. G. Van Rhee, P. Zijlstra, T. G. A. Verhagen, J. Aarts, M. I. Katsnelson, J. C. Maan, M. Orrit, and P. C. M. Christianen, "Giant magnetic susceptibility of gold nanorods detected by magnetic alignment," *Physical Review Letters*, vol. 111, no. 12, pp. 1–5, 2013.

[189] A. Hernando, A. Ayuela, P. Crespo, and P. M. Echenique, "Giant diamagnetism of gold nanorods," *New Journal of Physics*, vol. 16, 2014.

[190] B. M. van der Zande, G. J. Koper, and H. N. Lekkerkerker, "Alignment of rod-shaped gold particles by electric fields," *The Journal of Physical Chemistry B*, vol. 103, no. 28, pp. 5754–5760, 1999.

[191] W. Ahmed, E. S. Kooij, A. Van Silfhout, and B. Poelsema, "Quantitative analysis of gold nanorod alignment after electric field-assisted deposition," *Nano Letters*, vol. 9, no. 11, pp. 3786–3794, 2009.

[192] P. Zijlstra, M. van Stee, N. Verhart, Z. Gu, and M. Orrit, "Rotational diffusion and alignment of short gold nanorods in an external electric field.," *Physical chemistry chemical physics : PCCP*, vol. 14, no. 13, pp. 4584–8, 2012.

[193] A. Martin, C. Schopf, A. Pescaglini, A. O'Riordan, and D. Iacopino, "Synthesis, optical properties and self-assembly of gold nanorods," *Journal of Experimental Nanoscience*, vol. 7, no. 6, pp. 688–702, 2012.

[194] A. Pescaglini, A. O'Riordan, A. J. Quinn, and D. Iacopino, "Controlled assembly of Au nanorods into 1D architectures by electric field assisted deposition," *Journal of Materials Chemistry C*, vol. 2, no. 33, p. 6810, 2014.

[195] Q. Liu, Y. Cui, D. Gardner, X. Li, S. He, and I. I. Smalyukh, "Self-alignment of plasmonic gold nanorods in reconfigurable anisotropic fluids for tunable bulk metamaterial applications," *Nano Letters*, vol. 10, no. 4, pp. 1347–1353, 2010.

[196] C.-C. Cheng, M.-H. Liu, C.-Y. Mou, and Y.-F. Chen, "Controllable orientation of assembled gold nanorods on unstructured substrates," *RSC Advances*, vol. 3, no. 39, pp. 17696–17699, 2013.

[197] C. Kuemin, L. Nowack, L. Bozano, N. D. Spencer, and H. Wolf, "Oriented assembly of gold nanorods on the single-particle level," *Advanced Functional Materials*, vol. 22, no. 4, pp. 702–708, 2012.

[198] B. M. van der Zande, L. Pages, R. A. Hikmet, and A. van Blaaderen, "Optical properties of aligned rod-shaped gold particles dispersed in poly (vinyl alcohol) films," *The Journal of Physical Chemistry B*, vol. 103, no. 28, pp. 5761–5767, 1999.

[199] D. Vanmaekelbergh, L. K. Van Vugt, H. E. Bakker, F. T. Rabouw, B. D. Nijs, R. J. A. Van Dijk-Moes, M. A. Van Huis, P. J. Baesjou, and A. Van Blaaderen, "Shape-dependent multiexciton emission and whispering gallery modes in supraparticles of CdSe/multishell quantum dots," *ACS Nano*, vol. 9, no. 4, pp. 3942–3950, 2015.

[200] X. Ye, J. A. Millan, M. Engel, J. Chen, B. T. Diroll, S. C. Glotzer, and C. B. Murray, "Shape alloys of nanorods and nanospheres from self-assembly," *Nano Letters*, vol. 13, no. 10, pp. 4980–4988, 2013.

[201] Y. Nagaoka, T. Wang, J. Lynch, D. Lamontagne, and Y. C. Cao, "Binary assembly of colloidal semiconductor nanorods with spherical metal nanoparticles," *Small*, vol. 8, no. 6, pp. 843–846, 2012.

[202] H. E. Bakker, S. Dussi, B. L. Droste, T. H. Besseling, C. L. Kennedy, E. I. Wiegant, B. Liu, A. Imhof, M. Dijkstra, and A. van Blaaderen, "Phase diagram of binary colloidal rod-sphere mixtures

from a 3d real-space analysis of sedimentation–diffusion equilibria," *Soft Matter*, vol. 12, no. 45, pp. 9238–9245, 2016.

[203] I. Ahmad, H. J. W. Zandvliet, and E. S. Kooij, "Shape-induced separation of nanospheres and aligned nanorods," *Langmuir*, vol. 30, no. 27, pp. 7953–7961, 2014.

[204] H. Su, Y. Zhong, T. Ming, J. Wang, and K. S. Wong, "Extraordinary Surface Plasmon Coupled Emission Using Core / Shell Gold Nanorods," *The Journal of Physical Chemistry C*, vol. 116, pp. 9259–9264, 2012.

[205] Q. Zhan, X. Zhang, Y. Zhao, J. Liu, and S. He, "Tens of thousands-fold upconversion luminescence enhancement induced by a single gold nanorod," *Laser and Photonics Reviews*, vol. 9, no. 5, pp. 479–487, 2015.

[206] H. U. Yang, J. D'Archangel, M. L. Sundheimer, E. Tucker, G. D. Boreman, and M. B. Raschke, "Optical dielectric function of silver," *Physical Review B*, vol. 91, no. 23, p. 235137, 2015.

[207] F. Sigworth, "Imagic, MRC and DM3 file i/o." Retrieved from: mathworks.com/matlabcentral/fileexchange/27021-imagic–mrc-and-dm3-file-i-o (03-11-2016). Copyright ©2010, Fred Sigworth. All rights reserved.

Appendix A

List of chemicals and apparatus

A.1 Chemicals and glassware

All chemicals were used as received without further purification. The following chemicals were used: chloroauric acid trihydrate ($HAuCl_{4.3}H_2O$, Acros Organics no. 411070010), hexadecyltrimethylammonium bromide (CTAB, >98%, TLC no. H0081), sodium oleate (NaOL, >97%, TLC no. O0057), $AgNO_3$ (≥99.0%, Sigma-Aldrich no. 209139), L-ascorbic acid (AA, vitamin C, ≥99%, Sigma-Aldrich no. A5960), hydrochloric acid (HCl 37% aqueous solution, Sigma-Aldrich no. 258148), nitric acid (HNO_3, 65% aqueous solution, Acros Organics no. 124660025), hydroquinone (≥99%, Fluka no. 53960), Sodium dodecyl sulfate (SDS, ≥99%, Sigma-Aldrich no. 436143), NaOH (Acros Organics no. 134070010), dextran (average mol wt 1,500,000–2,800,000, Sigma-Aldrich no. D5376), butylamine (99.5%, Sigma-Aldrich no. 471305), octadecyltrimethoxysilane (OTMS, 90%, Sigma-Aldrich no. 376213), cyclohexane (≥99.8%, Sigma-Aldrich no. C100307), toluene (≥99.5%, Sigma-Aldrich no. 179418), ethylene glycol (≥99.5%, Fluka no. 03750), tetraethyl orthosilicate (TEOS, 98%, Sigma-Aldrich no. 131903), sodium silicate solution (≥27% SiO_2 basis, Purum ≥10% NaOH. Sigma-Aldrich no. 13729), ethanol (100%, Interchema no. I-AS.102.46D), methanol (prac., Interchema no. 603-001-00-X), (3-mercaptopropyl)trimethoxysilane (MPTMS, 95%, Sigma-Aldrich no. 175617), (3-aminopropyl)triethoxysilane (APTES, 99%, Sigma-Aldrich no. 440140), hydrogen peroxide (H_2O_2, 30 wt%, Sigma-Aldrich no. 216763).

Solutions of $NaBH_4$, AA, $AgNO_3$, sodium silicate, TEOS, H_2O_2, APTES and MPTMS were always prepared directly prior to use. Nanopure water was produced using a Millipore Direct-Q UV and had a resistivity of 18.2 MΩ. All glassware and stirring beans used were cleaned with *Aqua Regia* (a 3:1 V/V mixture of concentrated hydrochloric acid and concentrated nitric acid), rinsed with copious amounts of nanopure water and dried in an oven, except for 2, 4, 20 and 40 mL single-use glass scintillation vials which were used as received unless stated otherwise. Volumetric quantities were determined using the appropriate Finn-pipettes unless stated otherwise.

A.2 Apparatus

The following centrifuges were used:

- Eppendorf 5415C with an F-45-18-11 fixed angle rotor for 2 mL Eppendorf tubes
- Eppendorf 5424R with an FA-45-24-11 fixed angle rotor for 2 mL Eppendorf tubes
- Eppendorf 5430R with an FA-45-24-11 fixed angle rotor for 5 mL Eppendorf tubes
- Hettich Rotina 380R with a 1720 fixed angle rotor for 15 mL and 50 mL centrifuge tubes
- Hettich Rotina 360R with a 5699 swinging bucket rotor for 15 mL and 50 mL centrifuge tubes or glass scintillation vials
- Centrikon T-324 with a fixed angle rotor for 50 mL centrifuge tubes

Extinction spectra were recorded with a Bruker Vertex 70 FT-IR with a quartz beamsplitter and a Si diode detector.

The following electron microscopes were used:

- Fei Tecnai 10 operated at 100 kV for BF-TEM
- Fei Tecnai 12 operated at 120 kV for BF-TEM
- Fei Tecnai 20 with a FEG operated at 200 kV for BF-TEM, (HA)ADF-STEM and secondary-electron SEM
- Fei Talos F200X with a FEG operated at 200 kV for BF-TEM, (HA)ADF-STEM, HR-EDX and tomography
- Phenomworld Phenom Pro operated at 10 kV for low-resolution BSE-SEM
- Fei Helios NanoLab DualBeam operated at 22.5 kV for SE and BS-SEM and with a gallium ion beam FIB-SEM.

Appendix B

Additional data

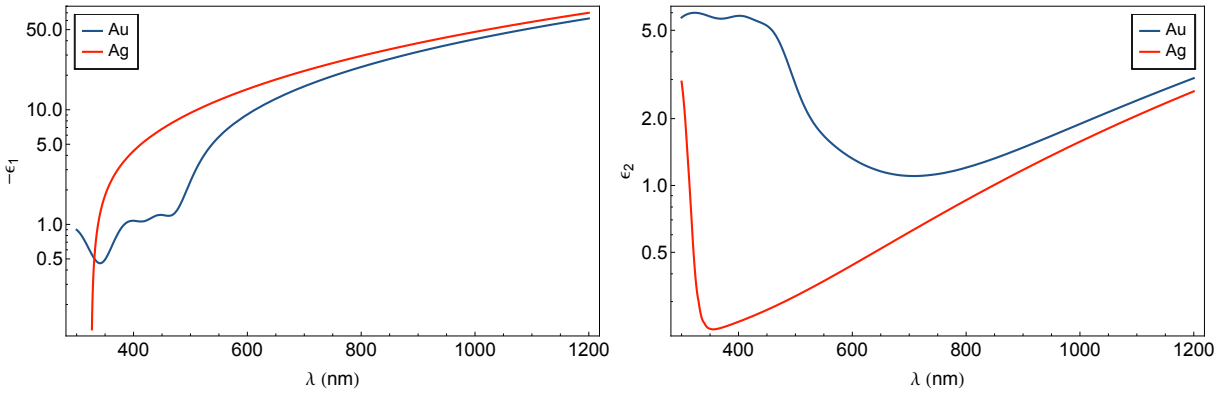

Figure B.1: Logarithmic plots of the negative real ($-\epsilon_1$, left) and imaginary parts (ϵ_2, right) of the dielectric functions for gold and silver. The data were obtained from ref. [61] (Au) and ref. [206] (Ag).

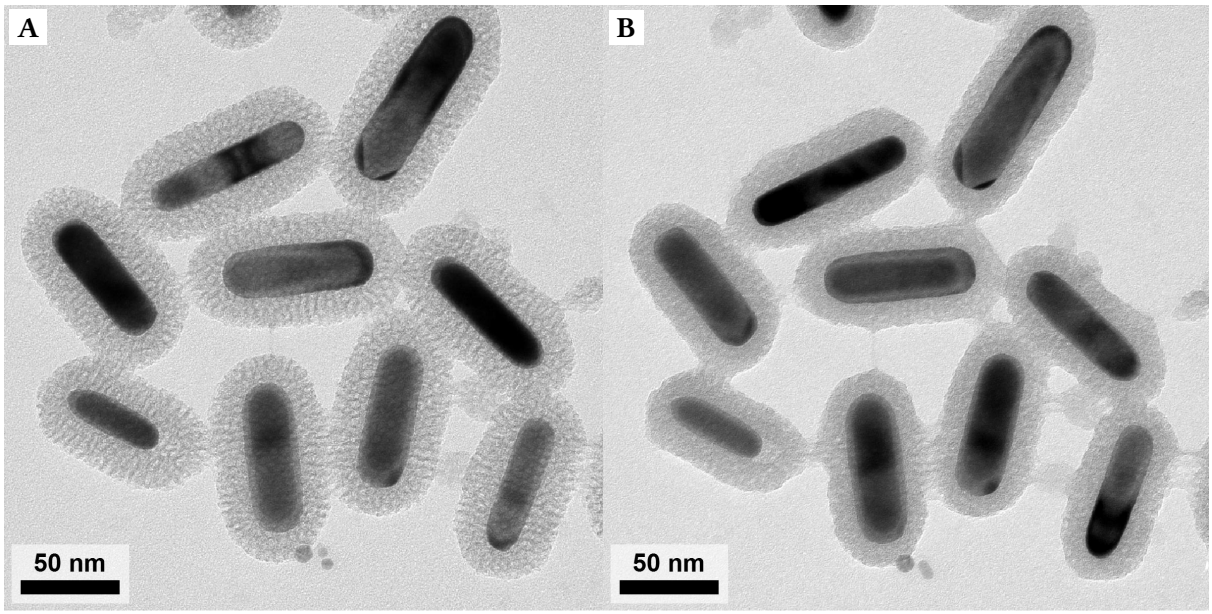

Figure B.2: Beam damage effects in the TEM. A: AuAg CSNRs imaged at low beam intensity; the porous structure of the silica shell can be seen. B: destruction of the silica shell structure when the same area is imaged with a medium electron intensity.

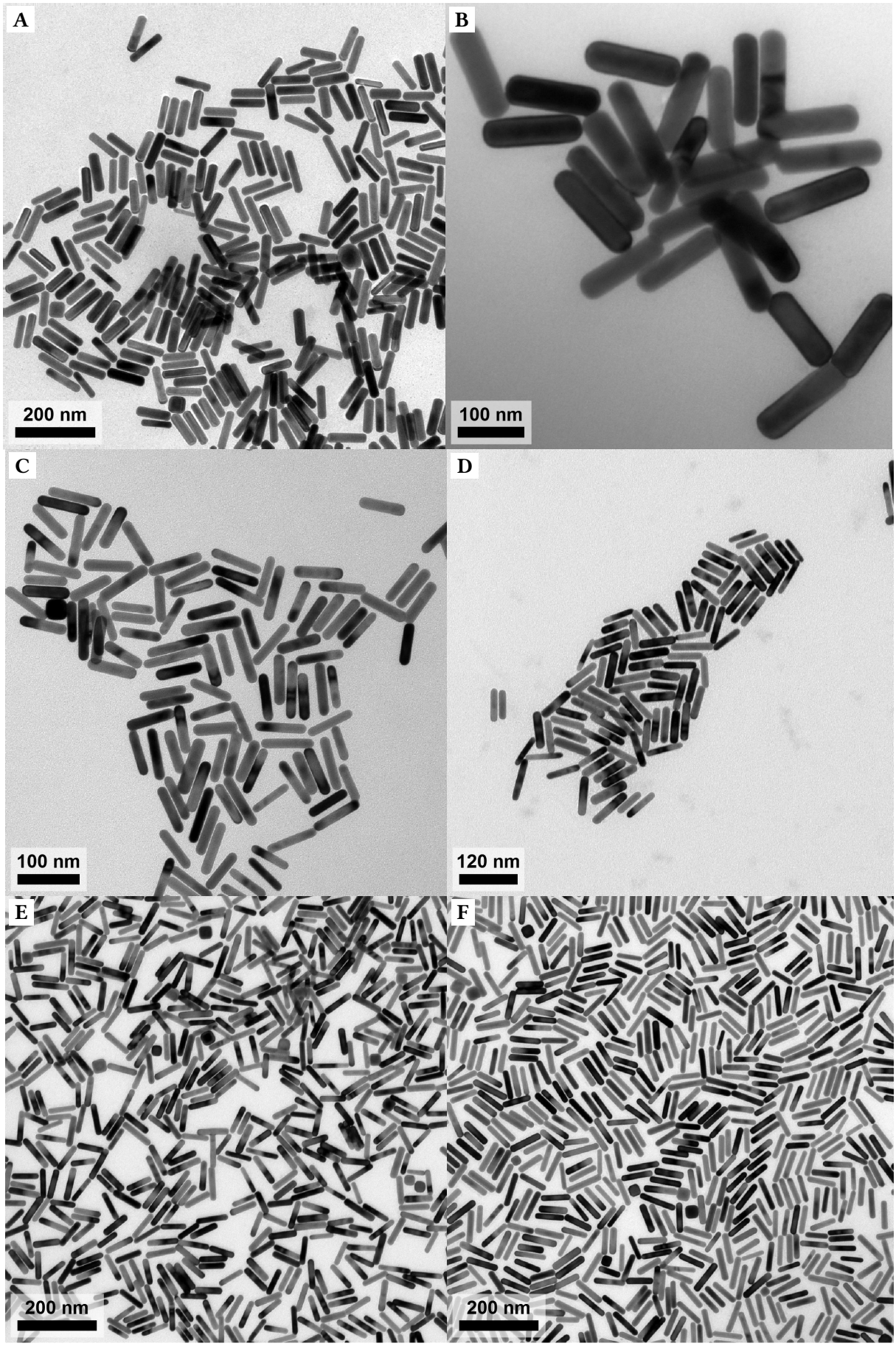

Figure B.3: Different batches of AuNRs prepared with the YM1 method.

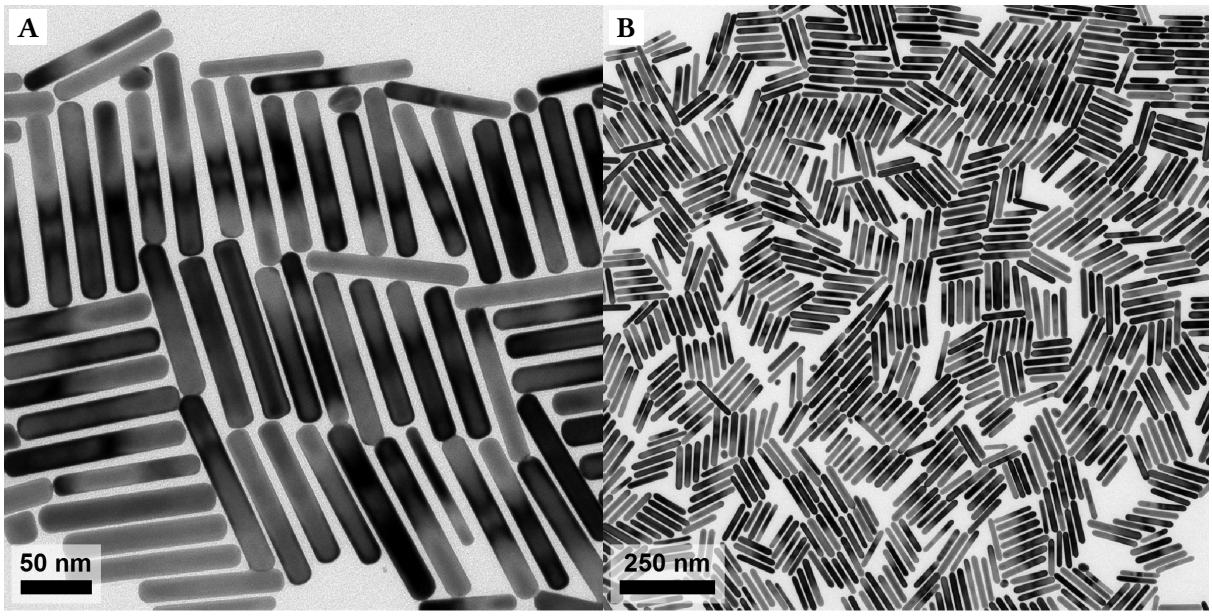

Figure B.4: The two batches of AuNRs prepared with the YM2 method.

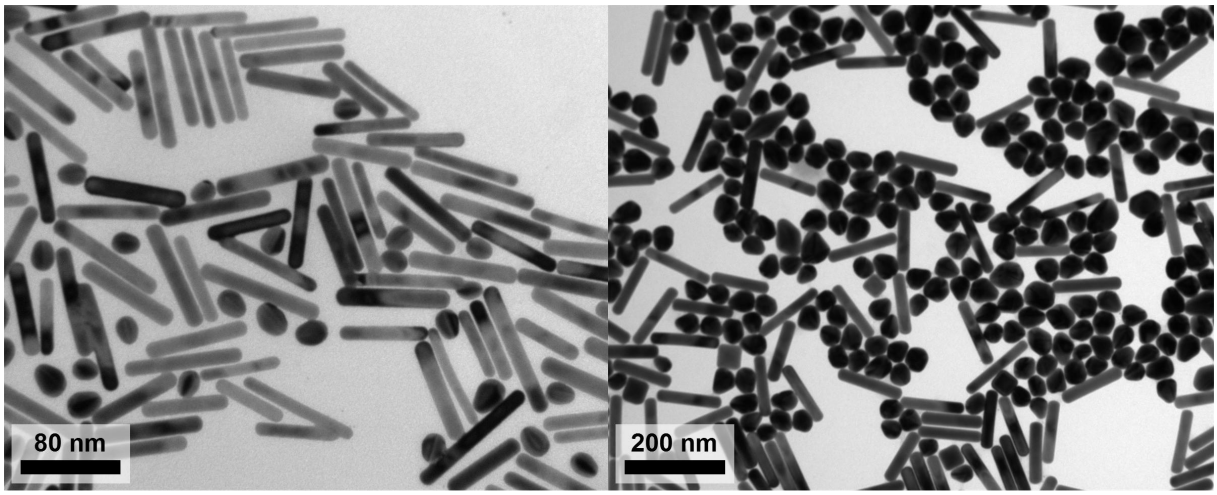

Figure B.5: Two synthesis batches where many non-rodlike particles (shape contaminants) were observed. Left: spherical particles present when precipitation of AgCl was observed after addition of HCl using a YM3 method. Right: YM6 synthesis with a larger CTAB concentration.

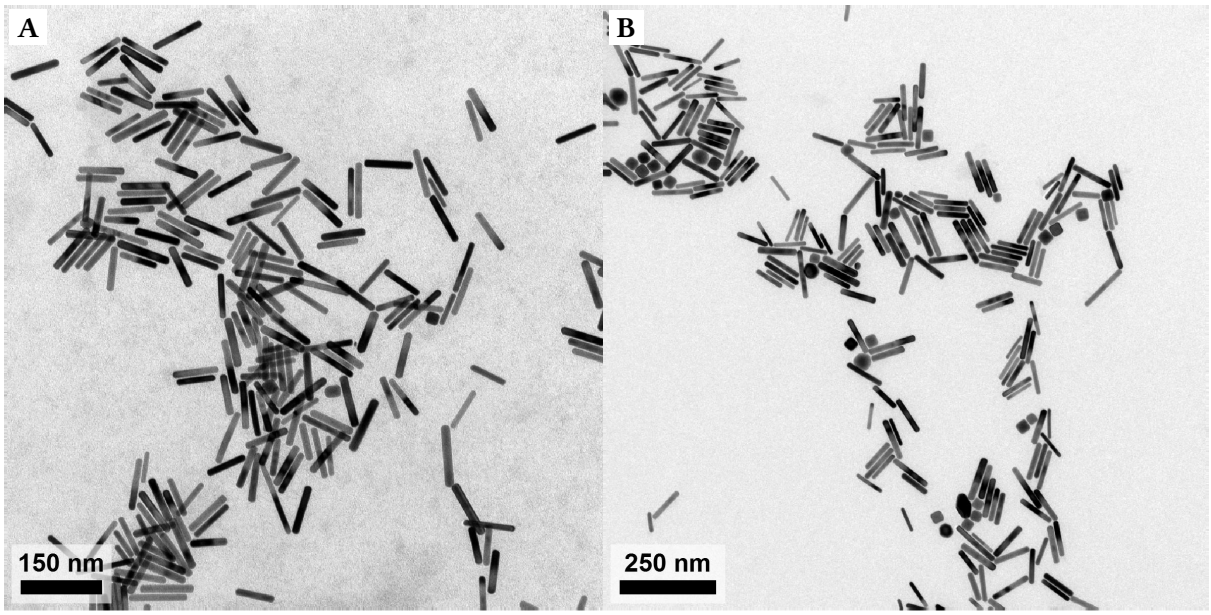

Figure B.6: Fractions from the bottom (A) and side (B) of a centrifuge tube.

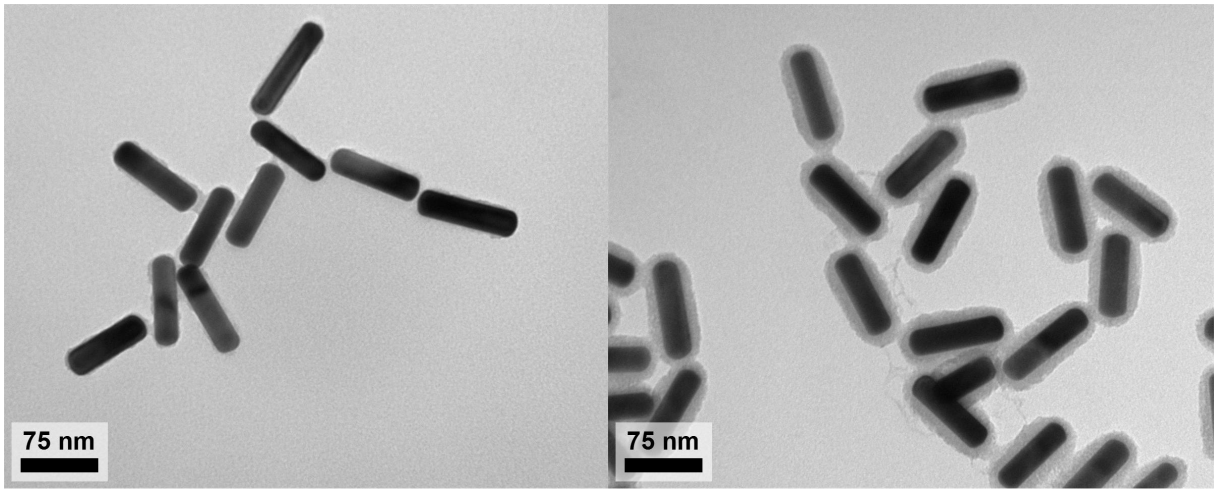

Figure B.7: Evolution of the *meso*-SiO_2 coating over time. Left: 45 minutes after the first TEOS addition (just before the second). Right: 45 minutes after the second TEOS addition

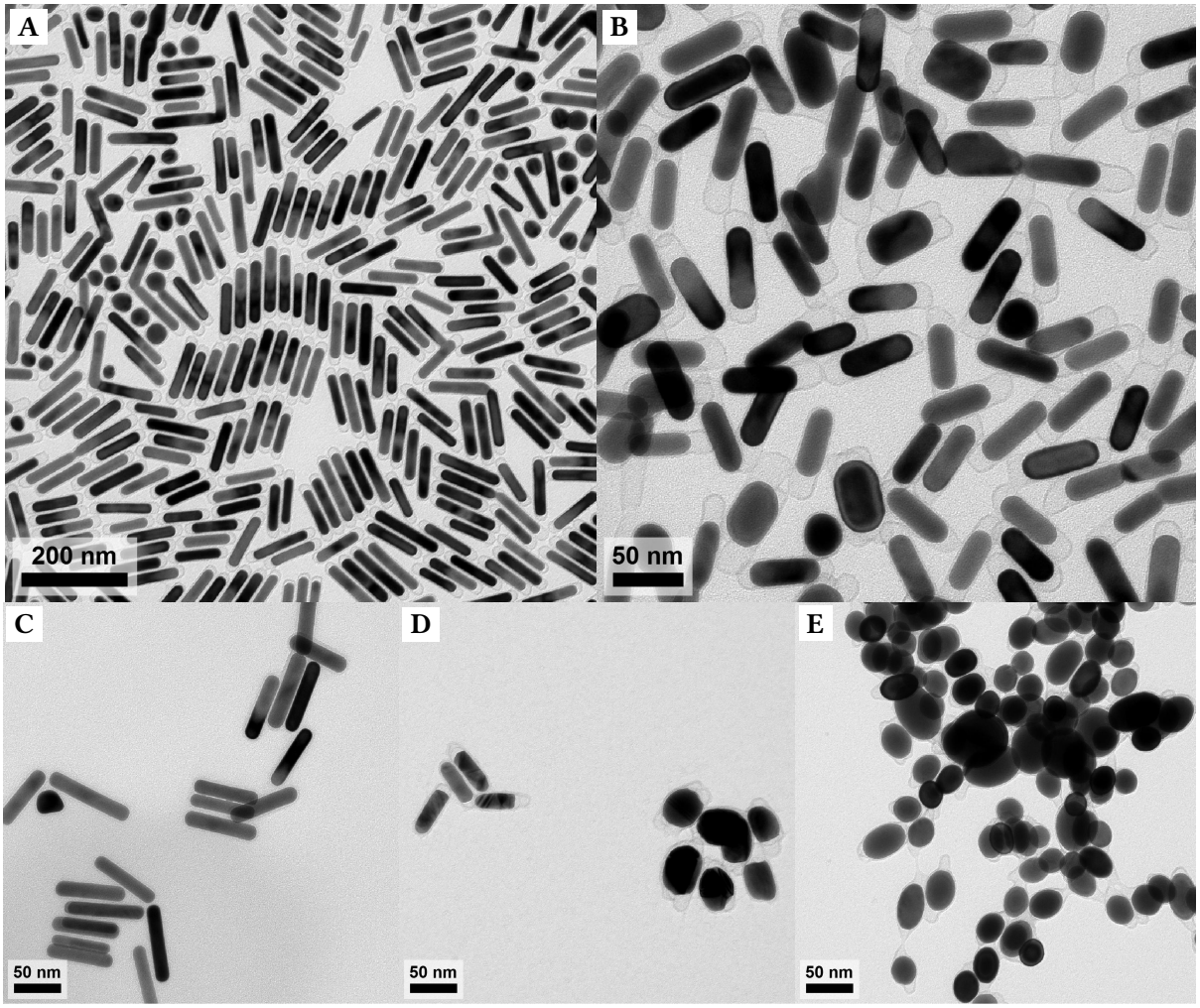

Figure B.8: TEM images of deformation of AuNRs in the thin SiO_2 shell. A&B: representative images of the specific areas on the TEM grid where deformed particles were observed. This accounted in total for less than ~5% of particles. A–C: three areas near each other on the same TEM grid. In this case, very severe deformation was seen.

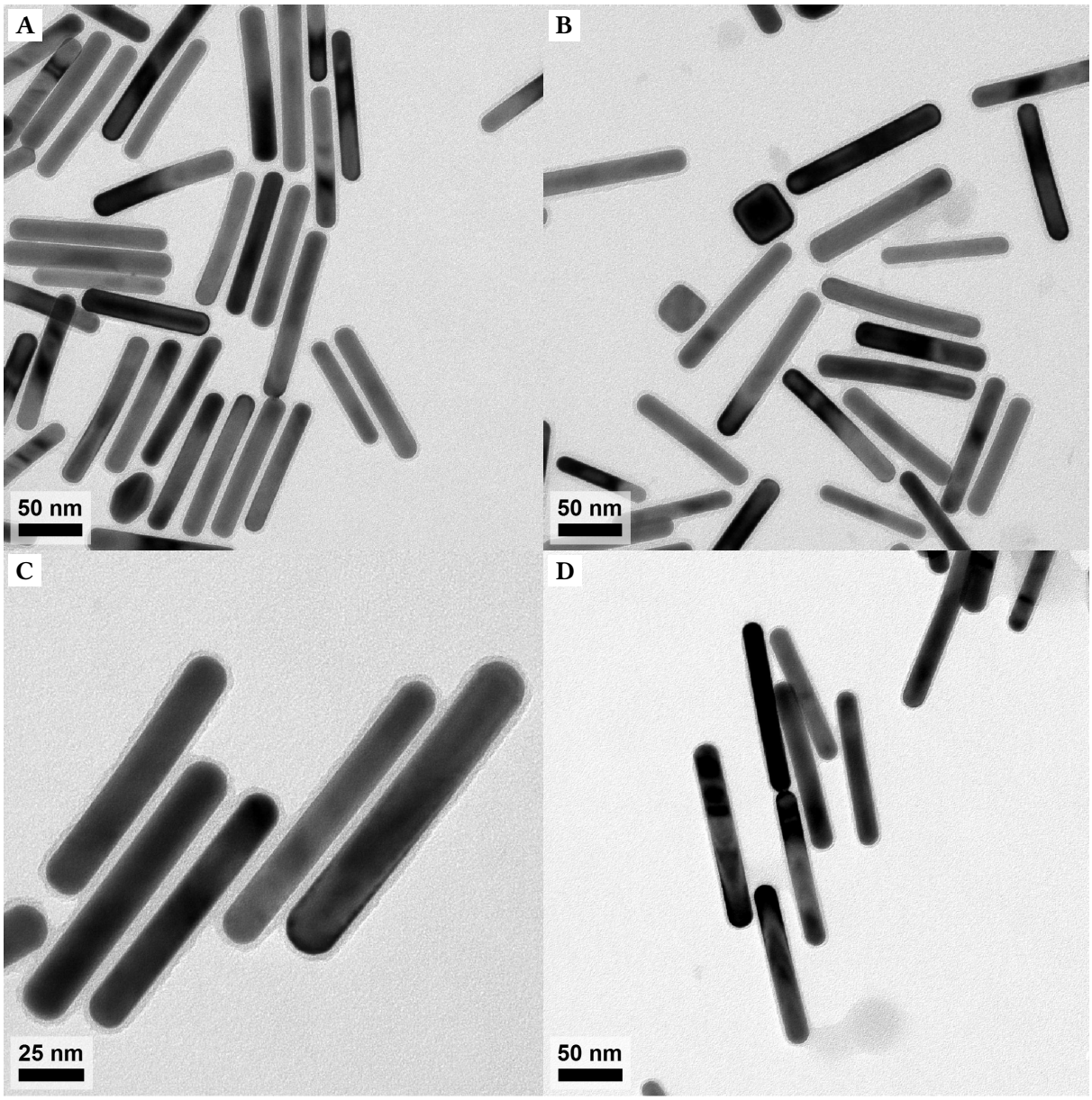

Figure B.9: Additional TEM images of AuNR@thin-SiO_2. All images are of different samples made using the same protocol. The average thickness of the silica shell varied between 2 and 4 nm

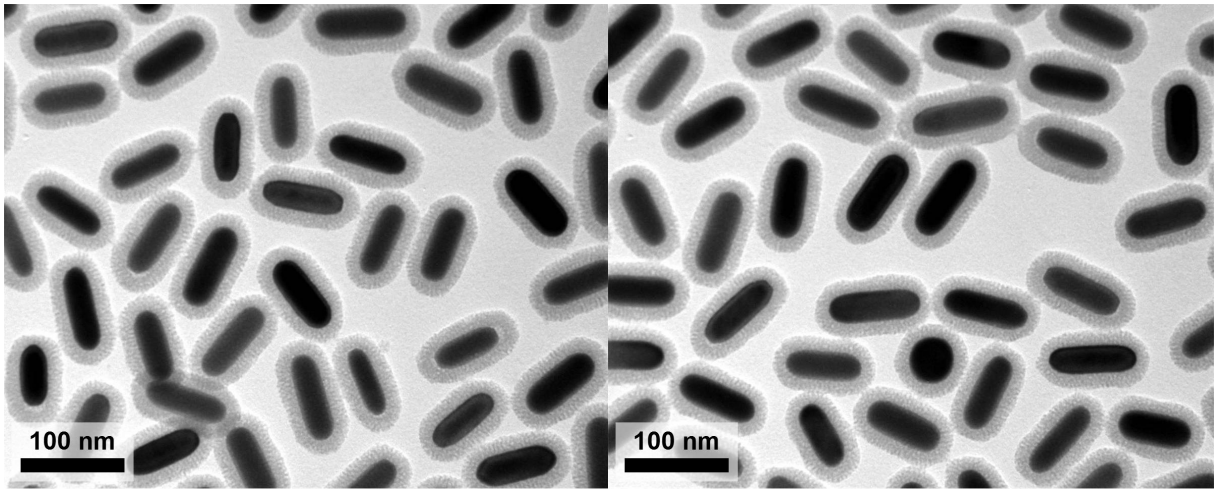

Figure B.10: Representative BF-TEM images of AuAg CSNRs grown at reduced temperature.

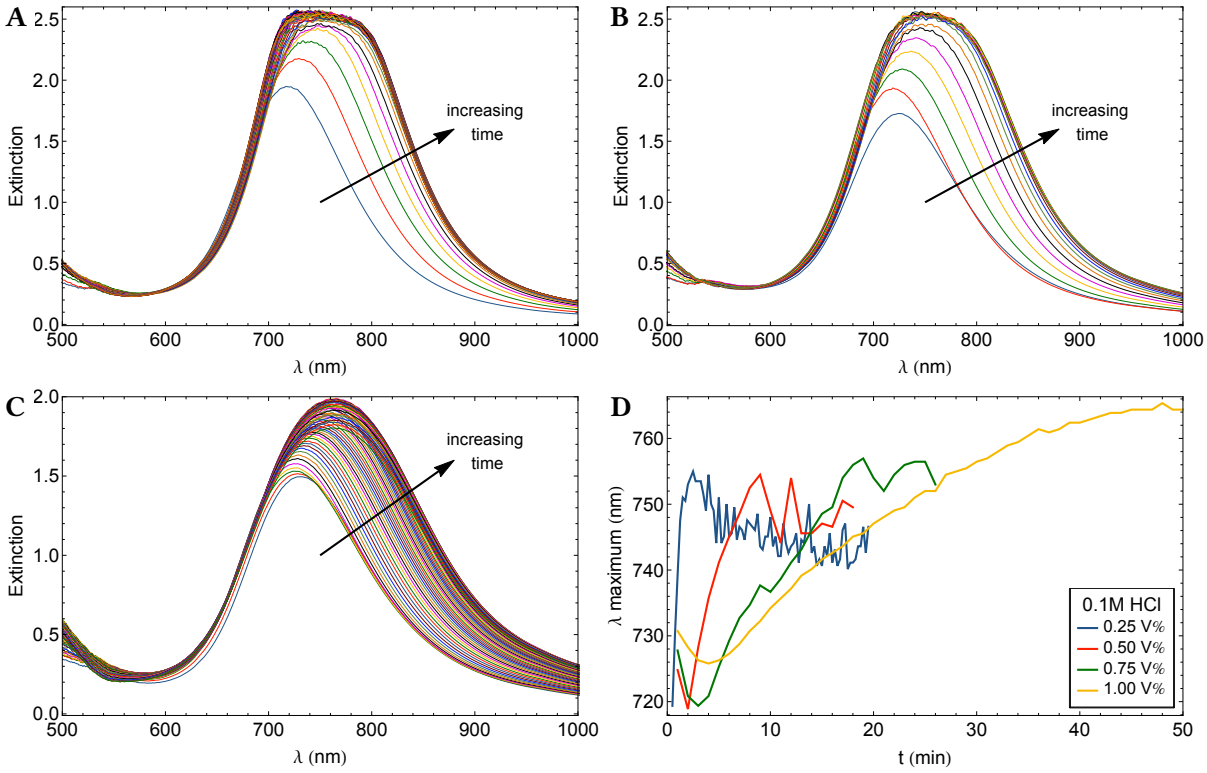

Figure B.11: FTIR extinction spectra of CS-NRs taken during the silver deposition. A: evolution of the spectrum over time during the silver deposition at pH 3.7 (0.25 V%) with a time interval of 15 seconds between the start of the measurements. B: pH 3.3 (0.50 V%) with a time interval of 1 minute. C: pH 3.0 (1.00 V%) with a time interval of 1 minute between the start of the measurements. D: wavelength of the LSPR maximum as a function of the reaction time.

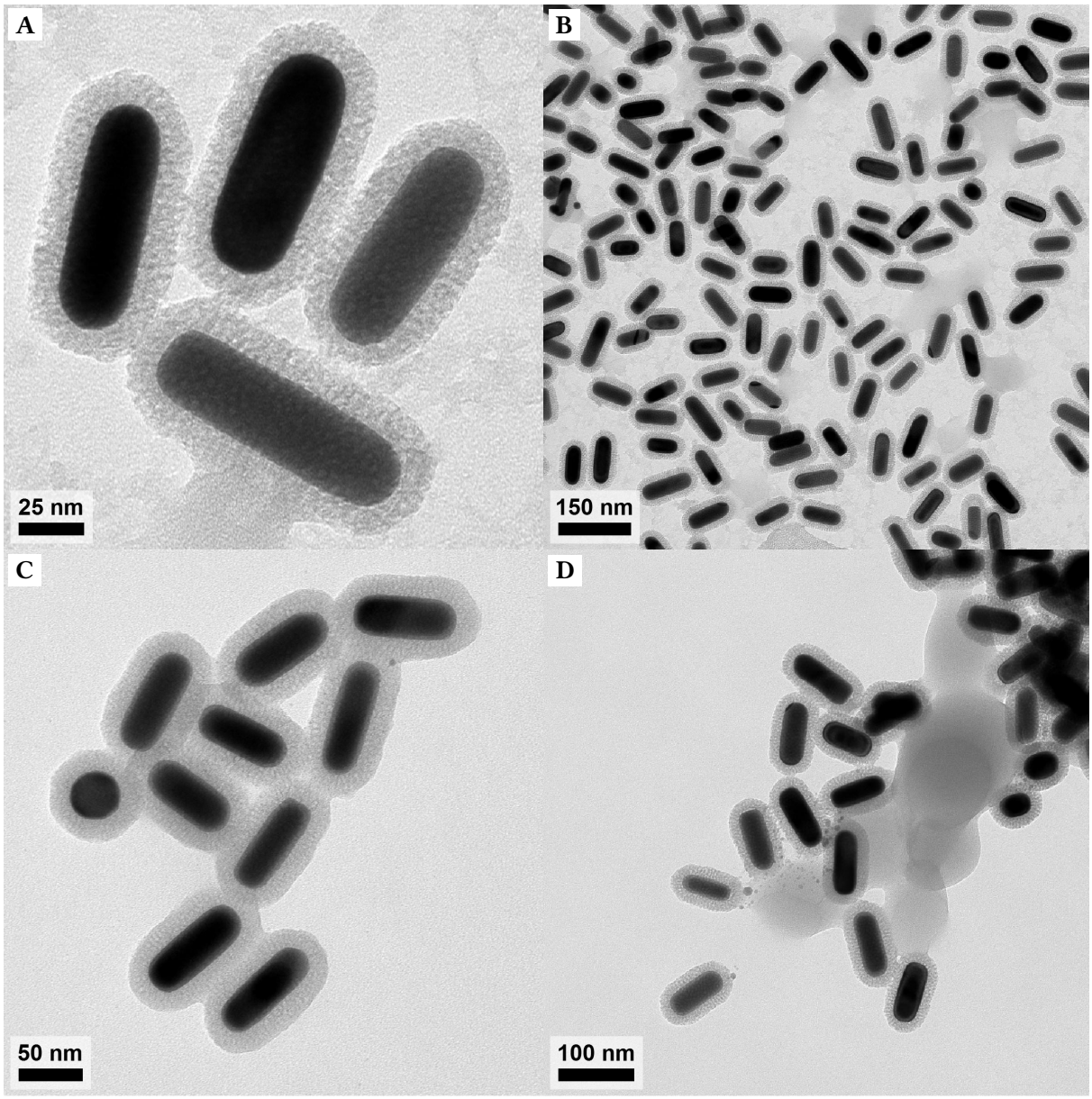

Figure B.12: BF-TEM images of alloying experiments. A&B: AuAg CSNRs alloyed in 80/20 N_2/CO at 500 °C. No deformation or core-shell structure was observed. C: AuAg CSNRs after 4 h at 200 °C in synthetic air, the particles still have a core-shell structure. D: AuAg CSNRs after 24 h at 200 °C in synthetic air, the particles still have a core-shell structure and show only very minor signs of deformation.

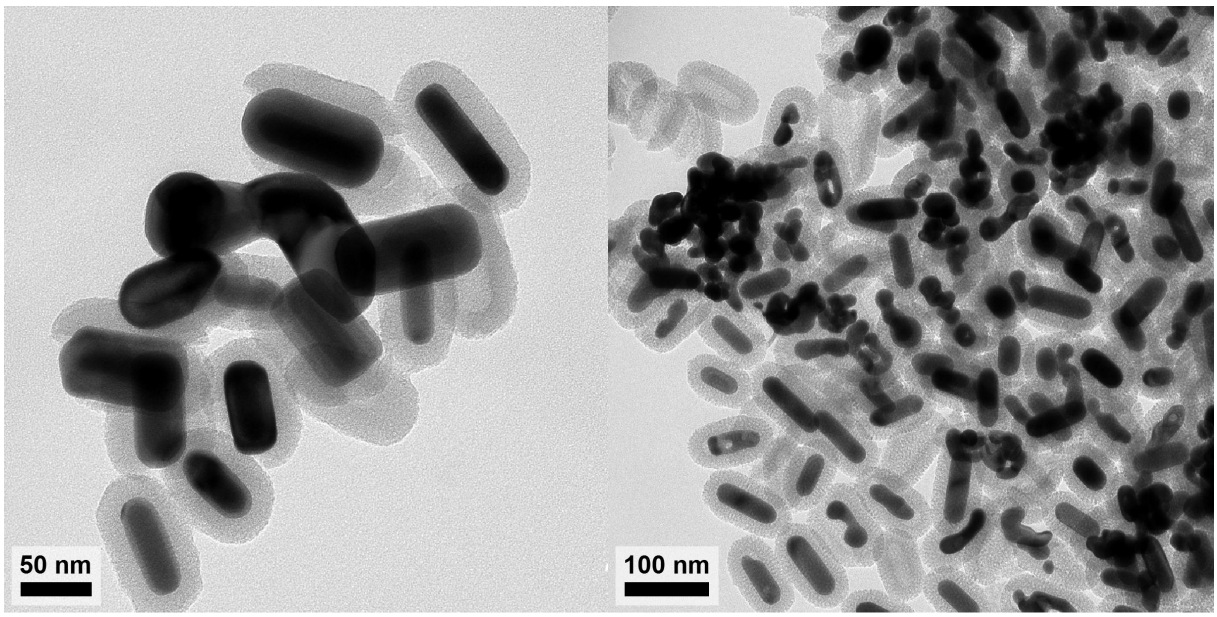

Figure B.13: TEM images of AuAg-CSNRs with a very large silver content (left) and the same particles after alloying and subsequent dealloying with concentrated HNO_3.

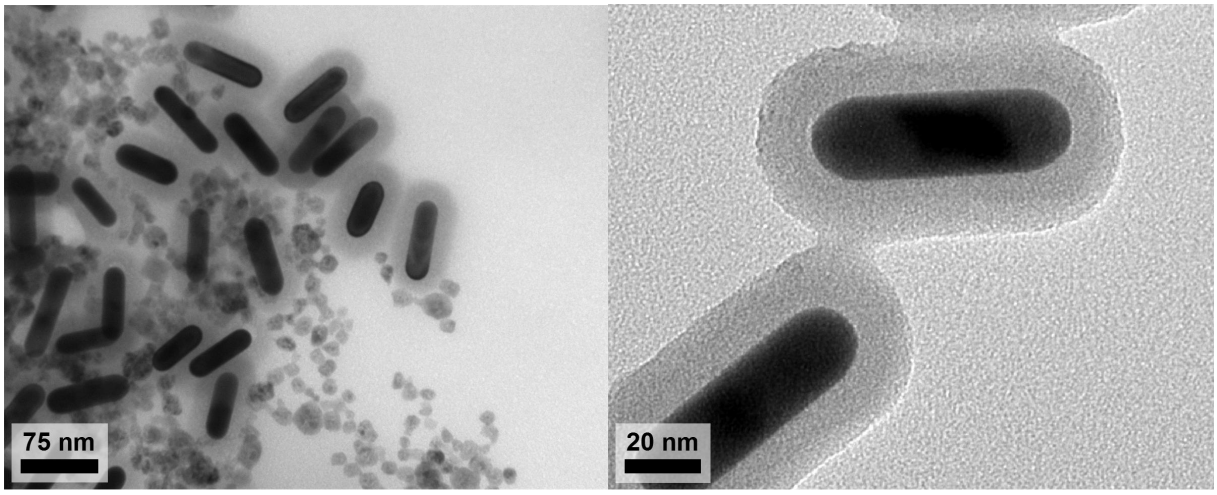

Figure B.14: TEM images of AuNRs after attempted copper(oxide) growth. Left: secondary nucleation when AA at high pH and high concentration is used. Right: AuNRs that underwent a peak shift upon attempted silver deposition. No core-shell structure was observed.

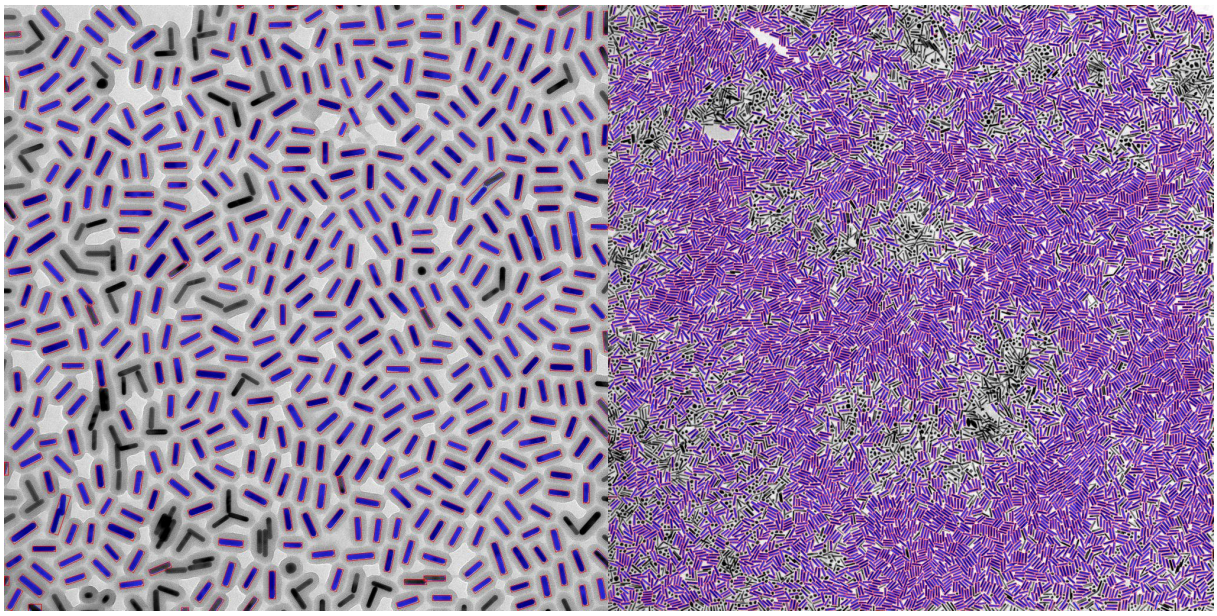

Figure B.15: Results of the custom tracking code for TEM images of AuNRs, the tracked features are highlighted in blue and the corresponding minimum bounding box used for the orientation determination is shown in red.

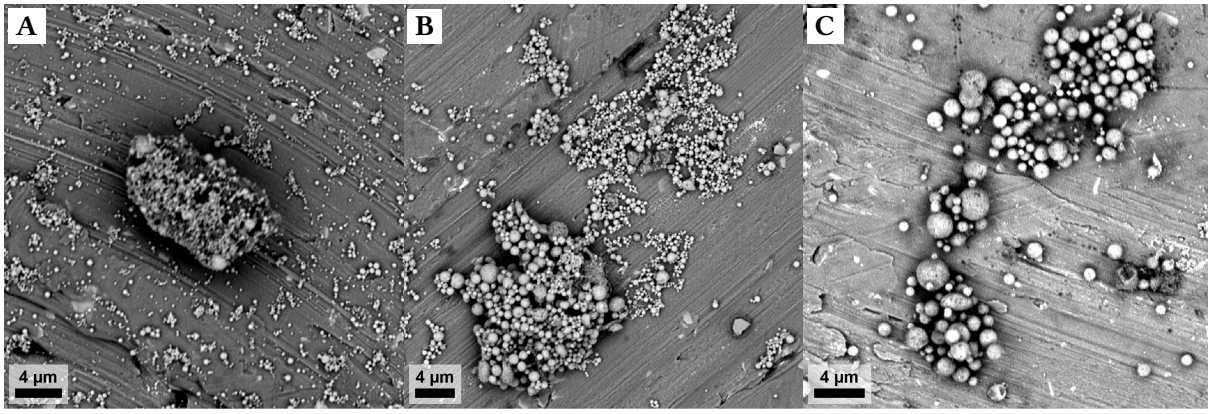

Figure B.16: Low resolution SEM images of supraparticles of AuNR@*meso*-SiO_2 made with different emulsification methods. A: shear-cell, B: sonication, C: shaking and vortex mixing. Grooves in the background are features of the SEM-stub used and not a result of the sample.

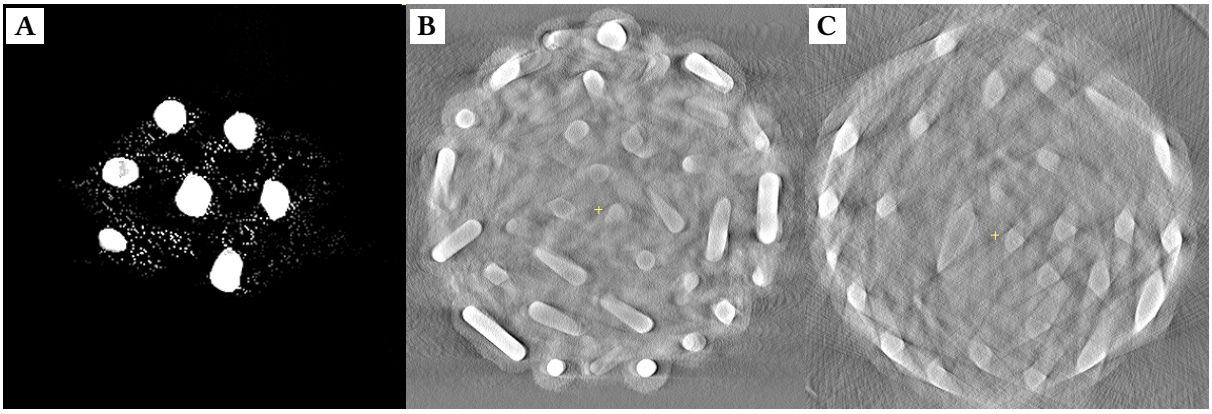

Figure B.17: A: xy orthoslice of a DART reconstruction of the small supraparticle. B & C: xy and xz orthoslices of a WBP reconstruction of the large supraparticle.

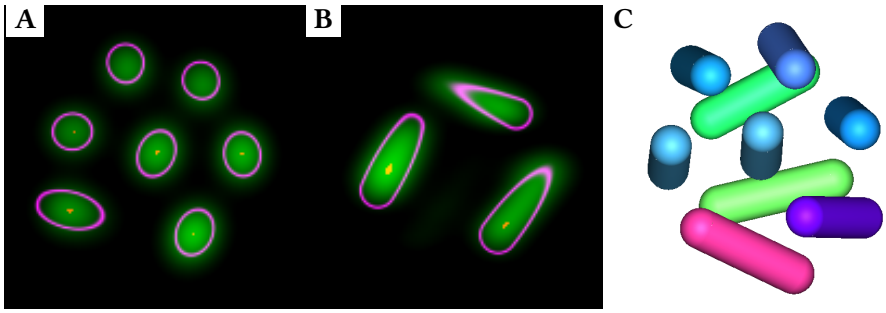

Figure B.18: 3D particle tracking in of the tomographic reconstruction. A&B: overlays of the tracked rods (purple) over the tomography stack after binning, blurring and background subtraction (green) in the xy and xz planes respectively. C: visualisation of the resulting track where the colour indicates the orientation.

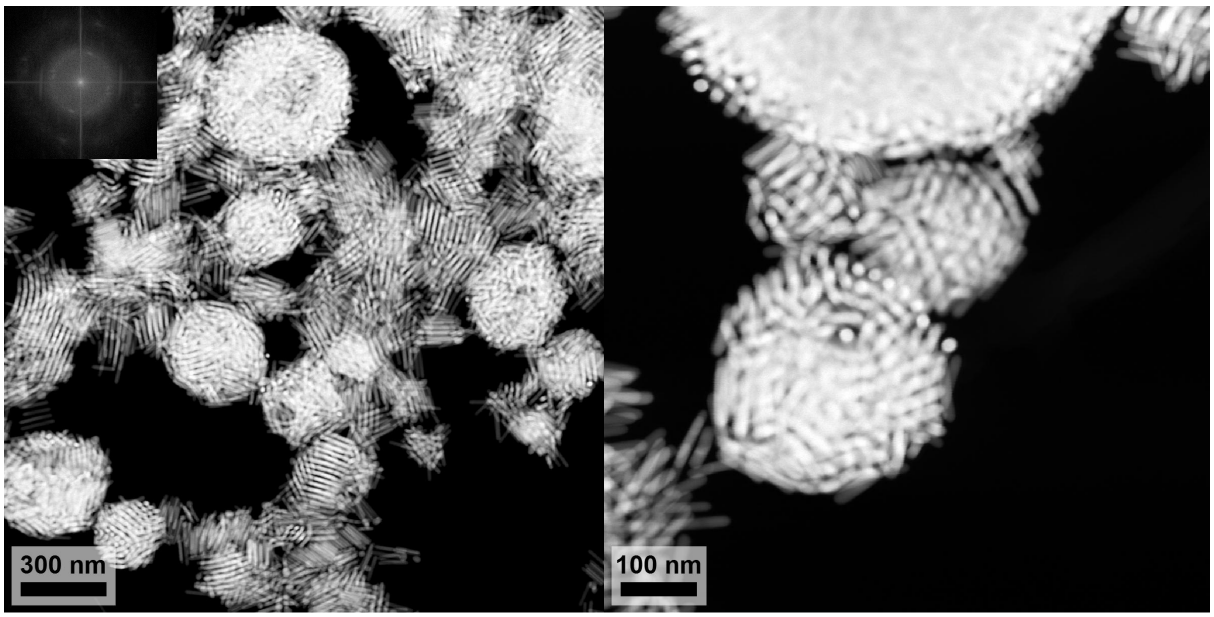

Figure B.19: Left: low magnification HAADF-STEM overview showing the preferred side-by-side ordering of the rods. The inset shows a FFT of the left image where the first ring corresponds with the particle-particle distance (20.5 nm). Right: side-by-side alignment in ordered supraparticles made from AuNRs with $AR = 5.0$.

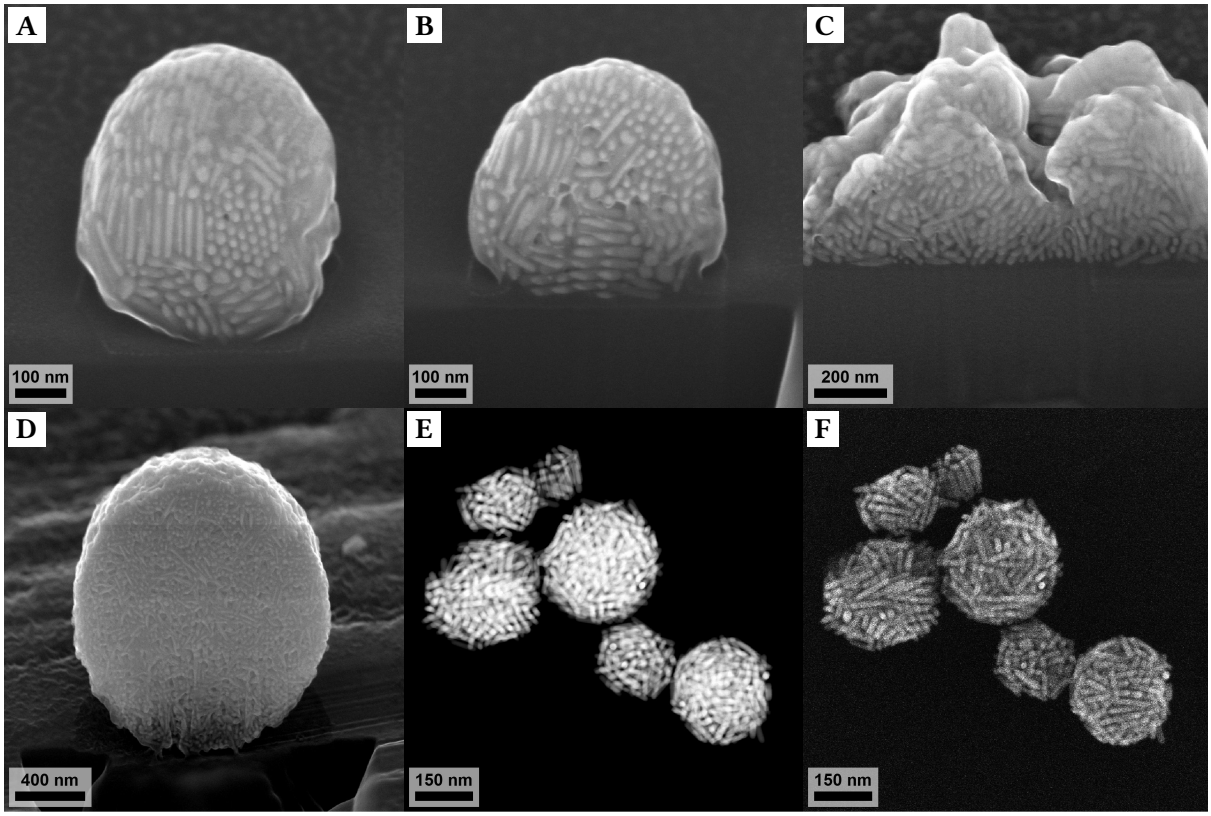

Figure B.20: A&B: slices from FIB-SEM measurements on ordered supraparticle. C: cross-section of a nonspherical ensamble of AuNRs in the sample shown in D&E. D: FIB-SEM cross-section of a large supraparticle consisting of AuNRs with a rough inhomogeneous silica coating. The contrast was digitally enhanced. The AuNRs are randomly oriented in the particle. E&F: HAADF-STEM and SE-SEM images of unordered supraparticles. AuNRs with AR=5 were used.

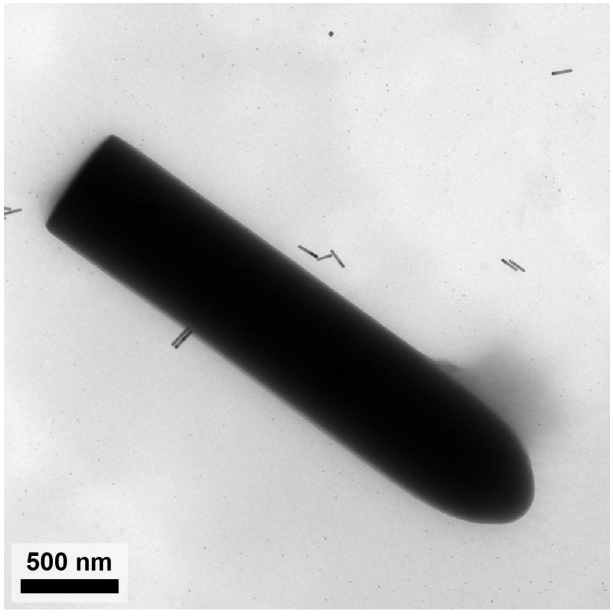

Figure B.21: Size-comparison of a silica rod as frequently used for self-assembly experiments of rod-like particles and the AuNRs used in this research.

Appendix C

Supplementary code

The following is the Wolphram Mathematica [169] code used for the calculation of the orientational correlation functions of 2D BF-TEM images:

```
(*Load data*)
image = ImageResize[ImageTake[Import["image.tif"], 4096], 2048];

(*Settings for tracking*)
minwidth = 8;
maxwidth = 20;
minAR = 4;

(*Run the rodtracking*)
edges = EdgeDetect[image, 1, 0.20];
components = MorphologicalComponents[FillingTransform[edges]];
selected = SelectComponents[components, {"Width", "Length"}, #1 > minwidth && #1 < maxwidth &&
    #2/#1 > minAR &];

(*Get the result*)
data = ComponentMeasurements[{image, selected}, {"Centroid", "Orientation"}][[All, 2]];
coordinates = data[[1 ;;, 1]];
orientation = Mod[data[[All, 2]], Pi] - Pi / 2;

(*Show the result*)
boxes = ComponentMeasurements[{image, selected}, "MinimalBoundingBox"][[;; , 2]];
Show[HighlightImage[image, selected // Image, "HighlightColor" -> Blue], Graphics[{Transparent,
     EdgeForm[Red], Polygon /@ boxes}]]

(*Set range for the order parameter calculation*)
minR = 10;
maxR = 300;
deltaR = 2;

(*Show progress of the calculation*)
ProgressIndicator[Dynamic[i], {1, Length[coordinates]}]
ProgressIndicator[Dynamic[min], {minR, maxR}]

(*Run the orientational correlation function calculation*)
nf = Nearest[coordinates];
radius = {}; s = {}; bin = {};
Table[(*start loop min over all distances*)
  max = min + deltaR;
  theta = {};
  Do[(*start loop i over all particles*)
    a = Complement[nf[coordinates[[i]], {Infinity, max}], nf[coordinates[[i]], {Infinity, min
        }]];
    rot = orientation[[Position[coordinates, #][[1, 1]]]] & /@ a;
    theta = Join[theta, Abs[Mod[orientation[[i]] - #, Pi, -Pi/2] & /@ rot]];
    , {i, Length[coordinates]}
```

```
  ];(*end loop i*)
  bin = Append[bin, min + 0.5*deltaR];
  s = Append[s, 2*Mean[Cos[theta]^2] - 1];
  , {min, minR, maxR, deltaR}
];(*end loop min*)
result = Transpose[{bin, s}];

(*Plot the result*)
ListLinePlot[result, PlotRange -> {{minR, maxR}, {0, 1}}]
```

The following is a code for MATLAB using the ASTRA Toolbox (for reconstruction) and IMagic [207] (for importing and exporting MRC files). The code performs a SIRT reconstruction using 30 iterations of a 512×512 dataset with tilt angles from −70° to 68° in 2° increments. A volume of 415×415×415 pixels is reconstructed.

```
% load data
A = im2double(ReadMRC('binned_tiltseries.mrc'));
proj_data = permute(A(:,:,1:end),[1,3,2]);

% Create volume and projection geometries
angles = linspace2(-70,70,70)/180*pi;
vol_geom = astra_create_vol_geom(415, 415, 415);
proj_geom = astra_create_proj_geom('parallel3d', 1.0, 1.0, 512, 512, angles);
rec_id = astra_mex_data3d('create', '-vol', vol_geom);
proj_id = astra_mex_data3d('create', '-proj3d', proj_geom, proj_data);

% Set up the parameters for a SIRT reconstruction using the GPU
iterations = 30;
cfg = astra_struct('SIRT3D_CUDA');
cfg.ReconstructionDataId = rec_id;
cfg.ProjectionDataId = proj_id;
cfg.option.MinConstraint = 0;

% Create and run the algorithm object
alg_id = astra_mex_algorithm('create', cfg);
astra_mex_algorithm('iterate', alg_id, iterations);

% Get the result
rec = astra_mex_data3d('get', rec_id);

% Rotate, normalise and save the result
rec = permute(rec,[1,3,2]);
rec(rec > 0.01) = 0.01;
rec = (rec-min(rec(:))) ./ (max(rec(:))-min(rec(:)));
WriteMRC(rec,1,reconstruction_SIRT_30.mrc');

% Clean up of memory
astra_mex_algorithm('delete', alg_id);
astra_mex_data3d('delete', rec_id);
astra_mex_data3d('delete', proj_id);
```